STABILITY OF FIBRE-REINFORCED VISCOUS FLOWS

by

CRAIG ROY HOLLOWAY

A thesis submitted to
The University of Birmingham
for the degree of
DOCTOR OF PHILOSOPHY

Lead Supervisor: Dr Rosemary J. Dyson
Co-Supervisor: Prof. David J. Smith

School of Mathematics
College of Engineering and Physical Sciences
The University of Birmingham
May 2017

Abstract

This thesis focusses on two models (inactive and active) for fibre-reinforced viscous flows, examples of which may be found in numerous industrial and biological applications.

In chapters 2-4 we consider Ericksen's model for a transversely isotropic fluid, which treats suspensions of non-motile particles as a continuum with an evolving preferred direction; this model describes fibrous materials as diverse as extracellular matrix, textile tufts and cellulose microfibers. Linear stability analyses of transversely isotropic viscous fluid between two rotating co-axial cylinders and two horizontal boundaries of different temperatures are undertaken in chapters 3 and 4 respectively. In both cases, the inclusion of transversely isotropic effects delays the onset of instability.

In chapter 5 we describe a framework commonly used to model active suspensions, which has been applied to suspensions of self-propelling bacteria, algae and sperm, and artificial swimmers. Through linking this model for an active suspension with that for a transversely isotropic fluid, we identify previously neglected components of the stress tensor that significantly alter the rheology. In chapter 6 we examine the linear stability of isotropic and nearly-aligned suspensions of elongated particles, before giving a summary of our findings in chapter 7.

Acknowledgements

I would like to thank my supervisors Dr Rosemary Dyson and Dr David Smith for their help and encouragement during my time at the University of Birmingham.

I would also like to thank EPSRC for funding my doctoral studies, as well as U21 and the IMA for funding my research trip to visit Dr Edward Green and Dr Richard Clarke at the University of Adelaide and the University of Auckland respectively.

I would like to thank the University of Birmingham postgraduate students who have made my time as a PhD student so enjoyable. Particular thanks go to Gemma Cupples and Dr Meurig Gallagher for helpful discussions about my research.

Last but not least, I would like to thank my wife Sarah for her understanding and positivity over the last few years. My parents, Andrea and Chris, receive my deepest gratitude for the unwavering support of my studies. Without them I would have never got this far.

CONTENTS

List of Publications **v**

1 Introduction **1**

2 Transversely isotropic fluids **8**

2.1 Governing equations 9

2.1.1 Transversely isotropic stress tensor 9

2.1.2 Kinematic equation for fibre evolution 10

2.2 Interpreting the parameters of the transversely isotropic model 13

2.3 Parameter values 14

2.3.1 Capillary viscometry 15

2.3.2 Dilute regime 17

2.3.3 Semi-dilute regime 21

2.4 Summary 24

3 Linear Taylor-Couette stability of a transversely isotropic fluid **26**

3.1 Governing equations and steady state solution 28

3.1.1 Boundary conditions 29

3.1.2 Non-dimensionalisation 29

3.1.3 Steady state 30

3.2 Stability 32

3.2.1 Linear stability analysis 32

3.2.2 Numerical solution method 37

3.3 Results . . . 40
3.4 Discussion . . . 44

4 Linear Rayleigh-Bénard stability of a transversely isotropic fluid 48
4.1 Governing equations . . . 51
4.1.1 Boundary conditions . . . 52
4.1.2 Non-dimensionalisation . . . 53
4.1.3 Steady state . . . 55
4.2 Stability . . . 56
4.2.1 Linear stability analysis . . . 57
4.2.2 Kinematic equation . . . 60
4.2.3 Normal mode solutions . . . 61
4.3 Numerical solution method . . . 62
4.3.1 Chebyshev differentiation matrix . . . 63
4.3.2 Eigenvalue problem . . . 64
4.3.3 Boundary conditions . . . 65
4.3.4 Eigenvalue problem . . . 67
4.3.5 Numerical convergence study . . . 68
4.4 Results . . . 69
4.4.1 Forms of critical curves . . . 81
4.5 Discussion . . . 85

5 Fundamental connections between models of active suspensions and transversely isotropic fluids 88
5.1 Introduction . . . 88
5.2 Governing equations . . . 90
5.2.1 Stress tensor . . . 92
5.2.2 Active stress contribution . . . 93
5.2.3 Influence of non-spherical particles on the bulk stress . . . 98

5.3 Aligned suspension 99
5.4 Conclusion 102

6 Linear stability of isotropic and nearly-aligned suspensions of elongated particles **104**

6.1 Introduction 104
6.2 Governing equations 105
6.2.1 Governing equation for concentration field 106
6.2.2 Non-dimensionalisation 107
6.3 Linear stability of a nearly-aligned suspension 108
6.3.1 Governing equations 109
6.3.2 Linear stability analysis 110
6.3.3 Plane-wave solutions 112
6.3.4 Results 120
6.4 Linear stability of an isotropic suspension 120
6.4.1 Linear stability analysis 121
6.4.2 Plane wave perturbations 126
6.4.3 Numerical method 126
6.4.4 Results 127
6.5 Summary 128

7 Conclusions **134**

7.1 Summary of findings 135
7.2 Future work 141

Appendices **143**

A Boussinesq approximation **144**

A.1 Equations 144
A.2 Equations of motion 148

A.3 Heat equation 151
A.4 Condensed form 152

B Eliminating pressure from the conservation of momentum equation for the transversely isotropic Rayleigh-Bénard problem 154

C Deriving an equation for concentration of a self-motile suspension with translational Brownian motion 157

D Deriving an equation for the director field of a self-motile suspension with translational Brownian motion 159

E Deriving a dispersion relation for a suspension of self-motile nearly-aligned particles 161

LIST OF PUBLICATIONS

1. C. R. Holloway, R. J. Dyson, and D. J. Smith. Linear Taylor-Couette stability of a transversely isotropic fluid. *Proc. R. Soc. Lond. A*, 471(2178) : 20150141, 2015. ISSN 1364 – 5021.

2. C. R. Holloway, G.Cupples, D.J. Smith, J. E. F. Green, R. J. Clarke, and R. J. Dyson. Fundamental connection between models of active suspensions and transversely isotropic fluids. arXiv preprint arXiv:1608.01451 (2016).

Chapters 2 and 3 have been published as 1, whilst chapter 5 is available as 2. Chapters 4 and 6 are in preparation as two manuscripts.

LIST OF FIGURES

1.1 Scanning electron microscopy image of collagen gel [2], showing the fibrous microstructure of the material. Image is licensed under CC BY-SA 3.0. . . 2

1.2 A Couette device where Taylor vortices (fluid doughnuts) are visible [87]. Image is licensed under CC BY-SA 4.0. 3

1.3 Hexagonal patterns appearing which signify the occurrence of convection currents in a solution of gold paint dissolved in acetone [89]. Image is licensed under CC BY-SA 3.0. 4

1.4 Observations of collective bacteria motion by Sokolov *et al.* [78]. Bacteria images for (a) dilute $n_a L^2 = 1.7$ and (b) concentrated $n_a L^2 = 5.6$ suspensions, where n_a is the number of bacteria per unit area and L is the cell length. Vector fields for (c) velocity and (d) orientation of bacteria for the configuration shown in image (b). The vector and orientation fields are different as the bacteria are affected by the background flow, caused by their collective motions. Copyright (2007) by the American Physical Society. 6

2.1 A schematic diagram showing the advection of a short section of fibre over a small time step δt^*. 11

2.2 A schematic diagram of the two-dimensional deformations in the plane of fibres considered in equations (2.14), (2.15), and (2.16), where the fibres are aligned in the x^*-direction. Sub-figures (a) and (b) show an extensional flow orthogonal and parallel to the fibre direction respectively, whilst (c) shows a shear flow. 14

2.3 Schematic diagram of laminar flow in a straight capillary tube. The fluid enters the tube with a volumetric flow rate Q^*, the cylinder has radius ζ^*. The pressure drop ΔP^* is measured over a known length ΔL^*. 15

2.4 Functional dependence of (a) $\mu^*/\bar{\mu}^*$, (b) $\mu_2^*/\bar{\mu}^*$, (c) $\mu_3^*/\bar{\mu}^*$, and (d) α_0, on the aspect ratio of the fibres (r) in a dilute regime. Reproduced from Lipscomb [54]. 20

2.5 Schematic diagram of aligned fibres intersecting a unit plane perpendicular to their direction. 22

3.1 A schematic diagram of a Couette device containing a fibre-laden fluid. The inner and outer cylinders have radii R_1^* and R_2^*. The outer cylinder is fixed, whilst the inner cylinder rotates with angular velocity ω^*. 26

3.2 Steady state velocity as a function of radius. (a) The steady state velocity as a function of r, for a gap ratio $\eta = 0.5$ and angular velocity $\Omega = 100$. (b) A schematic diagram showing how this flow profile appears through a cross-section of the cylinders. 31

3.3 Marginal stability curves for different viscosity parameters μ_2 and μ_3 taking $\eta = 0.5$. Both Figures show the curves of the least eigenvalue $T_l(k)$. (a) The marginal stability curves for changes in anisotropic extensional viscosity μ_2, where the arrow indicates the direction of increase ($\mu_2 = 0, 250, 500, 750, 1000,\ \mu_3 = 0$). (b) Marginal stability curves where the anisotropic shear viscosity μ_3 also varies, arrows again show the direction of increasing μ_2, ($\mu_2 = 0, 250, 500, 750, 1000$). 40

3.4 Critical wave-number (k_c) for changes in the anisotropic extensional viscosity μ_2, and anisotropic shear viscosity μ_3 taking $\eta = 0.5$, note that qualitatively similar results are obtained for all gap widths considered. (a) Critical wave-number for increases in μ_3, where the arrow indicates increasing μ_2 ($\mu_2 = 0, 250, 500, 750, 1000$). (b) Critical wave-number for increases in μ_2, where the arrow indicates increasing μ_3 ($\mu_3 = 0, 250, 500, 750, 1000$). 42

3.5 Critical Taylor number (T_c) for changes in the anisotropic extensional viscosity (μ_2), and the anisotropic shear viscosity (μ_3) taking $\eta = 0.5$. (a) Critical Taylor number for increases in μ_3, where the arrow indicates increasing μ_2 ($\mu_2 = 0, 250, 500, 750, 1000$). (b) Critical Taylor number for increases in μ_2, where the arrow indicates increasing μ_3 ($\mu_3 = 0, 250, 500, 750, 1000$). . 43

3.6 Examining how changes in the gap ratio (η), for different values μ_2 and μ_3 affect the critical wave-number (k_c) and critical angular velocity of the inner cylinder (Ω_c). (a) Shows the effect on k_c for varying η, μ_2, and μ_3, where the arrows show the direction of increasing μ_2 ($\mu_2 = 0, 500, 1000$). (b) Shows the effect upon Ω_c for varying η, μ_2, and μ_3, where the arrow shows the direction of increasing μ_2 ($\mu_2 = 0, 500, 1000$). 43

3.7 Qualitative dependence of maximum achievable LD signal on gap width. (a) Critical average shear rate $\langle e_{r\theta} \rangle_c$ at the critical angular velocity of the inner cylinder. (b) Hypothesised saturating relationship between average shear stress and alignment $\mathcal{A}(\langle e_{r\theta} \rangle)$, based on Figure 3 in McLachlan *et al.* [59]. (c) Critical average shear rate multiplied by dimensionless gap thickness $(1 - \eta) \langle e_{r\theta} \rangle_c$, indicating the hypothetical magnitude of signal in the regime where alignment and shear stress are linearly related. (d) Hypothesised signal calculated from the saturating function $\mathcal{A}$ indicating the magnitude of signal in the saturating regime. We note the indicative signal we propose is the simplest that could be chosen, however other forms of this relation may apply. 45

4.1 A schematic diagram of the Rayleigh-Bénard setup. The lower and upper boundaries are located at $z^* = 0$ and $z^* = d^*$ at temperatures T_0^* and T_1^*. The leading order preferred direction is given by the angle $\theta^{(0)}$. 48

4.2 Maximum relative error in wave-number (E_k^R) and Rayleigh number (E_R^R) for changes in the number of Chebyshev polynomials (N), and iterative stopping parameters for the critical wave-number (k_{Tol}) and critical Rayleigh number (R_{Tol}). (a) Relative error in wave-number for increases in N and R_{Tol} for $k_{Tol} = 10^{-5}$, where the arrow indicates increasing N. (b) Relative error in wave-number for increases in N and k_{Tol} for $R_{Tol} = 10^{-5}$, where the arrow indicates increasing N. (c) Relative error in Rayleigh number for increases in N and R_{Tol} for $k_{Tol} = 10^{-5}$, where the arrow indicates increasing N. (d) Relative error in Rayleigh number for increases in N and k_{Tol} for $R_{Tol} = 10^{-5}$, where the arrow indicates increasing N. 70

4.3 Critical wave-number (k_c) for changes in the anisotropic extensional viscosity (μ_2), the anisotropic shear viscosity (μ_3), and the preferred direction in the fluid at steady state ($\theta^{(0)}$) when both boundaries are rigid. In each subfigure the arrows indicate increasing μ_2 ($\mu_2 = 0, 10, 100, 250, 500, 1000$) for (a) $\mu_3 = 0$, (b) $\mu_3 = 10$, (c) $\mu_3 = 100$, and (d) $\mu_3 = 1000$. 72

4.4 Critical wave-number (k_c) for changes in the anisotropic extensional viscosity (μ_2), the anisotropic shear viscosity (μ_3), and the preferred direction in the fluid at steady state ($\theta^{(0)}$) when both boundaries are free. In each subfigure the arrows indicate increasing μ_2 ($\mu_2 = 0, 10, 100, 250, 500, 1000$) for (a) $\mu_3 = 0$, (b) $\mu_3 = 10$, (c) $\mu_3 = 100$, and (d) $\mu_3 = 1000$. 73

4.5 Critical wave-number (k_c) for changes in the anisotropic extensional viscosity (μ_2), the anisotropic shear viscosity (μ_3), and the preferred direction in the fluid at steady state ($\theta^{(0)}$) when the bottom boundary is rigid and the top boundary is free. In each subfigure the arrows indicate increasing μ_2 ($\mu_2 = 0, 10, 100, 250, 500, 1000$) for (a) $\mu_3 = 0$, (b) $\mu_3 = 10$, (c) $\mu_3 = 100$, and (d) $\mu_3 = 1000$. 74

4.6 Critical Rayleigh number ($\mathcal{R}_c$) for changes in the anisotropic extensional viscosity (μ_2), the anisotropic shear viscosity (μ_3), and the preferred direction in the fluid at steady state ($\theta^{(0)}$) when both boundaries are rigid. In each subfigure the arrows indicate increasing μ_2 ($\mu_2 = 0, 10, 100, 250, 500, 1000$) for (a) $\mu_3 = 0$, (b) $\mu_3 = 10$, (c) $\mu_3 = 100$, and (d) $\mu_3 = 1000$. 76

4.7 Critical Rayleigh number ($\mathcal{R}_c$) for changes in the anisotropic extensional viscosity (μ_2), the anisotropic shear viscosity (μ_3), and the preferred direction in the fluid at steady state ($\theta^{(0)}$) when both boundaries are free. In each subfigure the arrows indicate increasing μ_2 ($\mu_2 = 0, 10, 100, 250, 500, 1000$) for (a) $\mu_3 = 0$, (b) $\mu_3 = 10$, (c) $\mu_3 = 100$, and (d) $\mu_3 = 1000$. 78

4.8 Critical Rayleigh number ($\mathcal{R}_c$) for changes in the anisotropic extensional viscosity (μ_2), the anisotropic shear viscosity (μ_3), and the preferred direction in the fluid at steady state ($\theta^{(0)}$) when the bottom boundary is rigid and the top boundary is free. In each subfigure the arrows indicate increasing μ_2 ($\mu_2 = 0, 10, 100, 250, 500, 1000$) for (a) $\mu_3 = 0$, (b) $\mu_3 = 10$, (c) $\mu_3 = 100$, and (d) $\mu_3 = 1000$. 79

4.9 Relative changes to the critical wave-number (k_c), described by the fitted equation (4.98), for changes in the anisotropic extensional (μ_2) and anisotropic shear (μ_3) viscosities for the three different boundary types. In each subfigure the dashed and solid lines represent $\mu_3 = 50$ and $\mu_3 = 1000$ respectively, with the black, blue and red lines representing rigid-rigid, rigid-free and free-free boundary pairs respectively. (a) The relative magnitude of $\cos 4\theta^{(0)}$ ($f_1(e^{-f_5\mu_2} - 1)/(f_2 + \mu_3)k_n$), and (b) the relative decrease to k_c ($f_3\mu_2/(f_4 + \mu_3)k_N$), where k_N is the critical wave-number of a Newtonian fluid for each boundary type. 82

4.10 Comparison of fitted curves with data points for the critical wave-number k_c. The fit for (a) $\mu_3 = 50$ and (b) $\mu_3 = 1000$, where black, blue and red correspond to rigid-rigid, rigid-free and free-free boundary pairs and circles represent data points. We choose $\theta^{(0)} = 0$ so that we represent the largest error between the fitted curves and the data. 83

4.11 Relative changes to the critical Rayleigh number ($\mathcal{R}_c$), described by the fitted equation (4.99), for changes in the anisotropic extensional (μ_2) and anisotropic shear (μ_3) viscosities for different boundary types. In each subfigure the dashed and solid lines represent $\mu_3 = 100$ and $\mu_3 = 1000$ respectively, with the black, blue and red lines representing rigid-rigid, rigid-free and free-free boundary pairs respectively. (a) The relative magnitude of $\cos 4\theta^{(0)}$ $((-g_1/(\mu_3 + 1) + g_2)\mu_2/\mathcal{R}_N)$ and (b) the relative increase to $\mathcal{R}_c$ $((-g_3/(\mu_3^{1/2} + 1) + g_4)\mu_2/\mathcal{R}_N)$, where $\mathcal{R}_N$ is the critical Rayleigh number of a Newtonian fluid for each boundary type. 84

4.12 Comparison of fitted curves with data points for the critical Rayleigh number $\mathcal{R}_c$. The fit for (a) $\mu_3 = 50$ and (b) $\mu_3 = 1000$, where black, blue and red correspond to rigid-rigid, rigid-free and free-free boundary pairs and circles represent data points. We choose $\theta^{(0)} = 0$ so that we represent the largest error between the fitted curves and the data. 84

5.1 A schematic diagram showing the coordinate system used to model the particle distribution function N^*. The particle's position in space is given by the vector $\boldsymbol{x}^* = (x^*, y^*, z^*)$ and its orientation is given by the unit vector $\hat{\boldsymbol{p}}$. 91

5.2 Schematic diagram showing the position of the Stokeslets and their direction to form the stresslet for a (a) puller and (b) pusher. 94

6.1 Schematic diagram to illustrate the different particle shapes when (a) $\alpha_0 = 0.75$, (b) $\alpha_0 = 0.85$ and (c) $\alpha_0 = 0.95$. 106

6.2 Schematic diagrams of (a) an aligned suspension and (b) an isotropic suspension of rod-like particles 109
6.3 The real part of the growth rate ($\mathbb{R}(s)$) for changes in the volume fraction $\phi = 0, 0.1, 0.2$, where the arrow indicates the direction of increase, shape parameter $\alpha_0 = 0.85$ and wave direction (a) $\theta = \pi/8$, (b) $\theta = \pi/4$ and (c) $\theta = 3\pi/8$. 116
6.4 The real part of the growth rate ($\mathbb{R}(s)$) for changes in the volume fraction $\phi = 0, 0.1, 0.2$, where the arrow indicates the direction of increase, shape parameter $\alpha_0 = 0.85$ and wave magnitude (a) $k = 0$, (b) $k = 0.1$ and (c) $k = 1$. 117
6.5 The real part of the growth rate ($\mathbb{R}(s)$) for changes in the shape parameter $\alpha_0 = 0.75, 0.85, 0.95$, where the arrow indicates the direction of increase, volume fraction $\phi = 0.1$ and wave magnitude (a) $k = 0$, (b) $k = 0.1$ and (c) $k = 1$. 118
6.6 The real part of the growth rate ($\mathbb{R}(s)$) for changes in the shape parameter $\alpha_0 = 0.75, 0.85, 0.95$, where the arrow indicates the direction of increase, volume fraction $\phi = 0.1$ and wave direction (a) $\theta = \pi/8$, (b) $\theta = \pi/4$ and (c) $\theta = 3\pi/8$. 119
6.7 A visualisation of the convergence of Newton's method to find the roots of the nonlinear dispersion relation, where $\tilde{\lambda} = x + iy$. The darker the colour the faster the convergence, whilst each colour is a different root. Convergence for (a) $k = 1/8$, (b) $k = 1/4$, (c) $k = 3/8$ and (d) $k = 5/8$. . . 127
6.8 The real part of the dispersion relation for changing volume fraction $\phi = 0, 0.05, 0.1$, where the arrow shows the direction of increase, for fixed shape parameters (a) $\alpha_0 = 0.75$, (b) $\alpha_0 = 0.85$, (c) $\alpha_0 = 0.95$. 129
6.9 The imaginary part of the dispersion relation for changing volume fraction $\phi = 0, 0.05, 0.1$, where the arrow shows the direction of increase, for fixed shape parameters (a) $\alpha_0 = 0.75$, (b) $\alpha_0 = 0.85$, (c) $\alpha_0 = 0.95$. 130

LIST OF TABLES

4.1 The parameter values from curve fitting for the critical wave-number given in equation (4.98) for the different combinations of boundary conditions. . 81

4.2 The parameter values from curve fitting for the critical Rayleigh number in equation (4.99) for the different combinations of boundary conditions. . 83

CHAPTER 1

INTRODUCTION

This thesis is concerned with modelling suspensions of elongated particles in a solvent fluid. We consider two types of particle, *'active'* and *'passive'*; particles are termed *active* if they can propel themselves through the fluid, and *passive* if they have no mechanism of self-propulsion, reorienting due to the background flow and hydrodynamic interactions only. Our aim is to investigate how the rheological changes, induced by the presence of elongated particles in solution, alter the stability characteristics of well-known flow regimes; as well as identifying when these important properties have been neglected in the existing literature.

Fluids containing suspensions of particles are found in numerous industrial and biological applications. Examples involving passive particles include (but are not limited to) solutions of DNA [57], fibrous proteins of the cytoskeleton [16, 47], synthetic bio-nanofibres [59], extracellular matrix [23, 29] and plant cell walls [22]. When the suspension is active, the particle we model may represent micro-organisms that are capable of self-propulsion, such as self-propelling bacteria or spermatozoa; these suspensions exhibit phenomena such as collective behaviour [35, 42, 45, 49, 65, 66, 72] and, as observed recently, superfluidity [55]. Collections of artificial swimmers may also exhibit the properties of active matter [21, 28, 39, 64, 91].

We will give a detailed literature review at the beginning of each chapter, so each chapter is as self-contained as possible, we do however provide a brief overview and motivation

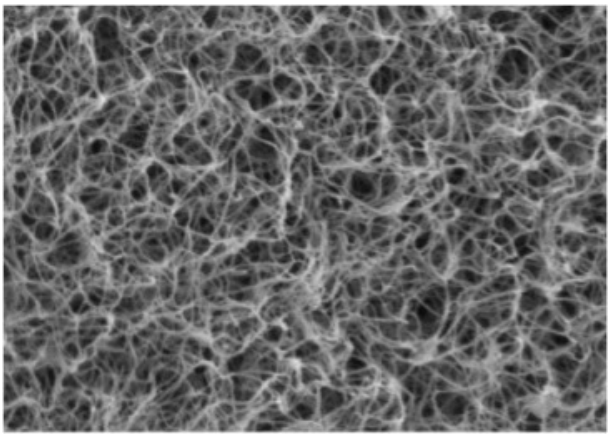

Figure 1.1: Scanning electron microscopy image of collagen gel [2], showing the fibrous microstructure of the material. Image is licensed under CC BY-SA 3.0.

of each chapter here.

In chapter 2 we describe Ericksen's model for a transversely isotropic fluid. This model has been used to model many biological situations, such as the influence of extra-cellular matrix anisotropy and cell-matrix interaction on tissue architecture [23] or the mechanical behaviour of biological gels (such as collagen gels) which have a fibrous microstructure [29] (figure 1.1). Tufts of textile fibres undergoing the carding process have also been treated as a transversely isotropic material [52]. In this thesis we apply Ericksen's model to suspensions of elongated particles/fibres. The presence of these fibres can significantly alter the rheology of the fluid, and hence must be incorporated in any modelling undertaken. A transversely isotropic model treats these suspensions as a continuum with an evolving preferred direction, through a modified stress tensor incorporating four viscosity-like parameters. These parameters intuitively correspond to an isotropic viscosity, an active component, and anisotropic extensional and shear viscosities.

In chapter 3 we consider the axisymmetric linear Taylor-Couette stability of a transversely isotropic viscous fluid, contained between two rotating co-axial cylinders, and determine the critical wave and Taylor numbers for varying gap width and inner cylinder velocity (assuming the outer cylinder is fixed). The critical Taylor number corresponds to the highest angular velocity of the inner cylinder for which a given experimental setup remains stable, and the flow is laminar. As the angular velocity is increased above the

Figure 1.2: A Couette device where Taylor vortices (fluid doughnuts) are visible [87]. Image is licensed under CC BY-SA 4.0.

critical Taylor number the first fluid instability to occur is the appearance of Taylor vortices ('fluid doughnuts', Figure 1.2); the critical wave-number corresponds to the height of these doughnuts. Through the inclusion of transversely isotropic effects, the onset of instability is delayed, increasing the range of stable operating regimes. This effect is felt most strongly through the incorporation of the anisotropic shear viscosity, although the anisotropic extensional viscosity also contributes. The changes to the rheology induced by the presence of the fibres therefore significantly alters the dynamics of the system, and hence should not be neglected. This problem is both interesting theoretically, as a canonical example from traditional fluid mechanics, as well as practically, as Couette devices are used, in combination with linear dichroism spectroscopy, to analyse long biological molecules in suspension. Flow linear dichroism is particularly useful for particles with high aspect ratio; one current area of interest is exploiting flow linear dichroism for pathogen detection [63].

In chapter 4 we examine the linear Rayleigh-Bénard stability of a transversely isotropic

Figure 1.3: Hexagonal patterns appearing which signify the occurrence of convection currents in a solution of gold paint dissolved in acetone [89]. Image is licensed under CC BY-SA 3.0.

fluid. Here the fluid is contained between two infinite horizontal planes of different temperatures, which may be a combination of either rigid or free; we determine the critical wave and Rayleigh numbers for a variety of steady state preferred directions and boundary types. Rayleigh-Bénard convection was first observed experimentally by Bénard [8] who melted wax in a metal dish which was heated from below. Bénard noticed that once the base of the dish was heated above a certain temperature hexagonal patterns developed on the surface of the wax, and it was this observation that allowed him to deduce the presence of convection currents in the wax below (figure 1.3). The appearance of the convection current is related to the change in density across the fluid layer, which is in turn due to the temperature difference between the bottom and top boundaries; instability will only occur if the lower boundary is warmer than the upper [20]. Rayleigh [67] was the first to form a mathematical model of this experiment, using equations for the energy and state of an infinite layer of fluid, bounded by two stationary horizontal boundaries of different constant uniform temperatures. The governing equations are stated under the Boussinesq approximations, where the full model for a compressible fluid, which should be used as density is not constant, may be simplified. The Boussinesq approximations state the fluctuations in density which appear result from thermal (as opposed to pressure) effects, and in the equations for conservation of mass and momentum, density variations

may be neglected except when they are coupled to the gravitational acceleration in the buoyancy force. Spiegel & Veronis [81] show, through a self-consistent approximation, the conditions under which the Boussinesq approximations are valid. We show this in Appendix A. Rayleigh was able to determine the critical wave and Rayleigh numbers when both boundaries were 'free', however to determine the critical values of other combinations of boundary types (rigid-rigid and rigid-free) numerical techniques are required [18]. The critical Rayleigh number corresponds to the largest temperature difference between the two boundaries for which a given experimental setup will remain stable. Once the Rayleigh number increases above the critical value convection currents appear, where the width of the convection currents correspond to the critical wave-number. When the fluid is transversely isotropic, a steady state exists when the fluid is stationary, and there is a single constant preferred direction. Through the inclusion of transversely isotropic effects, we find the onset of instability is delayed. Similarly to chapter 3, the anisotropic shear viscosity has a significant impact on the critical Rayleigh number, with the anisotropic extensional viscosity contributing less. Increases in the anisotropic extensional viscosity give a greater dependance of the critical wave and Rayleigh numbers on the steady state preferred direction.

In chapter 5 we introduce a continuum model for an active fluid, and identify the fundamental connection between models of active suspensions and transversely isotropic fluids. Suspensions of self-motile, elongated particles are a topic of significant current interest, exemplifying a form of 'active matter.' Examples include self-propelling bacteria, algae and sperm, and artificial swimmers; with suspensions of these cells able to exhibit phenomena such as collective behaviour (figure 1.4 [78]). The continuum model we describe couples a Fokker-Planck equation, for a particle distribution function, to a pair of Cauchy momentum equations, for the background fluid velocity. Current models take account of the isotropic and active stresses, but by making fundamental connections between active suspensions and Ericksen's model for a transversely isotropic fluid, we reveal previously neglected components of the stress tensor that significantly alter the

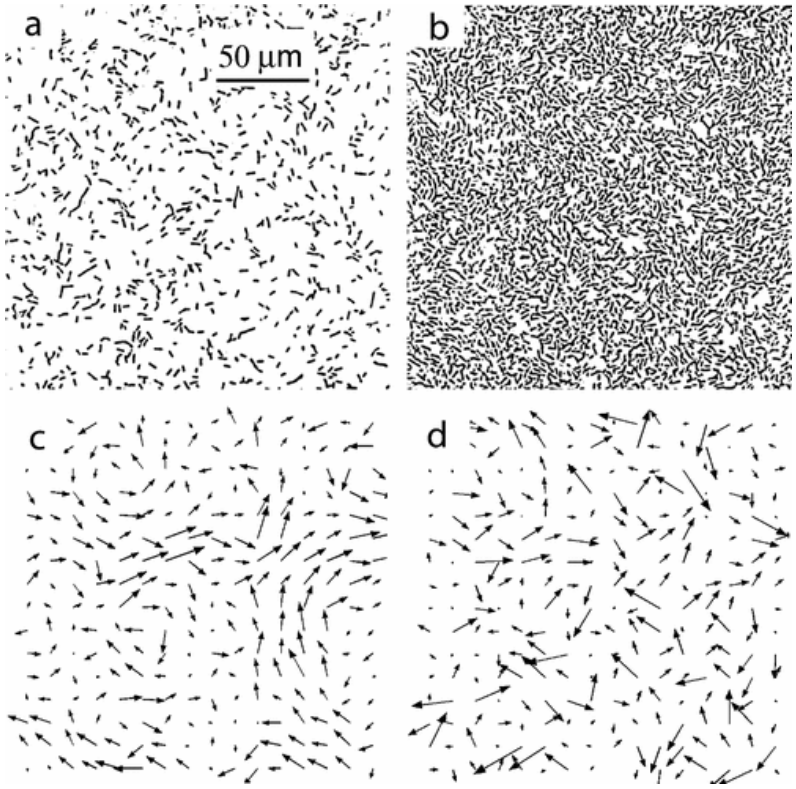

Figure 1.4: Observations of collective bacteria motion by Sokolov *et al.* [78]. Bacteria images for (a) dilute $n_a L^2 = 1.7$ and (b) concentrated $n_a L^2 = 5.6$ suspensions, where n_a is the number of bacteria per unit area and L is the cell length. Vector fields for (c) velocity and (d) orientation of bacteria for the configuration shown in image (b). The vector and orientation fields are different as the bacteria are affected by the background flow, caused by their collective motions. Copyright (2007) by the American Physical Society.

rheology; these components correspond to the anisotropic extensional and shear viscosities, representing the interactions between non-spherical particles with the surrounding fluid.

In chapter 6 we analyse the linear stability of isotropic and nearly-aligned suspensions of elongated particles, when there is no background flow. These systems are interesting because they appear commonly in nature, such as large-scale colonies of bacteria [35, 66], as well as having technological applications, where artificial micro-swimmers are designed to perform various functions [21, 28]; therefore understanding the underlying mechanics of these physical systems is important. We consider plane wave perturbations to the base state, to determine the dispersion relations for dilute suspensions of particles; these

relations describe how a perturbation, with a given wave-number and direction, will grow or decay in time. When the suspension is dilute, the inclusion of anisotropic effects does not alter the physical properties of the fluid or particles required for instability to occur, however they do alter the rate at which perturbations grow and the range of wave-numbers which are unstable.

CHAPTER 2

TRANSVERSELY ISOTROPIC FLUIDS

Fibre-laden fluids are found in numerous industrial and biological contexts, including solutions of DNA [57], fibrous proteins of the cytoskeleton [16, 47], synthetic bio-nanofibres [59], extracellular matrix [29, 23] and plant cell walls [22]. The presence of fibres can significantly alter the rheology and thus their effects must be taken into account. These suspensions can be modelled as a class of anisotropic fluids, for which there is a single preferred direction, and all properties of the fluid are identical normal to this direction. Fluids which exhibit these properties are termed transversely isotropic.

To examine the behaviour of a transversely isotropic fluid, we must define an appropriate constitutive law. We use the constitutive equation derived by Ericksen [24], the simplest form of stress tensor that is linearly dependent upon strain rate and obeys the required invariances to have a single preferred direction (*i.e.* $\boldsymbol{a}$ is physically indistinguishable from $-\boldsymbol{a}$ and the tensor remains of the same form after a coordinate transform) . This model introduces four viscosity-like parameters describing the anisotropic behaviour of the material, along with a preferred direction that evolves according to a kinematic equation. This equation involves a parameter α_0 which may be linked to certain properties of the fluid. When $\alpha_0 > 1$ Ericksen's model has not been shown to represent any physical situation, however in the range $0 < \alpha_0 < 1$, α_0 can be related to the shape of the

fibres by the relation

$$\alpha_0 = \frac{r^2 - 1}{r^2 + 1}, \tag{2.1}$$

where $r = r_1^*/r_2^*$ is the aspect ratio, r_1^* the major axis and r_2^* the minor axis of the fibre. These particles exhibit time-periodic behaviour and hence no steady state is achievable when Brownian effects are neglected, as shown by Jeffery [43]. Green and Friedman [29] derived a kinematic equation corresponding to $\alpha_0 = 1$; this limit of Jeffery's model for fibres which have a large aspect ratio [22] does exhibit steady state alignment. The four viscosity-like parameters intuitively correspond to an isotropic solvent viscosity, a tension due to the presence of fibres, and anisotropic extensional and shear viscosities.

2.1 Governing equations

Here, and in the following, stars denote dimensional variables and parameters. Mass conservation and momentum balance leads to the generalised Navier-Stokes equations

$$\boldsymbol{\nabla}_{\boldsymbol{x}}^* \cdot \boldsymbol{u}^* = 0, \tag{2.2}$$

$$\rho^* \left(\frac{\partial \boldsymbol{u}^*}{\partial t^*} + \left(\boldsymbol{u}^* \cdot \boldsymbol{\nabla}_{\boldsymbol{x}}^* \right) \boldsymbol{u}^* \right) = \boldsymbol{\nabla}_{\boldsymbol{x}}^* \cdot \boldsymbol{\sigma}^*, \tag{2.3}$$

where ρ^* is the constant density of the fluid, $\boldsymbol{u}^*$ is velocity, $\boldsymbol{\nabla}_{\boldsymbol{x}}$ the gradient operator in Cartesian space, t^* is time, and $\boldsymbol{\sigma}^*$ is a transversely isotropic stress tensor that must be specified.

2.1.1 Transversely isotropic stress tensor

Ericksen's stress tensor requires a single preferred direction of the fibres, given by the unit vector $\boldsymbol{a}$, which may vary with both position and time [24]. This is the most general symmetric form of the stress tensor which is linear in rate of strain and where the direction

of the fibres is physically indistinguishable. By neglecting that fibres may rotate about the axis $\boldsymbol{a}$, the stress tensor is given as

$$\boldsymbol{\sigma}^* = -\, p^* \boldsymbol{I} + 2\mu^* \boldsymbol{e}^* + \mu_1^* \boldsymbol{a}\,\boldsymbol{a} + \mu_2^* \boldsymbol{a}\,\boldsymbol{a}\,\boldsymbol{a}\,\boldsymbol{a} : \boldsymbol{e} + 2\mu_3^* \left(\boldsymbol{a}\,\boldsymbol{a} \cdot \boldsymbol{e} + \boldsymbol{e}^* \cdot \boldsymbol{a}\,\boldsymbol{a}\right), \tag{2.4}$$

where p^* is the pressure, $\boldsymbol{e}^* = (\boldsymbol{\nabla}_{\boldsymbol{x}}^* \boldsymbol{u}^* + \boldsymbol{\nabla}_{\boldsymbol{x}}^* \boldsymbol{u}^{*T})/2$ is the rate-of-strain tensor, $\boldsymbol{I}$ is the identity tensor, and μ^*, μ_2^*, and μ_3^* are viscosities, whilst μ_1^* is a stress. The physics underlying this stress tensor will be discussed in section 2.2, however, for now we proceed under the assumption that this is a valid model for a transversely-isotropic fluid.

Ericksen's stress tensor is derived under the assumptions that the unit vector $\boldsymbol{a}$ is invariant under the transformation $\boldsymbol{a} \to -\boldsymbol{a}$, that the fluid is incompressible, and that the resulting tensor should be linear in rate of strain. The stress tensor should also be invariant under orthogonal coordinate transforms, *i.e.* given an orthogonal transformation t_{ij} which takes x_i^* into $x_i^{*\prime} = t_{ij} x_j^*$ [62]

$$\sigma_{ij}^{*\prime} = t_{i\alpha} t_{j\beta} \sigma_{\alpha\beta}^*. \tag{2.5}$$

2.1.2 Kinematic equation for fibre evolution

A kinematic equation is required to explain how the preferred direction of the fibres evolves in reference to the flow, depending on their physical properties. Ericksen's evolution equation for $\boldsymbol{a}$ based on the appropriate invariances and linear dependence upon $\boldsymbol{\nabla}_{\boldsymbol{x}}^* \boldsymbol{u}^*$ is

$$\frac{\partial \boldsymbol{a}}{\partial t^*} + \left(\boldsymbol{u}^* \cdot \boldsymbol{\nabla}_{\boldsymbol{x}}\right) \boldsymbol{a} - \boldsymbol{\omega}^* \cdot \boldsymbol{a} = \alpha_0 \left(\boldsymbol{e}^* \cdot \boldsymbol{a} - \boldsymbol{e} : \boldsymbol{a}\,\boldsymbol{a}\,\boldsymbol{a}\right). \tag{2.6}$$

The vorticity tensor $\boldsymbol{\omega}^* = [\boldsymbol{\nabla}_{\boldsymbol{x}}^* \boldsymbol{u}^* - (\boldsymbol{\nabla}_{\boldsymbol{x}}^* \boldsymbol{u}^*)^T]/2$, and α_0 is a constant which describes the properties of the fibres in suspension [24].

We consider a special case of this condition (corresponding to $\alpha_0 = 1$) that is applicable for fibres with large aspect ratio, by following the derivation of Green & Friedman [29] by

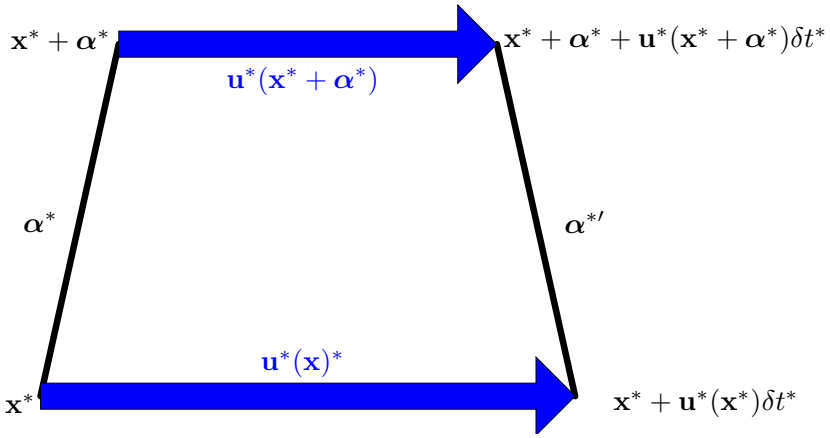

Figure 2.1: A schematic diagram showing the advection of a short section of fibre over a small time step δt^*.

considering how a short section of fibre is advected by a flow $\boldsymbol{u}^*$. Consider the setup shown in Figure 2.1, where a fibre initially located between the points $\boldsymbol{x}^*$ and $\boldsymbol{x}^* + \boldsymbol{\alpha}^*$ is advected by the flow for some small time step δt^*, so the fibre is located between $\boldsymbol{x}^* + \boldsymbol{u}^*(\boldsymbol{x}^*)\delta t^*$ and $\boldsymbol{x}^* + \boldsymbol{\alpha}^* + \boldsymbol{u}^*\left(\boldsymbol{x}^* + \boldsymbol{\alpha}^*\right)\delta t^*$ after advection. This allows us to write:

$$\boldsymbol{\alpha}^{*\prime} = \boldsymbol{\alpha}^* + \boldsymbol{u}^*\left(\boldsymbol{x}^* + \boldsymbol{\alpha}^*\right)\delta t^* - \boldsymbol{u}^*(\boldsymbol{x}^*)\delta t^*, \tag{2.7}$$

where $\boldsymbol{\alpha}^*$ describes the initial length and direction of the fibre, and $\boldsymbol{\alpha}^{*\prime}$ the position and length after it has been advected. Now, using a Taylor Series expansion

$$\boldsymbol{u}^*(\boldsymbol{x}^* + \boldsymbol{\alpha}^*) = \boldsymbol{u}^*(\boldsymbol{x}^*) + (\boldsymbol{\alpha} \cdot \boldsymbol{\nabla}_{\boldsymbol{x}}^*)\, \boldsymbol{u}^*(\boldsymbol{x}^*) + \mathcal{O}\left(|\boldsymbol{\alpha}^*|^2\right), \tag{2.8}$$

and as we consider only a short section of fibre ($|\boldsymbol{\alpha}^*|$ small), equation (2.7) may be written as

$$\frac{\boldsymbol{\alpha}^{*\prime} - \boldsymbol{\alpha}^*}{\delta t^*} = (\boldsymbol{\alpha}^* \cdot \boldsymbol{\nabla}_{\boldsymbol{x}}^*)\, \boldsymbol{u}^*(\boldsymbol{x}^*), \tag{2.9}$$

where we have neglected small terms. Taking the limit $\delta t^* \to 0$ in equation (2.9) gives

$$\frac{\partial \boldsymbol{\alpha}^*}{\partial t^*} + (\boldsymbol{u}^* \cdot \boldsymbol{\nabla}_{\boldsymbol{x}}^*)\, \boldsymbol{\alpha}^* = (\boldsymbol{\alpha}^* \cdot \boldsymbol{\nabla}_{\boldsymbol{x}}^*)\, \boldsymbol{u}^*, \tag{2.10}$$

where the left hand side of equation (2.9) has become a convective derivative. Since our primary interest will be in the direction of the fibres and not their length, we define $\boldsymbol{\alpha}^* = \xi^* \boldsymbol{a}$, where ξ^* is a scalar which describes the length of the section of fibre and $\boldsymbol{a}$ is the unit vector for the fibre direction. Substituting this expression for $\boldsymbol{\alpha}^*$ into equation (2.10) yields

$$\frac{\partial \boldsymbol{a}}{\partial t^*} + (\boldsymbol{u}^* \cdot \boldsymbol{\nabla}_{\boldsymbol{x}}^*)\, \boldsymbol{a} + \frac{\dot{\xi}^*}{\xi^*} \boldsymbol{a} = (\boldsymbol{a} \cdot \boldsymbol{\nabla}_{\boldsymbol{x}}^*)\, \boldsymbol{u}^*, \tag{2.11}$$

where $\dot{\xi}^*/\xi^*$ is the fractional rate of extension of the material in the fibre direction. By taking the scalar product of equation (2.11) with $\boldsymbol{a}$ and exploiting that $\boldsymbol{a}$ is a unit vector, we find

$$\frac{\dot{\xi}^*}{\xi^*} = \boldsymbol{a} \cdot \left[(\boldsymbol{a} \cdot \boldsymbol{\nabla}_{\boldsymbol{x}}^*)\, \boldsymbol{u}^* \right], \tag{2.12}$$

and the fractional rate of extension from equation (2.11) may be eliminated to give

$$\frac{\partial \boldsymbol{a}}{\partial t^*} + (\boldsymbol{u}^* \cdot \boldsymbol{\nabla}_{\boldsymbol{x}}^*)\, \boldsymbol{a} + \boldsymbol{a}\,\boldsymbol{a}\,\boldsymbol{a} : \boldsymbol{\nabla}_{\boldsymbol{x}}^* \boldsymbol{u}^* = (\boldsymbol{a} \cdot \boldsymbol{\nabla}_{\boldsymbol{x}}^*)\, \boldsymbol{u}^*. \tag{2.13}$$

Note since $|\boldsymbol{a}| = 1$, the model encodes only the local alignment direction of fibres and not their length. This result generalizes Jeffery's treatment of the motion of long ellipsoidal particles [43], which align in the direction of the principal rate of strain [22].

2.2 Interpreting the parameters of the transversely isotropic model

We may interpret each of the parameters in equation (2.4) physically. By setting $\mu_1^* = \mu_2^* = \mu_3^* = 0$, the stress tensor for an incompressible isotropic fluid is recovered, with viscosity μ^*. The parameter μ^* is the isotropic component of the solvent viscosity, modified by the volume fraction of fibres [22]. Observe that the third term in equation (2.4) is independent of strain rate and only related to $\boldsymbol{a}$. Therefore μ_1^* implies the existence of a stress in the fluid even if it is instantaneously at rest, and can be interpreted as a tension in the fibre direction [29].

The parameters μ_2^* and μ_3^* may be interpreted by considering two-dimensional deformations in the plane of the fibres, where the active stress in the fibres is zero *i.e.* $\mu_1^* = 0$. In each case we assume the fibres are aligned horizontally in the x^*-direction of the (x^*, y^*)-Cartesian plane, *i.e.* $\boldsymbol{a} = (1, 0)$. We note the following examples are not physically realistic as they do not conserve mass, however we believe they are important as a tool for understanding the constituent properties of the stress tensor. Schematic representations of the three deformations we consider are shown in Figure 2.2.

The first deformation to consider is an extensional flow perpendicular to the fibre direction, represented by the velocity vector $\boldsymbol{u}^* = (0, v^*(y))$; the stress tensor under these assumptions is given by

$$\boldsymbol{\sigma}^* = -p^* \boldsymbol{I} + 2\mu^* \frac{\mathrm{d}v^*}{\mathrm{d}y^*} \hat{\boldsymbol{y}}\hat{\boldsymbol{y}}, \tag{2.14}$$

where $\hat{\boldsymbol{y}}$ is the unit vector in the y^*-direction (Figure 2.2(a)). Therefore, the extensional viscosity perpendicular to the fibre direction is $\mu_\perp^* = \mu^*$. The second deformation is given by the extensional flow parallel to the fibre direction, with corresponding velocity $\boldsymbol{u}^* = (u^*(x), 0)$ and stress tensor

$$\boldsymbol{\sigma}^* = -p^* \boldsymbol{I} + (2\mu^* + \mu_2^* + 4\mu_3^*) \frac{\partial u^*}{\partial x^*} \hat{\boldsymbol{x}}\hat{\boldsymbol{x}}, \tag{2.15}$$

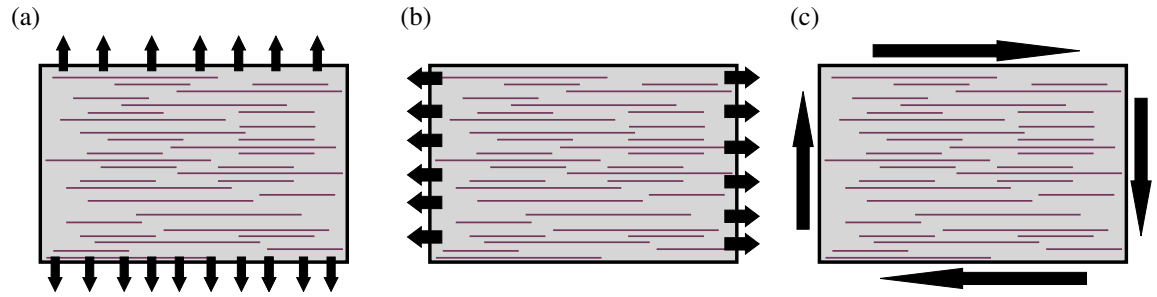

Figure 2.2: A schematic diagram of the two-dimensional deformations in the plane of fibres considered in equations (2.14), (2.15), and (2.16), where the fibres are aligned in the x^*-direction. Sub-figures (a) and (b) show an extensional flow orthogonal and parallel to the fibre direction respectively, whilst (c) shows a shear flow.

where $\hat{\boldsymbol{x}}$ is the unit vector in the x^*-direction (Figure 2.2(b)). The extensional viscosity parallel to the fibre direction is $\mu^*_{||} = \mu^* + (\mu^*_2 + 4\mu^*_3)/2$. The final deformation we consider is given by a shear flow $\boldsymbol{u}^* = (u^*(y), v^*(x))$ (Figure 2.2(c)), in this case the stress tensor is

$$\boldsymbol{\sigma}^* = -p\boldsymbol{I} + (\mu^* + \mu^*_3)\,\frac{\partial u^*}{\partial y^*}\hat{\boldsymbol{x}}\hat{\boldsymbol{y}}, \tag{2.16}$$

and the shear viscosity is $\mu^*_s = \mu^* + \mu^*_3$. By comparing the three different viscosities $\mu^*_\perp$, $\mu^*_{||}$ and μ^*_s, observe μ^*_2 contributes only to $\mu^*_{||}$ while μ^*_3 distinguishes $\mu^*_\perp$ from μ^*_s. Therefore, we interpret μ^*_2 as the anisotropic extensional viscosity and μ^*_3 as the anisotropic shear viscosity [29, 22, 70].

2.3 Parameter values

In order to use this model in practice it is necessary to estimate the rheological parameters of the fluid, however data are required on these parameters in bio-molecular suspensions of interest. In this section we propose how capillary viscometry may be used to determine the shear viscosity (μ^*_s) of a transversely isotropic fluid (section 2.3.1), examine how Batchelor's analysis of statistically homogeneous suspensions of dilute rods [6] may be used to estimate all of the viscosity-like parameters (μ^*, μ^*_2, μ^*_3), when the transversely

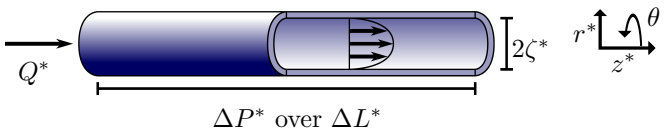

Figure 2.3: Schematic diagram of laminar flow in a straight capillary tube. The fluid enters the tube with a volumetric flow rate Q^*, the cylinder has radius ζ^*. The pressure drop ΔP^* is measured over a known length ΔL^*.

isotropic fluid represents a dilute suspension of rod-like particles (section 2.3.2), and finally investigate how Batchelor's analysis of the extensional flow of aligned rods [7] may be used to relax the diluteness assumption in section 2.3.2, determining the value of the anisotropic extensional viscosity μ_2^* in this case (section 2.3.3). We do not discuss the parameter μ_1^* here, as it corresponds to active behaviour, instead we investigate its meaning in chapter 5 which focusses on active fluids.

2.3.1 Capillary viscometry

A viscometer is a device which is used to measure the flow parameters of a fluid. We will describe the application of a standard viscometer, the capillary viscometer, which could be used to find estimates of the shear viscosity $\mu_s^* = \mu^* + \mu_3^*$.

We model the flow inside a capillary viscometer (figure 2.3) as flow down a cylindrical pipe. When the fluid is Newtonian capillary viscometers rely upon the application of Poiseuille's law, which relates the volumetric flow rate Q^*, the pressure difference ΔP^* over some length ΔL^*, and the radius of the pipe ζ^*, to find the shear viscosity of the fluid [4]. We therefore form an equation, similar to Poiseuille's Law, for the steady flow of a transversely isotropic fluid down a cylindrical pipe.

We adopt a cylindrical coordinate system where the z^*-axis is coincident with the centre line of the pipe, the radius of the pipe is r^*, and the azimuthal angle is given by θ. We assume the velocity of the pipe is purely in the z^*-direction and only a function of the radius, the pressure in the pipe is a function of z^* only, and the fibres align purely in

the z^*-direction, *i.e.*

$$\boldsymbol{u}^* = (0, 0, w^*(r^*)), \qquad p^* = p^*(z^*), \qquad \boldsymbol{a} = (0, 0, 1). \tag{2.17}$$

Under these assumptions the stress tensor (2.4) becomes

$$\boldsymbol{\sigma}^* = -p^* \boldsymbol{I} + \begin{pmatrix} 0 & 0 & (\mu^* + \mu_3^*) \frac{\mathrm{d}w^*}{\mathrm{d}r^*} \\ 0 & 0 & 0 \\ (\mu^* + \mu_3^*) \frac{\mathrm{d}w^*}{\mathrm{d}r^*} & 0 & 0 \end{pmatrix}. \tag{2.18}$$

To find the anisotropic shear viscosity we solve the Stokes equations

$$\boldsymbol{\nabla}_{\boldsymbol{x}} \cdot \boldsymbol{\sigma}^* = \boldsymbol{\nabla}_{\boldsymbol{x}} p^*, \tag{2.19}$$

$$\iff \left(\frac{\mu^* + \mu_3^*}{r^*} \right) \frac{\mathrm{d}}{\mathrm{d}r^*} \left(r^* \frac{\mathrm{d}w^*}{\mathrm{d}r^*} \right) = \frac{\mathrm{d}p^*}{\mathrm{d}z^*}. \tag{2.20}$$

Multiplying equation (2.20) by r^* and integrating with respect to r^* gives

$$(\mu^* + \mu_3^*)\, r^* \frac{\mathrm{d}w^*}{\mathrm{d}r^*} = \frac{r^{*2}}{2} \frac{\mathrm{d}p^*}{\mathrm{d}z^*} + C_1, \tag{2.21}$$

where C_1 is a constant. Dividing equation (2.21) by r^* and integrating gives

$$(\mu^* + \mu_3^*)\, w^* = \frac{r^{*2}}{4} \frac{\mathrm{d}p^*}{\mathrm{d}z^*} + C_1 \ln r^* + C_2. \tag{2.22}$$

Since w^* needs to be finite at $r = 0$, the constant $C_1 = 0$. Assuming there is no-slip at the cylinder walls, *i.e.* $w^* = 0$ at $r^* = \zeta^*$ gives

$$(\mu^* + \mu_3^*)\, w^* = \frac{1}{4} \frac{\mathrm{d}p^*}{\mathrm{d}z^*} \left(r^{*2} - \zeta^{*2} \right). \tag{2.23}$$

As we assume the pressure decreases linearly across the length of the pipe, we have

$$\frac{\mathrm{d}p^*}{\mathrm{d}z^*} = -\frac{\Delta P^*}{\Delta L^*}, \tag{2.24}$$

substituting this into equation (2.23) gives

$$\left(\mu^* + \mu_3^*\right) w^* = \frac{\Delta P^* \left(\zeta^{*2} - r^{*2}\right)}{4\Delta L^*}. \tag{2.25}$$

The total volume of fluid that flows through the viscometer, per unit time, is given by the volumetric flow rate,

$$Q^* = \int_{r^*=0}^{\zeta^*} \int_{\theta=0}^{2\pi} w^* r^* \,\mathrm{d}\theta \,\mathrm{d}r^*, \tag{2.26}$$

$$= \int_{r^*=0}^{\zeta^*} 2\pi \frac{\Delta P^* \left(\zeta^{*2} r^* - r^{*3}\right)}{4\left(\mu^* + \mu_3^*\right)\Delta L^*} \,\mathrm{d}r^*, \tag{2.27}$$

$$= \frac{\pi \zeta^{*4} \Delta P^*}{8\left(\mu^* + \mu_3^*\right)\Delta L^*}. \tag{2.28}$$

Rearranging equation (2.28) yields

$$\mu_s^* = \mu^* + \mu_3^* = \frac{\pi \zeta^{*4} \Delta P^*}{8 Q^* \Delta L^*}, \tag{2.29}$$

where every parameter on the right hand side of equation (2.29) is known. Capillary viscometry may therefore be used to calculate the value of the shear viscosity μ_s^* in terms of the cylinder radius of the viscometer, the pressure difference across the length of the viscometer and also the volumetric flow rate. This analysis holds for any fluid that may be described as transversely isotropic.

2.3.2 Dilute regime

We now discuss how physical arguments may be used to determine the viscosity-like parameters when the transversely isotropic fluid represents a dilute suspension of elongated

particles [6], to do this we follow Lipscomb *et al.* [54].

First note the bulk stress of a dilute suspension of axisymmetric ellipsoids may be written

$$\boldsymbol{\sigma}_B^* = -P^*\boldsymbol{I} + 2\bar{\mu}^*\boldsymbol{e}^* + \phi\sum \boldsymbol{\sigma}_p^*, \tag{2.30}$$

where P^* is the pressure, $\boldsymbol{I}$ is the identity tensor, ϕ is the volume fraction of included fibrous material, $\boldsymbol{\sigma}_p^*$ is the stress acting on the surface of the ellipsoid, and the sum is carried out over all particles. This relation is only valid if the suspension is dilute i.e. $nr_1^{*3} \ll 1$, where n is the fibre number density and r_1^* is the fibre half-length [75]. The stress acting on the surface of the ellipsoid was calculated by Jeffery [43]. Jeffery assumed the flow far from the ellipsoid is steady and homogeneous, motion is sufficiently slow so that inertial forces are negligible and the particle translates with the velocity of the fluid. Under these assumptions Jeffery determined the velocity and pressure fields surrounding the particle, and hence the stress acting on the surface of the ellipsoid:

$$\boldsymbol{\sigma_p^*} = \frac{8\bar{\mu}^*}{r_1^* r_2^{*2}} \begin{pmatrix} e_{11}^*/6B_0'' & e_{12}^*/2B_0'(4r_1^{*2}+r_2^{*2}) & e_{13}^*/2B_0'(4r_1^{*2}+r_2^{*2}) \\ e_{12}^*/2B_0'(4r_1^{*2}+r_2^{*2}) & \Delta_{22}^* & e_{23}^*/4A_0'r_2^{*2} \\ e_{13}^*/2B_0'(4r_1^{*2}+r_2^{*2}) & e_{23}^*/4A_0'r_2^{*2} & \Delta_{33}^* \end{pmatrix}, \tag{2.31}$$

$$\Delta_{22}^* = e_{22}^*/4A_0'r_2^{*2} + e_{11}^*(B_0'' - A_0'')/12r_2^{*2}B_0''A_0',$$

$$\Delta_{33}^* = e_{33}^*/4A_0'r_2^{*2} + e_{11}^*(B_0'' - A_0'')/12r_2^{*2}B_0''A_0'.$$

Here A_0', A_0'', B_0', and B_0'' are elliptic integrals, which were evaluated by Giesekus [26], and

are given as follows

$$A_0' = \frac{r^2\left(3\gamma + 2r^2 - 5\right)}{4\, r_1^* r_2^{*4} \left(r^2-1\right)^2}, \qquad B_0' = \frac{\left(-3r^2\gamma + r^2 + 2\right)}{r_1^* r_2^{*4}\left(r^2-1\right)^2}, \tag{2.32}$$

$$A_0'' = \frac{r^2\left[\left(1-r^2\right)\gamma + 2r^2 + 1\right]}{4 r_1^* r_2^{*2}(r^2-1)^2}, \qquad B_0'' = \frac{r^2\left[\left(2r^2+1\right)\gamma - 3\right]}{r_1^* r_2^{*2}\left(r^2-1\right)^2}, \tag{2.33}$$

where $r = r_1^*/r_2^*$ is the fibre aspect ratio, r_2^* is the minor axis of the particle and γ is defined by

$$\gamma = \frac{1}{2r(r^2-1)^{1/2}} \log\left[\frac{r + (r^2-1)^{1/2}}{r - (r^2-1)^{1/2}}\right] \text{ for } r > 1, \tag{2.34}$$

$$\gamma = \frac{1}{r(1-r^2)^{1/2}} \tan^{-1}\left[\frac{(1-r^2)^{1/2}}{r}\right] \text{ for } r < 1. \tag{2.35}$$

Now the constitutive equations (2.4) and (2.6) proposed by Ericksen [24] may be equated with Jeffery's model by transforming the constitutive equations of Ericksen into the coordinate system used by Jeffery; this may be achieved by choosing $\boldsymbol{a} = (1,0,0)$ as the unique axis of a single ellipsoid of revolution, and $\alpha_0 = (r^2-1)/(r^2+1)$ as the shape parameter. In this coordinate system the transversely isotropic stress tensor (2.4) becomes

$$\boldsymbol{\sigma}^* = \begin{pmatrix} -p^* + \mu_1^* + (2\mu^* + \mu_2^* + 4\mu_3^*)e_{11}^* & 2(\mu^* + \mu_3^*)e_{12}^* & 2(\mu^* + \mu_3^*)e_{13}^* \\ 2(\mu^* + \mu_3^*)e_{12}^* & -p^* + 2\mu^* e_{22}^* & \mu^* e_{23}^* \\ 2(\mu^* + \mu_3^*)e_{13}^* & \mu^* e_{23}^* & -p^* + 2\mu^* e_{33}^* \end{pmatrix}. \tag{2.36}$$

Equating equation (2.31) with equation (2.36) gives the viscosity-like parameters

$$\begin{aligned} \mu^* &= \bar{\mu}^*/2r_1^* r_2^{*4} A_0', \\ \mu_1^* &= 0, \\ \mu_2^* &= \bar{\mu}^*\left[1/r_1^* r_2^{*4} A_0' + 1A_0''/r_1^* r_2^{*4} B_0'' A_0' - 4/(2r_1^* r_2^{*2} B_0'(4r_1^{*2} + r_2^{*2}))\right], \\ \mu_3^* &= \bar{\mu}^*\left[1/(r_1^* r_2^{*2} B_0'(4r_1^{*2} + r_2^{*2})) - 1/2r_1^* r_2^{*4} A_0'\right]. \end{aligned} \tag{2.37}$$

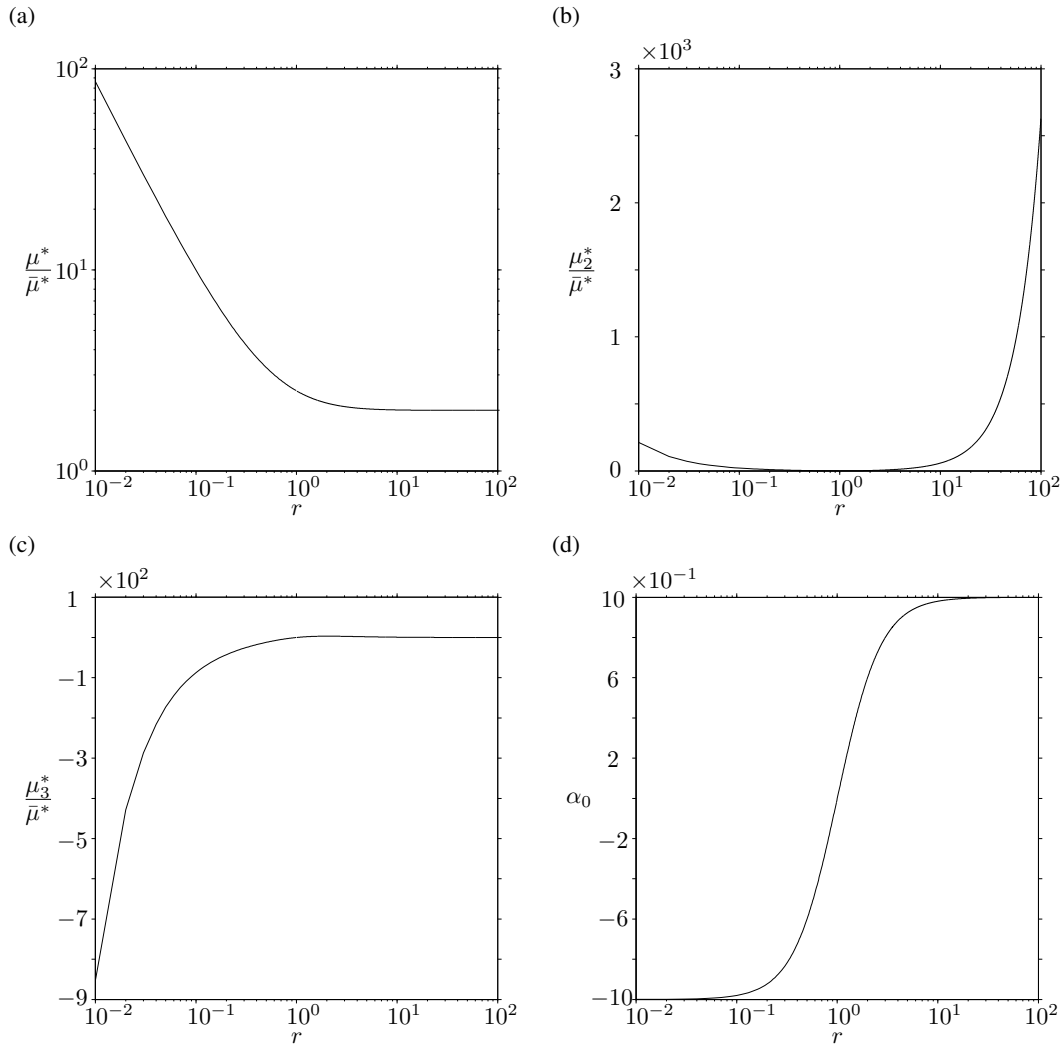

Figure 2.4: Functional dependence of (a) $\mu^*/\bar{\mu}^*$, (b) $\mu_2^*/\bar{\mu}^*$, (c) $\mu_3^*/\bar{\mu}^*$, and (d) α_0, on the aspect ratio of the fibres (r) in a dilute regime. Reproduced from Lipscomb [54].

Here $\mu_1^* = 0$ as Batchelor's theory corresponds to passive suspensions of particles, hence the active component of Ericksen's stress tensor is zero. In Figure 2.4 we plot the functional dependence of $\mu^*/\bar{\mu}^*$, $\mu_2^*/\bar{\mu}^*$, $\mu_3^*/\bar{\mu}^*$, and α_0 on the aspect ratio for $0 < r < \infty$.

We now examine the limit of the fibre aspect ratio $r \to \infty$, this corresponds to an infinitely long fibre. In this limit, equations (2.37) reduce to

$$\mu^* = 2\bar{\mu}^*, \qquad \mu_2^* = \frac{\bar{\mu}^* r^2}{\log(r)}, \qquad \mu_1^* = \mu_3^* = 0. \tag{2.38}$$

and the stress tensor (2.4) becomes

$$\boldsymbol{\sigma}^* = -\, p^* \boldsymbol{I} + 4\bar{\mu}^* \boldsymbol{e}^* + \frac{\bar{\mu}^* r^2}{\log(r)} \boldsymbol{a}\,\boldsymbol{a}\,\boldsymbol{a}\,\boldsymbol{a} : \boldsymbol{e}. \tag{2.39}$$

Equation (2.39) represents a limit of the transversely isotropic stress tensor corresponding to a dilute suspension of infinitely long particles. However, this dilute limit requires rods to be very widely spaced, and will not be valid in many real-world applications. For this regime to hold we require $nr_1^{*3} \ll 1$, which when the aspect ratio of the fibres is large will only hold for extremely small volume fractions of fibres. Although this theory is limited, it does allow us to see that elongated particles will make a much greater contribution to the stress than spherical particles that are a similar size. This is due to the final term in equation (2.39) which would be zero for a suspension of spherical particles.

2.3.3 Semi-dilute regime

Next we consider how the assumptions on diluteness may be relaxed to gain information on the parameters in the model. Following authors such as Dyson and Jensen [22], we apply the work of Batchelor [7] who considered a suspension of rigid elongated particles suspended in a Newtonian fluid, undergoing a pure straining motion in the x^*-direction, where each particle is free to translate and rotate with the surrounding fluid and is small enough so that inertia may be neglected.

Consider n particles of length $2r_1^*$ aligned in the x^*-direction of a unit volume. Then n is the number density of particles and the average number of particles that intersect a plane normal to the x^*-axis is $2nr_1^*$ (figure 2.5) [5]. Therefore, the average distance between neighbouring intersections is a length of order

$$h^* = (2nr_1^*)^{-1/2}\,. \tag{2.40}$$

The ratio r_1^*/h^* may be used to describe the relative important of interactions between the

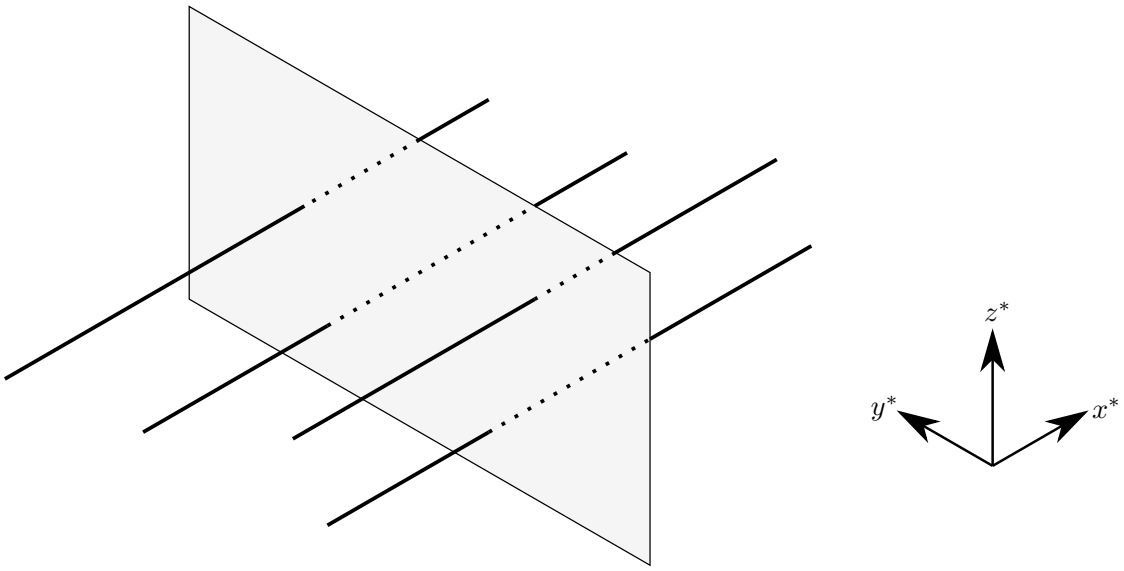

Figure 2.5: Schematic diagram of aligned fibres intersecting a unit plane perpendicular to their direction.

particles. In a dilute suspension (section 2.3.2) the spacing between the particles must be much greater than their length *i.e.* $r_1^*/h^* \ll 1$. Another regime that may be considered is the *semi-dilute regime*, where the length of the particles is much greater than the spacing between the particles, which is itself much larger than the particles radius, *i.e.*

$$r_2^* \ll h^* \ll r_1^*. \tag{2.41}$$

This corresponds to $nr_1^{*3} \gg 1$ and $\phi \ll 1$ [75].

In the semi-dilute regime, the fluid surrounding the particles must move in the gap between the particles. As the lateral spacing between particles is small when compared with the particle length, the spatial gradients of fluid velocity in the x^*-direction are small relative to those in the y^*- and z^*-directions; also the difference between the local and average velocities is a vector approximately in the x^*-direction. The x^*-component of the velocity vector of the fluid surrounding the particles may therefore be written as

$$\frac{\partial^2 u^*}{\partial y^{*2}} + \frac{\partial^2 u^*}{\partial z^{*2}} = 0, \tag{2.42}$$

where inertial forces are negligible between adjoining particles.

Batchelor [5] showed that this is the governing equation for a fluid surrounding an elongated particle within a distance from the particle that is small compared to its length. Since it is assumed $h^* \ll r_1^*$ the surrounding fluid always satisfies this condition and equation (2.42) holds everywhere in the surrounding fluid.

The problem must be closed by choosing appropriate boundary conditions on u^*, which are formulated by assuming there is no-slip on the particles' surfaces. This allows for the force per unit particle length exerted on the surrounding fluid to be given as

$$\boldsymbol{F}^* = \frac{-2\pi\bar{\mu}^* e_{11}^* x^*}{\log(h^*/r_2^*)}, \tag{2.43}$$

where e_{11}^* is the rate of extension in the x^*-direction of the surrounding fluid.

In the case of a transversely isotropic fluid (*i.e.* a fluid with a preferred direction $\boldsymbol{a}$) the bulk stress due to the presence of the particles may be approximated as

$$\boldsymbol{\sigma}_p^* = -\frac{\boldsymbol{a}\,\boldsymbol{a}}{V^*} \sum r_1^{*2} \int_{-1}^{1} \boldsymbol{a} \cdot \boldsymbol{F}^* s \,\mathrm{d}s, \tag{2.44}$$

where the summation is over the many particles in a volume V^*, in which conditions are statistically homogeneous, and $\boldsymbol{F}^*$ is the force per unit length exerted by the particle on the surrounding fluid at station s (where sr_1^* denotes the distance along the particle's axis from its centre).

Substituting equation (2.43) into equation (2.44) allows for the evaluation of the particle stress

$$\boldsymbol{\sigma}_p^* = (\hat{\boldsymbol{x}}\,\hat{\boldsymbol{x}})\,\bar{\mu}^* e_{11}^* \frac{4\pi}{3V^*} \sum \frac{r_1^{*3}}{\log(h^*/r_2^*)}, \tag{2.45}$$

where $\hat{\boldsymbol{x}}$ is a unit vector in the x^* direction [7]. Now using the volume of an ellipsoid to

be $4\pi r_1^* r_2^{*2}/3$, we may rewrite equation (2.45) to give

$$\boldsymbol{\sigma}_p^* = (\hat{\boldsymbol{x}}\,\hat{\boldsymbol{x}})\,\bar{\mu}^* e_{11}^* \sum \phi \frac{r^2}{\log(h^*/r_2^*)}, \tag{2.46}$$

where $r = r_1^*/r_2^*$ is the aspect ratio.

We may now compare this result to the transversely isotropic stress tensor in a similar way to that described in section 2.3.2. The equation for the bulk stress given in equation (2.30) is still valid, and so we again notice that we must equate the particle stress (equation (2.45)) with the transformed constitutive equations of Ericksen (equation (2.36)). This allows us to interpret the anisotropic extensional viscosity (modulo a logarithmic factor $\log(h^*/r_2^*)$) as

$$\mu_2^* \propto \bar{\mu}^* \phi r^2, \tag{2.47}$$

where $\bar{\mu}^*$ is the solvent viscosity, ϕ is the volume fraction of fibres, and r is the fibre aspect ratio. Therefore, as the fibre's aspect ratio is extremely large the anisotropic extensional viscosity may be much larger than the solvent viscosity, even for relatively small volume fractions of fibres [22]. We also expect the anisotropic shear viscosity is different in the semi-dilute regime to the dilute regime, however we are not aware of any existing literature which describes the value of the anisotropic shear viscosity in a semi-dilute regime.

2.4 Summary

In this chapter we have presented Ericksen's model for a transversely isotropic fluid, and discussed both new and established theories for choosing the parameters of the model. However, due to uncertainty in these parameters, we will present results for a wide range of parameters in the remainder of this thesis. The model consists of conservation of mass and momentum statements (equations (2.2) and (2.3)), a constitutive equation (2.4) relating the stress in the fluid to the preferred direction ($\boldsymbol{a}$) and rate-of-strain tensor ($\boldsymbol{e}$), and the

kinematic equation (2.13) which describes the evolution of the preferred direction. This model must be closed with appropriate boundary conditions.

In section 2.1, the conservation of mass and momentum statements, along with the transversely-isotropic stress tensor, are taken from Ericksen [24]. We follow the derivation of Green and Friedman [29] to derive the kinematic condition, corresponding to infinitely long fibres. In section 2.2 we describe the physical interpretation of the anisotropic viscosities, following the literature, however we are the first to show the justification for the definition of the anisotropic extensional and shear viscosities. In section 2.3 we are the first to suggest the use of capillary viscometry to determine the anisotropic shear viscosity. However, the determination of parameter values in dilute and semi-dilute regimes follows Lipscomb et al. [54] and Batchelor [7] respectively.

We will use this model to examine the linear Taylor-Couette and Rayleigh-Bénard stability of a transversely isotropic fluid in chapters 3 and 4 respectively. In chapter 5 we link this model to that of an active fluid, in particular the importance of including the anisotropic extensional and shear viscosities in the constitutive relation for stress of an active fluid is identified. This link also allows for other important physical effects, such as dispersion about the preferred direction, to be included in Ericksen's model, as well as identifying how a simple modification to the kinematic equation (2.6) allows Ericksen's model to capture the behaviour of a uniform suspension of perfectly-aligned active swimmers, we examine a simple case of this in chapter 6.

CHAPTER 3

LINEAR TAYLOR-COUETTE STABILITY OF A TRANSVERSELY ISOTROPIC FLUID

We consider the linear stability of transversely isotropic fluids within a Couette device [14] (two rotating co-axial cylinders, as shown in Figure 3.1), to an axisymmetric perturbation. This flow setup is pertinent to flow linear dichroism, a technique used for analysing long biological molecules in suspension; it is also a canonical example in traditional fluid mechanics for the stability analysis of viscous flows (see Acheson [1]).

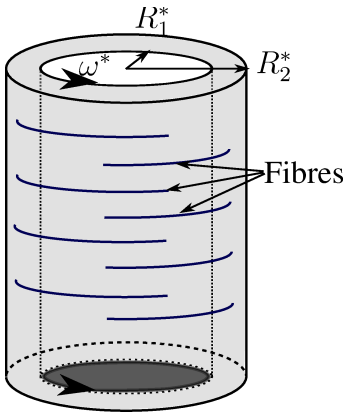

Figure 3.1: A schematic diagram of a Couette device containing a fibre-laden fluid. The inner and outer cylinders have radii R_1^* and R_2^*. The outer cylinder is fixed, whilst the inner cylinder rotates with angular velocity ω^*.

At low angular velocity, the flow of a Newtonian fluid is laminar and purely azimuthal. Taylor [85] examined the stability of this flow both experimentally and analytically, under the assumption of small gap width (relative to the outer cylinder's radius). As angular velocity is increased the flow loses stability and gives way to axisymmetric Taylor vortices;

these can be visualised as a stack of fluid doughnuts. This is the first in a sequence of instabilities leading to turbulence as angular velocity is increased further. Using linear stability analysis, Taylor established a condition on the angular velocities of the rotating cylinders and kinematic viscosity of the fluid. The assumption of small gap width has since been relaxed via numerical techniques, see for example Dominguez *et al.* [18].

Linear dichroism (LD) spectroscopy is a technique for studying the structure of bio-molecules; this technique exploits the difference in absorption of horizontally and vertically polarised light by a horizontally aligned sample. Flow LD works with bio-molecules in suspension and produces alignment through an applied shear flow [15] such as Couette [57, 69] or channel flow [59]. The method is particularly useful for particles with high aspect ratio, such as DNA [34], protein fibres [16, 56, 77], and photosynthetic pigment-protein complexes [25]; one current area of interest is exploiting flow LD for pathogen detection [63]. The requirement to maximise signal production leads to a trade-off however; large shear rates produce higher degrees of fibre alignment (and hence improved signal to noise ratio), but increasing the inner cylinder angular velocity too high leads to a fluid instability which destroys all signal. Stability of Couette flow of a fibre-laden fluid is therefore of practical as well as theoretical interest.

Leslie [53] extended Taylor's analysis to a transversely isotropic fluid, still assuming a small gap width, taking $|\alpha_0| > 1$, and setting the active parameter $\mu_1 = 0$. Leslie's analysis focused upon the effect of α_0, as opposed to the different viscosity-like parameters, on the onset of instability. Wan and Lin [88] expanded on Leslie's study to consider finite gap widths, and the effect of extensional anisotropic viscosity. However, they neglected the effects of anisotropy in the shear viscosity and assume that the fibres instantaneously align with the streamlines.

Motivated by the linear dichroism applications discussed above, in which we are considering very long and thin molecules within a Couette device with a non-small gap width (relative to the outer cylinder's radius), we will work with $\alpha_0 = 1$, finite gap width, and retain all four viscosity-like parameters (including the active μ_1 term). Defining

$\alpha_0 = (r^2 - 1)/(r^2 + 1)$ in the range $0 < \alpha_0 < 1$, we observe $\alpha_0 = 1$ corresponds to fibres with an infinite aspect ratio. We consider the stability of an axisymmetric perturbation since, by analogy with the isotropic case, we suggest this will be the first instability to arise.

We briefly discuss the equations and derive the steady state of the transversely isotropic model (section 3.1), and then undertake a linear stability analysis, leading to an eigenvalue problem which is solved numerically (section 3.2). The effect of variations in viscosity-like parameters and gap width on the marginal stability curves is considered (section 3.3), whilst we conclude with discussion of the results in section 3.4.

3.1 Governing equations and steady state solution

The governing equations consist of conservation of mass and momentum statements (equations (2.2) and (2.3)) in terms of the fluid velocity $\boldsymbol{u}^*$, constant fluid density ρ^* and time t^*. To capture the extra stress generated by the inclusion of elongated particles in the solution, we adopt the constitutive relation for stress proposed by Ericksen [24] (equation (2.4)), which is the simplest form of the stress tensor that is linear in strain rate and obeys all of the required invariances [22]. This relation introduces a single preferred direction, $\boldsymbol{a}$ within the fluid, we model the evolution of this direction using equation (2.13) proposed by Green & Friedman [29], which is a special case of the relation proposed by Ericksen (corresponding to $\alpha_0 = 1$ in equation (2.6)). Due to the physical dimensions of the system, we adopt a cylindrical coordinate system with radial, azimuthal, and axial components (r^*, θ, z^*), where the components of velocity are (u^*, v^*, w^*).

3.1.1 Boundary conditions

We take the inner and outer cylinders to have radii R_1^* and R_2^* respectively, and apply no-slip boundary conditions

$$\begin{aligned} \boldsymbol{u}^* &= (0, R_1^*\omega^*, 0) \quad \text{at } r^* = R_1^*, \\ \boldsymbol{u}^* &= \mathbf{0} \qquad\qquad\quad \text{at } r^* = R_2^*, \end{aligned} \tag{3.1}$$

such that the outer cylinder remains fixed, whilst the inner cylinder rotates with angular velocity ω^*, see Figure 3.1. In the remainder of this chapter we will look for an axisymmetric solution which automatically satisfies the required periodicity conditions.

3.1.2 Non-dimensionalisation

We non-dimensionalise the model by scaling the independent and dependent variables via:

$$t^* = \frac{\rho^* R_2^{*2}}{\mu^*} t, \qquad \boldsymbol{u}^* = \frac{\mu^*}{\rho^* R_2^*} \boldsymbol{u}, \qquad (r^*, z^*) = R_2^*(r, z), \qquad (p^*, \boldsymbol{\sigma}^*) = \frac{\mu^{*2}}{\rho^* R_2^{*2}} (p, \boldsymbol{\sigma}), \tag{3.2}$$

where variables without asterisks denote dimensionless quantities, as chosen in [13, 18, 60].

The incompressibility condition (2.2) and the kinematic equation (2.13) remain unchanged by this scaling,

$$\boldsymbol{\nabla}_{\boldsymbol{x}} \cdot \boldsymbol{u} = 0, \tag{3.3}$$

$$\frac{\partial \boldsymbol{a}}{\partial t} + (\boldsymbol{u} \cdot \boldsymbol{\nabla}_{\boldsymbol{x}})\, \boldsymbol{a} + \boldsymbol{a}\, \boldsymbol{a}\, \boldsymbol{a} : \boldsymbol{\nabla}_{\boldsymbol{x}} \boldsymbol{u} = (\boldsymbol{a} \cdot \boldsymbol{\nabla}_{\boldsymbol{x}})\, \boldsymbol{u}. \tag{3.4}$$

The momentum balance (2.3) becomes

$$\frac{\partial \boldsymbol{u}}{\partial t} + (\boldsymbol{u} \cdot \boldsymbol{\nabla}_{\boldsymbol{x}})\, \boldsymbol{u} = (\boldsymbol{\nabla}_{\boldsymbol{x}} \cdot \boldsymbol{\sigma})\,. \tag{3.5}$$

Non-dimensionalising the stress tensor (2.4) yields the dimensionless stress tensor

$$\boldsymbol{\sigma} = -\,p\,\boldsymbol{I} + 2\,\boldsymbol{e} + \mu_1\,\boldsymbol{a}\,\boldsymbol{a} + \mu_2\,\boldsymbol{a}\,\boldsymbol{a}\,\boldsymbol{a}\,\boldsymbol{a} : \boldsymbol{e} + 2\,\mu_3\,(\boldsymbol{a}\,\boldsymbol{a}\cdot\boldsymbol{e} + \boldsymbol{e}\cdot\boldsymbol{a}\,\boldsymbol{a})\,, \tag{3.6}$$

where the following non-dimensional parameters have been introduced

$$\mu_1 = \frac{\mu_1^*\rho^* R_2^{*2}}{\mu^{*2}}, \qquad \mu_2 = \frac{\mu_2^*}{\mu^*}, \qquad \mu_3 = \frac{\mu_3^*}{\mu^*}. \tag{3.7}$$

Here μ_1 is the ratio of the effects of tension in the fibres to the transverse shear viscosity, whilst μ_2 and μ_3 are the ratios of the extensional viscosity and shear viscosity in the fibre direction to the transverse shear viscosity respectively [29].

Finally, the boundary conditions (3.1), in dimensionless form, are

$$\begin{aligned} &\boldsymbol{u} = (0, \eta\,\Omega, 0) \text{ at } r = \eta, \\ &\boldsymbol{u} = \boldsymbol{0} \qquad\qquad \text{at } r = 1, \end{aligned} \tag{3.8}$$

where $\eta = R_1^*/R_2^*$ is the gap ratio, and $\Omega = \rho^* R_2^{*2}\omega^*/\mu^*$ is the non-dimensional rotational velocity of the inner cylinder; this is equivalent to a Reynolds number. The model consists of three governing equations (3.3)-(3.5) for $\boldsymbol{u}$, p, and $\boldsymbol{a}$, subject to constitutive law (3.6) and boundary conditions (3.8).

3.1.3 Steady state

Assuming axisymmetry and treating the cylinders as infinitely long, we look for a steady state solution that only depends on r. Taking the fluid velocity and fibres to align purely in the azimuthal direction we make the ansatz

$$\boldsymbol{u}^{(0)} = (0, V^{(0)}(r), 0), \qquad \boldsymbol{a}^{(0)} = (0, 1, 0), \qquad p = P^{(0)}(r). \tag{3.9}$$

Under these assumptions, equations (3.3) and (3.4) are automatically satisfied and the momentum equation (3.5) is reduced to a pair of non-trivial equations

$$\frac{\mathrm{d}P^{(0)}(r)}{\mathrm{d}r} = -\frac{\mu_1}{r} + \frac{\left(V^{(0)}\right)^2}{r}, \tag{3.10}$$

$$0 = (1+\mu_3)\left(\frac{\mathrm{d}^2V^{(0)}}{\mathrm{d}r^2} + \frac{1}{r}\frac{\mathrm{d}V^{(0)}}{\mathrm{d}r} - \frac{V^{(0)}}{r}\right). \tag{3.11}$$

Using the no-slip boundary conditions (3.8) at the cylinder walls, we solve to find

$$\begin{aligned} V^{(0)}(r) &= \frac{\beta}{2}\left(\frac{1}{r} - r\right), \\ P^{(0)}(r) &= -\mu_1 \log(r) + \frac{\beta^2}{8}\left(r^2 - \frac{1}{r^2} - 4\log(r)\right) + p_0, \end{aligned} \tag{3.12}$$

where $\beta = 2\eta^2\Omega/(1-\eta^2)$, and p_0 is some arbitrary pressure constant. We note the inclusion of an additional logarithmic term in the pressure equation, when compared with the Newtonian case. This term represents the extra stress induced by the active nature of the material. The velocity profile is shown in Figure 3.2.

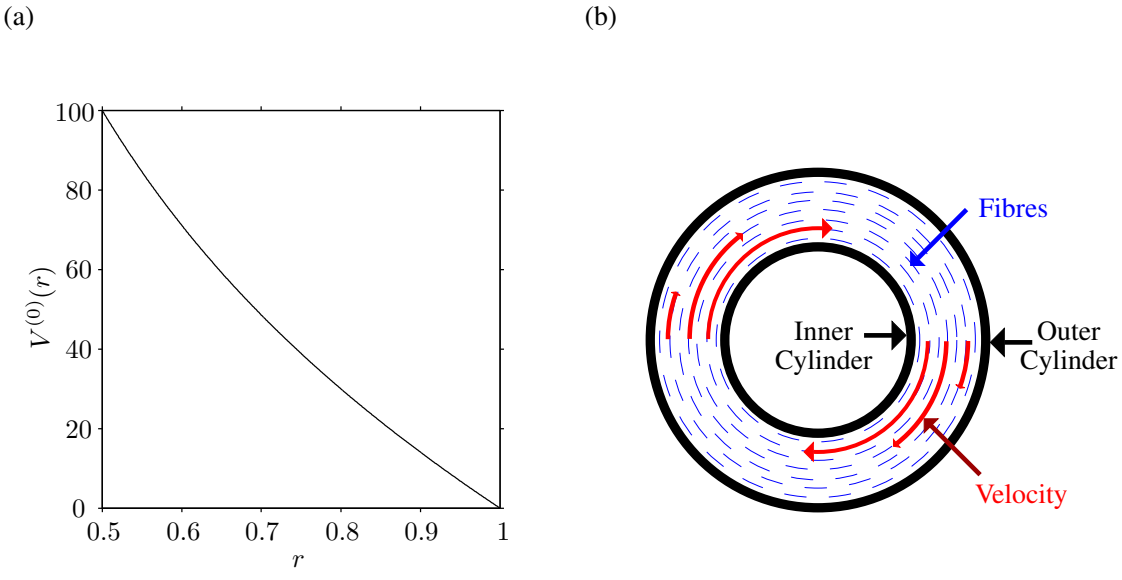

Figure 3.2: Steady state velocity as a function of radius. (a) The steady state velocity as a function of r, for a gap ratio $\eta = 0.5$ and angular velocity $\Omega = 100$. (b) A schematic diagram showing how this flow profile appears through a cross-section of the cylinders.

3.2 Stability

3.2.1 Linear stability analysis

We consider the stability of solution (3.12) to an axisymmetric perturbation, such that

$$\boldsymbol{u}(r,z,t) = \boldsymbol{u}^{(0)}(r,z,t) + \epsilon\,\boldsymbol{u}^{(1)}(r,z,t) + \mathcal{O}\left(\epsilon^2\right), \tag{3.13}$$

$$\boldsymbol{a}(r,z,t) = \boldsymbol{a}^{(0)}(r,z,t) + \epsilon\,\boldsymbol{a}^{(1)}(r,z,t) + \mathcal{O}\left(\epsilon^2\right), \tag{3.14}$$

where $0 < \epsilon \ll 1$. Since $\boldsymbol{a}$ is a unit vector

$$|\boldsymbol{a}| = \boldsymbol{a}^{(0)} \cdot \boldsymbol{a}^{(0)} + 2\epsilon\left(\boldsymbol{a}^{(0)} \cdot \boldsymbol{a}^{(1)}\right) + \mathcal{O}\left(\epsilon^2\right) = 1, \tag{3.15}$$

must hold. Therefore the θ component of the alignment vector $\boldsymbol{a}_\theta$ must be zero. Using the steady state solution (3.12) the velocity and director fields must take the form

$$\boldsymbol{u} = \left(\epsilon\,u^{(1)} + \mathcal{O}\left(\epsilon^2\right), V^{(0)}(r) + \epsilon\,v^{(1)} + \mathcal{O}\left(\epsilon^2\right), \epsilon\,w^{(1)} + \mathcal{O}\left(\epsilon^2\right)\right), \tag{3.16}$$

$$\boldsymbol{a} = \left(\epsilon\,a_r^{(1)} + \mathcal{O}\left(\epsilon^2\right), 1 + \mathcal{O}\left(\epsilon^2\right), \epsilon\,a_z^{(1)} + \mathcal{O}\left(\epsilon^2\right)\right). \tag{3.17}$$

The incompressibility condition (3.3) (becomes at next order)

$$\frac{1}{r}\frac{\partial}{\partial r}\left(r u^{(1)}\right) + \frac{\partial w^{(1)}}{\partial z} = 0. \tag{3.18}$$

In order to calculate the momentum balance (3.5) we must first calculate the components of the stress tensor (3.6):

$$\sigma_{rr} = -p^{(1)} + 2\,\frac{\partial u^{(1)}}{\partial r} + 2\mu_3 a_r^{(1)} r\,\frac{\mathrm{d}}{\mathrm{d}r}\left(\frac{V^{(0)}}{r}\right), \tag{3.19}$$

$$\sigma_{\theta\theta} = -p^{(1)} + \frac{1}{r}\left(2+\mu_2+4\mu_3\right)u^{(1)} + \left(\mu_2+2\mu_3\right)a_r^{(1)} r\,\frac{\mathrm{d}}{\mathrm{d}r}\left(\frac{V^{(0)}}{r}\right), \tag{3.20}$$

$$\sigma_{zz} = -p^{(1)} + 2\,\frac{\partial w^{(1)}}{\partial z}, \tag{3.21}$$

$$\sigma_{r\theta} = \left(1+\mu_3\right) r\,\frac{\partial}{\partial r}\left(\frac{v^{(1)}}{r}\right) + \mu_1 a_r^{(1)}, \tag{3.22}$$

$$\sigma_{rz} = \left(\frac{\partial u^{(1)}}{\partial z} + \frac{\partial w^{(1)}}{\partial r}\right) + \mu_3 a_z^{(1)} r\,\frac{\mathrm{d}}{\mathrm{d}r}\left(\frac{V^{(0)}}{r}\right), \tag{3.23}$$

$$\sigma_{\theta z} = \left(1+\mu_3\right)\frac{\partial v^{(1)}}{\partial z} + \mu_1 a_z^{(1)}. \tag{3.24}$$

The components of the momentum balance (3.5) therefore take the form (at next order)

$$\begin{aligned}\frac{\partial u^{(1)}}{\partial t} - 2\frac{V^{(0)}v^{(1)}}{r} = &-\frac{\partial p^{(1)}}{\partial r} + \frac{\partial^2 u^{(1)}}{\partial r^2} + \frac{1}{r}\frac{\partial u^{(1)}}{\partial r} - \frac{u^{(1)}}{r^2} + \frac{\partial^2 u^{(1)}}{\partial z^2} \\ &-\mu_2\left\{\frac{u^{(1)}}{r^2} + a_r^{(1)} r\,\frac{\mathrm{d}}{\mathrm{d}r}\left(\frac{V^{(0)}}{r}\right)\right\} \\ &+2\mu_3\left\{\frac{\partial}{\partial r}\left(a_r^{(1)} r\,\frac{\mathrm{d}}{\mathrm{d}r}\left(\frac{V^{(0)}}{r}\right)\right) - 2\frac{u^{(1)}}{r^2} + r\,\frac{\mathrm{d}}{\mathrm{d}r}\left(\frac{V^{(0)}}{r}\right)\frac{\partial a_z^{(1)}}{\partial z}\right\},\end{aligned} \tag{3.25}$$

$$\begin{aligned}\frac{\partial v^{(1)}}{\partial t} + \frac{u^{(1)}}{r}\,\frac{\mathrm{d}}{\mathrm{d}r}\left(rV^{(0)}\right) = &\left(1+\mu_3\right)\left\{\frac{\partial^2 v^{(1)}}{\partial r^2} + \frac{1}{r}\frac{\partial v^{(1)}}{\partial r} - \frac{v^{(1)}}{r^2} + \frac{\partial v^{(1)}}{\partial z}\right\} \\ &+\mu_1\left\{\frac{\partial a_r^{(1)}}{\partial r} + \frac{\partial a_z^{(1)}}{\partial z}\right\},\end{aligned} \tag{3.26}$$

$$\begin{aligned}\frac{\partial w^{(1)}}{\partial t} = &-\frac{\partial p^{(1)}}{\partial z} + \frac{\partial^2 w^{(1)}}{\partial r^2} + \frac{1}{r}\frac{\partial w^{(1)}}{\partial r} + \frac{\partial^2 w^{(1)}}{\partial z^2} \\ &+2\frac{\mu_3}{r}\,\frac{\partial}{\partial r}\left\{a_z^{(1)} r^2\,\frac{\mathrm{d}}{\mathrm{d}r}\left(\frac{V^{(0)}}{r}\right)\right\}.\end{aligned} \tag{3.27}$$

Finally, the kinematic equation (3.4) (gives at next order)

$$\frac{\partial a_r^{(1)}}{\partial t} = 0, \tag{3.28}$$

$$\frac{\partial a_z^{(1)}}{\partial t} = 0. \tag{3.29}$$

Therefore corrections to the director field do not appear at $\mathcal{O}(\varepsilon)$, but may occur at higher order. Also, by inspecting the system (3.18), (3.25)-(3.29), we see that the tension in the fibres (μ_1) plays no role in determining the stability of the perturbation. We set $\boldsymbol{a}^{(1)} = \mathbf{0}$, upon which the components of the momentum balance (3.25)-(3.32) reduce to

$$\frac{\partial u^{(1)}}{\partial t} - 2\frac{V^{(0)}v^{(1)}}{r} = -\frac{\partial p^{(1)}}{\partial r} + \frac{1}{r}\frac{\partial u^{(1)}}{\partial r} - (1+\mu_2+4\mu_3)\frac{u^{(1)}}{r^2} + \frac{\partial^2 u^{(1)}}{\partial r^2} + \frac{\partial^2 u^{(1)}}{\partial z^2}, \tag{3.30}$$

$$\frac{\partial v^{(1)}}{\partial t} + \frac{u^{(1)}}{r}\frac{\mathrm{d}}{\mathrm{d}r}\left(rV^{(0)}\right) = (1+\mu_3)\left(\frac{\partial^2 v^{(1)}}{\partial r^2} + \frac{1}{r}\frac{\partial v^{(1)}}{\partial r} - \frac{v^{(1)}}{r^2} + \frac{\partial v^{(1)}}{\partial z}\right), \tag{3.31}$$

$$\frac{\partial w^{(1)}}{\partial t} = -\frac{\partial p^{(1)}}{\partial z} + \frac{\partial^2 w^{(1)}}{\partial r^2} + \frac{1}{r}\frac{\partial w^{(1)}}{\partial r} + \frac{\partial^2 w^{(1)}}{\partial z^2}. \tag{3.32}$$

We propose the solution takes the form

$$\begin{aligned} u^{(1)} &= u'(r)e^{st}\cos(kz), \quad v^{(1)} = v'(r)e^{st}\cos(kz), \\ w^{(1)} &= w'(r)e^{st}\sin(kz), \quad p^{(1)} = p'(r)e^{st}\cos(kz), \end{aligned} \tag{3.33}$$

where k is the wave-number and s is the growth rate. Using this ansatz the components of the momentum equations (3.25)-(3.32) become

$$su' - \frac{2V^{(0)}v'}{r} = -\frac{\mathrm{d}p'}{\mathrm{d}r} + \frac{\mathrm{d}^2u'}{\mathrm{d}r^2} + \frac{1}{r}\frac{\mathrm{d}u'}{\mathrm{d}r} - (1+\mu_2+4\mu_3)\frac{u'}{r^2} - k^2u', \tag{3.34}$$

$$sv' + \frac{u'}{r}\frac{\partial}{\partial r}\left(rV^{(0)}\right) = (1+\mu_3)\left(\frac{\mathrm{d}^2v'}{\mathrm{d}r^2} + \frac{1}{r}\frac{\mathrm{d}v'}{\mathrm{d}r} - \frac{v'}{r^2} - k^2v'\right) \tag{3.35}$$

$$sw' = kp' + \frac{\mathrm{d}^2w'}{\mathrm{d}r^2} + \frac{1}{r}\frac{\mathrm{d}w'}{\mathrm{d}r} - k^2w', \tag{3.36}$$

with the incompressibility condition (3.18) becoming

$$\frac{\mathrm{d}u'}{\mathrm{d}r} + \frac{u'}{r} + kw' = 0. \tag{3.37}$$

Now adopting the convention $D = \mathrm{d}/\,\mathrm{d}r$ and $\widehat{D} = \mathrm{d}/\,\mathrm{d}r + 1/r$, equations (3.34)-(3.37) become

$$\left(\widehat{D}D - k^2 - \frac{(1+\mu_2+4\mu_3)}{r^2} - s\right)u' + 2\frac{V^{(0)}v'}{r} = \frac{\mathrm{d}p'}{\mathrm{d}r}\,, \tag{3.38}$$

$$(1+\mu_3)\left(D\widehat{D} - k^2 - s\right)v' = u'\left(\frac{\mathrm{d}V^{(0)}}{\mathrm{d}r} + \frac{v'}{r}\right), \tag{3.39}$$

$$\left(\widehat{D}D - k^2 - s\right)w' = -kp', \tag{3.40}$$

$$\widehat{D}u' + kw' = 0. \tag{3.41}$$

We may reduce our system of equations (3.38)-(3.41) as we have four equations in three unknowns. To do this substitute the incompressibility condition (3.41) into the w' component of the conservation of momentum equations (3.40)

$$\left(\widehat{D}D - k^2 - s\right)\widehat{D}u' = k^2p'. \tag{3.42}$$

Substituting equation (3.42) into equation (3.38) we may eliminate pressure

$$k^2\left(\widehat{D}D - k^2 - \frac{1+\mu_2+4\mu_3}{r^2} - s\right)u' + \frac{2V^{(0)}v'k^2}{r} = D\left(\widehat{D}D - k^2 - s\right)\widehat{D}u'. \tag{3.43}$$

Now using

$$\widehat{D}D = D\widehat{D} + \frac{1}{r^2}, \tag{3.44}$$

equation (3.43) may be rewritten as

$$\left[\left(D\widehat{D}-k^2-s\right)\left(D\widehat{D}-k^2\right)-\frac{k^2\left(\mu_2+4\mu_3\right)}{r^2}\right]u'=\frac{2V^{(0)}v'k^2}{r}. \tag{3.45}$$

Substituting for the steady state velocity $V^{(0)}$ in equations (3.39) and (3.45) gives the pair of equations

$$\begin{aligned}\left[\left(D\widehat{D}-k^2-s\right)\left(D\widehat{D}-k^2\right)+\frac{k^2\left(\mu_2+4\mu_3\right)}{r^2}\right]u'&=\beta k^2\left(\frac{1}{r^2}-1\right)v',\\ \left(D\widehat{D}-k^2-s\right)v'&=-\frac{\beta}{1+\mu_3}u',\end{aligned} \tag{3.46}$$

Recall that $\mu_2+4\mu_3$ represents the enhancement to the anisotropic extensional viscosity versus that perpendicular to fibres and $1+\mu_3$ represents the shear viscosity of the fluid in the fibre direction, enhanced by the presence of fibres. Equations (3.46) must be solved subject to the boundary conditions (3.8) rewritten as

$$u'=Du'=v'=0 \quad \text{at} \quad r=\eta,1. \tag{3.47}$$

Following the same convention as Dominguez-Lerma *et al.* [18], we present our results in terms of the Taylor number T, which may be related to β and the physical parameters via

$$T=\frac{(1-\eta)^5(1+\eta)}{2\eta^2}\beta^2=\frac{2(R_2^*-R_1^*)^3R_1^{*2}}{R_2^{*4}(R_1^*+R_2^*)}\Omega^2. \tag{3.48}$$

For a rotating fluid the Taylor number relates the importance of inertial to viscous effects and is proportional to the angular velocity [46]. The Taylor number represents an eigenvalue of the problem (3.46), *i.e.* for a given dimensionless axial wave-number k, there will be non-trivial solution u', v' to the problem (3.46) only for certain values of T. There will be some least eigenvalue $T_l(k)$ corresponding to each particular wave-number k, and it is the least of these values over all k that we seek. This minimum value is often termed the critical Taylor number (T_c), and is used to determine the physical conditions under which

instability first occurs [1].

3.2.2 Numerical solution method

To determine the marginal stability curve we set $s = 0$ in equations (3.46), and calculate the minimum eigenvalue β of the resulting differential system, for a range of wavelengths k. We find the critical wavelength k_c, eigenvalue β_c and Taylor number T_c for variations in the non-dimensional parameters η, μ_2, and μ_3. When T is greater than the critical value T_c (or equivalently β is greater than the critical value β_c), instability will occur. These critical values depend on the mechanical and geometric properties of the system, along with the angular velocity of the inner cylinder, and determine whether a given experimental set up will display instability. These instabilities occur in the form of fluid doughnuts, spaced with wavelength k_c.

We solve the boundary value problem (3.46)-(3.47) numerically using a shooting method [18, 19, 68]. Three independent solutions (u_1, v_1), (u_2, v_2) and (u_3, v_3) to equations (3.46) are found, which satisfy the respective initial value problems (IVP1-3) at $r = \eta$ (*c.f.* [19]),

	Boundary Conditions	Extended Conditions	
IVP1 :	$u_1 = v_1 = Du_1 = 0,$	$Dv_1 = 1, D^2u_1 = 0, D^3u_1 = 0,$	(3.49)
IVP2 :	$u_2 = v_2 = Du_2 = 0,$	$Dv_2 = 0, D^2u_2 = 1, D^3u_2 = 0,$	(3.50)
IVP3 :	$u_3 = v_3 = Du_3 = 0,$	$Dv_3 = 0, D^2u_3 = 0, D^3u_3 = 1.$	(3.51)

Here the boundary conditions in IVP1-3 are equivalent to the boundary conditions (3.47) at $r = \eta$, whilst the extended conditions in IVP1-3 are chosen to form a basis of solutions.

Hence we may express

$$\begin{aligned} u' &= C_1 u_1 + C_2 u_2 + C_3 u_3, \\ v' &= C_1 v_1 + C_2 v_2 + C_3 v_3, \\ Du' &= C_1 Du_1 + C_2 Du_2 + C_3 Du_3, \end{aligned} \tag{3.52}$$

where constants C_1, C_2 and C_3 are chosen to satisfy the boundary conditions (3.47) at $r = 1$. The existence of non-zero solutions of the linear system (3.52) requires

$$\begin{vmatrix} u_1 & u_2 & u_3 \\ v_1 & v_2 & v_3 \\ Du_1 & Du_2 & Du_3 \end{vmatrix} = 0, \tag{3.53}$$

at $r = 1$ [18, 19]. In practice we solve equations (3.46) as a system of first order ordinary differential equations for six variables Y_1-Y_6,

$$\frac{\mathrm{d}Y_1}{\mathrm{d}r} = Y_2, \tag{3.54}$$

$$\frac{\mathrm{d}Y_2}{\mathrm{d}r} = Y_3, \tag{3.55}$$

$$\frac{\mathrm{d}y_3}{\mathrm{d}r} = Y_4, \tag{3.56}$$

$$\begin{aligned} \frac{\mathrm{d}Y_4}{\mathrm{d}r} = &-\frac{2}{r}Y_4 + \frac{3}{r^2}Y_3 - \frac{3}{r^3}Y_2 + \frac{3}{r^4}Y_1, -2k^2\left(Y_3 + \frac{Y_2}{r} - \frac{Y_1}{r^2}\right) \\ &- \left(k^4 - \frac{k^2(\mu_2 + 4\mu_3)}{r^2}\right) Y_1 + k^2\beta\left(\frac{1}{r^2} - 1\right) Y_5, \end{aligned} \tag{3.57}$$

$$\frac{\mathrm{d}Y_5}{\mathrm{d}r} = Y_6, \tag{3.58}$$

$$\frac{\mathrm{d}Y_6}{\mathrm{d}r} = -\frac{Y_6}{r} + \frac{Y_5}{r^2} + k^2 Y_5 - \frac{\beta Y_1}{1 + \mu_3}, \tag{3.59}$$

where

$$Y_1 = u', \qquad Y_2 = \frac{\mathrm{d}u'}{\mathrm{d}r}\,, \tag{3.60}$$

$$Y_3 = \frac{\mathrm{d}^2u'}{\mathrm{d}r^2}\,, \qquad Y_4 = \frac{\mathrm{d}^3u'}{\mathrm{d}r^3}\,, \tag{3.61}$$

$$Y_5 = v', \qquad Y_6 = \frac{\mathrm{d}v'}{\mathrm{d}r}\,. \tag{3.62}$$

This numerical procedure is implemented in MATLAB. The inbuilt function ODE45 is used to find the solution of the initial value problem, for a given set of parameters (μ_2, μ_3, η) and guess β^G. The correct value of β, which gives the zero determinant described in equation (3.53), is then determined using FZERO, which calculates the determinant related to various values of β^G until the determinant is less than 2.2×10^{-6}. This critical value of β is then stored with the value of the wave number to allow the marginal stability curves to be plotted. The minimum of each marginal stability curve is then calculated using FMINSEARCH, which is an iterative method that is said to converge when the change in critical wave and Taylor numbers between successive iterations are both less than 10×10^{-4}.

To validate our numerical procedure, we compared our results with those of Dominguez *et al.* [18] for the Newtonian case, *i.e.* $\mu_2 = \mu_3 = 0$ and found agreement of the critical values to within 0.1%. To accommodate uncertainty in parameter values, we have performed an extensive parameter search for a wide range of gap ratios and viscosities from 0 to 1000 times the isotropic component of viscosity. Results were calculated in intervals of 10 for the viscosity parameters μ_2 and μ_3 (similar behaviour was observed for viscosities below 100 when calculated in intervals of 0.1, however the data are not presented here), and 0.025 for the gap ratio η; data are available from the University of Birmingham institutional repository.

3.3 Results

We first determine the marginal stability curves $T_l(k)$; for any value of k, an experimental setup satisfying $T < T_l(k)$ is stable for that wavelength, whereas if T lies above $T_l(k)$ the system is unstable. We calculate these curves for a range of non-dimensional parameters representing the gap ratio η, the anisotropic extensional viscosity μ_2, and the anisotropic shear viscosity μ_3. The effect of tension in the fibre direction μ_1 was not varied, because this parameter does not affect the stability of the perturbation at this order. We determine the critical wave and Taylor numbers for each tuple of non-dimensional parameters (η, μ_2, μ_3) by finding the wave-number at which $T_l(k)$ is minimal. Provided that the Taylor number for a given experiment lies below this critical value, the system will be stable for all wavelengths.

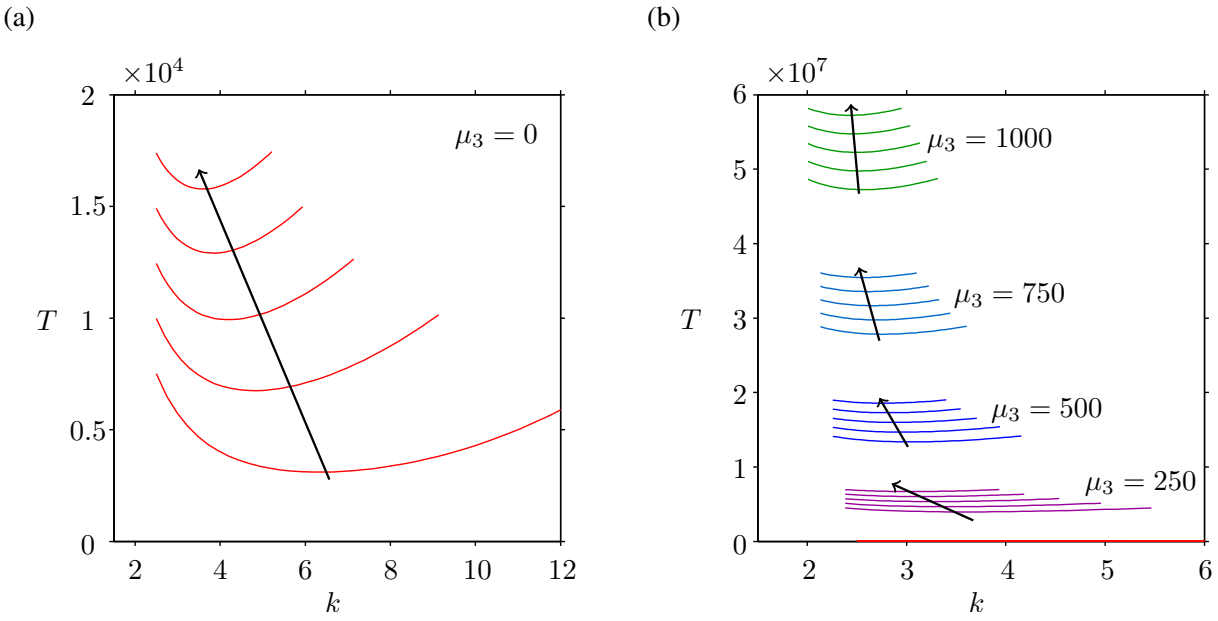

Figure 3.3: Marginal stability curves for different viscosity parameters μ_2 and μ_3 taking $\eta = 0.5$. Both Figures show the curves of the least eigenvalue $T_l(k)$. (a) The marginal stability curves for changes in anisotropic extensional viscosity μ_2, where the arrow indicates the direction of increase ($\mu_2 = 0, 250, 500, 750, 1000$, $\mu_3 = 0$). (b) Marginal stability curves where the anisotropic shear viscosity μ_3 also varies, arrows again show the direction of increasing μ_2, ($\mu_2 = 0, 250, 500, 750, 1000$).

Increasing the anisotropic extensional viscosity (μ_2), whilst neglecting anisotropic shear viscosity ($\mu_3 = 0$), leads to more concave marginal stability curves, along with

higher Taylor numbers for the corresponding wave-number (figure 3.3(a)), *i.e.* instability is suppressed. Raising the anisotropic shear viscosity also leads to more concave marginal stability curves and higher Taylor numbers for corresponding wave-numbers (figure 3.3(b)). Instability is also suppressed as μ_3 increases, however for commensurate increases in the anisotropic extensional and shear viscosities the marginal stability curves are substantially different. Increases in the shear viscosity increase convexity and Taylor numbers far more than increases in the extensional viscosity. Greater suppression of the instability is obtained for increases in μ_3 compared to μ_2. The marginal stability curves shown in figure 3.3 were computed by first choosing the minimum wave number of interest and calculating the corresponding critical Taylor number. The wave number is then incremented and corresponding critical Taylor number calculated and stored until the new critical Taylor number is greater than the first, upon which the numerical procedure is terminated. We have also verified the marginal stability curves have only one turning point for a representative sample of the parameter values and wider range of the wave number k.

Figure 3.4 shows the critical wavelength k_c as a function of μ_3 for selected values of μ_2, and as a function of μ_2 for selected values of μ_3. The critical wave-number k_c is a decreasing function of each parameter *i.e.* the fluid doughnuts which appear have longer wavelength, however increases in μ_3 cause a larger reduction to k_c than corresponding increases in μ_2.

Similar results are plotted in Figure 3.5 for T_c as a function of μ_2 and μ_3. Increasing either μ_2 or μ_3 leads to a higher critical Taylor number (greater suppression of instability). However, again the dependence of the critical Taylor number on the anisotropic extensional viscosity μ_2 is much weaker than that on the anisotropic shear viscosity μ_3.

Finally, we consider the effect of the gap width parameter η. Decreasing the gap between the cylinders (increasing η) leads to an increase in the critical wave-number k_c (*i.e.* larger fluid doughnuts are formed). The change in the critical wave-number due to μ_2 and μ_3 is greater when the gap between the cylinders is large (small η), than when the

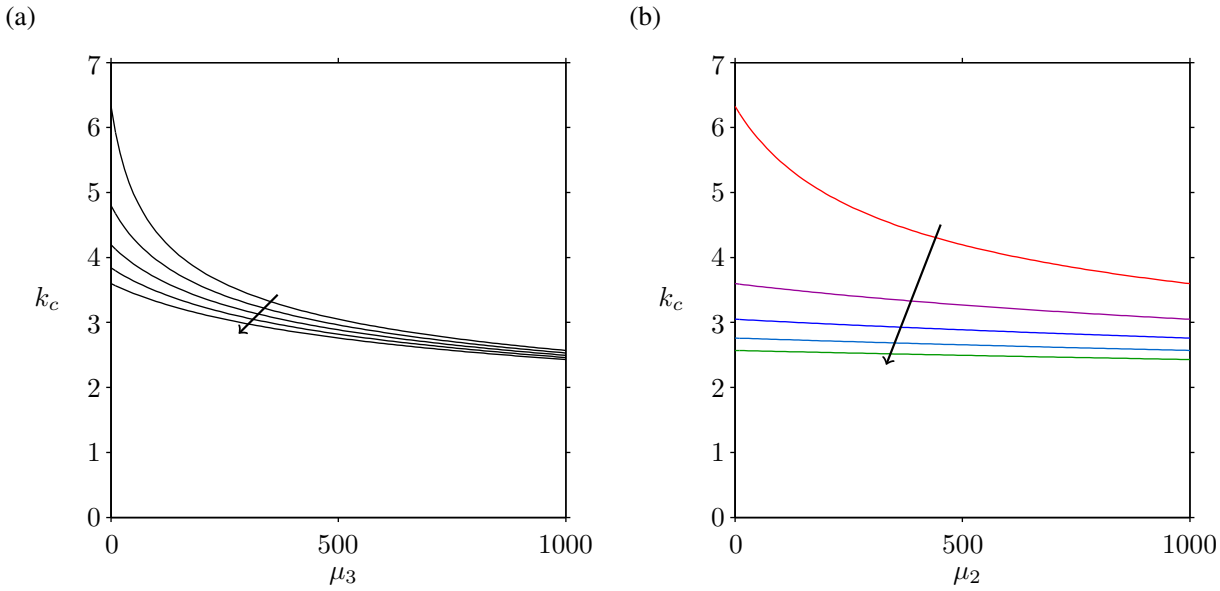

Figure 3.4: Critical wave-number (k_c) for changes in the anisotropic extensional viscosity μ_2, and anisotropic shear viscosity μ_3 taking $\eta = 0.5$, note that qualitatively similar results are obtained for all gap widths considered. (a) Critical wave-number for increases in μ_3, where the arrow indicates increasing μ_2 ($\mu_2 = 0, 250, 500, 750, 1000$). (b) Critical wave-number for increases in μ_2, where the arrow indicates increasing μ_3 ($\mu_3 = 0, 250, 500, 750, 1000$).

gap width is small (large η) as shown in Figure 3.6(a).

Rather than look at the effect of η directly on the critical Taylor number (which itself contains η), we instead consider the critical value of the angular velocity of the inner cylinder, Ω_c. Increasing η (decreasing the inter-cylinder gap) decreases the critical angular velocity Ω_c, until η approaches approximately 0.8, whereupon the critical angular velocity increases again Figure 3.6(b). This therefore describes the minimum of the marginal stability curves, which if the aim is to find the maximum achievable inner cylinder velocity where the fluid remains linearly stable is the worst operating regime. However, we discuss the dependence of the achievable linear dichroism signal in relation to the critical angular velocity in the next section, in conjunction with other effects.

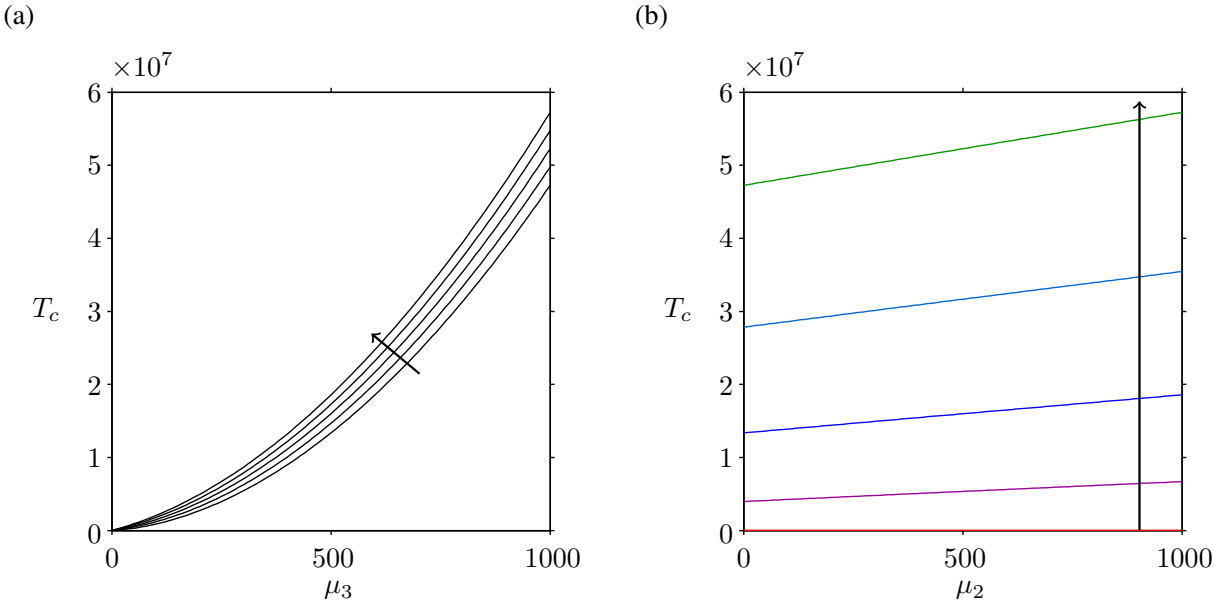

Figure 3.5: Critical Taylor number (T_c) for changes in the anisotropic extensional viscosity (μ_2), and the anisotropic shear viscosity (μ_3) taking $\eta = 0.5$. (a) Critical Taylor number for increases in μ_3, where the arrow indicates increasing μ_2 ($\mu_2 = 0, 250, 500, 750, 1000$). (b) Critical Taylor number for increases in μ_2, where the arrow indicates increasing μ_3 ($\mu_3 = 0, 250, 500, 750, 1000$).

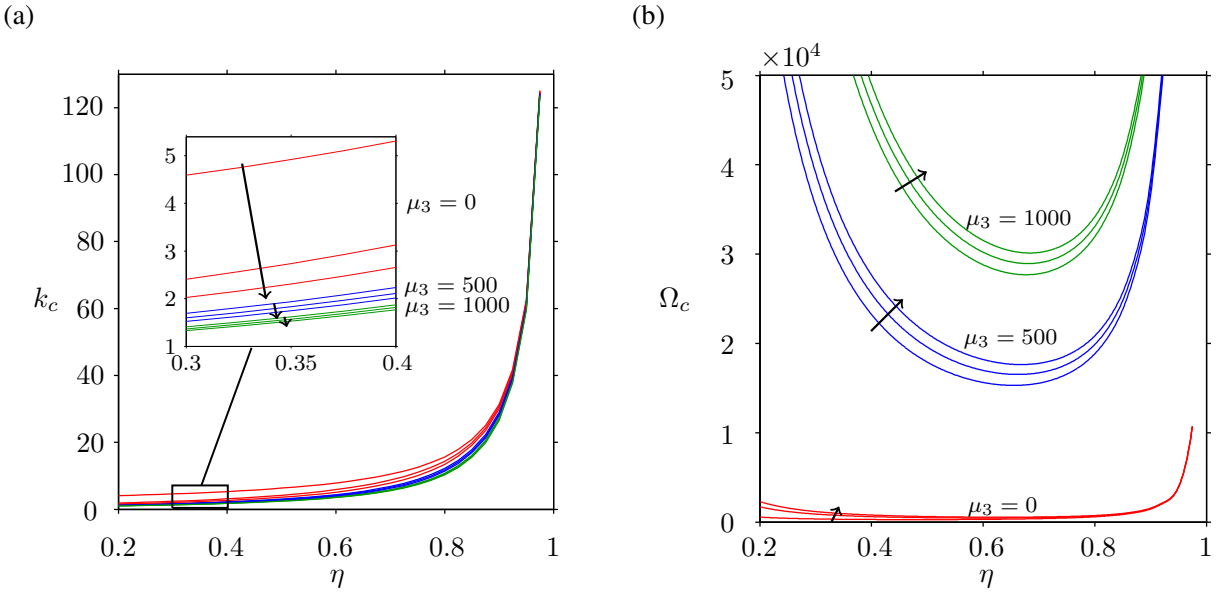

Figure 3.6: Examining how changes in the gap ratio (η), for different values μ_2 and μ_3 affect the critical wave-number (k_c) and critical angular velocity of the inner cylinder (Ω_c). (a) Shows the effect on k_c for varying η, μ_2, and μ_3, where the arrows show the direction of increasing μ_2 ($\mu_2 = 0, 500, 1000$). (b) Shows the effect upon Ω_c for varying η, μ_2, and μ_3, where the arrow shows the direction of increasing μ_2 ($\mu_2 = 0, 500, 1000$).

3.4 Discussion

In this chapter we extended the work of Taylor and others [85, 18, 68, 19] to study the axisymmetric linear stability of a transversely isotropic viscous fluid, contained in a Couette device. Similarly to Leslie [53], we utilised the stress tensor and kinematic equation first proposed by Ericksen [24] to model a transversely isotropic fluid. However, we chose an alternative case of the kinematic equation which corresponds to fibres with a large aspect ratio, this was motivated by considering long slender fibres that align in shear flow. Numerically we presented results for a range of gap ratios from 0.2 to 0.975; in typical applications this ratio is approximately 0.82 [57].

The parameter μ_3, which describes the ratio of the shear viscosity in the fibre direction to the transverse shear viscosity, is much more important in determining the stability of the flow than μ_2, which describes the ratio of the extensional viscosity to the transverse shear viscosity. While our results agree with those of Wan and Lin [88] in the effect of μ_2, we find that μ_3 has a more significant effect and therefore must be included. Although the tension in the fibres, μ_1, was retained within the calculations, it does not influence the final stability analysis.

For values of the gap ratio less than 0.8, *i.e.* for a large gap width (relative to the outer cylinder's radius) between the cylinders, the critical angular velocity of the inner cylinder is a decreasing function of the gap ratio. However for larger values of the gap ratio, *i.e.* a narrow gap width, the critical angular velocity increases as viscous effects dominate over the inertial effects giving rise to instability; more energy is then needed for the perturbation to become unstable.

Understanding the stability of fibre-laden fluids in Couette devices is relevant to flow linear dichroism (LD) spectroscopy [57]. Maximising the shear rate, whilst still remaining in the stable flow regime, produces the strongest fibre alignment and hence signal. By considering the rheological changes induced by the presence of fibres, we showed that the critical angular velocity of the inner cylinder at the onset of instability is much higher than previously thought. Exploiting this understanding may enable stronger signals to

be recovered from the use of LD Couette devices across a range of fibre types.

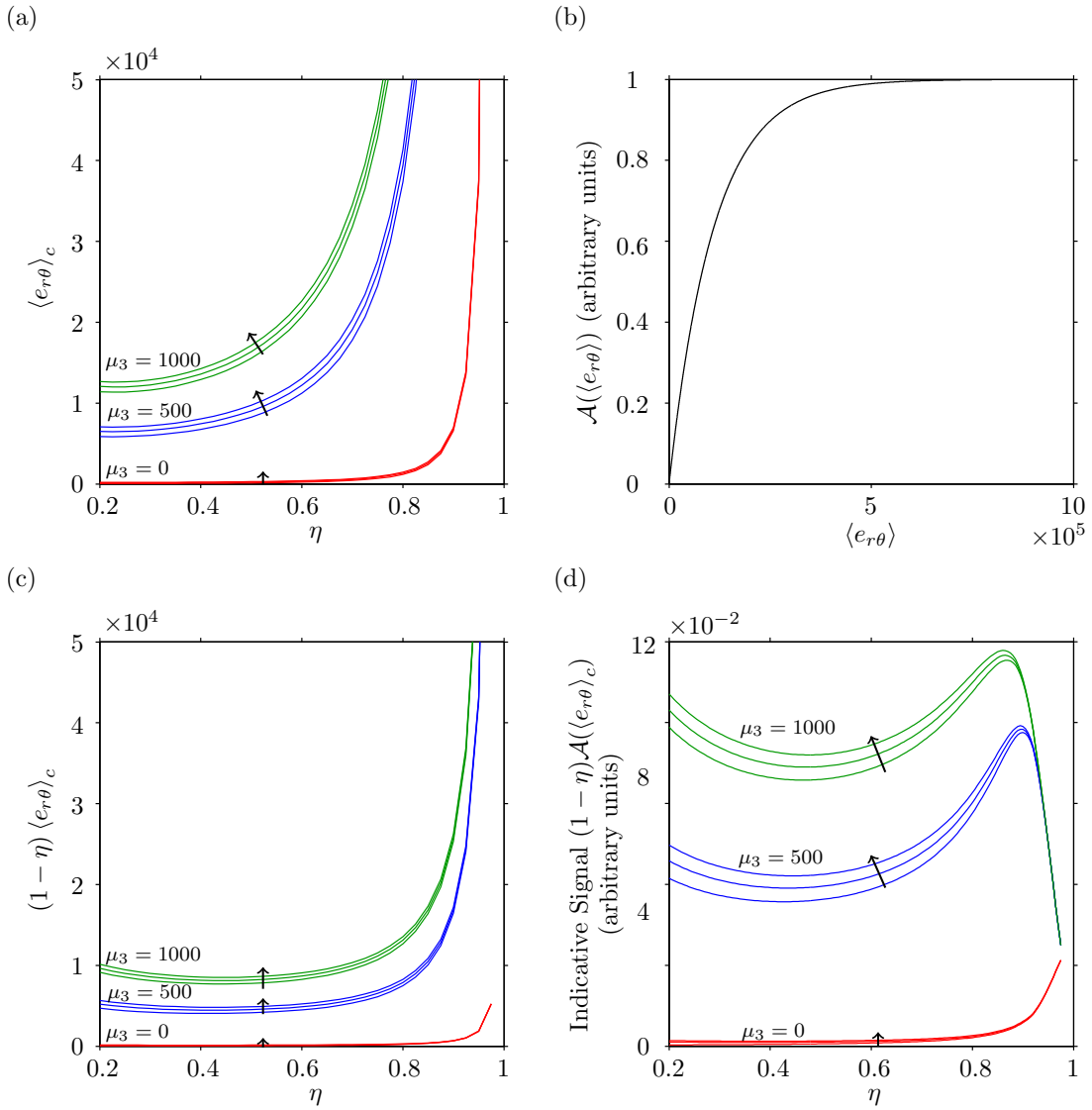

Figure 3.7: Qualitative dependence of maximum achievable LD signal on gap width. (a) Critical average shear rate $\langle e_{r\theta} \rangle_c$ at the critical angular velocity of the inner cylinder. (b) Hypothesised saturating relationship between average shear stress and alignment $\mathcal{A}(\langle e_{r\theta} \rangle)$, based on Figure 3 in McLachlan *et al.* [59]. (c) Critical average shear rate multiplied by dimensionless gap thickness $(1-\eta)\langle e_{r\theta} \rangle_c$, indicating the hypothetical magnitude of signal in the regime where alignment and shear stress are linearly related. (d) Hypothesised signal calculated from the saturating function $\mathcal{A}$ indicating the magnitude of signal in the saturating regime. We note the indicative signal we propose is the simplest that could be chosen, however other forms of this relation may apply.

It is instructive to consider how our results on critical angular velocity may relate to the strength of shear-induced alignment, and hence LD signal. To do this we must consider the dependence of average shear rate on signal, and the production of signal as

polarised light passes through the depth of fluid (figure 3.7). In Figure 3.7(a) we consider the average shear rate

$$\langle e_{r\theta} \rangle = \frac{1}{1-\eta} \int_{\eta}^{1} e_{r\theta} r \, \mathrm{d}r, \tag{3.63}$$

at the critical angular velocity Ω_c. Alignment is an increasing function of shear rate [59] and hence higher alignment should be obtained for narrower gap widths (relative to the cylinder ratio). This alignment function $\mathcal{A}$ could be linear in average shear rate or could be a saturating function, as shown in Figure 3.7(b), depending on the experimental setup [59]. Conversely a narrower gap width provides less sample to interact with incident light producing a weaker signal for a given alignment. Thus the interplay of these two effects must be taken into consideration, as shown in Figure 3.7(c,d). We see that in the saturating regime an optimal gap width may be determined (observe the local maxima in Figure 3.7(d)), this optimum is a feature of incorporating the mechanical properties of the fibres and the precise location will depend on the functional form of $\mathcal{A}$ as appropriate to the experiment in question.

In order to use this model in practice it is necessary to estimate the rheological parameters of the fluid, the most crucial being μ^* and μ_3^*, however data are required on these parameters in bio-molecular suspensions of interest. These could be determined from standard rheological techniques such as Couette or capillary viscometry, such as those described in Barnes *et al.* [4]. Our linear stability analysis could then be used to determine the other relevant parameter μ_2^*, by fitting to experimental data on the onset of instability. Alternatively, as shown in section 2.3.3, Batchelor's analysis of extensional flow of aligned rods [7] can be interpreted to identify that $\mu_2^* \propto \bar{\mu}\,\phi\,\hat{r}^2$ (modulo a logarithmic factor) where $\bar{\mu}$ is the solvent viscosity, $\phi(\ll 1)$ is the volume fraction of fibres and $\hat{r}(\gg 1)$ is the fibre aspect ratio [22].

In future work we will consider the instability of a non-symmetric perturbation to the steady state, in addition to the dispersion of fibres about the average direction. Through the link identified in chapter 5, between Ericksen's transversely isotropic fluid and an active fluid, the framework needed to investigate the dispersion of fibres about the average

direction has been established. We also aim to include the effect of entanglement between individual fibres and establish how this may change the stability of the flow.

In this chapter we adopted the conservation of mass and momentum statements, along with the transversely-isotropic stress tensor, of Ericksen [24] and couple this to the kinematic condition derived by Green and Friedman [29]. This is the first time this model has been used to analyse the linear Taylor-Couette stability of a transversely-isotropic fluid. However, Leslie [53] and Wan and Lin [88] have applied the model described by Ericksen [24]; we extend the work of Leslie by considering large gap width and the work of Wan and Lin by considering non-zero anisotropic shear viscosity. We are the first to use a transversely-isotropic model in the context of flow-linear dichroism, and therefore our results add new insight into this research area.

In this chapter we have used the transversely isotropic fluid model proposed in chapter 2 to examine the linear Taylor-Couette stability of a transversely isotropic fluid. In chapter 4 we will perform a similar stability analysis of a canonical example in fluid mechanics Rayleigh-Bénard convection.

CHAPTER 4

LINEAR RAYLEIGH-BÉNARD STABILITY OF A TRANSVERSELY ISOTROPIC FLUID

Rayleigh-Bénard convection is a canonical example in traditional fluid mechanics for the stability analysis of viscous flows; we extend this analysis to transversely isotropic fluids. We consider the linear stability of a transversely isotropic fluid contained between two infinitely-long horizontal boundaries of different temperatures (as shown in Figure 4.1) to a small arbitrary perturbation. Three different combinations of boundary types are considered, (1) both boundaries are rigid (2) both free and (3) the bottom boundary is rigid and the top is free. One application of our theory is to fibre-laden fluids, however it holds for any fluid which may be described as transversely isotropic.

Rayleigh-Bénard convection was first observed experimentally by Bénard [8] who melted wax in a metal dish which was heated from below. Bénard noticed that once the base of the dish was heated above a certain temperature hexagonal patterns developed on the surface of the wax, and it was this observation that allowed him to deduce

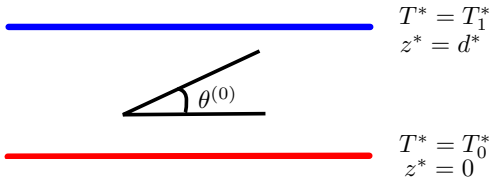

Figure 4.1: A schematic diagram of the Rayleigh-Bénard setup. The lower and upper boundaries are located at $z^* = 0$ and $z^* = d^*$ at temperatures T_0^* and T_1^*. The leading order preferred direction is given by the angle $\theta^{(0)}$.

the presence of convection currents in the wax below [20]. Other important examples of thermally driven flows can be found in the atmosphere [32], in the oceans [58], in buildings [41], and in metal production processes [11], with more examples discussed in the detailed review of Ahlers *et al.* [3].

Rayleigh [67] was the first to form a mathematical model of this experiment, using equations for the energy and state of an infinite layer of fluid, bounded by two stationary horizontal boundaries of different constant uniform temperatures. The governing equations are stated under the Boussinesq approximations, where the full model for a compressible fluid, which should be used as density is not constant, may be simplified. The Boussinesq approximations state the fluctuations in density which appear result from thermal (as opposed to pressure) effects, and in the equations for conservation of mass and momentum, density variations may be neglected except when they are coupled to the gravitational acceleration in the buoyancy force. Spiegel & Veronis [81] show, through a self-consistent approximation, the conditions under which the Boussinesq approximations are valid. We show this in Appendix A.

Under the Boussinesq approximations, the model is composed of the incompressible Navier-Stokes equations,

$$\boldsymbol{\nabla}_{\boldsymbol{x}}^{*} \cdot \boldsymbol{u}^{*} = 0, \tag{4.1}$$

$$\rho_0^{*}\left(\frac{\partial \boldsymbol{u}^{*}}{\partial t^{*}} + \left(\boldsymbol{u}^{*} \cdot \boldsymbol{\nabla}_{\boldsymbol{x}}^{*}\right)\boldsymbol{u}^{*}\right) = -\boldsymbol{\nabla}_{\boldsymbol{x}} p^{*} + \bar{\mu}^{*}\boldsymbol{\nabla}_{\boldsymbol{x}}^{*2}\boldsymbol{u}^{*} - \rho^{*} g^{*}\hat{\boldsymbol{z}}, \tag{4.2}$$

where the body-force term describing the buoyancy of the fluid is related to the variable density ρ^{*} and the acceleration due to gravity g^{*}, $\boldsymbol{u}^{*}$ is the fluid velocity, p^{*} pressure, t^{*} time, $\bar{\mu}^{*}$ shear viscosity, and ρ_0^{*} the density at temperature T_0^{*} of the lower boundary; an advection-diffusion equation for temperature,

$$\frac{\partial T^{*}}{\partial t^{*}} + \left(\boldsymbol{u}^{*} \cdot \boldsymbol{\nabla}_{\boldsymbol{x}}^{*}\right) T^{*} = \kappa^{*}\nabla_{x}^{*2} T^{*}, \tag{4.3}$$

where κ^{*} is the coefficient of thermometric conductivity [13], and a constitutive relation

for density

$$\rho^* = \rho_0^* \left(1 - \alpha^* \left(T^* - T_0^*\right)\right), \tag{4.4}$$

which is a linear function of temperature and independent of pressure [20]. Here α^* is the coefficient of volume expansion. By using the Boussinnesq approximation, the only place variable density appears in the governing equations is in the body force term describing buoyancy; it is this term that drives instability. Modelling the fluid in this way is applicable when variations in temperature are small, as variations of the thermodynamic properties (*i.e.* viscosity, thermal diffusivity and density) will also be small. To see this, observe for a fluid that is stationary at steady state, the acceleration of the fluid is much less than the acceleration due to gravity, so the thermodynamic properties may be considered constant in terms only related to the movement of the fluid. However, the buoyancy term contains a product between the acceleration due to gravity and the fluid density, and there is no guarantee this term will be smaller than other terms in the governing equation, and so the density can not be assumed constant in this term [13, 20]. These governing equations are analysed using normal modes, where a wave-number and growth parameter are introduced.

Rayleigh [67] was able to solve the problem explicitly when the two boundaries were free with zero tangential stress; this has been simulated in experiments by replacing the bottom boundary with a layer of much less viscous fluid (leaving the top boundary free) [27]. The surface tension between the two fluids will be negligible providing the dimensionless capillary number, which represents the relative effect of viscous forces versus surface tension, is large. To determine the conditions where instability occurs for other combinations of boundary types, numerical techniques are required [20].

We briefly discuss the equations and derive the steady state of the transversely isotropic model (section 4.1), and then undertake a linear stability analysis, leading to an eigenvalue problem which is solved numerically (sections 4.2-4.3). The effect of variations in viscosity-

like parameters and the steady state preferred direction on the marginal stability curves is considered (section 4.4), we conclude with discussion of the results in section 4.5.

4.1 Governing equations

We adopt a two dimensional Cartesian coordinate system (x^*, z^*), and velocity vector $\boldsymbol{u}^* = (u^*, w^*)$. Here, and in the following, stars denote dimensional variables and parameters. In formulating our governing equations we make use of the Boussinesq approximation [13], treating the density as constant in all terms except for the term describing the external force on the fluid due to gravity. The analysis performed in Appendix A will follow similarly, as the viscosity coefficients are assume to be constant. Mass conservation and momentum balance leads to the generalized Navier-Stokes equations

$$\boldsymbol{\nabla}^*_{\boldsymbol{x}} \cdot \boldsymbol{u}^* = \boldsymbol{0}, \tag{4.5}$$

$$\rho_0^* \left(\frac{\partial \boldsymbol{u}^*}{\partial t^*} + \left(\boldsymbol{u}^* \cdot \boldsymbol{\nabla}^*_{\boldsymbol{x}} \right) \boldsymbol{u}^* \right) = -\boldsymbol{\nabla}^*_{\boldsymbol{x}} p^* + \boldsymbol{\nabla}^*_{\boldsymbol{x}} \cdot \boldsymbol{\sigma}^* - \rho^* g^* \hat{\boldsymbol{z}}, \tag{4.6}$$

where ρ_0^* is the density at temperature T_0^* of the lower boundary, ρ^* is the variable density of the fluid, t^* is time, p^* is the pressure, g^* is the acceleration due to gravity, $\hat{\boldsymbol{z}}$ is the unit vector in the z^*-direction, and $\boldsymbol{\sigma}^*$ is the transversely isotropic stress tensor proposed by Ericksen (equation (2.4)). Ericksen's stress tensor incorporates the single preferred direction $\boldsymbol{a}$, which may vary in both position and time. We model the evolution of this direction via the kinematic equation proposed by Green and Friedman [29] (equation (2.13)), this is a special case of the equation proposed by Ericksen [24] corresponding to $\alpha_0 = 1$ in equation (2.6). We assume there is no active beahviour *i.e.* $\mu_1 = 0$, therefore the stress tensor (2.4) is given by

$$\boldsymbol{\sigma}^* = 2\mu^* \boldsymbol{e}^* + \mu_2^* \boldsymbol{a}\,\boldsymbol{a}\,\boldsymbol{a}\,\boldsymbol{a} : \boldsymbol{e} + 2\mu_3^* \left(\boldsymbol{a}\,\boldsymbol{a} \cdot \boldsymbol{e} + \boldsymbol{e} \cdot \boldsymbol{a}\,\boldsymbol{a} \right). \tag{4.7}$$

We assume that the temperature and density of the fluid are governed by equations (4.3) and (4.4) respectively, where we have assumed both quantities are independent of the presence of fibres.

4.1.1 Boundary conditions

We consider a transversely isotropic fluid which is contained between two boundaries at $z^* = 0$ and $z^* = d^*$. We will consider a mixture of two types of bounding surfaces; for both types of surface we assume perfect conduction of heat and that the normal component of velocity is zero, *i.e.*

$$\begin{aligned} T^* = T_0^* \text{ and } w^* = 0, \text{ at } z^* = 0, \\ T^* = T_1^* \text{ and } w^* = 0, \text{ at } z^* = d^*. \end{aligned} \tag{4.8}$$

The distinction between the types of bounding surfaces is then made through the final two boundary conditions. If the surface is rigid we impose no-slip boundary conditions, if the surface is free we impose zero-lateral stress, *i.e.*

$$\begin{aligned} u^* = 0 \text{ on a rigid surface}, \\ \frac{\partial u^*}{\partial x^*} = 0 \text{ on a free surface}. \end{aligned} \tag{4.9}$$

Results will be presented from three groups of boundary conditions: when both surfaces are rigid, both surfaces are free, and when the bottom surface is rigid and the top surface is free.

4.1.2 Non-dimensionalisation

The model is non-dimensionalised by scaling the independent and dependent variables via:

$$\boldsymbol{x}^* = d^*\boldsymbol{x}, \qquad t^* = \frac{d^{*2}}{\kappa^*}t, \qquad \boldsymbol{u}^* = \frac{\kappa^*}{d^*}\boldsymbol{u}, \tag{4.10}$$

$$T^* = \beta^* d^* T, \qquad (p^*, \boldsymbol{\sigma}^*) = \frac{\rho_0^* \kappa^{*2}}{d^{*2}}(p, \boldsymbol{\sigma}), \qquad \rho^* = \rho_0^* \rho, \tag{4.11}$$

where variables without asterisks denote dimensionless quantities, and β^* is the transverse temperature gradient, as chosen in Drazin [20], *i.e.* $\beta^* = (T_0^* - T_1^*)/d^*$. The incompressibility condition (4.5) and the kinematic equation (2.13) remain unchanged by this scaling,

$$\boldsymbol{\nabla}_{\boldsymbol{x}} \cdot \boldsymbol{u} = 0, \tag{4.12}$$

$$\frac{\partial \boldsymbol{a}}{\partial t} + (\boldsymbol{u} \cdot \boldsymbol{\nabla}_{\boldsymbol{x}})\, \boldsymbol{a} + \boldsymbol{a}\,\boldsymbol{a}\,\boldsymbol{a} : \boldsymbol{\nabla}_{\boldsymbol{x}} \boldsymbol{u} = (\boldsymbol{a} \cdot \boldsymbol{\nabla}_{\boldsymbol{x}})\, \boldsymbol{u}. \tag{4.13}$$

The momentum balance (4.6) becomes

$$\frac{\partial \boldsymbol{u}}{\partial t} + (\boldsymbol{u} \cdot \boldsymbol{\nabla}_{\boldsymbol{x}})\, \boldsymbol{u} = -\boldsymbol{\nabla}_{\boldsymbol{x}} p + \boldsymbol{\nabla}_{\boldsymbol{x}} \cdot \boldsymbol{\sigma} - \frac{\mathcal{R}\mathcal{P}}{\mathcal{B}} \rho \hat{\boldsymbol{z}}, \tag{4.14}$$

where we have introduced the following dimensionless parameters

$$\mathcal{B} = \alpha^* \beta^* d^*, \qquad \mathcal{R} = \frac{\alpha^* \beta^* d^{*4} g^* \rho_0^*}{\kappa \mu^*}, \qquad \mathcal{P} = \frac{\mu^*}{\rho_0^* \kappa^*}. \tag{4.15}$$

The Rayleigh number $\mathcal{R}$ is a dimensionless parameter relating the stabilising effects of molecular diffusion of momentum to the destabilising effects of buoyancy [20, 46, 84], and the Prandtl number $\mathcal{P}$ relates the kinematic viscosity of the fluid to its thermal conductivity [13]. Small values of the Prandtl number indicate heat diffuses quickly compared to the fluid velocity, with the converse true for large values of $\mathcal{P}$. Non-dimensionalising

the stress tensor (4.7) yields the dimensionless stress tensor

$$\boldsymbol{\sigma} = \mathcal{P}\left(2\,\boldsymbol{e} + \mu_2\,\boldsymbol{a}\,\boldsymbol{a}\,\boldsymbol{a}\,\boldsymbol{a} : \boldsymbol{e} + 2\mu_3\left(\boldsymbol{a}\,\boldsymbol{a}\,\cdot\boldsymbol{e} + \boldsymbol{e}\cdot\boldsymbol{a}\,\boldsymbol{a}\right)\right), \tag{4.16}$$

where the non-dimensional rate of strain tensor, $\boldsymbol{e} = (\boldsymbol{\nabla}_{\boldsymbol{x}}\boldsymbol{u} + \boldsymbol{\nabla}_{\boldsymbol{x}}\boldsymbol{u}^T)/2$, and the following non-dimensional parameters have been introduced

$$\mu_2 = \frac{\mu_2^*}{\mu^*}, \qquad\qquad \mu_3 = \frac{\mu_3^*}{\mu^*}. \tag{4.17}$$

Here μ_2 and μ_3 are the ratios of the extensional viscosity and shear viscosity in the fibre direction to the transverse shear viscosity, respectively [29, 38].

The constitutive equation (4.4) for variable density is non-dimensionalised to give

$$\rho = 1 + \mathcal{B}\left(T_0 - T\right), \tag{4.18}$$

where $T_0 = T_0^*/\beta^* d^*$ and equation (4.3), which governs the temperature distribution, becomes

$$\frac{\partial T}{\partial t} + \left(\boldsymbol{u}\cdot\boldsymbol{\nabla}_{\boldsymbol{x}}\right)T = \nabla_{\boldsymbol{x}}^2 T. \tag{4.19}$$

Finally, the boundary conditions (4.8) and (4.9), in dimensionless form, are

$$\begin{aligned} T = T_0, \text{ and } w = 0, \text{ at } z = 0, \\ T = T_1, \text{ and } w = 0, \text{ at } z = 1, \end{aligned} \tag{4.20}$$

where $T_1 = T_1^*/\beta^* d^*$. The distinction between the type of surface is given by

$$\begin{aligned} u = 0 \text{ on a rigid surface}, \\ \frac{\partial u}{\partial x} = 0 \text{ on a free surface}. \end{aligned} \tag{4.21}$$

The model consists of four governing equations (4.12), (4.13), (4.14), (4.19) for $\boldsymbol{u}$,

$\boldsymbol{a}$, p and T, respectively, subject to constitutive laws (4.16) and (4.18) with boundary conditions (4.20) and(4.21).

4.1.3 Steady state

Assuming the parallel boundaries are infinitely long in the x-direction, we look for a steady state solution where the fluid is stationary and the preferred direction in the fluid is described by the constant angle $\theta^{(0)}$ to the x-axis (Figure 4.1), *i.e.* $\boldsymbol{u}^{(0)} = \mathbf{0}$ and $\boldsymbol{a}^{(0)} = (\cos\theta^{(0)}, \sin\theta^{(0)})$. When the fluid velocity is stationary the steady state equation for temperature is

$$\nabla_{\boldsymbol{x}}^2 T^{(0)} = 0. \tag{4.22}$$

Solving equation (4.22) subject to the boundary conditions (4.20) gives

$$T^{(0)} = (T_1 - T_0)\, z + T_0. \tag{4.23}$$

Noting that $T_1 - T_0 = -1$, equation (4.23) is rewritten as

$$T^{(0)} = T_0 - z. \tag{4.24}$$

Substituting this solution for temperature into the constitutive relation for density (4.18) gives the steady state density distribution

$$\rho^{(0)} = 1 + \mathcal{B}\, z. \tag{4.25}$$

As there is no spatial variation in the fibre orientation field and the fluid is stationary the momentum balance (4.16) is reduced to

$$\boldsymbol{\nabla}_{\boldsymbol{x}} p = -\frac{\mathcal{R}\mathcal{P}}{\mathcal{B}} \rho^{(0)} \hat{\boldsymbol{z}}. \tag{4.26}$$

The components of equation (4.26) are therefore

$$\frac{\partial p^{(0)}}{\partial x} = 0, \tag{4.27}$$

$$\frac{\partial p^{(0)}}{\partial z} = -\frac{\mathcal{RP}}{\mathcal{B}}\rho^{(0)}. \tag{4.28}$$

From equation (4.27) it is clear pressure is a function of z only. Substituting the density solution (4.25) into equation (4.28) gives

$$\frac{\mathrm{d}p^{(0)}}{\mathrm{d}z} = -\frac{\mathcal{RP}}{\mathcal{B}}\left(1 + \mathcal{B}\, z\right), \tag{4.29}$$

$$\Leftrightarrow p^{(0)} = p_0 - \frac{\mathcal{RP}}{\mathcal{B}}\left(z + \frac{\mathcal{B}\, z^2}{2}\right), \tag{4.30}$$

where p_0 is some arbitrary pressure constant. Therefore the steady state is given by

$$\boldsymbol{u}^{(0)} = 0, \qquad p^{(0)} = p_0 - \frac{\mathcal{RP}}{\mathcal{B}}\left(z + \frac{\mathcal{B}\, z^2}{2}\right), \tag{4.31}$$

$$T^{(0)} = T_0 - z, \qquad \rho^{(0)} = 1 + \mathcal{B}\, z. \tag{4.32}$$

4.2 Stability

We now examine the linear stability of the steady state described by equations (4.31)-(4.32), for the three different combinations of boundary types. We derive the first-order perturbation equations for an arbitrary perturbation, which are transformed into a generalised eigenvalue problem by assuming the solution takes the form of normal modes.

4.2.1 Linear stability analysis

We consider the stability of the steady state solution to a perturbation,

$$\boldsymbol{u}(x,z,t) = \varepsilon \boldsymbol{u}^{(1)}(x,z,t) + \mathcal{O}\left(\varepsilon^2\right), \tag{4.33}$$

$$p(r,z,t) = p^{(0)} + \varepsilon p^{(1)}(x,z,t) + \mathcal{O}\left(\varepsilon^2\right), \tag{4.34}$$

$$T(x,z,t) = T^{(0)} + \varepsilon T^{(1)}(x,z,t) + \mathcal{O}\left(\varepsilon^2\right), \tag{4.35}$$

$$\theta(x,z,t) = \theta^{(0)} + \varepsilon \theta^{(1)}(x,z,t) + \mathcal{O}\left(\varepsilon^2\right). \tag{4.36}$$

where $0 < \varepsilon \ll 1$. We have proposed a perturbation to the fibre orientation angle $\theta^{(0)}$ and not the alignment vector $\boldsymbol{a}$ directly, therefore we must identify the form of $\boldsymbol{a}$. First consider

$$\boldsymbol{a} = \Big(\cos\left(\theta(x,z,t)\right), \sin\left(\theta(x,z,t)\right)\Big), \tag{4.37}$$

note this vector is clearly a unit vector as required. Taylor-expanding $\cos\theta$ and $\sin\theta$ about $\theta = \theta^{(0)}$, gives

$$\cos(\theta) = \cos\theta^{(0)} - (\theta - \theta^{(0)})\sin\theta^{(0)} - \frac{1}{2}(\theta - \theta^{(0)})^2\cos\theta^{(0)} + \cdots, \tag{4.38}$$

$$\sin(\theta) = \sin\theta^{(0)} + (\theta - \theta^{(0)})\cos\theta^{(0)} - \frac{1}{2}(\theta - \theta^{(0)})^2\sin\theta^{(0)} + \cdots. \tag{4.39}$$

Now describe the general angle θ as a small perturbation from the uniform steady state angle $\theta^{(0)}$, *i.e.* $\theta = \theta^{(0)} + \varepsilon\theta^{(1)}$ as in equation (4.36), equations (4.38) and (4.39) may be rewritten as

$$\cos(\theta) = \cos\theta^{(0)} - \varepsilon\theta^{(1)}\sin\theta^{(0)} + \cdots, \tag{4.40}$$

$$\sin(\theta) = \sin\theta^{(0)} + \varepsilon\theta^{(1)}\cos\theta^{(0)} + \cdots, \tag{4.41}$$

so $\boldsymbol{a}$ takes the form

$$\boldsymbol{a} = \left(\cos\theta^{(0)} - \varepsilon\theta^{(1)}\sin\theta^{(0)}, \sin\theta^{(0)} + \varepsilon\theta^{(1)}\cos\theta^{(0)}\right) + \mathcal{O}\left(\varepsilon^2\right). \tag{4.42}$$

Using the ansatz given in equations (4.33)-(4.36) and (4.42) we may state the following governing equations at first order. The incompressibility condition (4.12) becomes (at next order)

$$\boldsymbol{\nabla}_{\boldsymbol{x}} \cdot \boldsymbol{u}^{(1)} = 0, \tag{4.43}$$

with conservation of momentum (4.14) given by

$$\frac{\partial \boldsymbol{u}^{(1)}}{\partial t} = -\boldsymbol{\nabla}_{\boldsymbol{x}} p^{(1)} + \boldsymbol{\nabla}_{\boldsymbol{x}} \cdot \boldsymbol{\sigma}^{(1)} - \frac{\mathcal{R}\mathcal{P}}{\mathcal{B}}\rho^{(1)}\hat{\boldsymbol{z}}. \tag{4.44}$$

The first order constitutive relations for stress (4.16) and fluid density (4.18) are given by

$$\boldsymbol{\sigma}^{(1)} = \mathcal{P}\left(2\boldsymbol{e}^{(1)} + \mu_2 \boldsymbol{a}^{(0)}\boldsymbol{a}^{(0)}\boldsymbol{a}^{(0)}\boldsymbol{a}^{(0)} : \boldsymbol{e}^{(1)} + 2\mu_3\left(\boldsymbol{a}^{(0)}\boldsymbol{a}^{(0)} \cdot \boldsymbol{e}^{(1)} + \boldsymbol{e}^{(1)} \cdot \boldsymbol{a}^{(0)}\boldsymbol{a}^{(0)}\right)\right), \tag{4.45}$$

$$\rho^{(1)} = -\mathcal{B}T^{(1)}, \tag{4.46}$$

where $\boldsymbol{e}^{(1)} = (\boldsymbol{\nabla}_{\boldsymbol{x}}\boldsymbol{u}^{(1)} + (\boldsymbol{\nabla}_{\boldsymbol{x}}\boldsymbol{u}^{(1)})^T)/2$ is the first order rate-of-strain tensor. Notice equations (4.43)-(4.46) are independent of the first order alignment vector

$$\boldsymbol{a}^{(1)} = \left(-\theta^{(1)}\sin\theta^{(0)}, \theta^{(1)}\cos\theta^{(0)}\right), \tag{4.47}$$

which is in turn governed by

$$\frac{\partial \boldsymbol{a}^{(1)}}{\partial t} + \boldsymbol{a}^{(0)}\boldsymbol{a}^{(0)}\boldsymbol{a}^{(0)} : \boldsymbol{\nabla}_{\boldsymbol{x}}\boldsymbol{u}^{(1)} = \left(\boldsymbol{a}^{(0)} \cdot \boldsymbol{\nabla}_{\boldsymbol{x}}\right)\boldsymbol{u}^{(1)}. \tag{4.48}$$

Finally, the equation governing temperature at next order is

$$\frac{\partial T^{(1)}}{\partial t} - w^{(1)} = \nabla_{\boldsymbol{x}}^2 T^{(1)}. \tag{4.49}$$

The boundary conditions become homogeneous at first order, and are given by

$$w^{(1)} = u^{(1)} = T^{(1)} = 0 \text{ on a rigid surface,} \tag{4.50}$$

$$w^{(1)} = \frac{\partial u^{(1)}}{\partial x} = T^{(1)} = 0 \text{ on a free surface.} \tag{4.51}$$

The components of the stress tensor (equation (4.45)) are

$$\sigma_{xx}^{(1)} = \mathcal{P}\left(2e_{xx}^{(1)} + \mu_2 \cos^2\theta^{(0)}\, A_e^{(1)} + 2\mu_3\left(2\, e_{xx}^{(1)} \cos^2\theta^{(0)} + e_{xy}^{(1)} \sin 2\theta^{(0)}\right)\right), \tag{4.52}$$

$$\sigma_{xy}^{(1)} = \mathcal{P}\left(2e_{xy}^{(1)} + \frac{\mu_2}{2}\, A_e^{(1)} \sin 2\theta^{(0)} + 2\mu_3\left(e_{xy}^{(1)} + e_{xz}^{(1)} \cos 2\theta^{(0)}\right)\right), \tag{4.53}$$

$$\sigma_{zz}^{(1)} = \mathcal{P}\left(2e_{zz}^{(1)} + \mu_2\, A_e^{(1)} \sin^2\theta^{(0)} + 2\mu_3\left(e_{xz}^{(1)} \sin 2\theta^{(0)} + 2\, e_{zz}^{(1)} \sin^2\theta^{(0)}\right)\right), \tag{4.54}$$

where we have substituted the leading order alignment vector $\boldsymbol{a}^{(0)} = (\cos\theta^{(0)}, \sin\theta^{(0)})$ and defined

$$A_e^{(1)} = e_{xx}^{(1)} \cos 2\theta^{(0)} + e_{xz}^{(1)} \sin 2\theta^{(0)}. \tag{4.55}$$

The pressure is eliminated from the momentum equation (4.44) (appendix B), and com-

ponents of stress are substituted to give

$$\begin{aligned}\frac{1}{\mathcal{P}}\nabla_{\boldsymbol{x}}^2\frac{\partial u^{(1)}}{\partial t} &= \left(1+\mu_2\frac{\sin^2 2\theta^{(0)}}{4}+\mu_3\right)\nabla_{\boldsymbol{x}}^4 u^{(1)} \\ &\quad+\mu_2\left(\frac{\sin 4\theta^{(0)}}{2}\left(\frac{\partial^4 u^{(1)}}{\partial x\partial z^3}-\frac{\partial^4 u^{(1)}}{\partial x^3\partial z}\right)+\cos 4\theta^{(0)}\frac{\partial^4 u^{(1)}}{\partial x^2\partial z^2}\right),\end{aligned} \tag{4.56}$$

$$\begin{aligned}\frac{1}{\mathcal{P}}\nabla_{\boldsymbol{x}}^2\frac{\partial w^{(1)}}{\partial t} &= \left(1+\mu_2\frac{\sin^2 2\theta^{(0)}}{4}+\mu_3\right)\nabla_{\boldsymbol{x}}^4 w^{(1)}+\mathcal{R}\frac{\partial^2 T^{(1)}}{\partial x^2} \\ &\quad+\mu_2\left(\frac{\sin 4\theta^{(0)}}{2}\left(\frac{\partial^4 w^{(1)}}{\partial x\partial z^3}-\frac{\partial^4 w^{(1)}}{\partial x^3\partial z}\right)+\cos 4\theta^{(0)}\frac{\partial^4 w^{(1)}}{\partial x^2\partial z^2}\right).\end{aligned} \tag{4.57}$$

4.2.2 Kinematic equation

We may rewrite the components of the kinematic equation (4.48) in terms of $\theta^{(0)}$ and $\theta^{(1)}$:

$$-\sin\theta^{(0)}\frac{\partial\theta^{(1)}}{\partial t}+\cos\theta^{(0)}A_u^{(1)}=\cos\theta^{(0)}\frac{\partial u^{(1)}}{\partial x}+\sin\theta^{(0)}\frac{\partial u^{(1)}}{\partial z}, \tag{4.58}$$

$$\cos\theta^{(0)}\frac{\partial\theta^{(1)}}{\partial t}+\sin\theta^{(0)}A_u^{(1)}=\cos\theta^{(0)}\frac{\partial w^{(1)}}{\partial x}+\sin\theta^{(0)}\frac{\partial w^{(1)}}{\partial z}, \tag{4.59}$$

$$\text{where } A_u^{(1)}=\cos 2\theta^{(0)}\frac{\partial u^{(1)}}{\partial x}+\frac{\sin 2\theta^{(0)}}{2}\left(\frac{\partial u^{(1)}}{\partial z}+\frac{\partial w^{(1)}}{\partial x}\right). \tag{4.60}$$

We simplify this set of equations to a single equation (coupled with $|\boldsymbol{a}|=1$). Multiplying equation (4.58) by $\cos\theta^{(0)}$ and equation (4.59) by $\sin\theta^{(0)}$ gives

$$-\frac{\sin 2\theta^{(0)}}{2}\frac{\partial\theta^{(1)}}{\partial t}+\cos^2\theta^{(0)}A_u^{(1)}=\cos^2\theta^{(0)}\frac{\partial u^{(1)}}{\partial x}+\frac{\sin 2\theta^{(0)}}{2}\frac{\partial u^{(1)}}{\partial z}, \tag{4.61}$$

$$\frac{\sin 2\theta^{(0)}}{2}\frac{\partial\theta^{(1)}}{\partial t}+\sin^2\theta^{(0)}A_u^{(1)}=\frac{\sin 2\theta^{(0)}}{2}\frac{\partial w^{(1)}}{\partial x}+\sin^2\theta^{(0)}\frac{\partial w^{(1)}}{\partial z}. \tag{4.62}$$

Summing equation (4.61) and (4.62) gives

$$A_u^{(1)}=\cos 2\theta^{(0)}\frac{\partial u^{(1)}}{\partial x}+\frac{\sin 2\theta^{(0)}}{2}\left(\frac{\partial u^{(1)}}{\partial z}+\frac{\partial w^{(1)}}{\partial x}\right), \tag{4.63}$$

which is true by definition (4.60), and is therefore always satisfied. Multiplying equation (4.58) by $\sin\theta^{(0)}$ and equation (4.59) by $\cos\theta^{(0)}$

$$-\sin^2\theta^{(0)}\,\frac{\partial\theta^{(1)}}{\partial t}+\frac{\sin 2\theta^{(0)}}{2}A_u^{(1)}=\frac{\sin 2\theta^{(0)}}{2}\,\frac{\partial u^{(1)}}{\partial x}+\sin^2\theta^{(0)}\,\frac{\partial u^{(1)}}{\partial z}\,, \tag{4.64}$$

$$\cos^2\theta^{(0)}\,\frac{\partial\theta^{(1)}}{\partial t}+\frac{\sin 2\theta^{(0)}}{2}A_u^{(1)}=\cos^2\theta^{(0)}\,\frac{\partial w^{(1)}}{\partial x}+\frac{\sin 2\theta^{(0)}}{2}\,\frac{\partial w^{(1)}}{\partial z}\,. \tag{4.65}$$

Subtracting equation (4.64) from equation (4.65) gives

$$\frac{\partial\theta^{(1)}}{\partial t}=\cos^2\theta^{(0)}\,\frac{\partial w^{(1)}}{\partial x}-\sin^2\theta^{(0)}\,\frac{\partial u^{(1)}}{\partial z}-\sin 2\theta^{(0)}\,\frac{\partial u^{(1)}}{\partial x}\,, \tag{4.66}$$

Notice equations (4.56), (4.57) and (4.66) are decoupled, and so we may solve the stability problem by considering only equations (4.49) and (4.57) with appropriate boundary conditions on $w^{(1)}$ and $T^{(1)}$. The x-component of velocity and alignment angle may then be calculated from the solution for $w^{(1)}$.

4.2.3 Normal mode solutions

We propose the solution to equations (4.49) and (4.57) takes the form

$$w^{(1)}=w'(z)e^{st+ikx}, \qquad\qquad T^{(1)}=T'(z)e^{st+ikx}, \tag{4.67}$$

where k is the wave-number and s is the growth rate. Using this ansatz, equations (4.49) and (4.57) become

$$\left[\left(1+\mu_2\frac{\sin^2 2\theta^{(0)}}{4}+\mu_3\right)\left(D^2-k^2\right)^2+\mu_2\left(i\,\frac{\sin 4\theta^{(0)}}{2}\left(kD^3-k^3D\right)-\cos 4\theta^{(0)}k^2D^2\right)\right]w'$$

$$-\mathcal{R}k^2T'=\frac{s}{\mathcal{P}}\left(D^2-k^2\right)w', \tag{4.68}$$

$$w'+\left[D^2-k^2\right]T'=sT', \tag{4.69}$$

where we have adopted the convention $D = \mathrm{d}/\,\mathrm{d}z$. Equations (4.68) and (4.69) form an eigenvalue problem which must be solved subject to the boundary conditions (4.20) and (4.21) rewritten as

$$\begin{aligned} w' = Dw' = T' = 0 \text{ on a rigid surface,} \\ w' = D^2w' = T' = 0 \text{ on a free surface.} \end{aligned} \tag{4.70}$$

The growth rate s represents an eigenvalue to equations (4.68) and (4.69), *i.e.* for a given dimensionless wave-number k there will be non-trivial solutions (w', T') to equations (4.68) and (4.69) only for certain values of s. We establish for each wave-number k the maximum Rayleigh number $\mathcal{R}_l(k)$ such that the real part of all eigenvalues s are negative, *i.e.* the largest Rayleigh number such that the perturbation is stable and any disturbance decays to zero. The minimum of $\mathcal{R}_l(k)$ is of particular interest, and is termed the critical Rayleigh number ($\mathcal{R}_c$), it is used to determine the physical conditions under which instability first occurs [1, 20, 46]. If for a given experimental setup $\mathcal{R} < \mathcal{R}_c$ then any perturbation decays exponentially to zero. The corresponding value of k at $\mathcal{R}_c$ is also of interest, it describes the period of the convection currents and is termed the critical wave-number (k_c).

4.3 Numerical solution method

In order to determine the marginal stability curves $\mathcal{R}_l(k)$ we must solve for the velocity w' and temperature T' in equations (4.68) and (4.69). We do this using a Chebyshev collocation method. The Chebyshev collocation method is a spectral method that is capable of achieving ten digits of accuracy, where a finite difference or finite element method may only achieve two or three [86].

We use the $N+1$ Chebyshev points

$$z_i = \cos\left(\frac{i\pi}{N}\right), \qquad i = 0, 1, \ldots, N, \tag{4.71}$$

to construct the Nth order interpolating polynomials P^w and P^T to w' and T' respectively. These polynomials are constructed as Lagrange polynomials

$$P_j^i(z) = \frac{1}{A_j}\prod_{\substack{k=0\\k\neq j}}^{N}(z - z_k), \qquad A_j = \prod_{\substack{k=0\\k\neq j}}^{N}\left(z_j - z_k\right), \qquad i = w, T. \tag{4.72}$$

As there are $N+1$ collocation points for each Nth order polynomial, both polynomials are uniquely determined. Notice that the Chebyshev points are defined on an interval $[-1, 1]$ and so we must translate our coordinate system by using the substitution $Z = 2z - 1$. The eigenvalue equations (4.68) and (4.69) are now given by

$$\begin{aligned}\Bigg[\left(1 + \mu_2\frac{\sin^2 2\theta^{(0)}}{4} + \mu_3\right)\left(4D^2 - k^2\right)^2 \\ +\mu_2\left(i\,\sin 4\theta^{(0)}\left(4kD^3 - k^3D\right) - 2\cos 4\theta^{(0)}k^2D^2\right)\Bigg]w' - \mathcal{R}k^2T' = \frac{s}{\mathcal{P}}\left(4D^2 - k^2\right)w',\end{aligned} \tag{4.73}$$

$$w' + \left[4D^2 - k^2\right]T' = sT'. \tag{4.74}$$

4.3.1 Chebyshev differentiation matrix

We wish to construct the derivative of both the velocity and temperature to solve the eigenvalue problem defined by the equations (4.73) and (4.74). We assume the derivative of each of these variables, at the Chebyshev points z_i, is equal to the derivative of the Lagrange polynomial, *i.e.*

$$\frac{\mathrm{d}w_i}{\mathrm{d}z} = \frac{\mathrm{d}P^w(z_i)}{\mathrm{d}z}, \qquad \frac{\mathrm{d}T_i}{\mathrm{d}z} = \frac{\mathrm{d}P^T(z_i)}{\mathrm{d}z}. \tag{4.75}$$

As this operation is linear, it may be represented by matrix multiplication [86],

$$\frac{\mathrm{d}w_i}{\mathrm{d}z} = (D_N)_{ij}\, w_j, \qquad \frac{\mathrm{d}T_i}{\mathrm{d}z} = (D_N)_{ij}\, T_j, \tag{4.76}$$

where D_N is the $(N+1) \times (N+1)$ Chebyshev differentiation matrix.

The components of the Chebyshev differentiation matrix are given [86]

$$D_{00} = \frac{2N^2+1}{6}, \qquad D_{NN} = -\frac{2N^2+1}{6}, \tag{4.77}$$

$$D_{jj} = \frac{-x_j}{2(1-x_j^2)}, \qquad j = 1, \ldots, N-1, \tag{4.78}$$

$$D_{ij} = \frac{c_i(-1)^{i+j}}{c_j(x_i - x_j)}, \qquad i \neq j \quad i, j = 1, \ldots, N-1, \tag{4.79}$$

where

$$c_i = \begin{cases} 2 & i = 0 \text{ or } N, \\ 1 & \text{otherwise.} \end{cases} \tag{4.80}$$

To compute higher derivatives, simply apply the differentiation matrices repeatedly [86], for example

$$\frac{\mathrm{d}^2}{\mathrm{d}z^2} = \frac{\mathrm{d}}{\mathrm{d}z}\left(\frac{\mathrm{d}}{\mathrm{d}z}\right) = D_{ij} D_{jk}. \tag{4.81}$$

These Chebyshev matrices a computed using the m file *cheb.m* [86].

4.3.2 Eigenvalue problem

Using the Chebyshev differentiation matrix $\boldsymbol{D}$ the linear operators on w' and T' in equations (4.73) and (4.74) may be approximated. This allows us to form the generalised matrix eigenvalue problem

$$\boldsymbol{A}\,\boldsymbol{x} = s\,\boldsymbol{B}\,\boldsymbol{x}, \tag{4.82}$$

where s is the growth rate and eigenvalue of the problem, $\boldsymbol{A}$ and $\boldsymbol{B}$ are matrices which are discrete representations of the linear operators which act on w' and T', and the vector $\boldsymbol{x}$ contains the coefficients of the Lagrange polynomials which approximate w' and T' at the Chebyshev points (equivalently the values of w' and T' at the Chebyshev points) [86].

The matrices $\boldsymbol{A}$ and $\boldsymbol{B}$ are given as

$$\boldsymbol{A} = \begin{bmatrix} \boldsymbol{A}_{11} & -\mathcal{R}k^2\boldsymbol{I} \\ \boldsymbol{I} & 4\boldsymbol{D}^2 - k^2\boldsymbol{I} \end{bmatrix}, \tag{4.83}$$

$$\boldsymbol{B} = \begin{bmatrix} \frac{1}{\mathcal{P}}\left(4\boldsymbol{D}^2 - k^2\boldsymbol{I}\right) & \boldsymbol{0} \\ \boldsymbol{0} & \boldsymbol{I} \end{bmatrix}, \tag{4.84}$$

where $\boldsymbol{0}$ is an $(N+1)\times(N+1)$ matrix of zeros, $\boldsymbol{I}$ is the $(N+1)\times(N+1)$ identity matrix and

$$\begin{aligned} \boldsymbol{A}_{11} = &\left(1 + \mu_2\frac{\sin^2 2\theta^{(0)}}{4} + \mu_3\right)\left(16\boldsymbol{D}^4 - 16k^2\boldsymbol{D}^2 + k^4\boldsymbol{I}\right)^2 \\ &+ \mu_2\left(i\,\sin 4\theta^{(0)}\left(4k\boldsymbol{D}^3 - k^3\boldsymbol{D}\right) - 2\cos 4\theta^{(0)}k^2\boldsymbol{D}^2\right). \end{aligned} \tag{4.85}$$

We construct the matrices $\boldsymbol{A}$ and $\boldsymbol{B}$ in MATLAB for each tuple of parameters $\theta^{(0)}$, μ_2 and μ_3. However, the matrices are not full rank as we must apply boundary conditions to close the problem.

4.3.3 Boundary conditions

We adapt a method described by Hoepffner [37] to apply appropriate boundary conditions. This method reduces the solution space to only consider interpolants which satisfy the boundary conditions

$$T' = w' = 0 \text{ and } Dw' = 0 \text{ or } D^2w' = 0 \text{ at } z = -1, 1. \tag{4.86}$$

We begin by expressing all six boundary conditions in a matrix $\boldsymbol{C}$, where each row of $\boldsymbol{C}$ corresponds to a boundary condition. We apply the Dirichlet conditions by setting the corresponding element on the boundary to be zero, *i.e.* the first row of $\boldsymbol{C}$, which corresponds to $w = 0$ at $z = 1$ will be $(1, 0, \ldots, 0)$. We apply the derivative conditions by applying the appropriate derivative to the second or penultimate elements of w This allows us to write our homogeneous boundary conditions as

$$\boldsymbol{C}\,\boldsymbol{x} = \boldsymbol{0}. \tag{4.87}$$

We decompose the vector of unknowns $\boldsymbol{x}$, into the elements we wish to keep ($\boldsymbol{x}^k$), and the elements we wish to remove ($\boldsymbol{x}^r$). The elements we remove correspond to the elements the boundary conditions are applied to, *i.e.* $x_1, x_2, x_N, x_{N+1}, x_{N+2}$, and $x_{2(N+1)}$. We reorder $\boldsymbol{x}$ in equation (4.87) to give

$$\left(\boldsymbol{C}^k, \boldsymbol{C}^r\right) \begin{pmatrix} \boldsymbol{x}^k \\ \boldsymbol{x}^r \end{pmatrix} = \boldsymbol{0}. \tag{4.88}$$

By expanding equation (4.88)

$$\boldsymbol{C}^k\boldsymbol{x}^k + \boldsymbol{C}^r\boldsymbol{x}^r = \boldsymbol{0}, \tag{4.89}$$

$$\Rightarrow \boldsymbol{x}^r = -\left(\boldsymbol{C}^r\right)^{-1}\boldsymbol{C}^k\boldsymbol{x}^k. \tag{4.90}$$

the removed components $\boldsymbol{x}^r$ are expressed as a function of the components that are retained ($\boldsymbol{x}^k$). We now use equation (4.90) to implement the boundary conditions on equation (4.82). To do this, we reorder $\boldsymbol{x}$ as we did in equation (4.87) as well as the matrices $\boldsymbol{A}$ and $\boldsymbol{B}$ to give

$$\begin{pmatrix} \boldsymbol{A}^{kk} & \boldsymbol{A}^{kr} \\ \boldsymbol{A}^{rk} & \boldsymbol{A}^{rr} \end{pmatrix} \begin{pmatrix} \boldsymbol{x}^k \\ \boldsymbol{x}^r \end{pmatrix} = s \begin{pmatrix} \boldsymbol{B}^{kk} & \boldsymbol{B}^{kr} \\ \boldsymbol{B}^{rk} & \boldsymbol{B}^{rr} \end{pmatrix} \begin{pmatrix} \boldsymbol{x}^k \\ \boldsymbol{x}^r \end{pmatrix}. \tag{4.91}$$

As we are only interested in determining the elements of $\boldsymbol{x}^k$, we reduce equation (4.91) to

$$\boldsymbol{A}^{kk}\boldsymbol{x}^k + \boldsymbol{A}^{kr}\boldsymbol{x}^r = s\boldsymbol{B}^{kk}\boldsymbol{x}^k + \boldsymbol{B}^{kr}\boldsymbol{x}^r. \tag{4.92}$$

Using equation (4.90) this system of equations may be written in terms of $\boldsymbol{x}^k$ only

$$\left(\boldsymbol{A}^{kk} + \boldsymbol{A}^{kr}\boldsymbol{G}\right)\boldsymbol{x}^k = s\left(\boldsymbol{B}^{kk} + \boldsymbol{B}^{kr}\boldsymbol{G}\right)\boldsymbol{x}^k, \tag{4.93}$$

where $\boldsymbol{G} = -\left(\boldsymbol{C}^r\right)^{-1}\boldsymbol{C}^k$. Equation (4.93) constitutes a full-rank generalised matrix eigenvalue problem.

We may therefore construct the matrices $\boldsymbol{A}^{kk} + \boldsymbol{A}^{kr}\boldsymbol{G}$ and $\boldsymbol{B}^{kk} + \boldsymbol{B}^{kr}\boldsymbol{G}$ in MATLAB, and compute the eigenvalue s for a range of parameters $(\theta^{(0)}, \mu_2, \mu_3)$ and Rayleigh number $\mathcal{R}$ using the inbuilt eigenvalue solver *eig*; this solver employs the QZ-algorithm. We then determine the Rayleigh number for which the eigenvalue is zero using the MATLAB function *fzero*, *i.e.* disturbances neither grow nor decay and fminsearch to determine the critical wave and Rayleigh numbers.

4.3.4 Eigenvalue problem

We use the QZ-algorithm [61] to solve the generalised eigenvalue problem (4.82), however to improve the convergence characteristics of this iterative method we apply a pre-conditioner matrix $\boldsymbol{L}$ to matrices $\boldsymbol{A}$ and $\boldsymbol{B}$. We choose a diagonal pre-conditioner consisting of the maximum value of $\boldsymbol{A}$ in each row. To determine the marginal stability curves $\mathcal{R}_l(k)$ for each set of parameters $\theta^{(0)}, \mu_2$ and μ_3 we therefore solve the system

$$\boldsymbol{L}\,\boldsymbol{A}\,\boldsymbol{x} = s\boldsymbol{L}\,\boldsymbol{B}\,\boldsymbol{x}, \tag{4.94}$$

to find the maximum value of $\mathcal{R}$ for which all eigenvalues s are negative. As the Prandtl number ($\mathcal{P}$) only appears in combination with the growth rate s, we do not consider variations in $\mathcal{P}$ as we are interested in the marginal stability curves where $s = 0$.

We determine the minimum of each marginal stability curve, to find the critical Rayleigh number ($\mathcal{R}_c$) and corresponding critical wave-number (k_c), using the simplex search method of Lagarias et al. [48]. This is an iterative direct search method that does not use numerical or analytical gradients; the stopping condition was specified as a change in the critical wave-number and critical Rayleigh number of less than 10^{-5}.

To accommodate uncertainty in parameter values, we have performed an extensive parameter search for a wide range of steady state preferred directions ($0 \leqslant \theta^{(0)} \leqslant \pi/2$) and viscosities ($0 \leqslant \mu_2, \mu_3 \leqslant 1000$). Notice that the solution is periodic in the steady state preferred direction with period $\pi/2$.

To validate our numerical procedure we compared our results with those of Dominguez-Lerma *et al.* [18] and Rayleigh [67] for the Newtonian case, *i.e.* $\mu_2 = \mu_3 = 0$. When both boundaries are free, our numerical approximation of the Rayleigh number is within 10^{-12} of the known analytical result $27\pi^4/4$. When both boundaries are rigid our numerical approximation of the Rayleigh number is within 10^{-7} of that found by Dominguez-Lerma *et al.* [18]. A numerical convergence study was performed for non-zero μ_2, μ_3 and $\theta^{(0)}$.

4.3.5 Numerical convergence study

To control the accuracy of our numerical simulations we can change three parameters, N, k_{Tol} and $\mathcal{R}_{Tol}$, these parameters were varied until the truncation error in the spectral method and the truncation error associated with the iterative process for finding the minimum of the marginal stability curves were all less than 10^{-5}. The order of the Chebyshev polynomials (N) is chosen to give accurate approximations to the marginal stability curves. The remaining two parameters, k_{Tol} and $\mathcal{R}_{Tol}$, are used in the iterative process to find the minimum of each of these curves, *i.e.* the critical wave and Rayleigh numbers. The iterative process used to find the minimum of these curves is terminated when successive iterations have a change in the critical wave and Rayleigh numbers of less than k_{Tol} and $\mathcal{R}_{Tol}$ respectively.

To find the optimum combination of parameters we considered the following parameter

sets

$$\theta^{(0)} = 0, \frac{\pi}{20}, \frac{2\pi}{20}, \frac{3\pi}{20} \ldots, \frac{\pi}{2}, \tag{4.95}$$

$$\mu_2 = \mu_3 = 0, 10, 100, 200, 400, 600, 800, 1000,$$

$$k_{Tol} = 10^{-3}, 10^{-4}, 10^{-5}, 5 \times 10^{-6}, 10^{-6}, \tag{4.96}$$

$$\mathcal{R}_{Tol} = 10^{-3}, 10^{-4}, 10^{-5}, 5 \times 10^{-6}, \tag{4.97}$$

$$N = 10, 15, 20, \ldots, 40.$$

We assumed that the most accurate critical wave and Rayleigh numbers are given when $N = 40$, $k_{Tol} = 10^{-6}$ and $\mathcal{R}_{Tol} = 5 \times 10^{-6}$, and used these to calculate estimates of the absolute and relative error of our results for each tuple of parameters N, k_{Tol} and $\mathcal{R}_{Tol}$. We found that for our choice of parameters, $N = 30$ and $k_{Tol} = \mathcal{R}_{Tol} = 10^{-5}$, the maximum absolute error in the critical wave-number and critical Rayleigh numbers were of order 10^{-5}, which led to relative errors of order 10^{-6} for the critical wave-number and 10^{-11} for the critical Rayleigh number. The maximum relative errors for the range of parameters we investigated are shown in Figure 4.2.

4.4 Results

We first determine the marginal stability curves $\mathcal{R}_l(k)$; for any value of k, an experimental set-up satisfying $\mathcal{R} < \mathcal{R}_l(k)$ is stable for that wavelength, whereas if $\mathcal{R}$ lies above $\mathcal{R}_l(k)$ the system is unstable. We calculate these curves for a range of non-dimensional parameters representing the steady state preferred direction $\theta^{(0)}$, the anisotropic extensional viscosity μ_2 and the anisotropic shear viscosity μ_3 for different combinations of boundary conditions. We determine the critical wave and Rayleigh numbers for each tuple of non-dimensional parameters ($\theta^{(0)}, \mu_2$ and μ_3) by finding the wave-number at which $\mathcal{R}_l(k)$ is minimal. Provided that the Rayleigh number for a given experiment lies below this critical value, the system will be stable to small perturbations for all wavelengths and the

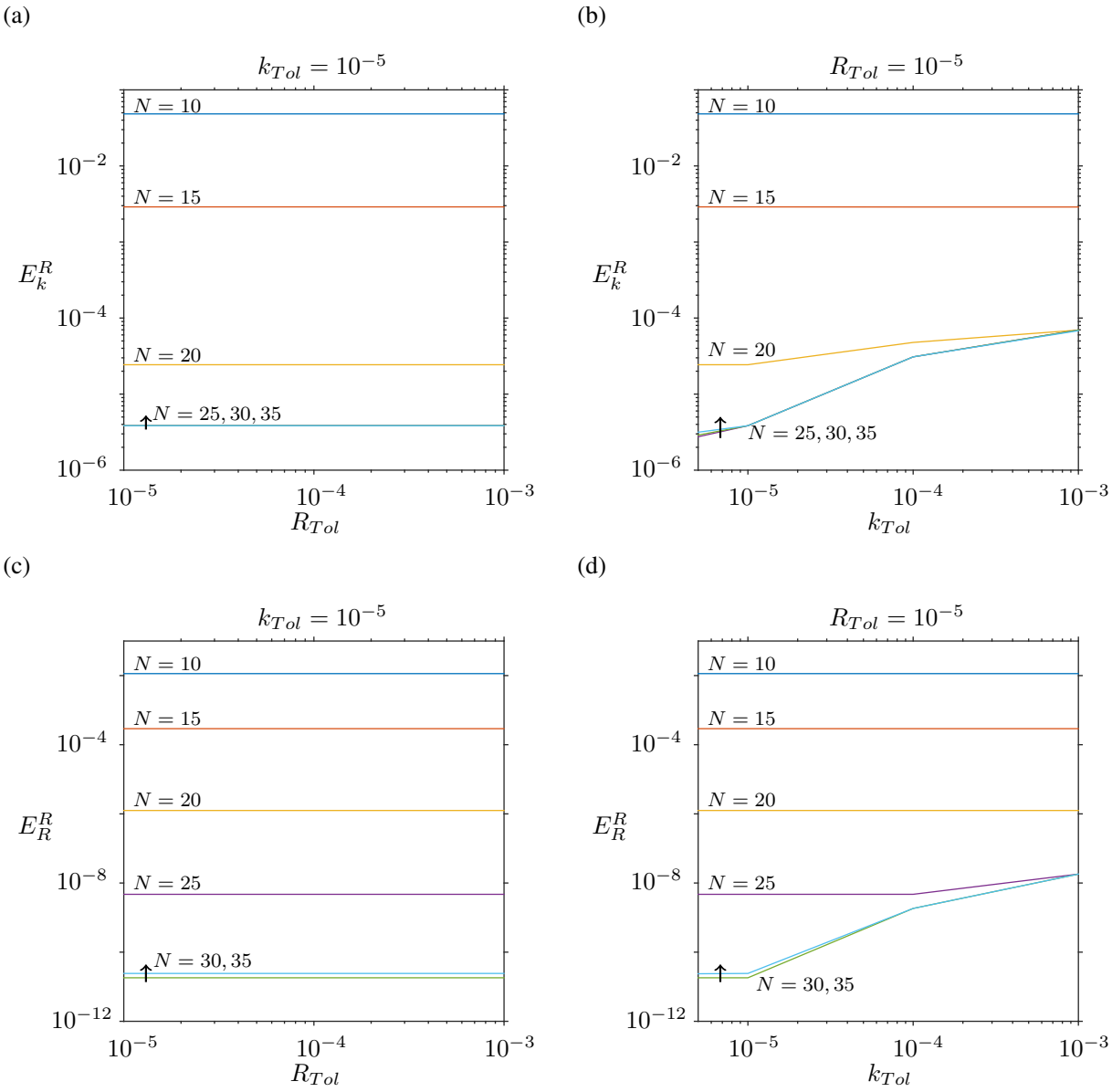

Figure 4.2: Maximum relative error in wave-number (E_k^R) and Rayleigh number (E_R^R) for changes in the number of Chebyshev polynomials (N), and iterative stopping parameters for the critical wave-number (k_{Tol}) and critical Rayleigh number (R_{Tol}). (a) Relative error in wave-number for increases in N and R_{Tol} for $k_{Tol} = 10^{-5}$, where the arrow indicates increasing N. (b) Relative error in wave-number for increases in N and k_{Tol} for $R_{Tol} = 10^{-5}$, where the arrow indicates increasing N. (c) Relative error in Rayleigh number for increases in N and R_{Tol} for $k_{Tol} = 10^{-5}$, where the arrow indicates increasing N. (d) Relative error in Rayleigh number for increases in N and k_{Tol} for $R_{Tol} = 10^{-5}$, where the arrow indicates increasing N.

fluid will be motionless.

Figure 4.3 shows the critical wave-number (k_c) as a function of the steady state preferred direction ($\theta^{(0)}$), for selected values of the anisotropic extensional (μ_2) and shear (μ_3) viscosities, when both boundaries are rigid. The critical wave-number is related to the width of a convection cell; increases in k_c reduce the width of the convection cell. Notice that Figures 4.3(a)-(d) are symmetric about $\theta^{(0)} = \pi/4$, where the maximum of k_c is achieved. In Figure 4.3(a) we examine the effect of the anisotropic extensional viscosity when the anisotropic shear viscosity is zero. The horizontal line corresponds to the Newtonian/isotropic case, and hence there is no dependence on the fibre direction $\theta^{(0)}$. As μ_2 is increased, the limiting form of the critical curve between $\pi/8 \leqslant \theta^{(0)} \leqslant 3\pi/8$ is quickly approached, with changes to μ_2 above 100 having only a small effect. In the ranges $0 \leqslant \theta^{(0)} \leqslant \pi/8$ and $3\pi/8 \leqslant \theta^{(0)} \leqslant \pi/2$, the changes to the critical wave-number occur much more slowly with respect to μ_2, with a local minimum occurring for values of μ_2 above 250 around $\theta^{(0)} = 0.1$ and $\theta^{(0)} = 1.5$. The impact of changing the anisotropic extensional viscosity on the wave-number is therefore dependent on the steady state fibre direction. If the fibres are aligned near horizontal or vertical, the wave-number is decreased and the width of the convection cell increased; if the fibre direction bisects horizontal and vertical at steady state, then the wave-number increases and hence the width of the convection cell decreases. Observing how the critical curves change between Figures 4.3(a)-(d) allows us to identify the impact of the anisotropic shear viscosity μ_3. As μ_3 is increased it dampens changes to the critical wave-number caused by changes in μ_2, nearly removing the dependence on $\theta^{(0)}$ completely in Figure 4.3(d) where $\mu_3 = 1000$. Similar results are obtained when both boundaries are free (figure 4.4), but where the critical wave-number of a Newtonian fluid (k_N) is smaller.

Figure 4.5 shows k_c as a function of $\theta^{(0)}$ for selected values of μ_2 and μ_3 when the lower boundary is rigid and the top free, and shows a more intricate dependence on the tuple of parameters $(\theta^{(0)}, \mu_2, \mu_3)$ than when upper and lower boundaries match. In Figure 4.5(a) the horizontal line corresponds to the Newtonian/isotropic case, and hence

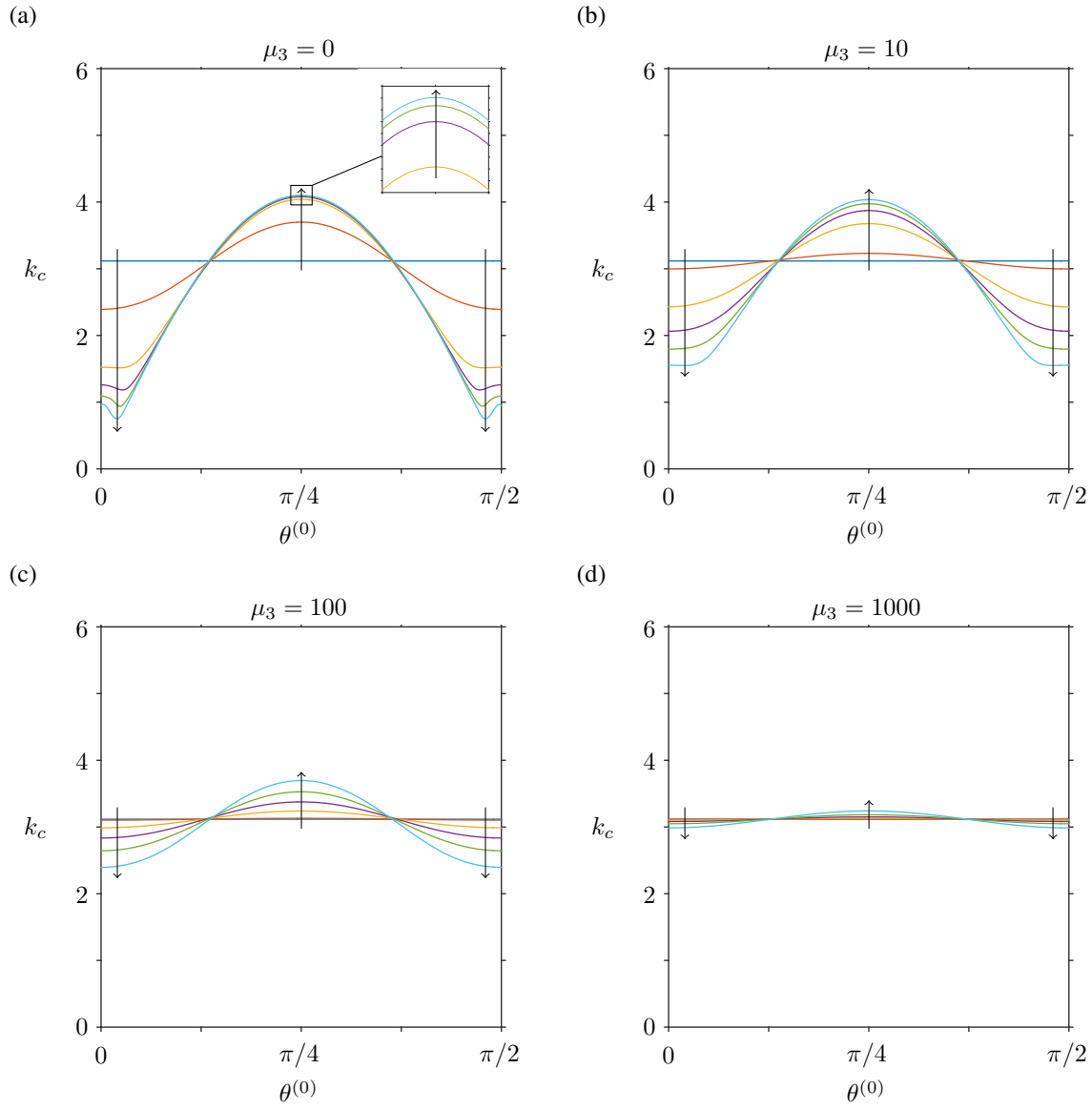

Figure 4.3: Critical wave-number (k_c) for changes in the anisotropic extensional viscosity (μ_2), the anisotropic shear viscosity (μ_3), and the preferred direction in the fluid at steady state ($\theta^{(0)}$) when both boundaries are rigid. In each subfigure the arrows indicate increasing μ_2 ($\mu_2 = 0, 10, 100, 250, 500, 1000$) for (a) $\mu_3 = 0$, (b) $\mu_3 = 10$, (c) $\mu_3 = 100$, and (d) $\mu_3 = 1000$.

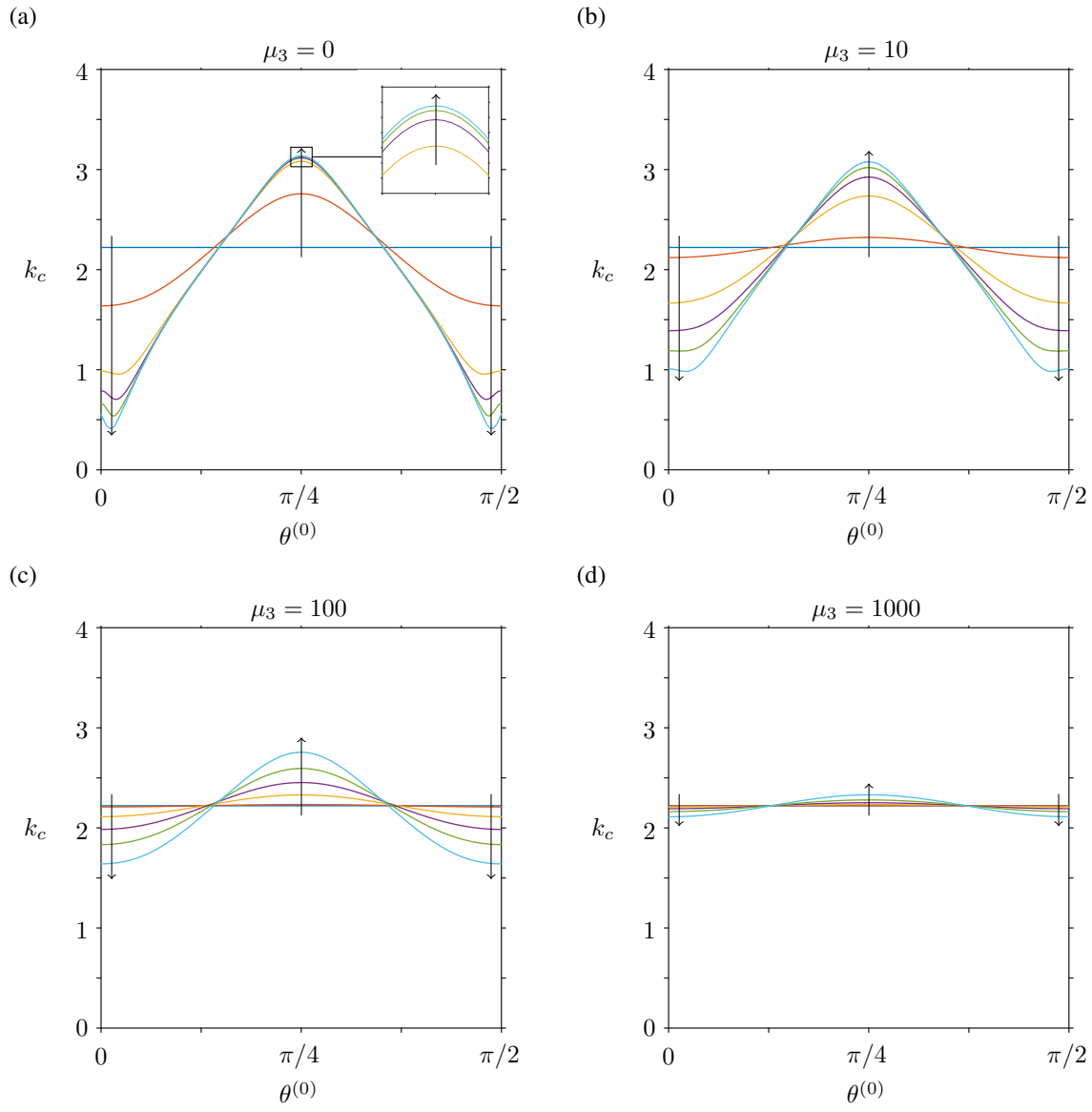

Figure 4.4: Critical wave-number (k_c) for changes in the anisotropic extensional viscosity (μ_2), the anisotropic shear viscosity (μ_3), and the preferred direction in the fluid at steady state ($\theta^{(0)}$) when both boundaries are free. In each subfigure the arrows indicate increasing μ_2 ($\mu_2 = 0, 10, 100, 250, 500, 1000$) for (a) $\mu_3 = 0$, (b) $\mu_3 = 10$, (c) $\mu_3 = 100$, and (d) $\mu_3 = 1000$.

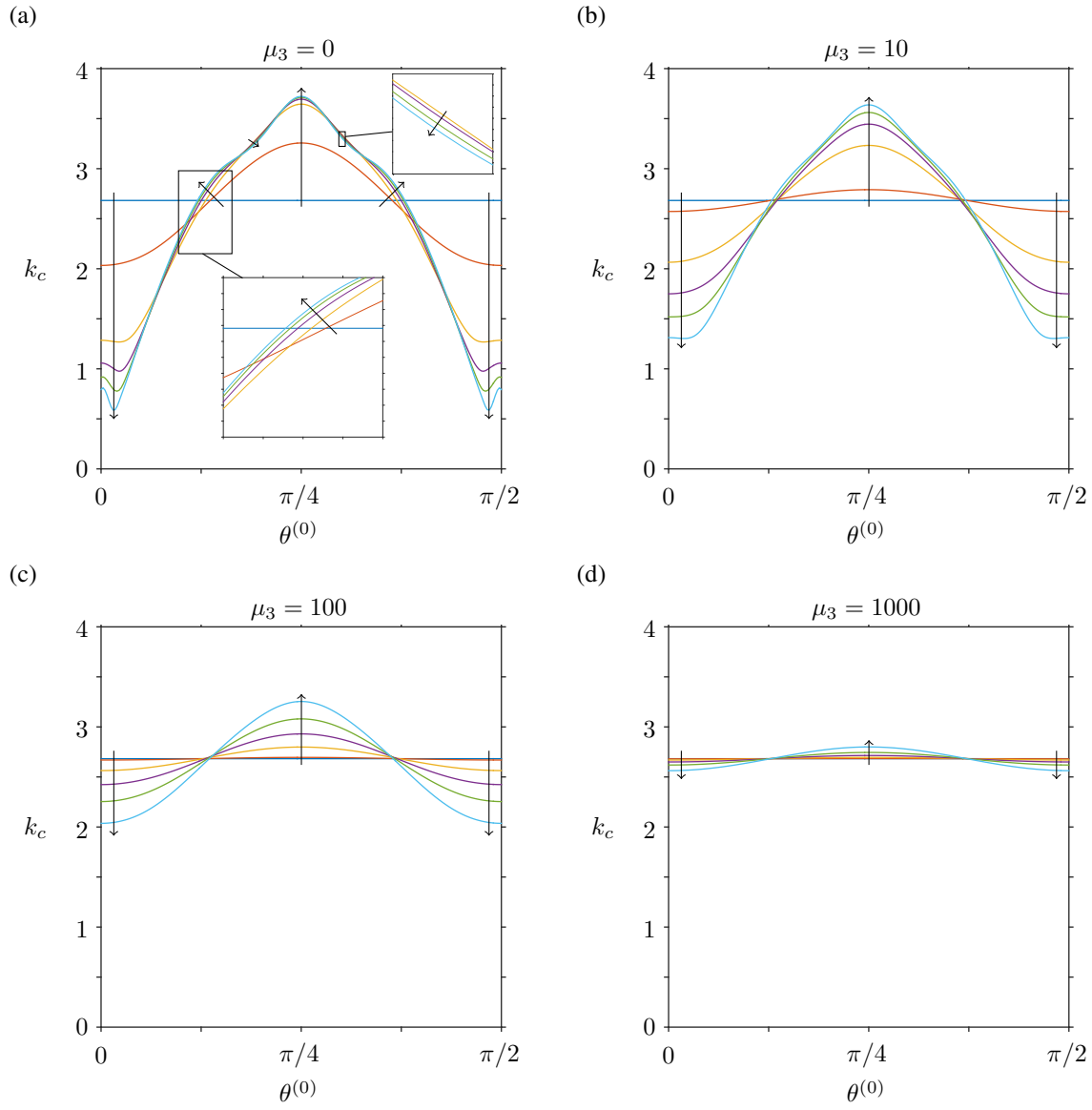

Figure 4.5: Critical wave-number (k_c) for changes in the anisotropic extensional viscosity (μ_2), the anisotropic shear viscosity (μ_3), and the preferred direction in the fluid at steady state ($\theta^{(0)}$) when the bottom boundary is rigid and the top boundary is free. In each subfigure the arrows indicate increasing μ_2 ($\mu_2 = 0, 10, 100, 250, 500, 1000$) for (a) $\mu_3 = 0$, (b) $\mu_3 = 10$, (c) $\mu_3 = 100$, and (d) $\mu_3 = 1000$.

has no dependence upon $\theta^{(0)}$ as expected. As μ_2 is increased the critical curves become more complex, in the range $0 \leqslant \theta^{(0)} \leqslant \pi/8$ and $3\pi/8 \leqslant \theta^{(0)} \leqslant \pi/2$ similar behaviour is observed to when both boundaries are the same; with the appearance of a local maximum at $\theta^{(0)} = 0, \pi/2$ and a global minimum for values of $\theta^{(0)} = 0.1, 1.4$. However, for $\theta^{(0)}$ between $\pi/8$ and $\pi/4$ an extra mode is introduced compared with the matching boundary cases, but this variation becomes small for values of μ_2 larger than 100. We again identify from Figures 4.5(a)-(d) μ_3 dampens the change in the critical wave-number due to μ_2, eventually removing the dependence on $\theta^{(0)}$ (figure 4.5(d)).

Figure 4.6 shows the critical Rayleigh number ($\mathcal{R}_c$) as a function of $\theta^{(0)}$ for changes in μ_2 and μ_3 when both boundaries are rigid. Figure 4.6(a) shows the change in $\mathcal{R}_c$ when the anisotropic shear viscosity is negligible, *i.e.* when $\mu_3 = 0$. The smallest horizontal line corresponds to the Newtonian case, and has no dependance on $\theta^{(0)}$ as expected. For $\mu_2 \lesssim 100$ this horizontal line is simply translated to higher values of $\mathcal{R}_c$, with little to no dependance on $\theta^{(0)}$. As μ_2 is increased further the shape of the critical curves change dramatically. Global minima occur at $\theta^{(0)} \approx 0.3, 1.2$, local maxima occur at $\theta^{(0)} = 0, \pi/2$, and the global maximum at $\theta^{(0)} = \pi/4$; the difference between the global minimum and maximum is approximately 10^4 for $\mu_2 = 1000$. Therefore when the anisotropic extensional viscosity is large and the anisotropic shear viscosity is negligible the steady state is most unstable for steady state fibre orientations near horizontal or vertical, with the most stable case when the steady state direction bisects the horizontal and vertical directions. Examining Figures 4.6(a)-(d) allows us identify how the anisotropic shear viscosity affects the stability of the steady state. We observe that increasing μ_3 increases $\mathcal{R}_c$, hence making the steady state more stable. However, the increase to $\mathcal{R}_c$ is not uniform for different values of $\theta^{(0)}$. This is most easily seen by noting when $\mu_2 = 1000$ and $\mu_3 = 0$ the most stable value of $\theta^{(0)} = \pi/4$, but as μ_3 is increased to 1000 this becomes the most unstable value. Therefore increasing the anisotropic shear viscosity has the most stabilising effect for values of the steady state fibre orientation near horizontal and vertical, and a much lesser effect when the steady state direction bisects the horizontal and vertical directions.

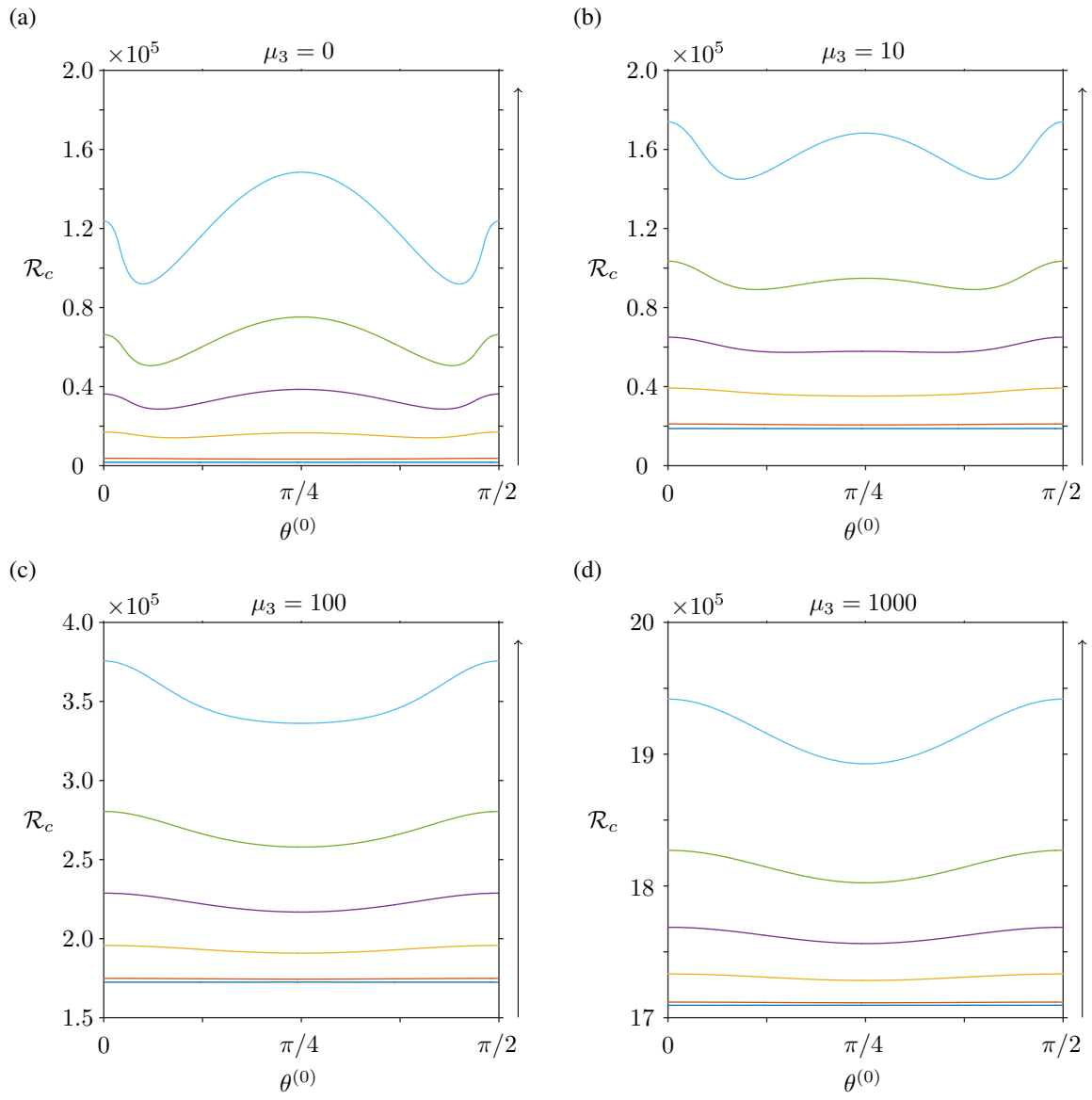

Figure 4.6: Critical Rayleigh number ($\mathcal{R}_c$) for changes in the anisotropic extensional viscosity (μ_2), the anisotropic shear viscosity (μ_3), and the preferred direction in the fluid at steady state ($\theta^{(0)}$) when both boundaries are rigid. In each subfigure the arrows indicate increasing μ_2 ($\mu_2 = 0, 10, 100, 250, 500, 1000$) for (a) $\mu_3 = 0$, (b) $\mu_3 = 10$, (c) $\mu_3 = 100$, and (d) $\mu_3 = 1000$.

However, increases in the anisotropic shear viscosity always stabilise the steady state for all choices of anisotropic extensional viscosity and steady state preferred directions.

Figure 4.7 shows the dependence of $\mathcal{R}_c$ on $\theta^{(0)}$ for selected values of μ_2 and μ_3 when both boundaries are free. In Figure 4.7(a) $\mu_3 = 0$ and the Newtonian case is represented by the lowest horizontal line. As μ_2 is increased a global maximum occurs at $\theta^{(0)} = 0$ and $\pi/2$ and global minimum at $\theta^{(0)} = \pi/4$, where $\mathcal{R}_c$ does not increase from the critical Rayleigh number for the Newtonian/isotropic case ($\mathcal{R}_c \approx R_N$). When the fibres are oriented near horizontal or vertical, increasing the anisotropic extensional viscosity increases the threshold at which instability occurs, but when the steady state preferred direction bisects the horizontal and vertical directions there is little change to the stability threshold with change to the anisotropic extensional viscosity. Figures 4.7(a)-(d) show that as μ_3 is increased, $\mathcal{R}_c$ increases regularly, smoothing out the points of inflection that occur for small values of μ_2. Therefore, increasing μ_3 stabilises the steady state for all values of $\theta^{(0)}$ and μ_2. Changes in anisotropic shear viscosity affect the magnitude of the critical Rayleigh number much more than changes to the anisotropic extensional viscosity.

Figure 4.8 shows the dependance of $\mathcal{R}_c$ on $\theta^{(0)}$ for selected values of μ_2 and μ_3, when the lower boundary is rigid and the upper free. In Figure 4.8(a) we recover the Newtonian/isotropic case, represented by the lowest horizontal line, and examine how μ_2 affects $\mathcal{R}_c$ when $\mu_3 = 0$. As μ_2 is increased $\mathcal{R}_c$ increases but not uniformly with respect to $\theta^{(0)}$. Global maxima occur at $\theta^{(0)} = 0, \pi/2$, local maxima at $\theta^{(0)} \approx \pi/8, 3\pi/8$, local minima at $\theta^{(0)} \approx \pi/16, 7\pi/16$ and the global minimum at $\theta^{(0)} = \pi/4$. Therefore increasing the anisotropic extensional viscosity increases the stability threshold most when, at steady state, the fibres are either horizontal or vertical, and least when they are directed at an angle $\pi/4$ radians. As μ_3 increases $\mathcal{R}_c$ is increased, with the local maxima and minima becoming less pronounced, disappearing completely once $\mu_3 \gtrsim 100$, this is identified by comparing Figures 4.8(a)-(d). Again, changes in μ_3 affect $\mathcal{R}_c$ far more than similar changes to μ_2. Therefore increases in the anisotropic shear viscosity stabilise the steady state, with the most stabilisation occurring when the fibres are orientated horizontally or

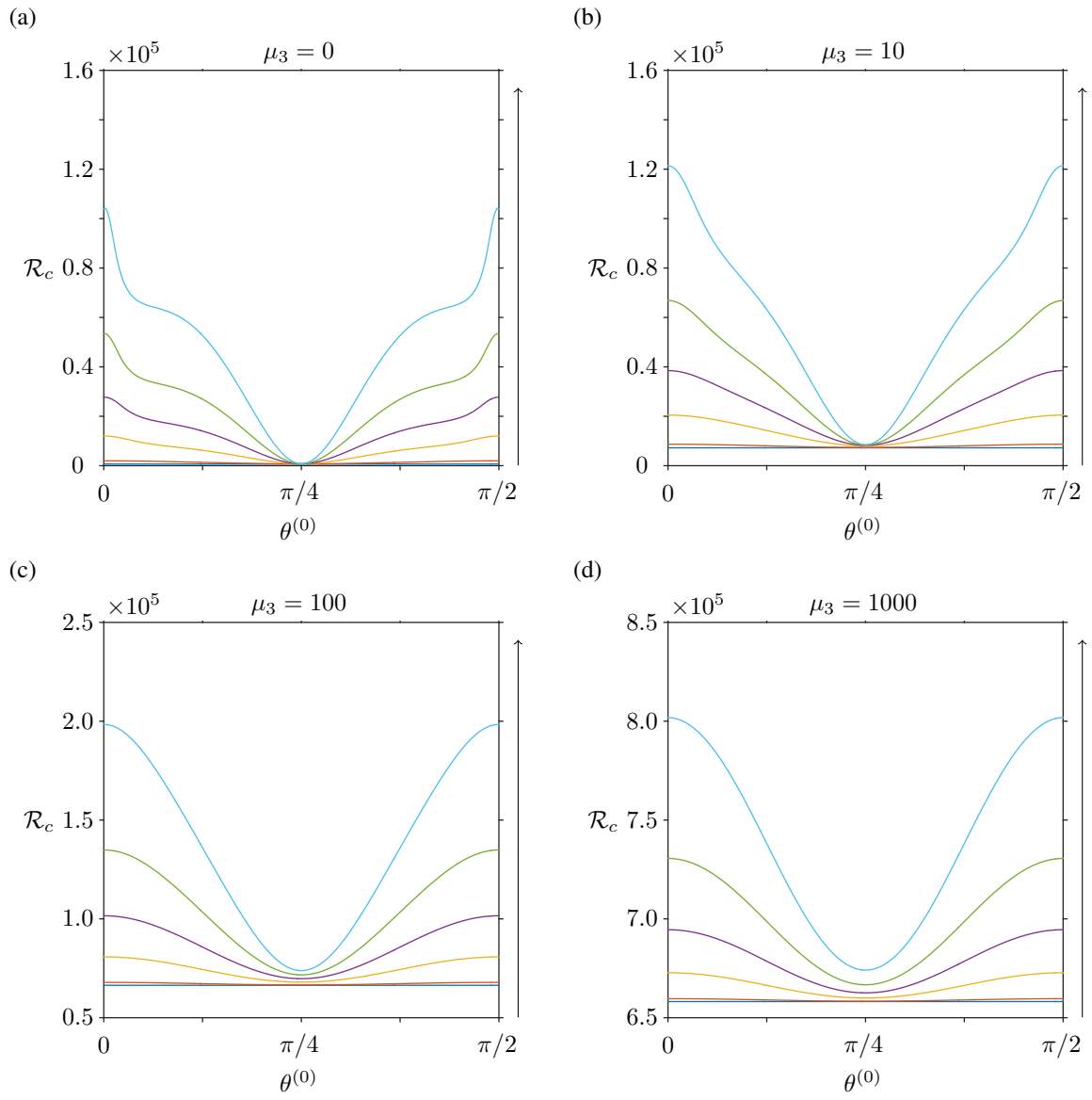

Figure 4.7: Critical Rayleigh number ($\mathcal{R}_c$) for changes in the anisotropic extensional viscosity (μ_2), the anisotropic shear viscosity (μ_3), and the preferred direction in the fluid at steady state ($\theta^{(0)}$) when both boundaries are free. In each subfigure the arrows indicate increasing μ_2 ($\mu_2 = 0, 10, 100, 250, 500, 1000$) for (a) $\mu_3 = 0$, (b) $\mu_3 = 10$, (c) $\mu_3 = 100$, and (d) $\mu_3 = 1000$.

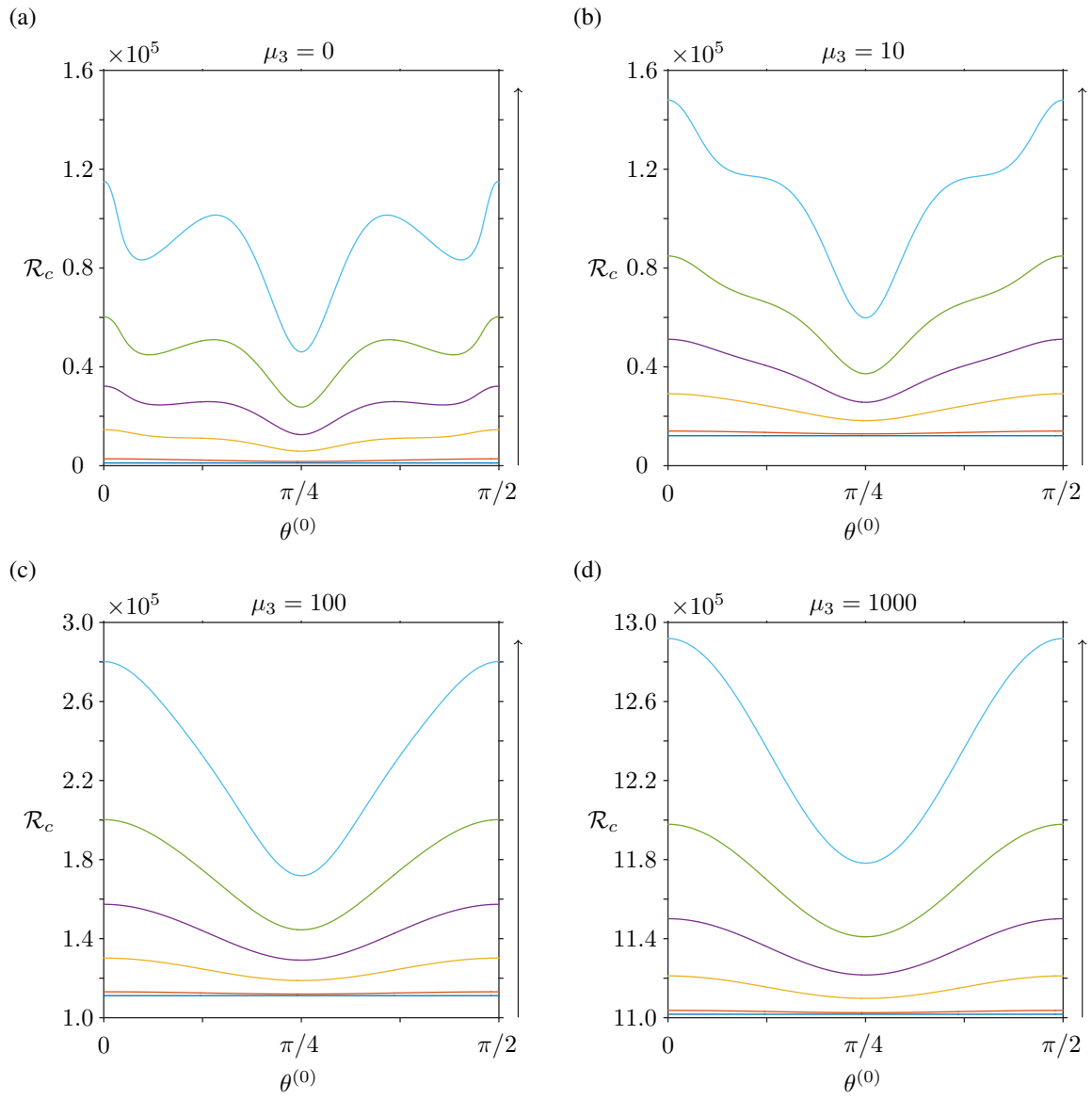

Figure 4.8: Critical Rayleigh number ($\mathcal{R}_c$) for changes in the anisotropic extensional viscosity (μ_2), the anisotropic shear viscosity (μ_3), and the preferred direction in the fluid at steady state ($\theta^{(0)}$) when the bottom boundary is rigid and the top boundary is free. In each subfigure the arrows indicate increasing μ_2 ($\mu_2 = 0, 10, 100, 250, 500, 1000$) for (a) $\mu_3 = 0$, (b) $\mu_3 = 10$, (c) $\mu_3 = 100$, and (d) $\mu_3 = 1000$.

vertically at steady state, and least when they bisect the horizontal and vertical directions.

Comparing Figures 4.3-4.8 allows us to examine the effect of the boundary conditions on the critical wave and critical Rayleigh numbers. Using Figures 4.3 and 4.4 we identify when the top and bottom boundaries are the same the curves for the critical wave-number take the same form, but with lower critical wave-numbers for the free-free boundaries than the rigid-rigid case. When the boundaries are mixed, and the anisotropic shear viscosity is negligible, two additional modes occur between $\pi/8 \leqslant \theta^{(0)} \leqslant 3\pi/8$. However, variation between the critical curves is small for medium - large values of the anisotropic extensional viscosity and all changes are dampened as the anisotropic shear viscosity is increased, similarly to the matching boundary case. Therefore, in all cases, the anisotropic extensional viscosity gives rise to variations in the critical wave-number with respect to the steady state preferred direction, which are dampened by increases in the anisotropic shear viscosity.

Comparing Figures 4.6-4.8 allows us to compare how the different boundary conditions affect the critical Rayleigh number. Similarly to the Newtonian/isotropic case the most stable pair of boundaries are rigid-rigid, with the most unstable free-free. In all boundary pairs increasing either the anisotropic extensional or shear viscosities increases the critical Rayleigh number, however changes in the anisotropic shear viscosity affect the stability threshold much more than equivalent changes to the anisotropic extensional viscosity.

We notice in Figures 4.6-4.8 the critical wave and Rayleigh numbers are the same for $\theta^{(0)}$ and $\pi/2 - \theta^{(0)}$, *i.e.* the material has the same stability characteristics when the preferred direction, at steady state, is horizontal or vertical, and alterations to either state cause similar changes to the stability. When the transversely-isotropic material is interpreted as a suspension of elongated particles, then this may be explained by noting purely horizontal or vertical particles will give rise to no rotational and only translational motion of the particles, when the fluid starts to move; therefore, the stability characteristics of these states should be similar. Changes to the steady state preferred direction by similar amounts should therefore give rise to similar changes in stability, as the same amount of

rotational motion of the particles will be introduced.

4.4.1 Forms of critical curves

Examining Figures 4.3-4.8 we notice, for medium to large values of the anisotropic shear viscosity, the critical curves are continuous with no sharp extrema (*i.e.* we expect the rate of change, of the critical values with $\theta^{(0)}$, to be continuous also). We therefore fit an analytic function to the sampled data, minimising the maximum absolute error between function and data. We do this for the critical wave-number using the simplex search method of Lagarias *et al.* [48] and for the critical Rayleigh number we use the nonlinear least squares method.

We assume the critical wave-number takes the empirical form ($\mu_3 > 40$)

$$k_c \approx \frac{f_1(e^{-f_5\mu_2} - 1)}{f_2 + \mu_3} \cos(4\theta^{(0)}) - \frac{f_3\mu_2}{f_4 + \mu_3} + k_N, \tag{4.98}$$

where k_N is the critical wave-number for a Newtonian fluid. From this curve fitting we confirm that as μ_3 becomes large the critical wave-number will tend to the Newtonian value, as μ_3 appears in the denominator of the first two terms in equation (4.98). It is also clear that when $\mu_2 = 0$ the critical wave-number k_c does not depend on $\theta^{(0)}$ or μ_3 and takes the same value as in the Newtonian case.

Boundary Type	f_1	f_2	f_3	f_4	f_5
rigid-rigid	175.9	107.3	12.8×10^{-3}	50.8	1.7×10^{-3}
rigid-free	91.1	67.7	5.3×10^{-3}	33.8	3.8×10^{-3}
free-free	284.4	259.5	3.7×10^{-3}	19.5	1.5×10^{-3}

Table 4.1: The parameter values from curve fitting for the critical wave-number given in equation (4.98) for the different combinations of boundary conditions.

Figure 4.9 shows how each term of equation (4.98) contributes to k_c. From Figure 4.9(a) we identify for small values of μ_2 and μ_3 the magnitude of the first term in equation (4.98) is largest when the combination of boundaries is rigid-free. However, as μ_2 is increased (μ_3 still small) the highest variation of k_c, with respect to $\theta^{(0)}$, occurs for the

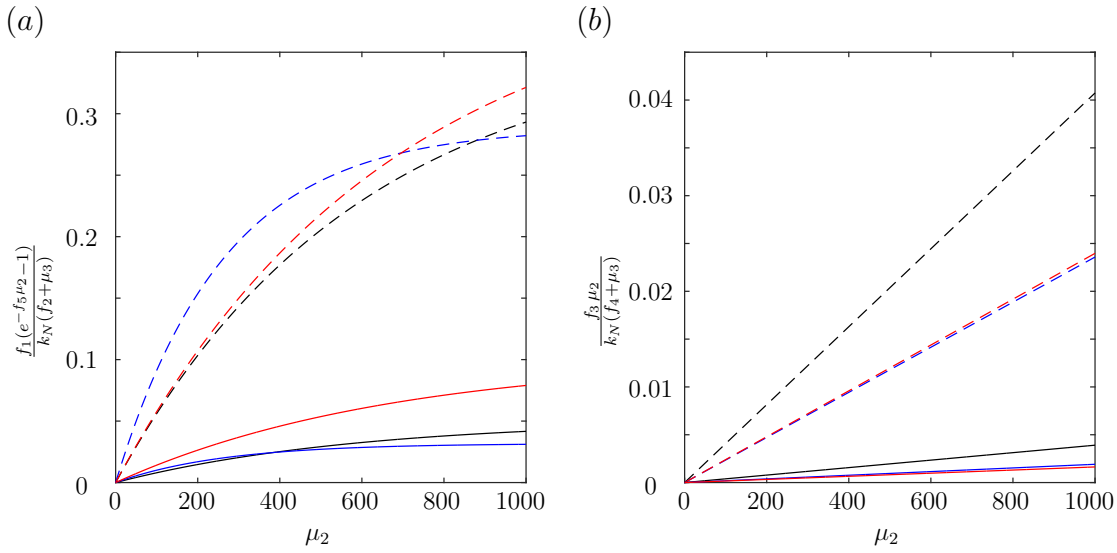

Figure 4.9: Relative changes to the critical wave-number (k_c), described by the fitted equation (4.98), for changes in the anisotropic extensional (μ_2) and anisotropic shear (μ_3) viscosities for the three different boundary types. In each subfigure the dashed and solid lines represent $\mu_3 = 50$ and $\mu_3 = 1000$ respectively, with the black, blue and red lines representing rigid-rigid, rigid-free and free-free boundary pairs respectively. (a) The relative magnitude of $\cos 4\theta^{(0)}$ ($f_1(e^{-f_5\mu_2} - 1)/(f_2 + \mu_3)k_n$), and (b) the relative decrease to k_c ($f_3\mu_2/(f_4 + \mu_3)k_N$), where k_N is the critical wave-number of a Newtonian fluid for each boundary type.

free-free boundary pair. As μ_3 is increased the amplitude of the $\cos 4\theta^{(0)}$ term decreases and the free-free boundary pair causes the largest variation of k_c with respect to $\theta^{(0)}$. Figure 4.9(b) shows how k_c decreases relative to k_N with changes in μ_2, μ_3 and boundary types. We see for all values of μ_2 and μ_3 the rigid-free and free-free boundary pairs reduce the critical wave-number similarly, however the biggest reduction occurs when both boundaries are rigid. As μ_3 is increased the reduction to k_c decreases. Figure 4.10 shows a comparison between the sampled data and fitted function, and illustrates the fit captures most of the information from the data.

We assume that the critical Rayleigh number takes the form ($\mu_3 > 100$)

$$\mathcal{R}_c \approx \left(\frac{-g_1}{\mu_3 + 1} + g_2\right)\mu_2 \cos(4\theta^{(0)}) + \left(\frac{-g_3}{\mu_3^{1/2} + 1} + g_4\right)\mu_2 + (g_5\mu_3 + g_6)\,. \tag{4.99}$$

The magnitude of the first term in equation (4.99) is shown in Figure 4.11(a), we observe for μ_2 positive $\mathcal{R}_c$ will always depend on $\theta^{(0)}$. Figure 4.11(a) also implies when both

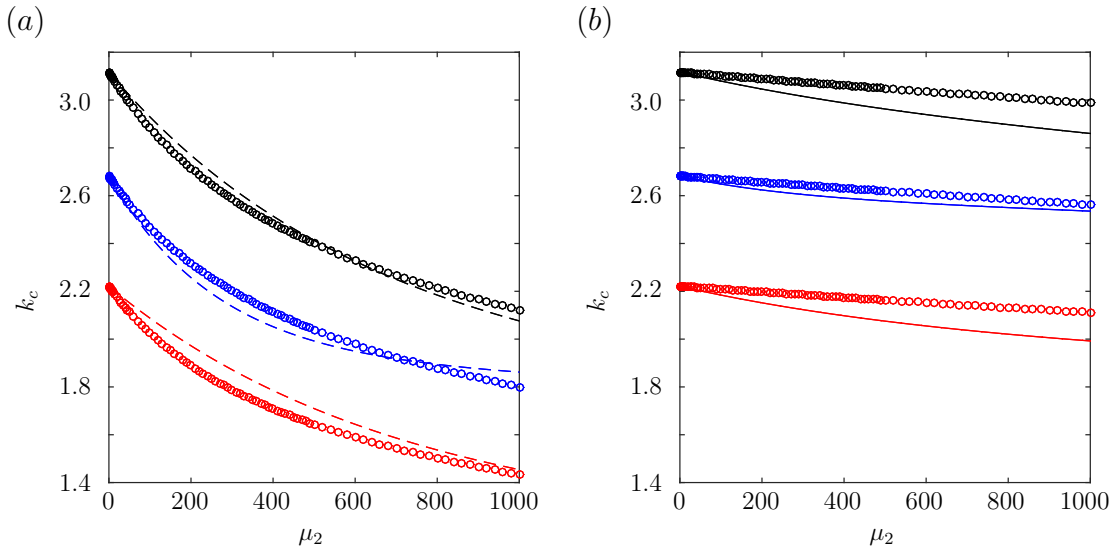

Figure 4.10: Comparison of fitted curves with data points for the critical wave-number k_c. The fit for (a) $\mu_3 = 50$ and (b) $\mu_3 = 1000$, where black, blue and red correspond to rigid-rigid, rigid-free and free-free boundary pairs and circles represent data points. We choose $\theta^{(0)} = 0$ so that we represent the largest error between the fitted curves and the data.

boundaries are free the biggest fluctuations in $\mathcal{R}_c$ with respect to $\theta^{(0)}$ occur, with the smallest fluctuations occurring when both boundaries are rigid. The increase to the critical wave-number with μ_2 and μ_3, described by the second term in equation (4.99), does not change with different combinations of boundary conditions (figure 4.11). The final constant g_6 is approximately equal to the critical Rayleigh number, for each respective boundary pair. Figure 4.12 shows both the analytic function and fitted data. We observe in both cases the fitted function underestimates the value of $\mathcal{R}_c$, with the fit being closer for smaller values of $\mathcal{R}_c$.

Boundary Type	g_1	g_2	g_3	g_4	g_5	g_6
rigid-rigid	448.4	25.2	431.6	221.4	1440.8	1706.4
rigid-free	388.8	57.3	238.5	141.3	796.0	1099.9
free-free	247.5	64.1	156.1	84.2	521.1	657.0

Table 4.2: The parameter values from curve fitting for the critical Rayleigh number in equation (4.99) for the different combinations of boundary conditions.

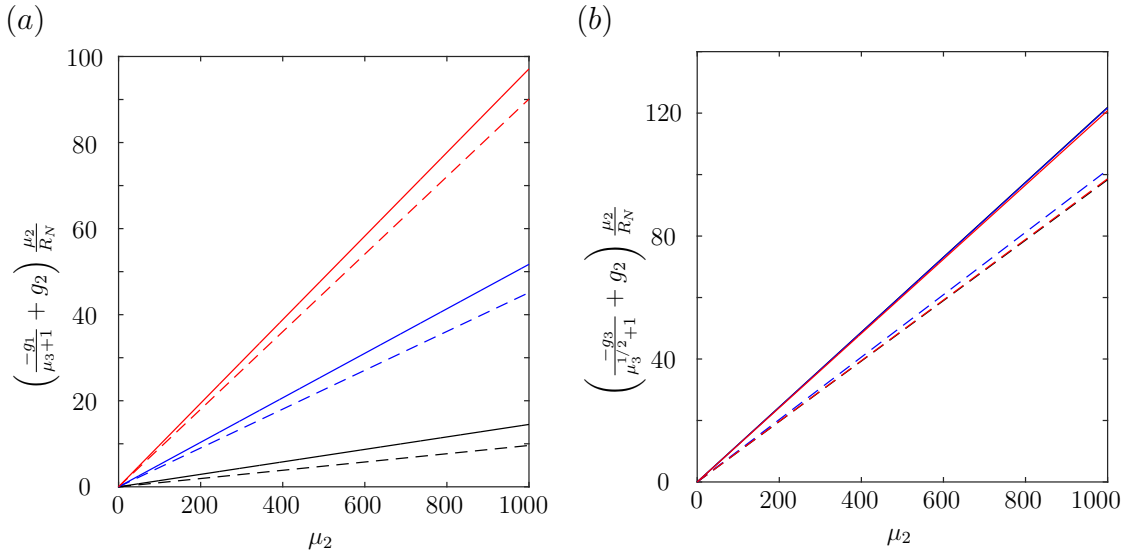

Figure 4.11: Relative changes to the critical Rayleigh number ($\mathcal{R}_c$), described by the fitted equation (4.99), for changes in the anisotropic extensional (μ_2) and anisotropic shear (μ_3) viscosities for different boundary types. In each subfigure the dashed and solid lines represent $\mu_3 = 100$ and $\mu_3 = 1000$ respectively, with the black, blue and red lines representing rigid-rigid, rigid-free and free-free boundary pairs respectively. (a) The relative magnitude of $\cos 4\theta^{(0)}$ $((-g_1/(\mu_3+1)+g_2)\mu_2/\mathcal{R}_N)$ and (b) the relative increase to $\mathcal{R}_c$ $((-g_3/(\mu_3^{1/2}+1)+g_4)\mu_2/\mathcal{R}_N)$, where $\mathcal{R}_N$ is the critical Rayleigh number of a Newtonian fluid for each boundary type.

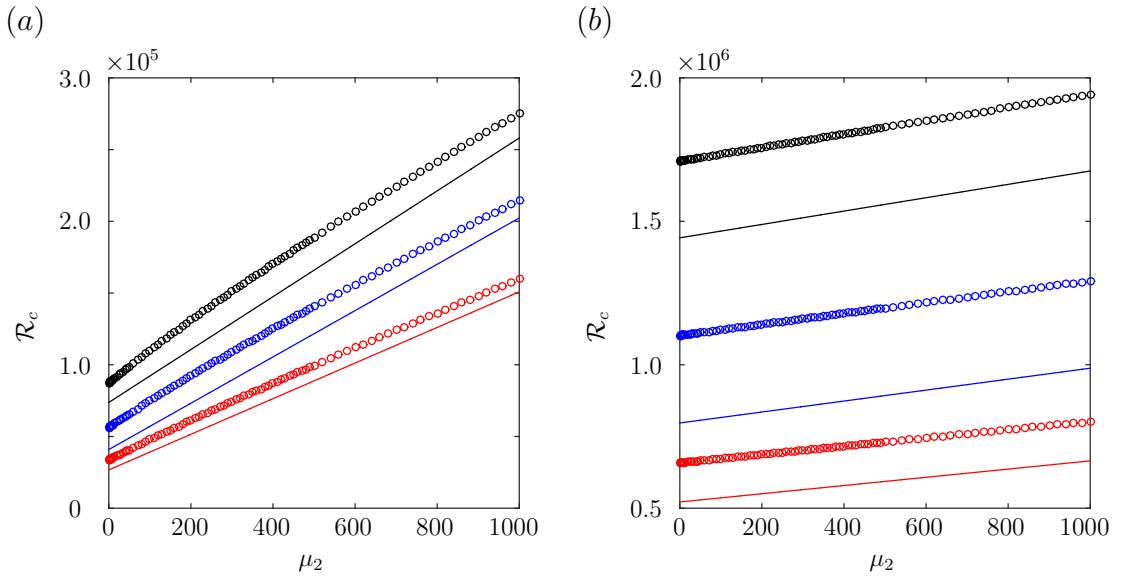

Figure 4.12: Comparison of fitted curves with data points for the critical Rayleigh number $\mathcal{R}_c$. The fit for (a) $\mu_3 = 50$ and (b) $\mu_3 = 1000$, where black, blue and red correspond to rigid-rigid, rigid-free and free-free boundary pairs and circles represent data points. We choose $\theta^{(0)} = 0$ so that we represent the largest error between the fitted curves and the data.

4.5 Discussion

In this chapter, we extended the work of Rayleigh to study the linear stability of a transversely isotropic viscous fluid, contained between two horizontal boundaries which are either rigid or free and of different temperatures. We used the stress tensor first proposed by Ericksen [24], with $\mu_1 = 0$, and a kinematic equation corresponding to fibres of a large aspect ratio to model a transversely isotropic fluid. Numerically, we presented results for a range of steady state preferred directions from 0 to $\pi/2$, this is equivalent to the full possible range of directions as the governing equations have a period of $\pi/2$.

Similarly to chapter 3 the parameter μ_3, which describes the ratio of the shear viscosity in the preferred direction to the transverse shear direction, is much more important in determining the stability of the flow than μ_2, which describes the ratio of the extensional viscosity to the transverse shear viscosity. How the value of this pair of parameters impacts upon the stability of the flow also depends on $\theta^{(0)}$, which describes the constant steady state preferred direction, as well as the type of boundary at the bottom and top of the fluid. Similarly to a Newtonian fluid, the most stable pair of boundaries are rigid-rigid, where the temperature difference between the two boundaries required to induce instability is the largest; the least stable boundary pair is free-free.

The rheological parameters μ_2 and μ_3 also have an impact on the critical wave-number k_c, which describes the width of the convection cells. We find for steady state preferred directions near horizontal or vertical, the width of the convection cell increases with the anisotropic extensional viscosity, when compared to a Newtonian fluid, and decreases when the preferred direction bisects the horizontal and vertical boundaries. The anisotropic shear viscosity dampens any changes to the critical wave-number caused by increases in the anisotropic extensional viscosity. If the anisotropic shear viscosity is large enough ($\mu_3 \geqslant 500$) then there is very little change to the critical wave-number, and hence convection cell size, with changes to the anisotropic extensional viscosity or steady state preferred direction.

To use this model in practice we must estimate the parameters of the model. Some

of the non-dimensional parameter groups are trivial to estimate, such as the Rayleigh number, however how parameters such as the anisotropic extensional and shear viscosities should be chosen is less clear. The methods that may be used to ascertain these parameter values are discussed in section 2.3.

The analysis we have undertaken in this chapter shows the stability characteristics of a transversely isotropic fluid are significantly different from those of a Newtonian fluid. Therefore when the fluid exhibits a preferred direction, such as a fibre-laden fluid, these effects should be taken into account.

In future work we will change the domain of our problem to consider a closed box, which is much more physically realistic, as well as considering the full nonlinear three-dimensional problem. Through the link identified in chapter 5, between active fluids and Ericksen's model for a transversely isotropic fluid, we will consider the linear stability of a suspension of swimming particles by considering non-zero μ_1 and modifying the kinematic equation to include particle swimming. We will also use this link to examine how dispersion about the preferred direction alters our results, as it is unlikely that there will be zero dispersion about the preferred direction.

We adopt the conservation of mass and momentum statements, along with the transversely-isotropic stress tensor, of Ericksen [24] and couple this to the kinematic condition derived by Green and Friedman [29]. This is the first time the linear Rayleigh-Bénard stability of a transversely-isotropic fluid has been considered. To our knowledge this is also the first time a Chebyshev collocation method has been used to find the linear stability of a transversely-isotropic fluid.

In this chapter we have applied the model of Ericksen's transversely isotropic fluid described in chapter 2 to examine the linear Rayleigh-Bénard stability of a transversely isotropic fluid. As reported in chapter 3, the parameter which describes the anisotropic shear viscosity is much more important in determining the stability than the parameter related to the anisotropic extensional viscosity. We have therefore shown, through two canonical examples, when there is a preferred direction in the fluid, the stability charac-

teristics are significantly different from those of a Newtonian fluid, therefore transversely isotropic effects must be taken into account.

CHAPTER 5

FUNDAMENTAL CONNECTIONS BETWEEN MODELS OF ACTIVE SUSPENSIONS AND TRANSVERSELY ISOTROPIC FLUIDS

5.1 Introduction

Fluids containing suspensions of particles are found in numerous industrial and biological applications. Examples involving passive particles are discussed in chapters 2-4 and include (but are not limited to) solutions of DNA [57], fibrous proteins of the cytoskeleton [16, 47], synthetic bio-nanofibres [59], extracellular matrix [29] and plant cell walls [22]. Suspensions comprising self-propelling bacteria or other micro-organisms are termed *active* [74]; these suspensions exhibit phenomena such as collective behaviour [35, 42, 45, 49, 65, 66, 72] and, as observed recently, superfluidity [55]. Collections of artificial swimmers may also exhibit the properties of active matter [21, 28, 39, 64, 91]. In order to understand these phenomena, it is vital to develop tractable and accurate continuum theories that capture the essential physics of suspensions of self-motile particles.

There are many different models that have been proposed to model suspensions of active particles in a solvent fluid. Two classes of model exist, particle based models, which model each particle separately, and continuum models, which model the suspension as a complex fluid. In this thesis we focus on a nonlinear continuum model, however we first give a brief summary of other models which model each particle separately.

Modelling each particle separately is extremely computationally expensive, however some significant progress has been made towards understanding the large-scale dynamics exhibited by suspensions of active swimmers. Hernandez-Ortiz *et al.* [33] developed a 'minimal' model of the swimmers, that captured the leading order far-field hydrodynamics, while keeping the structure of each swimmer simple. Each swimmer was a modelled as a rigid neutrally buoyant dumbbell, composed of two beads which are connected by a rigid rod. All drag forces act on these two beads with a 'phantom' flagellum providing a constant propulsive force on the particle and an equal and opposite force on the fluid. By coupling many of these particles together, through hydrodynamic interactions, the authors were able to reproduce experimental features such as correlated motions at high concentrations of swimmers. This dumbbell model has been generalised by Haines *et al.* [30, 31] to include a spheroidal body shape. It is also possible to describe the propulsion of the particle through a 'squirmer' model, such as that developed by Blake [9].

In this chapter we link active suspension models of solutions containing swimming microorganisms, such as those proposed by Pedley & Kessler [65] and Simha & Ramaswamy [76], with the mathematically simpler (inactive) transversely isotropic fluid first described by Ericksen [24], commonly used to describe fibre-reinforced media [29, 22, 23, 52, 38]. Ericksen's model consists of mass and momentum conservation equations together with an evolution equation for the fibre director field. The stress tensor depends on the fibre orientation and linearly on the rate of strain; it takes the simplest form that satisfies the required invariances.

By linking these models of active and inactive suspensions, we are able to determine the empirical parameters of the transversely isotropic model in terms of fundamental physical quantities relating to particle geometry, volume fraction and solute viscosity; furthermore we propose a modification to the kinematic equation which allows for the inclusion of swimming particles. At the same time, the connection between the two models reveals the importance of non-isotropic terms in the stress tensor when the suspended particles are elongated. These terms are known to influence the dynamics of fibre-laden flows

[70, 40, 80, 38] and yet are neglected in existing models of active suspensions of rod-like bacteria [73, 76, 82, 45].

The structure of this chapter is as follows: first we model the active particle position and direction distribution with a Fokker-Planck equation, making a standard phenomenological argument for the translational and rotational fluxes [73]. The background flow is subject to conservation of mass and momentum, with the constitutive relation for stress modified to include the interaction of the particles with the surrounding fluid, as well as isotropic and active stress contributions. Current models take account of these isotropic and active contributions to the stress, but neglect the influence of non-spherical particles on the bulk stress; it has been shown by Hinch & Leal [36] that this contribution is important for elongated particles [65]. Next we show that the active description of a uniformly-distributed, perfectly-aligned suspension is equivalent to Ericksen's model with a modified director evolution equation. This link enables a connection to be made between the parameters of Ericksen's model to fundamental physical quantities.

5.2 Governing equations

Consider a collection of particles suspended in a viscous, Newtonian fluid. The density of particles is sufficiently dilute that particles do not interact directly, only through their influence on the fluid. Each particle is modelled as a prolate spheroid with major axis r_1^*, minor axis r_2^*, aspect ratio $r = r_1^*/r_2^*$, and shape parameter $\alpha_0 = (r^2 - 1)/(r^2 + 1)$. The particle number density in physical and orientational space is denoted $N^*(\boldsymbol{x}^*, \hat{\boldsymbol{p}}, t^*)$ where $\boldsymbol{x}^*$ denotes the particle position, $\hat{\boldsymbol{p}}$ is orientation and t^* is time [17], visualised in Figure 5.1. This function is defined as

$$\frac{1}{V^*}\int_{V^*}\int_S N^*(\boldsymbol{x}^*, \hat{\boldsymbol{p}}, t^*)\,\mathrm{d}\hat{\boldsymbol{p}}\,\mathrm{d}\boldsymbol{x}^* = n_d^*, \tag{5.1}$$

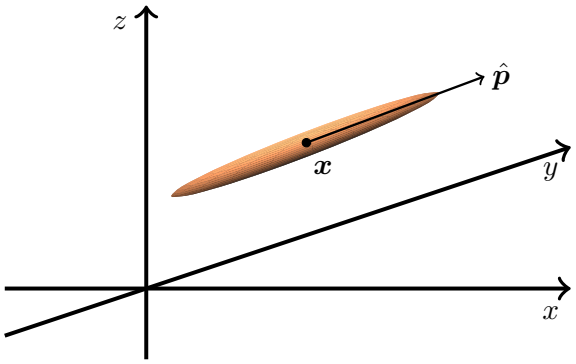

Figure 5.1: A schematic diagram showing the coordinate system used to model the particle distribution function N^*. The particle's position in space is given by the vector $\boldsymbol{x}^* = (x^*, y^*, z^*)$ and its orientation is given by the unit vector $\hat{\boldsymbol{p}}$.

where V^* is the volume of the spatial domain, S is the surface of the unit sphere in orientational space and n_d^* is the mean number density of particles in the suspension. The local particle director and concentration fields $\boldsymbol{a}(\boldsymbol{x}^*, t^*) = \langle \hat{\boldsymbol{p}} \rangle$ and c^* are defined such that

$$\boldsymbol{a} = \langle \hat{\boldsymbol{p}} \rangle (\boldsymbol{x}^*, t^*) = \frac{1}{c^*(\boldsymbol{x}^*, t^*)} \int_S \hat{\boldsymbol{p}}\, N^*(\boldsymbol{x}^*, \hat{\boldsymbol{p}}, t^*)\, \mathrm{d}\hat{\boldsymbol{p}}, \tag{5.2}$$

$$c^*(\boldsymbol{x}^*, t^*) = \int_S N^*(\boldsymbol{x}^*, \hat{\boldsymbol{p}}, t^*)\, \mathrm{d}\hat{\boldsymbol{p}}. \tag{5.3}$$

The bracket operator is defined over other quantities similarly.

The particle distribution function is assumed to be governed by a Fokker-Planck equation [74], giving a conservation law for N^*:

$$\frac{\partial N^*}{\partial t^*} + \boldsymbol{\nabla}_{\boldsymbol{x}}^* \cdot (\boldsymbol{U}^* N^*) + \boldsymbol{\nabla}_{\boldsymbol{p}} \cdot (\boldsymbol{\Omega}^* N^*) = 0, \tag{5.4}$$

where $\boldsymbol{\nabla}_{\boldsymbol{x}}^*$ denotes the gradient operator in physical space and $\boldsymbol{\nabla}_{\boldsymbol{p}}$ denotes the gradient operator on the unit sphere in orientation space. The particle translational velocity $\boldsymbol{U}^*$ is represented by the linear combination of the particle swimming velocity relative to a

background flow $U_s^*\hat{\boldsymbol{p}}$ and the local fluid velocity $\boldsymbol{u}^*$:

$$\boldsymbol{U}^* = U_s^*\hat{\boldsymbol{p}} + \boldsymbol{u}^*, \tag{5.5}$$

where we have neglected translational diffusion [72, 74].

Jeffery's equation [43] models the angular velocity of the particle as

$$\boldsymbol{\Omega}^* = (\boldsymbol{I} - \hat{\boldsymbol{p}}\,\hat{\boldsymbol{p}}) \cdot \left[(\alpha_0 \boldsymbol{e}^* + \boldsymbol{\omega}^*) \cdot \hat{\boldsymbol{p}}\right], \tag{5.6}$$

where the rate-of-strain tensor $\boldsymbol{e}^* = (\boldsymbol{\nabla}_{\boldsymbol{x}}^*\boldsymbol{u}^* + \boldsymbol{\nabla}_{\boldsymbol{x}}^*\boldsymbol{u}^{*T})/2$, the vorticity tensor $\boldsymbol{\omega}^* = (\boldsymbol{\nabla}_{\boldsymbol{x}}^*\boldsymbol{u}^* - \boldsymbol{\nabla}_{\boldsymbol{x}}^*\boldsymbol{u}^{*T})/2$ and the identity tensor is denoted $\boldsymbol{I}$. In equations (5.5) and (5.6) we follow ref. [72] and neglect angular diffusion.

Finally, the fluid velocity $\boldsymbol{u}^*(\boldsymbol{x}^*, t^*)$ is governed by the Cauchy momentum equations

$$\begin{aligned} \rho^* \frac{D\boldsymbol{u}^*}{Dt^*} &= \boldsymbol{\nabla}_{\boldsymbol{x}}^* \cdot \boldsymbol{\sigma}^*, \\ \boldsymbol{\nabla}_{\boldsymbol{x}}^* \cdot \boldsymbol{u}^* &= 0, \end{aligned} \tag{5.7}$$

where ρ^* is the fluid density and $\boldsymbol{\sigma}^*$ is the stress tensor, which must be prescribed by a constitutive law. Although the fluid containing the particles is assumed to be Newtonian and isotropic, the presence of the particles will induce anisotropic behaviour.

5.2.1 Stress tensor

Most models currently found in the literature take account of the isotropic ($\boldsymbol{\sigma}^{*I}$) and active ($\boldsymbol{\sigma}^{*S}$) contributions to the stress, but neglect the anisotropic contribution of the particles $\boldsymbol{\sigma}^{*P}$. We therefore follow Pedley & Kessler [65], via refs. [6, 36], and take an expression for the stress tensor of the form

$$\boldsymbol{\sigma}^* = \boldsymbol{\sigma}^{*I} + \boldsymbol{\sigma}^{*S} + \boldsymbol{\sigma}^{*P}. \tag{5.8}$$

The isotropic component takes the form

$$\boldsymbol{\sigma}^{*I} = -\bar{p}^* \, \boldsymbol{I} + 2 \, \bar{\mu}^* \, \boldsymbol{e}^*, \tag{5.9}$$

where $\bar{p}^*$ is the hydrostatic pressure and $\bar{\mu}^*$ is the solvent viscosity.

5.2.2 Active stress contribution

Active behaviour of force-free Stokesian swimmers is modelled by an equal and opposite propulsive force/drag pair acting along, and infinitesimally displaced in, the $\pm\hat{\boldsymbol{p}}$ direction. To derive the corresponding stress term, consider the Stokes flow equations

$$\boldsymbol{\nabla}_{\boldsymbol{x}} \cdot \boldsymbol{u}^* = 0, \tag{5.10}$$

$$\boldsymbol{\nabla}_{\boldsymbol{x}} \cdot \boldsymbol{\sigma}^{*d} = \boldsymbol{F}^* \delta \left(\boldsymbol{x}^* - \boldsymbol{y}^* \right), \tag{5.11}$$

where $\boldsymbol{y}^*$ is the position of the Stokeslet, $\boldsymbol{x}^*$ is the displacement from this position, δ is the three-dimensional Dirac delta function, $\boldsymbol{F}^* \delta \left(\boldsymbol{x}^* - \boldsymbol{y}^* \right)$ represents a point force at the position of the Stokeslet and the constitutive relation for stress is

$$\boldsymbol{\sigma}^{*d} = \bar{p}^* \, \boldsymbol{I} + \bar{\mu}^* \left(\boldsymbol{\nabla}^*_{\boldsymbol{x}} \boldsymbol{u}^* + \boldsymbol{\nabla}^*_{\boldsymbol{x}} \boldsymbol{u}^{*T} \right). \tag{5.12}$$

Equations (5.11) are coupled to the far field conditions

$$|\boldsymbol{u}^*|, \bar{p}^* \to 0 \text{ as } r_d^* \to \infty, \tag{5.13}$$

where $\boldsymbol{r}_d^* = \boldsymbol{x}^* - \boldsymbol{y}^*$ and $r_d^* = |\boldsymbol{r}_d^*|$. The solution of equations (5.11) is [6]

$$\boldsymbol{u}_S^*(\boldsymbol{r}_d^*) = \boldsymbol{F}^* \cdot \frac{\boldsymbol{S}^*(\boldsymbol{r}_d^*)}{8\pi\bar{\mu}^*}, \tag{5.14}$$

$$\bar{p}^*(\boldsymbol{r}_d^*) = \frac{\boldsymbol{F}^* \cdot \boldsymbol{r}_d^*}{4\pi r_d^{*3}}, \tag{5.15}$$

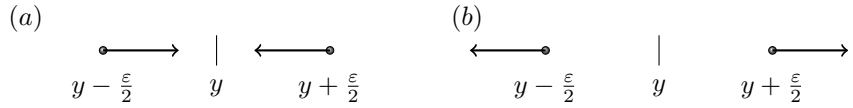

Figure 5.2: Schematic diagram showing the position of the Stokeslets and their direction to form the stresslet for a (a) puller and (b) pusher.

where

$$\boldsymbol{S}^* = \left(\frac{\boldsymbol{I}}{r_d^*} + \frac{\boldsymbol{r}_d^* \boldsymbol{r}_d^*}{r_d^{*3}} \right), \tag{5.16}$$

is the 'Oseen tensor' or 'Stokeslet' [44]. The velocity field associated with a single Stokeslet acting in the $\hat{\boldsymbol{p}}$ direction is therefore given by

$$\boldsymbol{u}_S^*(\boldsymbol{r}_d^*) = \frac{F^*}{8\pi\bar{\mu}^*} \hat{\boldsymbol{p}} \cdot \left(\frac{\boldsymbol{I}}{r_d^*} + \frac{\boldsymbol{r}_d^* \boldsymbol{r}_{\boldsymbol{d}}^*}{r_d^{*3}} \right), \tag{5.17}$$

where F^* is the force magnitude in the $\hat{\boldsymbol{p}}$ direction ($\boldsymbol{F}^* = F^* \hat{\boldsymbol{p}}$). We assume the swimmer may be approximated by two point sources a distance ε apart acting in opposite directions (figure 5.2). When the forces act towards each other, the swimmer is a *'puller'* (cells which are pulled forward, e.g. the biflagellated algae *Chlamydomonas* [50]) whilst when the forces act in opposite directions the cell is a pusher such as the bacteria *Escherichia coli* or *Bacillus subtilis* [50]. The velocity field of the resulting force pair is given by (assuming a puller to give a positive sign)

$$\boldsymbol{u}^*(\boldsymbol{r}_d^*) = \frac{1}{\varepsilon} \left(-\boldsymbol{u}_S^* \left(\boldsymbol{r}_d^* - \frac{\varepsilon}{2} \hat{\boldsymbol{p}} \right) + \boldsymbol{u}_S^* \left(\boldsymbol{r}_d^* + \frac{\varepsilon}{2} \hat{\boldsymbol{p}} \right) \right), \tag{5.18}$$

where the point forces are rescaled depending on the distance between the Stokeslets to maintain the strength of the resulting streslet. Using Taylor's theorem gives

$$\boldsymbol{u}^* = \frac{1}{\varepsilon} \Bigg(- \left[\boldsymbol{u}(\boldsymbol{r}_d^*) - \frac{\varepsilon}{2} \left(\hat{\boldsymbol{p}} \cdot \boldsymbol{\nabla}_{\boldsymbol{y}} \right) \boldsymbol{u}_S^* + \cdots \right] + \left[\boldsymbol{u}^*(\boldsymbol{r}_d^*) + \frac{\varepsilon}{2} \left(\hat{\boldsymbol{p}} \cdot \boldsymbol{\nabla}_{\boldsymbol{y}} \right) \boldsymbol{u}_S^*(\boldsymbol{r}_d^*) + \cdots \right] \Bigg) \tag{5.19}$$

Hence, assuming $\varepsilon \to 0$ and neglecting higher order terms

$$\boldsymbol{u}^* = \frac{F^*}{8\pi\bar{\mu}^*}\hat{\boldsymbol{p}} \cdot \boldsymbol{\nabla}_{\boldsymbol{y}}^* \left(\frac{\boldsymbol{I}}{r_d^*} + \frac{\boldsymbol{r}_d^* \boldsymbol{r}_d^*}{r_d^{*3}} \right) \cdot \hat{\boldsymbol{p}}. \tag{5.20}$$

We note the derivative of r_d^* may be calculated

$$\boldsymbol{\nabla}_{\boldsymbol{y}}^* \left(\frac{1}{r_d^*} \right) = \boldsymbol{\nabla}_{\boldsymbol{y}}^* \left[\left((\boldsymbol{x}^* - \boldsymbol{y}^*) \cdot (\boldsymbol{x}^* - \boldsymbol{y}^*) \right)^{1/2} \right], \tag{5.21}$$

$$= \frac{-1}{2} \left((\boldsymbol{x}^* - \boldsymbol{y}^*) \cdot (\boldsymbol{x}^* - \boldsymbol{y}^*) \right)^{-3/2} \left(-2(\boldsymbol{x}^* - \boldsymbol{y}^*) \right), \tag{5.22}$$

$$= \frac{\boldsymbol{r}_d^*}{r_d^{*3}}. \tag{5.23}$$

The velocity field (5.20) is therefore simplified as follows:

$$\boldsymbol{u}^* = \frac{F^*}{8\pi\bar{\mu}^*} \left(\frac{\boldsymbol{I}\,\boldsymbol{r}_{\boldsymbol{d}}^*}{r_d^{*3}} + \frac{3\,\boldsymbol{r}_d^*\,\boldsymbol{r}_d^*\,\boldsymbol{r}_d^*}{r_d^{*5}} - \frac{\boldsymbol{I}\,\boldsymbol{r}_d^* + \boldsymbol{r}_d^*\,\boldsymbol{I}}{r_d^{*3}} \right) : \hat{\boldsymbol{p}}\,\hat{\boldsymbol{p}}, \tag{5.24}$$

$$= \frac{F^*}{8\pi\bar{\mu}^*} \left(\frac{\boldsymbol{r}_d^*}{r_d^{*3}} \hat{\boldsymbol{p}}\,\hat{\boldsymbol{p}} + \frac{3\boldsymbol{r}_d^*\,\boldsymbol{r}_d^*\,\boldsymbol{r}_d^*}{r_d^{*5}} : \hat{\boldsymbol{p}}\,\hat{\boldsymbol{p}} - \frac{\hat{\boldsymbol{p}}}{r_d^{*3}} \cdot \hat{\boldsymbol{p}}\,\hat{\boldsymbol{p}} + \frac{\boldsymbol{r}_d^*}{r_d^{*3}}\,\hat{\boldsymbol{p}} \cdot \hat{\boldsymbol{p}} \right). \tag{5.25}$$

Using that $\hat{\boldsymbol{p}}$ is a unit vector, and $\boldsymbol{I} : \boldsymbol{r}_d^*\,\boldsymbol{r}_d^* = r_d^{*2}$, equation (5.25) may be further simplified

$$\boldsymbol{u}^* = \frac{3F^*\boldsymbol{r}_d^*\,\boldsymbol{r}_d^*\,\boldsymbol{r}_d^*}{8\pi\bar{\mu}^* r_d^{*5}} : \left(\hat{\boldsymbol{p}}\,\hat{\boldsymbol{p}} - \frac{\boldsymbol{I}}{3} \right), \tag{5.26}$$

which is the form of a symmetric stokes dipole ('stresslet') with tensorial strength proportional to $(\hat{\boldsymbol{p}}\,\hat{\boldsymbol{p}} - \boldsymbol{I}/3)$. The pressure field may be found similarly,

$$\bar{p}(\boldsymbol{r}_d^*) = F^*\hat{\boldsymbol{p}} \cdot \boldsymbol{\nabla}_{\boldsymbol{y}} \left(\frac{\boldsymbol{r}_d^* \cdot \hat{\boldsymbol{p}}}{4\pi r_d^{*3}} \right), \tag{5.27}$$

$$= \frac{3F^*\boldsymbol{r}_d^*\,\boldsymbol{r}_d^*}{4\pi r_d^{*5}} : \left(\hat{\boldsymbol{p}}\,\hat{\boldsymbol{p}} - \frac{\boldsymbol{I}}{3} \right). \tag{5.28}$$

The stress generated by the swimmer is found using equation (5.12)

$$\sigma_{il}^{*d} = \frac{3F^*}{8\pi}\left(\hat{p}_j\hat{p}_k - \frac{\delta_{jk}}{3}\right)\left(- 2\frac{r_j^* r_k^*}{r_d^{*5}}\delta_{il} - \frac{10 r_i^* r_j^* r_k^* r_l^*}{r_d^{*7}} + \frac{r_i^* r_j^* \delta_{kl} + r_i^* r_k^* \delta_{jl} + r_j^* r_k^* \delta_{il} + r_j^* r_k^* \delta_{il} + r_j^* r_l^* \delta_{ik} + r_k^* r_l^* \delta_{ij}}{r_d^{*5}}\right), \tag{5.29}$$

$$= \frac{3F^*}{4\pi}\left(\hat{p}_j\hat{p}_k - \frac{\delta_{jk}}{3}\right)\left(\frac{r_j^*\left(r_i^*\delta_{kl} + r_l^*\delta_{ik}\right)}{r_d^{*5}} - \frac{5 r_i^* r_j^* r_k^* r_l^*}{r_d^{*7}}\right), \tag{5.30}$$

where $r_i^* = (\boldsymbol{r}_d^*)_i$. Equation (5.30) can be rewritten in vector form

$$\boldsymbol{\sigma}^d = \frac{3F^*}{4\pi}\left(\hat{\boldsymbol{p}}\,\hat{\boldsymbol{p}} - \frac{\boldsymbol{I}}{3}\right) : \left(\frac{\boldsymbol{r}_d^*\left(\boldsymbol{r}_d^*\,\boldsymbol{I} + \boldsymbol{I}\,\boldsymbol{r}_d^*\right)}{r_d^{*5}} - \frac{5\boldsymbol{r}_d^*\,\boldsymbol{r}_d^*\,\boldsymbol{r}_d^*\,\boldsymbol{r}_d^*}{r_d^{*7}}\right). \tag{5.31}$$

To calculate the total contribution to the stress, assume the effective stress in the suspension is the ensemble average of the stress distribution in all realisations of the suspension. The formal expression for the effective stress is [6, 44]

$$\boldsymbol{\sigma}^{*\text{eff}} = \frac{1}{V^*}\int_{V^*} \boldsymbol{\sigma}^{d*}\,\mathrm{d}V^*, \tag{5.32}$$

$$= \frac{1}{V^*}\int_{V^* - \sum V_c^*} -\bar{p}^*\boldsymbol{I} + 2\bar{\mu}^*\boldsymbol{e}^*\,\mathrm{d}V^* + \sum_n \int_{V_c^*} \boldsymbol{\sigma}^d\,\mathrm{d}V_c^*, \tag{5.33}$$

where the volume integral has been decomposed into the portion where the constitutive relations for the fluid ($V^* - \sum V_c^*$) and particle (V_c^*) hold respectively. By noting

$$\boldsymbol{\sigma}^{*d} = \boldsymbol{\nabla}_{\boldsymbol{x}}^* \cdot \left(\boldsymbol{\sigma}^{*d}\boldsymbol{x}^*\right) - \left(\boldsymbol{\nabla}_{\boldsymbol{x}}^* \cdot \boldsymbol{\sigma}^{*d}\right)\boldsymbol{x}^*, \tag{5.34}$$

and $\boldsymbol{\nabla}_{\boldsymbol{x}}^* \cdot \boldsymbol{\sigma}^{*d} = 0$ for force free particles. The effective stress is therefore

$$\boldsymbol{\sigma}^{*\text{eff}} = \frac{1}{V^*}\int_{V^* - \sum V_c^*} -\bar{p}^*\boldsymbol{I} + 2\bar{\mu}^*\boldsymbol{e}^*\,\mathrm{d}V^* + \sum_n \int_{S_c^*} \boldsymbol{\sigma}^{*d}\cdot\hat{\boldsymbol{n}}\boldsymbol{x}^*\,\mathrm{d}S_c^*, \tag{5.35}$$

where the final term represents the surface tractions of the swimmer on the surface S_c^*, n is the number of particles in the volume of interest and $\hat{\boldsymbol{n}}$ is the unit normal to the

particles' surface. The integral of the rate of strain tensor $\boldsymbol{e}^*$ may be evaluated as

$$\int_{V^*-\sum V_c^*} 2\boldsymbol{e}^* \,\mathrm{d}V^* = \int_{V^*} 2\boldsymbol{e}^* \,\mathrm{d}V^* - \sum_n \int_{V_c^*} \boldsymbol{\nabla}_{\boldsymbol{x}}^* \boldsymbol{u}^* + \boldsymbol{\nabla}_{\boldsymbol{x}}^* \boldsymbol{u}^{*T} \,\mathrm{d}V^*, \tag{5.36}$$

$$= \int_{V^*} 2\boldsymbol{e}^* \,\mathrm{d}V^* - \sum_n \int_{S_c^*} \boldsymbol{u}^* \,\hat{\boldsymbol{n}} + \hat{\boldsymbol{n}}\, \boldsymbol{u}^* \,\mathrm{d}S_c^*, \tag{5.37}$$

where we have used the identity [1]

$$\int_{V^*} \boldsymbol{\nabla}_{\boldsymbol{x}} \boldsymbol{F}^* \,\mathrm{d}V^* = \int_{S^*} \boldsymbol{F}^* \,\hat{\boldsymbol{n}} \,\mathrm{d}S^*. \tag{5.38}$$

Combining these results together, the effective stress is

$$\boldsymbol{\sigma}^{*\mathrm{eff}} = -p^{*\mathrm{eff}} \boldsymbol{I} + 2\mu^* \int_{V^*} \boldsymbol{e}^* \,\mathrm{d}V^* + \boldsymbol{\sigma}^{*e}, \tag{5.39}$$

where $p^{*\mathrm{eff}}$ is the effective pressure, containing all isotropic parts of the effective stress, and the particle contribution is

$$\boldsymbol{\sigma}^{*e} = \frac{1}{V^*} \sum_n \int_{S_c^*} \boldsymbol{\sigma}^{*d} \cdot \hat{\boldsymbol{n}}\, \boldsymbol{x}^* - \mu^* \left(\boldsymbol{u}^* \,\hat{\boldsymbol{n}} + \hat{\boldsymbol{n}}\, \boldsymbol{u}^*\right) \mathrm{d}S_c^*. \tag{5.40}$$

For rigid particles, the velocity at the particle surface is a rigid body motion so the velocity terms in the integral vanish identically [44]

$$\boldsymbol{\sigma}^{*e} = \frac{1}{V^*} \sum_n \int_{S_c^*} \boldsymbol{\sigma}^{*d} \cdot \hat{\boldsymbol{n}}\, \boldsymbol{x}^* \,\mathrm{d}S_c^*. \tag{5.41}$$

Substituting for $\boldsymbol{\sigma}^{*d}$ from equation (5.31) gives

$$\boldsymbol{\sigma}^{*e} = \frac{3F^*}{4\pi V^*} \sum_n \left(\hat{\boldsymbol{p}}\,\hat{\boldsymbol{p}} - \frac{\boldsymbol{I}}{3}\right) : \int_{S_c^*} \left(\frac{\boldsymbol{r}_d^* \left(\boldsymbol{r}_d^* \boldsymbol{I} + \boldsymbol{I}\, \boldsymbol{r}_d^*\right)}{r_d^{*5}} - \frac{5\boldsymbol{r}_d^*\, \boldsymbol{r}_d^*\, \boldsymbol{r}_d^*\, \boldsymbol{r}_d^*}{r_d^{*7}}\right) \cdot \hat{\boldsymbol{n}}\, \boldsymbol{x}^* \,\mathrm{d}S_c^*. \tag{5.42}$$

We note the integral

$$A_{iabk} = \int_{S_c} \left(\frac{r_a^* \left(r_i^* \delta_{bk} + r_k^* \delta_{ib} \right)}{r_d^{*5}} - \frac{5 r_i^* r_a^* r_b^* r_k^*}{r_d^{*7}} \right) n_k x_j \, \mathrm{d}S_c \tag{5.43}$$

is isotropic, and therefore takes the form

$$A_{iabk} = \lambda_1 \delta_{ia} \delta_{bj} + \lambda_2 \delta_{ib} \delta_{aj} + \lambda_3 \delta_{ij} \delta_{ab}. \tag{5.44}$$

Substituting this form into equation (5.42) yields

$$\sigma^{*e} = \alpha_1^* \sum_n \left(\hat{\boldsymbol{p}} \hat{\boldsymbol{p}} - \frac{\boldsymbol{I}}{3} \right), \tag{5.45}$$

where $\alpha_1^* = 3F^*(\lambda_1 + \lambda_2)/4\pi V^*$ is a parameter, which could be positive or negative, quantifying the active stresslet strength.. Equations (5.41) and (5.45) give the macroscopic stress for a specific case of a particle suspension (when transversely-isotropic effects are neglected). However we wish to visualise all possible suspensions; therefore we integrate σ^{*e} over all possible particle directions to give the contribution to the stress due to active swimming as

$$\boldsymbol{\sigma}^{*S} = \alpha_1^* \int_S \left(\hat{\boldsymbol{p}} \, \hat{\boldsymbol{p}} - \frac{\boldsymbol{I}}{3} \right) N \, \mathrm{d}\hat{\boldsymbol{p}}, \tag{5.46}$$

$$= \alpha_1^* \, c^* \left\langle \hat{\boldsymbol{p}} \, \hat{\boldsymbol{p}} - \frac{\boldsymbol{I}}{3} \right\rangle. \tag{5.47}$$

5.2.3 Influence of non-spherical particles on the bulk stress

The components of the stress tensor that arise from the presence of suspended particles in the solvent take the form [6, 36]

$$\boldsymbol{\sigma}^{*P} = 4 \, c^* \, \bar{\mu}^* \, V_c^* \Big[\alpha_2 \, \boldsymbol{e}^* : \langle \boldsymbol{p} \, \boldsymbol{p} \, \boldsymbol{p} \, \boldsymbol{p} \rangle + \alpha_3 \left(\boldsymbol{e}^* \cdot \langle \boldsymbol{p} \, \boldsymbol{p} \rangle + \langle \boldsymbol{p} \, \boldsymbol{p} \rangle \cdot \boldsymbol{e}^* \right) + \alpha_4 \boldsymbol{e}^* + \alpha_5 \boldsymbol{I} \, \boldsymbol{e}^* : \langle \boldsymbol{p} \, \boldsymbol{p} \rangle \Big], \tag{5.48}$$

where V_c^* is the particle volume and α_i $(i = 2 \ldots 5)$ are constants.

The full model thus consists of a normalisation condition for N^* (5.1), where N^* is governed by the Fokker-Planck equation (5.4), with fluxes (5.5) and (5.6). The fluid velocity obeys conservation of mass and momentum (5.7), with a constitutive relation for stress given by equations (5.8), (5.9), (5.47) and (5.48).

5.3 Aligned suspension

In the following we drop the stars which denote dimensional quantities for convenience. Consider a uniform suspension $c(\boldsymbol{x}, t) = n_d$ which is perfectly aligned, with director field $\boldsymbol{a}(\boldsymbol{x}, t)$; the particle distribution function is then of the form

$$N(\boldsymbol{x}, \hat{\boldsymbol{p}}, t) = n_d \, \delta(\hat{\boldsymbol{p}} - \boldsymbol{a}), \tag{5.49}$$

where δ denotes the Dirac delta function [73]. In this case we need only consider how the average direction of the particles $\boldsymbol{a}$ evolves, and not the full distribution function N.

To derive an evolution equation for $\boldsymbol{a}$, we multiply equation (5.4) by $\hat{\boldsymbol{p}}$ and integrate over $\hat{\boldsymbol{p}}$ to give [73]

$$\begin{aligned} n_d \frac{\partial}{\partial t} \int_S \hat{\boldsymbol{p}} \, \delta(\hat{\boldsymbol{p}} - \boldsymbol{a}) \, \mathrm{d}\hat{\boldsymbol{p}} + n_d U_s \boldsymbol{\nabla}_{\boldsymbol{x}} \cdot \int_S \hat{\boldsymbol{p}} \, \hat{\boldsymbol{p}} \, \delta(\hat{\boldsymbol{p}} - \boldsymbol{a}) \, \mathrm{d}\hat{\boldsymbol{p}} + n_d \boldsymbol{\nabla}_{\boldsymbol{x}} \cdot \left(\boldsymbol{u} \int_S \hat{\boldsymbol{p}} \, \delta(\hat{\boldsymbol{p}} - \boldsymbol{a}) \, \mathrm{d}\hat{\boldsymbol{p}} \right) \\ - n_d \int_S (\boldsymbol{I} - \hat{\boldsymbol{p}} \, \hat{\boldsymbol{p}}) \cdot \left[(\alpha_0 \boldsymbol{e} + \boldsymbol{\omega}) \cdot \hat{\boldsymbol{p}} \right] \delta(\hat{\boldsymbol{p}} - \boldsymbol{a}) \, \mathrm{d}\hat{\boldsymbol{p}} = 0, \end{aligned} \tag{5.50}$$

where we have made use of the integration by parts formula

$$\int_S \hat{\boldsymbol{p}} \boldsymbol{\nabla}_{\boldsymbol{p}} \cdot (\boldsymbol{f} N) \, \mathrm{d}\hat{\boldsymbol{p}} = - \int_S \boldsymbol{f} N \, \mathrm{d}\hat{\boldsymbol{p}}. \tag{5.51}$$

Evaluating each of these integrals in turn gives

$$\frac{\partial \boldsymbol{a}}{\partial t} + (U_s \, \boldsymbol{a} + \boldsymbol{u}) \cdot \boldsymbol{\nabla}_{\boldsymbol{x}} \, \boldsymbol{a} - \boldsymbol{\omega} \cdot \boldsymbol{a} = \alpha_0 \left(\boldsymbol{e} \cdot \boldsymbol{a} - \boldsymbol{e} : \boldsymbol{a} \, \boldsymbol{a} \, \boldsymbol{a} \right). \tag{5.52}$$

The fibre evolution equation (2.6) of Ericksen [24] for a passive transversely isotropic fluid can then be recovered by setting the swimming speed to zero ($U_s = 0$).

The governing equations for the background flow (equations (5.7)) remain unchanged, however the stress tensor is now given by

$$\boldsymbol{\sigma} = -p\,\boldsymbol{I} + 2\mu\,\boldsymbol{e} + \mu_1\,\boldsymbol{a}\,\boldsymbol{a} + \mu_2\,\boldsymbol{a}\,\boldsymbol{a}\,\boldsymbol{a}\,\boldsymbol{a} : \boldsymbol{e} + 2\mu_3\,(\boldsymbol{a}\,\boldsymbol{a}\cdot\boldsymbol{e} + \boldsymbol{e}\cdot\boldsymbol{a}\,\boldsymbol{a}), \tag{5.53}$$

where the pressure has been modified such that,

$$p = \bar{p} + \frac{n_d\alpha_1}{3} - 4\,\bar{\mu}\,\phi\,\alpha_5\,\boldsymbol{a}\boldsymbol{a} : \boldsymbol{e}, \tag{5.54}$$

and the viscosity-like parameters are given by

$$\begin{aligned}
\mu &= \bar{\mu}\,(1 + 2\,\phi\,\alpha_4)\,,\\
\mu_2 &= 4\,\bar{\mu}\,\phi\,\alpha_2,\\
\mu_3 &= 2\,\bar{\mu}\,\phi\,\alpha_3.
\end{aligned} \tag{5.55}$$

The parameters μ, μ_2 and μ_3 are the viscosity-like parameters of Ericksen's model (section 2.3) and $\phi = n_d V_c$ is the volume fraction of the particles. Linking these models allows for these parameters to be approximated from Jeffery [43] (via [6, 10, 51, 65, 44]), given by

$$\begin{aligned}
\mu &= \bar{\mu}\left(1 + \frac{2\phi}{I_1}\right),\\
\mu_2 &= \frac{4\phi\bar{\mu}}{I_1}\left(1 + \frac{L_1}{L_2} - 2\frac{I_1}{I_2}\right),\\
\mu_3 &= \frac{4\phi\bar{\mu}}{I_1}\left(\frac{I_1}{I_2} - 1\right).
\end{aligned} \tag{5.56}$$

The quantities I_1, I_2, L_1 and L_2 are ellipsoidal integrals, given in terms of the aspect ratio

r:

$$
\begin{aligned}
I_1 &= \int_0^\infty \frac{2r}{(r^2+\lambda)^{1/2}(1+\lambda)^3}\,\mathrm{d}\lambda = \frac{r^2\left(2r^2-5+3\gamma\right)}{2\left(r^2-1\right)^2},\\
I_2 &= \int_0^\infty \frac{r\left(r^2+1\right)}{(r^2+\lambda)^{3/2}(1+\lambda)^2}\,\mathrm{d}\lambda = \frac{\left(r^2+1\right)\left(r^2+2-3r^2\gamma\right)}{\left(r^2-1\right)^2},\\
L_1 &= \int_0^\infty \frac{r\lambda}{(r^2+\lambda)^{1/2}(1+\lambda)^3}\,\mathrm{d}\lambda = \frac{r^2\left[2r^2+1-\gamma\left(4r^2-1\right)\right]}{4\left(r^2-1\right)^2},\\
L_2 &= \int_0^\infty \frac{r\lambda}{(r^2+\lambda)^{3/2}(1+\lambda)^2}\,\mathrm{d}\lambda = I_1 - 2L_1,\\
\text{where } \gamma &= \frac{\cosh^{-1} r}{r\left(r^2-1\right)^{1/2}}.
\end{aligned}
\tag{5.57}
$$

These results agree with those found by Lipscomb *et al.* [54], discussed in section 2.3, and are valid when the suspension is dilute.

Linking models of passive and active suspensions allows us to identify that the parameter μ_1 is directly related to the strength of the active stresslet α_1,

$$\mu_1 = n_d\,\alpha_1, \tag{5.58}$$

which has not been identified before. Therefore Ericksen's model for a transversely isotropic fluid may be used to model actively motile 'fibres', with a simple modification to the kinematic equation.

We have therefore recovered, from a general model for an active suspension of elongated particles, the model for a transversely isotropic fluid proposed by Ericksen [24], with a modification to the fibre evolution equation. By analogy with recent findings in the transversely isotropic field [22, 23, 38] as well as chapters 3 and 4, this suggests that the terms which have often been neglected from equation (5.48) will have a significant impact on the dynamics of suspensions of active elongated particles via the rheological parameters μ_2 and μ_3 [73, 76, 82].

5.4 Conclusion

We have linked models of active suspensions of elongated motile particles to the transversely isotropic fluid proposed by Ericksen [24], using a Fokker-Planck equation for the particle distribution function and the stress tensor of Pedley & Kessler [65], which includes the influence of non-spherical particles on the bulk stress. Under the assumption that the suspension is of spatially-uniform volume fraction and has perfect but perhaps spatially-varying alignment, Ericksen's four viscosity-like parameters may be determined in terms of fundamental physical quantities. These quantities include the active stresslet, particle aspect ratio, particle volume, mean number density of the particles and solvent viscosity. This linkage yields a physical basis for inferring these crucial mechanical parameters used in models such as [23, 29, 38]. The shear-independent term parameterised by μ_1 is found to model active behaviour. The transversely isotropic fluid of Ericksen may therefore be used to model actively motile 'fibres' by a simple modification to the fibre evolution equation. Linking these two frameworks provides a basis to extend Ericksen's model to include effects such as dispersion about the preferred direction.

Our modification to Ericksen's model can be considered as the simplest describing an orientated active suspension and including transversely isotropic effects; more refined approaches take into account fibre-dispersion formulated via the Q-tensor which is defined as the nematic moment $\langle \hat{\boldsymbol{p}}\hat{\boldsymbol{p}} - \boldsymbol{I}/3 \rangle$ [12, 90].

For models of near-spherical algae it is reasonable to assume that these non-isotropic stress terms have a small influence, justifying their neglect [65]. However, this near-spherical limit of the model has also been used to give insight into the dynamics of elongated rod-like bacterial suspensions [73, 76, 82]. The non-isotropic terms have been shown to have a significant effect on the system's emergent properties and flow stability within the transversely isotropic fluid research literature [23, 29, 38]; these terms therefore seem likely to have implications for earlier analysis of the critical concentration threshold and wavelengths of emergent patterns in active suspensions [71, 73, 82, 83]. Indeed (and perhaps somewhat paradoxically) in some bacterial suspension models, the additional

stress terms are invoked *a posteriori* to determine the extent to which a fluid's rheology is affected by the suspended particles [71, 74] but which are not taken into account when calculating the velocity field. Hydrodynamic effects associated with elongated active particles are important, and should be taken into account from the outset in future work.

In this chapter we show how models for active suspensions, described by Pedley and Kessler [65] and Simha and Ramaswamy [76], may be linked to the mathematically simpler model of Ericksen [24]. We do this by choosing the form of the distribution function for a perfectly aligned uniform suspension proposed by Saintillan and Shelley [72]. We believe this is the first time these models have been linked in this way. We note however that Pedley and Kessler build upon the work of Batchelor [6]. It has been shown by Lipscomb et al. [54] that the stress tensor proposed by Batchelor for a uniform aligned passive suspensions is equivalent to that of Ericksen, when the active behaviour of the material is neglected. Hence the parameter values for μ_2 and μ_3 in a dilute suspension have been previously identified by Lipscomb et al. [54]. However, through the link we propose we are able to identify a new physical interpretation of the μ_1 parameter, and also propose a simple modification to Ericksen's model to include swimming particles.

Active suspensions and transversely isotropic fluids are both biologically-relevant and physically-fascinating states of matter. Linking these two fields of research enables knowledge transfer, enabling extension of the transversely isotropic model (chapter 2) and identifying important components of the active suspension model which have previously been neglected. This link provides a framework to extend the results found in chapters 3 and 4 to include dispersion about the average direction. In chapter 6 we will investigate the linear stability of the uniformly distributed, perfectly aligned, suspension identified in this chapter to a plane wave perturbation.

CHAPTER 6

LINEAR STABILITY OF ISOTROPIC AND NEARLY-ALIGNED SUSPENSIONS OF ELONGATED PARTICLES

6.1 Introduction

In this chapter we examine the linear stability of suspensions of elongated particles, with zero background flow, in two distinct cases; when the particles are nearly aligned and when the suspension is isotropic, *i.e.* when particles have nearly zero dispersion at each point in space, and when the particles are perfectly randomly orientated. The particles may be either *'active'*, *i.e.* the particles can propel themselves through the fluid, or *'passive'*, *i.e.* the particles have no mechanism of self-propulsion, reorienting due to the background flow and hydrodynamic interactions only. To model these suspensions we follow a similar analysis to Saintillan & Shelley [72, 73], however we instead choose the model proposed by Pedley & Kessler [65], where the anisotropic terms (described in chapter 5) are included. These interactions are important in passive suspensions of rod-like particles, but their inclusion in active suspensions has previously been neglected. This chapter therefore focusses on the effect the extra particle stress, due to hydrodynamic interactions, has on the stability of isotropic and nearly-aligned suspensions of rod-like bacteria.

In section 6.2 we begin by stating the governing equations we adopt to model a suspension of rod-like particles. These equations constitute a Fokker-Planck equation, which

describes the evolution of a particle's orientation and position [45], coupled to conservation of mass and momentum equations for the background flow, where the constitutive relation for stress is adopted from Pedley and Kessler [65]. We conclude this section by non-dimensionalising our governing equations and variables. In section 6.3 we examine the linear stability of a nearly-aligned suspension of rod-like particles. Similarly to *ref.* [73] we propose a base state where the particles are perfectly aligned at each point in space with no background flow; this allows us to split the distribution function into a pair of equations for the particles' concentration and director fields. By considering plane wave perturbations to the base state, we find a dispersion relation and visualise the dependence of the growth parameter on the wave-number, wave-angle, shape parameter and volume fraction of particles. In section 6.4 we use the governing equations proposed in section 6.2 and through the form of the distribution function we consider an isotropic base state. Following Saintillan & Shelley [73] we examine the linear stability of this base state to plane wave perturbations, and find the corresponding dispersion relation for the growth parameter; we visualise the dependence of the growth parameter on the wave-number, shape parameter and volume fraction of particles. Finally in section 6.5 we give a summary of our findings.

6.2 Governing equations

We adopt the model proposed in Chapter 5, and consider a collection of particles suspended in a viscous, Newtonian fluid. The density of particles is sufficiently dilute that particles do not interact directly, only through their influence on the fluid. Each particle is modelled as a prolate spheroid with major axis r_1^*, minor axis r_2^*, aspect ratio $r = r_1^*/r_2^*$, and shape parameter $\alpha_0 = (r^2 - 1)/(r^2 + 1)$. The particle number density in physical and orientational space is denoted $N^*(\boldsymbol{x}^*, \hat{\boldsymbol{p}}, t)$ where $\boldsymbol{x}^*$ denotes the particle position, $\hat{\boldsymbol{p}}$ is orientation and t^* is time [17], visualised in Figure 5.1. This function is defined in equation (5.1) and governed by the Fokker-Planck equation (5.4), where the

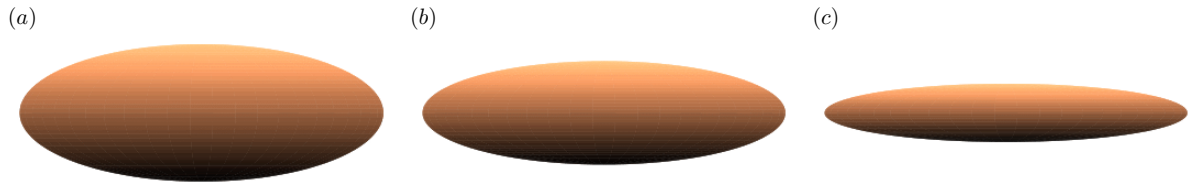

Figure 6.1: Schematic diagram to illustrate the different particle shapes when (a) $\alpha_0 = 0.75$, (b) $\alpha_0 = 0.85$ and (c) $\alpha_0 = 0.95$.

constitutive equations for the translational and rotational velocities are given in equations (5.5) and (5.6) respectively. The local particle director and concentration fields $\boldsymbol{a} = \langle \hat{\boldsymbol{p}} \rangle$ and c^* are defined in equations (5.2) and (5.3). The background flow $\boldsymbol{u}^*$ is modelled using the Cauchy momentum equations (5.7), with a constitutive relation for stress defined in equations (5.8), (5.9), (5.47) and (5.48).

6.2.1 Governing equation for concentration field

The local particle director ($\boldsymbol{a} = \langle \hat{\boldsymbol{p}} \rangle$) and concentration fields (c^*) are defined such that

$$\boldsymbol{a} = \langle \hat{\boldsymbol{p}} \rangle (\boldsymbol{x}^*, t^*) = \frac{1}{c^*(\boldsymbol{x}^*, t^*)} \int_S \hat{\boldsymbol{p}}\, N^*(\boldsymbol{x}^*, \hat{\boldsymbol{p}}, t^*)\, \mathrm{d}\hat{\boldsymbol{p}}, \tag{6.1}$$

$$c^*(\boldsymbol{x}^*, t^*) = \int_S N^*(\boldsymbol{x}^*, \hat{\boldsymbol{p}}, t^*)\, \mathrm{d}\hat{\boldsymbol{p}}. \tag{6.2}$$

To derive a governing equation for the concentration field $c^*(\boldsymbol{x}^*, t^*)$ we integrate equation (5.4) over $\hat{\boldsymbol{p}}$ and substitute for the translational flux velocity $\boldsymbol{U}$ (equation (5.5)) to give [73]

$$\frac{\partial c^*}{\partial t^*} + \boldsymbol{u}^* \cdot \boldsymbol{\nabla}^*_{\boldsymbol{x}} c^* = -U_s^* \boldsymbol{\nabla}^*_{\boldsymbol{x}} \cdot (c^* \boldsymbol{a}), \tag{6.3}$$

where U_s^* the particle swimming speed. A detailed derivation is shown in appendix C. Equation (6.3) is an advection-diffusion equation for the local concentration field c^*, with a source term $-U_s^* \boldsymbol{\nabla}^*_{\boldsymbol{x}} \cdot (c^* \boldsymbol{a})$.

6.2.2 Non-dimensionalisation

The governing equations are made dimensionless using the following scaling [73]:

$$\begin{aligned} \boldsymbol{u}^* &= U_s^* \boldsymbol{u}, & \boldsymbol{x}^* &= \frac{\boldsymbol{x}}{n_d^* r_1^{*2}}, & t^* &= \frac{t}{n_d^* r_1^{*2} U_s^*}, \\ p^* &= \mu^* U_s^* n_d^* r_1^{*2} p, & N^* &= n_d^* N, & c^* &= n_d^* c, \end{aligned} \tag{6.4}$$

where n_d^* is the mean number density of particles in the suspension. Note that $n_d^* r_1^{*2} = f_1 V_e^*/r_2^2 V^*$, where $V_e^* = 4\pi M r_1^* r_2^{*2}/3$ is the volume taken up by the total number of swimming particles (M) in a volume V^*.

The particle distribution function is now defined as (equation (5.1))

$$\frac{1}{V}\int_V \int_S N(\boldsymbol{x}, \hat{\boldsymbol{p}}, t)\, \mathrm{d}\hat{\boldsymbol{p}}\, \mathrm{d}\boldsymbol{x} = 1, \tag{6.5}$$

and governed by (equation (5.4))

$$\frac{\partial N}{\partial t} = -\boldsymbol{\nabla}_{\boldsymbol{x}} \cdot (\boldsymbol{U} N) - \boldsymbol{\nabla}_{\boldsymbol{p}} \cdot (\boldsymbol{\Omega} N)\,, \tag{6.6}$$

where the non-dimensional translational and rotational velocities of the particles are given by (equation (5.5) and (5.6))

$$\boldsymbol{U} = \hat{\boldsymbol{p}} + \boldsymbol{u}, \tag{6.7}$$

$$\boldsymbol{\Omega} = (\boldsymbol{I} - \hat{\boldsymbol{p}}\,\hat{\boldsymbol{p}}) \cdot \left[(\alpha_0 \boldsymbol{e} + \boldsymbol{\omega}) \cdot \hat{\boldsymbol{p}}\right]. \tag{6.8}$$

Here $\boldsymbol{e} = (\boldsymbol{\nabla}_{\boldsymbol{x}}\boldsymbol{u} + \boldsymbol{\nabla}_{\boldsymbol{x}}\boldsymbol{u}^T)/2$ is the rate-of-strain tensor and $\boldsymbol{\omega} = (\boldsymbol{\nabla}_{\boldsymbol{x}}\boldsymbol{u} - \boldsymbol{\nabla}_{\boldsymbol{x}}\boldsymbol{u}^T)/2$ is the vorticity tensor.

The local particle director and concentration fields (equations (6.1) and (6.2)) are

$$\boldsymbol{a}(\boldsymbol{x},t) = \langle \hat{\boldsymbol{p}} \rangle = \frac{1}{c(\boldsymbol{x},t)} \int_S \hat{p} N(\boldsymbol{x},\hat{\boldsymbol{p}},t)\,\mathrm{d}\hat{\boldsymbol{p}}, \tag{6.9}$$

$$c(\boldsymbol{x},t) = \int_S N(\boldsymbol{x},\hat{\boldsymbol{p}},t)\,\mathrm{d}\hat{\boldsymbol{p}}, \tag{6.10}$$

where the concentration field is governed by (equation (6.3))

$$\frac{\partial c}{\partial t} + \boldsymbol{u}\cdot\boldsymbol{\nabla}_{\boldsymbol{x}} c = -\boldsymbol{\nabla}_{\boldsymbol{x}}\cdot(c\boldsymbol{a})\,. \tag{6.11}$$

Finally, the momentum and continuity equations (5.7) simplify as

$$\boldsymbol{\nabla}_{\boldsymbol{x}}\cdot\boldsymbol{\sigma} = \boldsymbol{0}, \qquad\qquad \boldsymbol{\nabla}_{\boldsymbol{x}}\cdot\boldsymbol{u} = 0, \tag{6.12}$$

where inertia has been neglected and the constitutive relation for stress is given by

$$\begin{aligned}\boldsymbol{\sigma} = -p\,\boldsymbol{I} + 2\,\boldsymbol{e} + \alpha_1 \int_S \left(\hat{\boldsymbol{p}}\,\hat{\boldsymbol{p}} - \frac{\boldsymbol{I}}{3}\right) N\,\mathrm{d}\hat{\boldsymbol{p}} + 4\phi\Bigg\{ \alpha_2 \boldsymbol{e} : \int_S \hat{\boldsymbol{p}}\,\hat{\boldsymbol{p}}\,\hat{\boldsymbol{p}}\,\hat{\boldsymbol{p}}\,N\,\mathrm{d}\hat{\boldsymbol{p}} \\ + \alpha_3\left(\boldsymbol{e}\cdot\int_S \hat{\boldsymbol{p}}\,\hat{\boldsymbol{p}}\,N\,\mathrm{d}\hat{\boldsymbol{p}} + \int_S \hat{\boldsymbol{p}}\,\hat{\boldsymbol{p}}\,N\,\mathrm{d}\hat{\boldsymbol{p}}\cdot\boldsymbol{e}\right) + \alpha_4 \boldsymbol{e}\int_S N\,\mathrm{d}\hat{\boldsymbol{p}} + \alpha_5 \boldsymbol{e} : \int_S \hat{\boldsymbol{p}}\,\hat{\boldsymbol{p}}\,N\,\mathrm{d}\hat{\boldsymbol{p}}\,\boldsymbol{I}\Bigg\}\end{aligned} \tag{6.13}$$

Here $\phi = n_d^* V_c^*$ is the volume fraction of particles in solution and $\alpha_1 = \sigma_1^*/\bar{\mu}^* U_s^* r_1^{*2}$ is the non-dimensional stresslet strength.

6.3 Linear stability of a nearly-aligned suspension

We first consider the case when the particles are perfectly aligned at each point $\boldsymbol{x}$ and the background flow is zero to leading order, a schematic diagram is given in Figure 6.2. This situation may arise when a flow, that orientates the particles, is turned off.

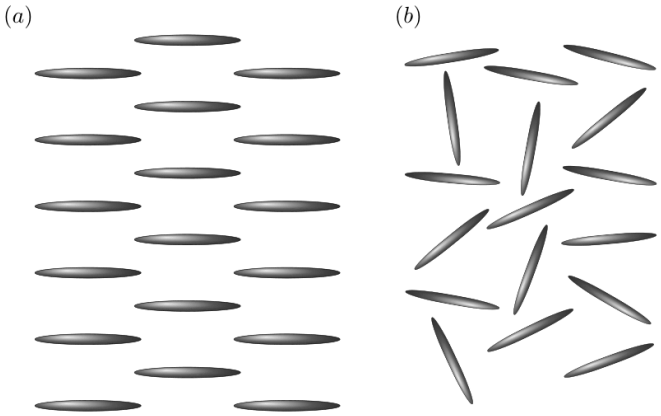

Figure 6.2: Schematic diagrams of (a) an aligned suspension and (b) an isotropic suspension of rod-like particles

6.3.1 Governing equations

For a nearly-aligned suspension the distribution function takes the form

$$N(\boldsymbol{x}, \hat{\boldsymbol{p}}, t) = c(\boldsymbol{x}, t)\delta\left(\hat{\boldsymbol{p}} - \boldsymbol{a}(\boldsymbol{x}, t)\right), \tag{6.14}$$

where δ denotes the Dirac delta function [73]. This is similar to the form of the distribution function chosen in chapter 5, but with non-uniform concentration. In this case we may reduce the evolution equation for the full distribution function (N) to a pair of equations for the concentration and director fields. The equation for concentration (equation (6.11)) is given by

$$\frac{\partial c}{\partial t} + \boldsymbol{\nabla}_{\boldsymbol{x}} \cdot \left[(\boldsymbol{a} + \boldsymbol{u})\, c\right] = 0. \tag{6.15}$$

To derive the evolution equation for the director field $\boldsymbol{a}$, multiply equation (6.6) by $\hat{\boldsymbol{p}}$ and integrate over $\hat{\boldsymbol{p}}$ to give [73],

$$\frac{\partial \boldsymbol{a}}{\partial t} = -\left(\boldsymbol{a} + \boldsymbol{u}\right) \cdot \boldsymbol{\nabla}_{\boldsymbol{x}} \boldsymbol{a} + \left(\boldsymbol{I} - \boldsymbol{a}\,\boldsymbol{a}\right) \cdot \left[(\alpha_0 \boldsymbol{e} + \boldsymbol{\omega}) \cdot \boldsymbol{a}\right], \tag{6.16}$$

where we have assumed the concentration is non-zero everywhere. A detailed derivation is shown in appendix D.

The governing equations for the background flow velocity remains unchanged (equations (6.12)), however the stress tensor is now given by

$$\begin{aligned}\boldsymbol{\sigma} = -p\,\boldsymbol{I} + 2\,\boldsymbol{e} + \alpha_1\, c(\boldsymbol{x},t)\left(\boldsymbol{a}\,\boldsymbol{a} - \frac{\boldsymbol{I}}{3}\right) \\ + 4\,\phi\, c(\boldsymbol{x},t)\left(\alpha_2 \boldsymbol{e} : \boldsymbol{a}\,\boldsymbol{a}\,\boldsymbol{a}\,\boldsymbol{a} + \alpha_3\left(\boldsymbol{e}\cdot\boldsymbol{a}\,\boldsymbol{a} + \boldsymbol{a}\,\boldsymbol{a}\cdot\boldsymbol{e}\right) + \alpha_4 \boldsymbol{e} + \alpha_5 \boldsymbol{e} : \boldsymbol{a}\,\boldsymbol{a}\,\boldsymbol{I}\right).\end{aligned} \tag{6.17}$$

If the particles are uniformly distributed ($c(\boldsymbol{x},t) = 1$), then this framework corresponds to Ericksen's model for a transversely isotropic fluid [24] when the swimming velocity is zero (chapter 5). In line with this literature we define α_2 and α_3 as the anisotropic extensional and shear viscosities respectively, and note that α_4 and α_5 may be combined with the solvent viscosity and hydrostatic pressure respectively.

The model consists of governing equations for the concentration (equation (6.15)) and director (equation (6.16)) fields of the particles, as well as conservation of mass and momentum statements for the fluid velocity (equation (6.12)), where the constitutive relation for stress is given by equation (6.17).

6.3.2 Linear stability analysis

Using the equations described in section 6.3, we analyse the linear stability of a suspension of particles aligned in the $\hat{\boldsymbol{z}}$-direction ($\boldsymbol{a}^{(0)} = \hat{\boldsymbol{z}}$). A base state exists when the fluid is motionless ($\boldsymbol{u}^{(0)} = \boldsymbol{0}$), the bacteria are uniformly distributed ($c^{(0)} = 1$), and the pressure is constant ($p^{(0)} = p_0$, where p_0 is some arbitrary pressure). We consider the stability of this state by considering the perturbation

$$\begin{aligned} c(\boldsymbol{x},t) &= 1 + \varepsilon c^{(1)}(\boldsymbol{x},t), & \boldsymbol{a} &= \hat{\boldsymbol{z}} + \varepsilon \boldsymbol{a}^{(1)}(\boldsymbol{x},t), \\ \boldsymbol{u}(\boldsymbol{x}) &= \varepsilon \boldsymbol{u}^{(1)}(\boldsymbol{x}), & p(\boldsymbol{x}) &= p_0 + \varepsilon p^{(1)}(\boldsymbol{x}), \end{aligned} \tag{6.18}$$

where $|\varepsilon| \ll 1$. We require $\boldsymbol{a}^{(1)} \cdot \hat{\boldsymbol{z}} = 0$, so that $\boldsymbol{a}$ remains a unit vector to order ε^2. To see this, observe that since $\boldsymbol{a}$ is a unit vector,

$$\left(\hat{\boldsymbol{z}} + \varepsilon \boldsymbol{a}^{(1)}\right) \cdot \left(\hat{\boldsymbol{z}} + \varepsilon \boldsymbol{a}^{(1)}\right) = 1, \tag{6.19}$$

$$\hat{\boldsymbol{z}} \cdot \hat{\boldsymbol{z}} + 2\varepsilon \left(\boldsymbol{a}^{(1)} \cdot \hat{\boldsymbol{z}}\right) + \mathcal{O}\left(\varepsilon^2\right) = 1. \tag{6.20}$$

Collecting at leading and first orders gives the required result.

Expanding equations (6.15) and (6.16), and retaining only terms of order ε only, we find [73]

$$\frac{\partial c^{(1)}}{\partial t} + \hat{\boldsymbol{z}} \cdot \boldsymbol{\nabla}_{\boldsymbol{x}} c^{(1)} + \boldsymbol{\nabla}_{\boldsymbol{x}} \cdot \boldsymbol{a}^{(1)} = 0, \tag{6.21}$$

$$\frac{\partial \boldsymbol{a}^{(1)}}{\partial t} + \hat{\boldsymbol{z}} \cdot \boldsymbol{\nabla}_{\boldsymbol{x}} \boldsymbol{a}^{(1)} = (\boldsymbol{I} - \hat{\boldsymbol{z}}\,\hat{\boldsymbol{z}}) \cdot \left(\alpha_0 \boldsymbol{e}^{(1)} + \boldsymbol{\omega}^{(1)}\right) \cdot \hat{\boldsymbol{z}}, \tag{6.22}$$

where $\boldsymbol{e}^{(1)} = (\boldsymbol{\nabla}_{\boldsymbol{x}} \boldsymbol{u}^{(1)} + \boldsymbol{\nabla}_{\boldsymbol{x}} \boldsymbol{u}^{(1)T})/2$ and $\boldsymbol{\omega}^{(1)} = (\boldsymbol{\nabla}_{\boldsymbol{x}} \boldsymbol{u}^{(1)} - \boldsymbol{\nabla}_{\boldsymbol{x}} \boldsymbol{u}^{(1)T})/2$. The momentum equations are given at order ϵ by

$$-\mu \nabla_{\boldsymbol{x}}^2 \boldsymbol{u}^{(1)} + \boldsymbol{\nabla}_{\boldsymbol{x}} q^{(1)} = \boldsymbol{\nabla}_{\boldsymbol{x}} \cdot \boldsymbol{\sigma}^{(1)}, \qquad \boldsymbol{\nabla}_{\boldsymbol{x}} \cdot \boldsymbol{u}^{(1)} = 0, \tag{6.23}$$

where $\mu = 1 + 2\phi\alpha_4$ is the enhanced shear viscosity due to the presence of the particles, $q^{(1)} = p^{(1)} - \alpha_1 c^{(1)}/3 - 4\phi\alpha_5 \boldsymbol{e}^{(1)} : \hat{\boldsymbol{z}}\hat{\boldsymbol{z}}$ is the effective pressure, and the constitutive relation for stress is given by

$$\boldsymbol{\sigma}^{(1)} = \alpha_1 \left(\boldsymbol{a}^{(1)}\hat{\boldsymbol{z}} + \hat{\boldsymbol{z}}\boldsymbol{a}^{(1)} + c^{(1)}\hat{\boldsymbol{z}}\hat{\boldsymbol{z}}\right) + 4\phi \left\{\alpha_2 \boldsymbol{e}^{(1)} : \hat{\boldsymbol{z}}\hat{\boldsymbol{z}}\hat{\boldsymbol{z}}\hat{\boldsymbol{z}} + \alpha_3 \left(\boldsymbol{e}^{(1)} \cdot \hat{\boldsymbol{z}}\hat{\boldsymbol{z}} + \hat{\boldsymbol{z}}\hat{\boldsymbol{z}} \cdot \boldsymbol{e}^{(1)}\right)\right\}. \tag{6.24}$$

6.3.3 Plane-wave solutions

We seek plane-wave solutions of the form

$$c^{(1)} = c'(\boldsymbol{k})e^{i\,\boldsymbol{k}\cdot\boldsymbol{x}+st}, \qquad \boldsymbol{a}^{(1)} = \boldsymbol{a}'(\boldsymbol{k})e^{i\,\boldsymbol{k}\cdot\boldsymbol{x}+st},$$
$$q^{(1)} = q'(\boldsymbol{k})e^{i\,\boldsymbol{k}\cdot\boldsymbol{x}+st}, \qquad \boldsymbol{u}^{(1)} = \boldsymbol{u}'(\boldsymbol{k})e^{i\,\boldsymbol{k}\cdot\boldsymbol{x}+st}, \tag{6.25}$$

where $\boldsymbol{k}$ is the wave vector and s the growth rate. Under this ansatz the equations for the first order concentration and alignment field (equations (6.21) and (6.22)) are given by

$$(s + i\hat{\boldsymbol{z}}\cdot\boldsymbol{k})\,c' = -i\boldsymbol{k}\cdot\boldsymbol{a}', \tag{6.26}$$
$$(s + i\hat{\boldsymbol{z}}\cdot\boldsymbol{k})\,\boldsymbol{a}' = (\boldsymbol{I} - \hat{\boldsymbol{z}}\,\hat{\boldsymbol{z}})\cdot\left(\alpha_0\boldsymbol{e}' + \boldsymbol{\omega}'\right)\cdot\hat{\boldsymbol{z}}, \tag{6.27}$$

where $\boldsymbol{e}' = i(\boldsymbol{k}\,\boldsymbol{u}' + \boldsymbol{u}'\,\boldsymbol{k})/2$ and $\boldsymbol{\omega}' = i(\boldsymbol{k}\,\boldsymbol{u}' - \boldsymbol{u}'\,\boldsymbol{k})/2$, whilst the conservation of mass and momentum equations become

$$\mu k^2\boldsymbol{u}' + i\boldsymbol{k}q' = i\boldsymbol{k}\cdot\boldsymbol{\sigma}', \qquad \boldsymbol{k}\cdot\boldsymbol{u}' = 0. \tag{6.28}$$

The constitutive relation for stress is now given by

$$\boldsymbol{\sigma}' = \alpha_1\left(\boldsymbol{a}'\hat{\boldsymbol{z}} + \hat{\boldsymbol{z}}\boldsymbol{a}' + c'\hat{\boldsymbol{z}}\hat{\boldsymbol{z}}\right) + 4\phi\left\{\alpha_2\boldsymbol{e}' : \hat{\boldsymbol{z}}\hat{\boldsymbol{z}}\hat{\boldsymbol{z}}\hat{\boldsymbol{z}} + \alpha_3\left(\boldsymbol{e}'\cdot\hat{\boldsymbol{z}}\hat{\boldsymbol{z}} + \hat{\boldsymbol{z}}\hat{\boldsymbol{z}}\cdot\boldsymbol{e}'\right)\right\}. \tag{6.29}$$

The effective pressure may be eliminated as follows: take the divergence of the conservation of momentum equation (6.28)

$$\mu k^2\left(\boldsymbol{k}\cdot\boldsymbol{u}'\right) - k^2q' = -k^2\hat{\boldsymbol{k}}\cdot\boldsymbol{\sigma}'\cdot\hat{\boldsymbol{k}}, \tag{6.30}$$

where $\hat{\boldsymbol{k}} = \boldsymbol{k}/|\boldsymbol{k}|$ is the unit vector in the $\boldsymbol{k}$ direction. Applying incompressibility and dividing by $-k^2$, equation (6.30) becomes

$$q' = \hat{\boldsymbol{k}} \cdot \boldsymbol{\sigma}' \cdot \hat{\boldsymbol{k}}. \tag{6.31}$$

Substituting this expression for the effective pressure into equation (6.28) yields

$$\mu k^2 \boldsymbol{u}' = \left(\boldsymbol{I} - \hat{\boldsymbol{k}}\,\hat{\boldsymbol{k}}\right) \cdot \boldsymbol{\sigma}' \cdot \boldsymbol{k}, \tag{6.32}$$

as $\boldsymbol{\sigma}'$ is symmetric. Utilising the constitutive relation for stress (6.29), the velocity is governed by

$$\begin{aligned}\left(1 + \frac{2\phi\alpha_3}{\mu}\left(\hat{\boldsymbol{k}} \cdot \hat{\boldsymbol{z}}\right)^2\right)\boldsymbol{u}' + \frac{2\phi}{\mu}\left(\boldsymbol{u}' \cdot \hat{\boldsymbol{z}}\right)\left(2\alpha_2\left(\hat{\boldsymbol{k}} \cdot \hat{\boldsymbol{z}}\right)^2 + \alpha_3\right)\left(\hat{\boldsymbol{z}} - \left(\hat{\boldsymbol{k}} \cdot \hat{\boldsymbol{z}}\right)\hat{\boldsymbol{k}}\right) \\ = \frac{i\alpha_1}{\mu k^2}\left(\boldsymbol{I} - \hat{\boldsymbol{k}}\hat{\boldsymbol{k}}\right) \cdot \left(\boldsymbol{a}'\hat{\boldsymbol{z}} + \hat{\boldsymbol{z}}\,\boldsymbol{a}' + c'\hat{\boldsymbol{z}}\,\hat{\boldsymbol{z}}\right) \cdot \boldsymbol{k}.\end{aligned} \tag{6.33}$$

The velocity is only non-zero if the wave vector $\boldsymbol{k}$ lies in the $(\hat{\boldsymbol{z}}, \boldsymbol{a}')$ plane, we observe this via contradiction. Suppose $\boldsymbol{k}$ does not lie in the $(\hat{\boldsymbol{z}}, \boldsymbol{a}')$ plane, then $\boldsymbol{k} \cdot \hat{\boldsymbol{z}} = \boldsymbol{k} \cdot \boldsymbol{a}' = 0$ and equation (6.33) becomes

$$\boldsymbol{u} + \frac{2\phi\alpha_3}{\mu}\hat{\boldsymbol{z}}\left(\boldsymbol{u} \cdot \hat{\boldsymbol{z}}\right) = 0. \tag{6.34}$$

Clearly the x and y components of velocity are zero, with the z component (w) given by

$$\left(1 + \frac{2\phi\alpha_3}{\mu}\right) w = 0. \tag{6.35}$$

As ϕ, α_3 and μ are all positive quantities, equation (6.35) only holds if $w = 0$. Therefore if $\boldsymbol{k}$ does not lie in the $(\hat{z}, \boldsymbol{a}')$ plane the velocity is zero. We have shown by contradiction that the velocity is only non-zero if $\boldsymbol{k}$ lies in the $(\hat{\boldsymbol{z}}, \boldsymbol{a}')$ plane.

Similarly to Saintillan & Shelley [73], we assume without loss of generality that $\boldsymbol{k}$ lies in this plane and define θ as the angle between $\boldsymbol{k}$ and $\hat{\boldsymbol{z}}$: $\boldsymbol{k} = k(\cos\theta\,\hat{\boldsymbol{z}} + \sin\theta\,\boldsymbol{a}'/a')$

(where $a' = |\boldsymbol{a}'|$). Assuming this form for the wave-vector, the concentration equation (6.26) becomes

$$\lambda c' = -i\,k\,a'\,\sin\theta, \tag{6.36}$$

where $\lambda = s + ik\cos\theta$. We may also derive expressions for the components of velocity; conservation of momentum (6.33) gives

$$\begin{aligned}
&\left[\left(1+\frac{2\phi\alpha_3\cos^2\theta}{\mu}\right)u_a - \frac{\phi u_z \sin 2\theta}{\mu}\left(2\alpha_2\cos^2\theta+\alpha_3\right)\right]\frac{\boldsymbol{a}'}{a'} \\
&+\left[\left(1+\frac{2\phi\alpha_3\cos^2\theta}{\mu}\right)+\frac{2\phi}{\mu}\left(2\alpha_2\cos^2\theta+\alpha_3\right)\left(1-\cos^2\theta\right)\right]u_z\hat{\boldsymbol{z}} \\
&=\frac{i\alpha_1}{\mu k}\left[\left(a'\cos\theta\cos 2\theta - c'\sin\theta\cos^2\theta\right)\frac{\boldsymbol{a}'}{a'} + \left(-a'\sin\theta\cos 2\theta - c'\cos\theta\sin^2\theta\right)\hat{\boldsymbol{z}}\right],
\end{aligned} \tag{6.37}$$

where u_a and u_z are the $\boldsymbol{a}'/a'$ and $\hat{\boldsymbol{z}}$ components of velocity respectively. Combining the $\hat{\boldsymbol{z}}$ component of equation (6.37) with equation (6.36), to eliminate c', gives

$$\lambda u_z' = \frac{i\alpha_1 a'}{k(\mu+2A_1)}\left(-\lambda\sin\theta\cos 2\theta - \frac{ik}{2}\sin 2\theta\sin^2\theta\right), \tag{6.38}$$

where $A_1 = \phi(2\alpha_2\cos^2\theta+\alpha_3)$. The $\boldsymbol{a}'/a'$ component of equation (6.37) gives

$$(\mu+2A_2)\,\lambda u_a - A_1\lambda u_z\sin 2\theta = \frac{i\alpha_1 a'}{k}\left(\lambda\cos\theta\cos 2\theta + \frac{ik}{4}\sin^2 2\theta\right), \tag{6.39}$$

where $A_2 = \phi\alpha_3\cos^2\theta$. Substituting u_z from equation (6.38) into equation (6.39) gives the a' component of velocity

$$\lambda u_a' = \frac{i\alpha_1(\mu+2A_1\cos^2\theta)a'}{k(\mu+2A_1)(\mu+2A_2)}\left(\lambda\cos\theta\cos 2\theta + \frac{ik\sin^2 2\theta}{4}\right). \tag{6.40}$$

Finally, the evolution equation for $\boldsymbol{a}'(\boldsymbol{k})$ is found by substituting the rate-of-strain and

vorticity tensors into equation (6.22), to give

$$\lambda a' = \frac{i}{2}\left((\alpha_0+1)\,u_a k_z + (\alpha_0-1)\,u_z k_a\right). \tag{6.41}$$

Substitution of the velocity components (6.38) and (6.40) leads to the dispersion relation

$$\lambda^2 + \frac{\alpha_1}{2}\left(A_3\,(\alpha_0+1)\cos^2\theta - A_4\,(\alpha_0-1)\sin^2\theta\right)\left(\lambda\cos 2\theta + \frac{ik}{2}\sin\theta\sin 2\theta\right) = 0, \tag{6.42}$$

where

$$A_3 = \frac{\mu + 2A_1\cos^2\theta}{(\mu+2A_1)(\mu+2A_2)} = \frac{\mu + 2\phi\cos^2\theta(2\alpha_2\cos^2\theta+\alpha_3)}{(\mu+2\phi(2\alpha_2\cos^2\theta+\alpha_3))(\mu+2\phi\alpha_3\cos^2\theta)}, \tag{6.43}$$

$$A_4 = \frac{1}{\mu+2A_1} = \frac{1}{\mu+2\phi(2\alpha_2\cos^2\theta+\alpha_3)}. \tag{6.44}$$

This is an eigenvalue problem for the growth rate s (via λ), the solution for which is obtained as

$$\lambda_\pm = \frac{1}{2}f(\theta)\cos 2\theta\left[1 \pm \left(1 + \frac{2ik\sin\theta\sin 2\theta}{f(\theta)\cos^2 2\theta}\right)^{1/2}\right], \tag{6.45}$$

$$s_\pm = \frac{1}{2}f(\theta)\cos 2\theta\left[1 \pm \left(1 + \frac{2ik\sin\theta\sin 2\theta}{f(\theta)\cos^2 2\theta}\right)^{1/2}\right] - ik\cos\theta, \tag{6.46}$$

where

$$f(\theta) = -\frac{\alpha_1}{2}\left(A_3(\alpha_0+1)\cos^2\theta - A_4(\alpha_0-1)\sin^2\theta\right). \tag{6.47}$$

As the volume fraction (ϕ) only appears in front of the anisotropic terms in equation (6.29), the solution of the eigenvalue problem derived by Saintillan & Shelley [72] is recovered by setting $\phi = 0$.

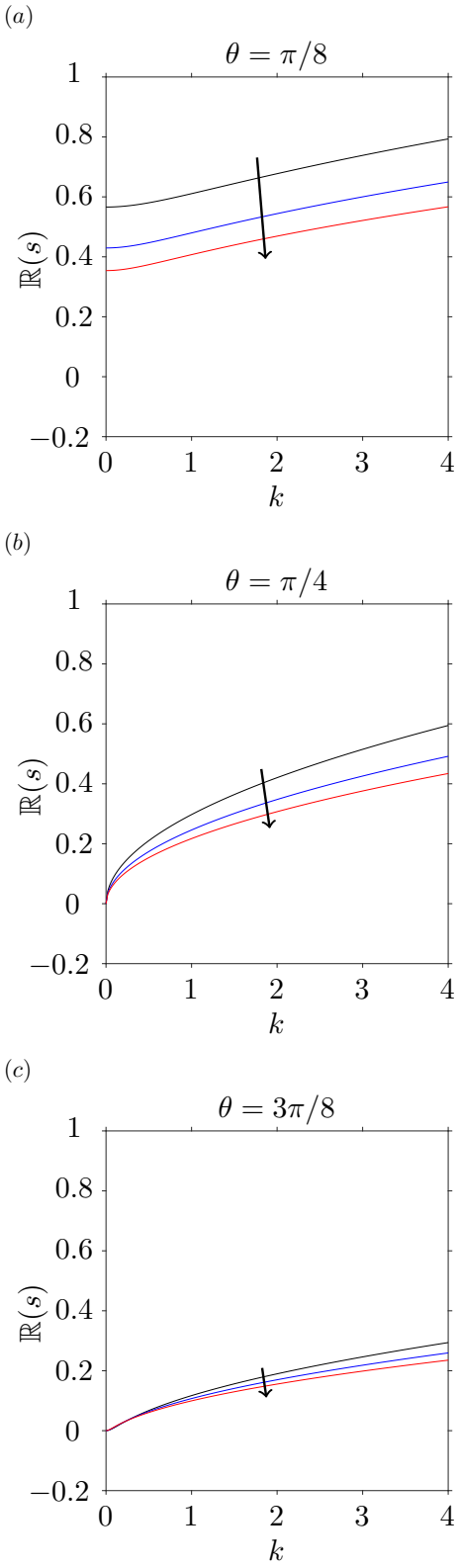

Figure 6.3: The real part of the growth rate ($\mathbb{R}(s)$) for changes in the volume fraction $\phi = 0, 0.1, 0.2$, where the arrow indicates the direction of increase, shape parameter $\alpha_0 = 0.85$ and wave direction (a) $\theta = \pi/8$, (b) $\theta = \pi/4$ and (c) $\theta = 3\pi/8$.

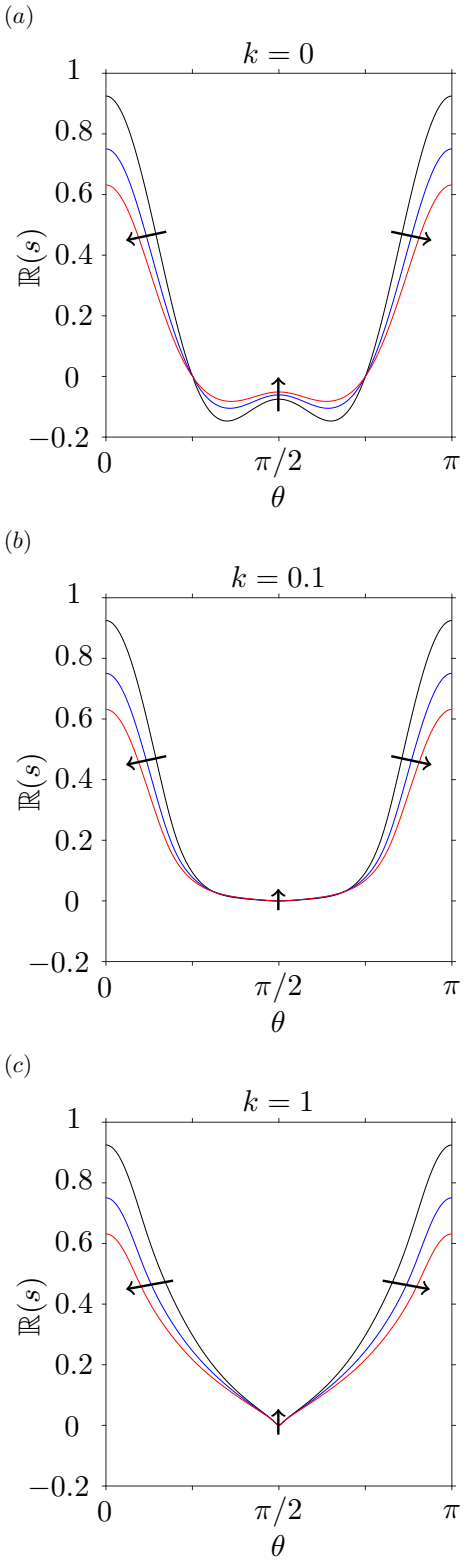

Figure 6.4: The real part of the growth rate ($\mathbb{R}(s)$) for changes in the volume fraction $\phi = 0, 0.1, 0.2$, where the arrow indicates the direction of increase, shape parameter $\alpha_0 = 0.85$ and wave magnitude (a) $k = 0$, (b) $k = 0.1$ and (c) $k = 1$.

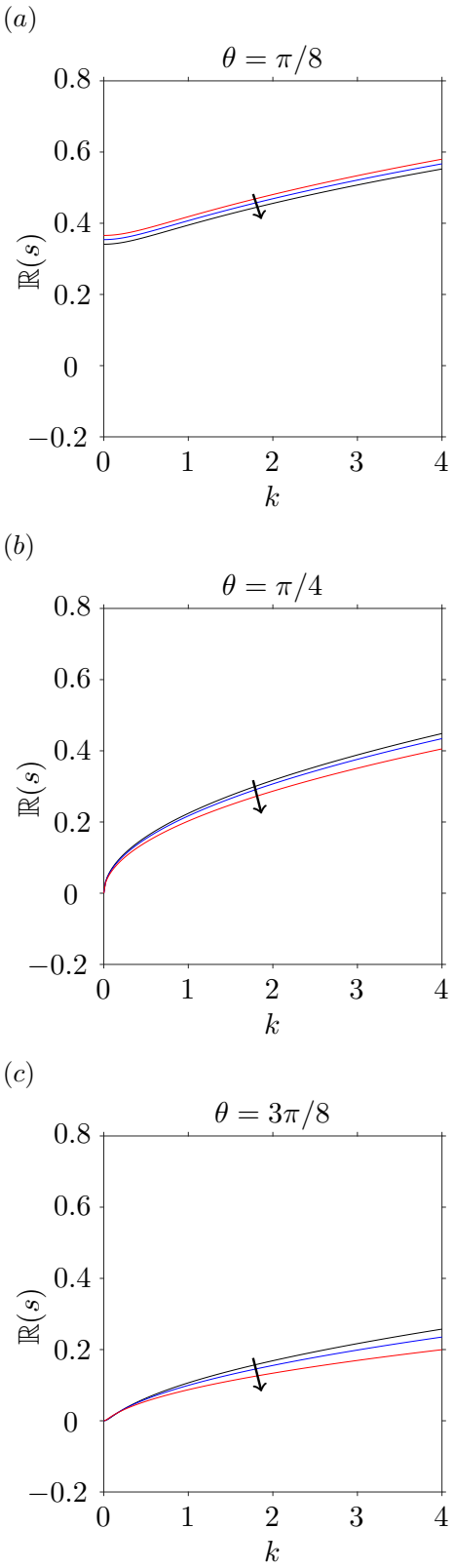

Figure 6.5: The real part of the growth rate ($\mathbb{R}(s)$) for changes in the shape parameter $\alpha_0 = 0.75, 0.85, 0.95$, where the arrow indicates the direction of increase, volume fraction $\phi = 0.1$ and wave magnitude (a) $k = 0$, (b) $k = 0.1$ and (c) $k = 1$.

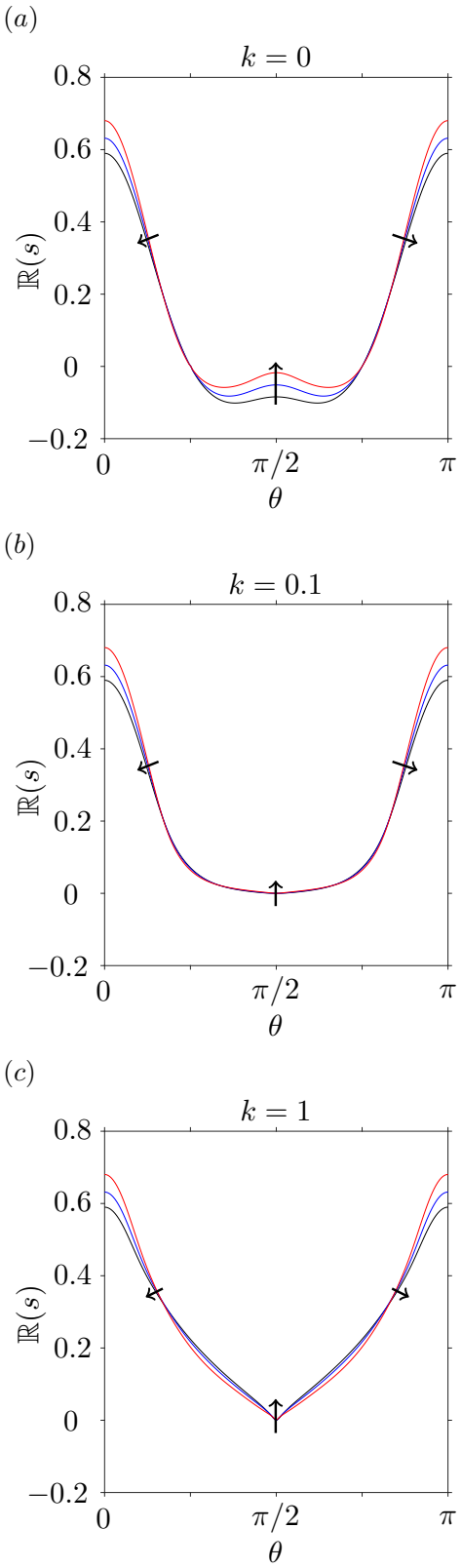

Figure 6.6: The real part of the growth rate ($\mathbb{R}(s)$) for changes in the shape parameter $\alpha_0 = 0.75, 0.85, 0.95$, where the arrow indicates the direction of increase, volume fraction $\phi = 0.1$ and wave direction (a) $\theta = \pi/8$, (b) $\theta = \pi/4$ and (c) $\theta = 3\pi/8$.

6.3.4 Results

For $k > 0$ we observe in Figure 6.3 there is always a positive growth rate; therefore, aligned suspensions are always unstable to concentration and orientation perturbations. This agrees with the results presented by Saintillan & Shelley [72, 73] which correspond to $\phi = 0$ (the black line in Figures 6.3-6.4). However, we predict the perturbations will grow more slowly as the volume fraction of particles is increased. This theory predicts the growth rate will increase with k, however if diffusion were included it would dampen and stabilize high-wave-number fluctuations [73]. From Figure 6.4 we note the largest change to the growth rate, with respect to change in volume fraction, occurs when the wave angle $\theta \in [0, \pi/8]$, and the least for $\theta = \pi/4$. Therefore the inclusion of the extra stress $\boldsymbol{\sigma}^P$ has the greatest effect when the wave acts in a similar direction to the alignment of the fibres.

From Figures 6.5 and 6.6 we identify that changes in the shape parameter α_0 have only a small effect on the predicted growth rates. A schematic diagram showing the difference between the particle shapes $\alpha_0 = 0.75, 0.85, 0.95$ is shown in Figure 6.1.

6.4 Linear stability of an isotropic suspension

We now examine how a suspension of particles, which are randomly orientated, behave when they are perturbed; to do this we perturb a uniform isotropic steady state where the background fluid is stationary:

$$\boldsymbol{u} = \varepsilon \boldsymbol{u}^{(1)}(\boldsymbol{x}, \hat{\boldsymbol{p}}, t), \qquad N = \frac{1}{4\pi}\left[1 + \varepsilon N^{(1)}(\boldsymbol{x}, \hat{\boldsymbol{p}}, t)\right]. \tag{6.48}$$

6.4.1 Linear stability analysis

When the perturbation (6.48) is adopted, the flux velocities (equations (6.7) and (6.8)) become

$$\boldsymbol{U} = \hat{\boldsymbol{p}} + \varepsilon \boldsymbol{u}^{(1)}, \tag{6.49}$$

$$\boldsymbol{\Omega} = (\boldsymbol{I} - \hat{\boldsymbol{p}}\,\hat{\boldsymbol{p}}) \cdot \left[\alpha_0 \varepsilon \left(\boldsymbol{e}^{(1)} + \boldsymbol{\omega}^{(1)} \right) \cdot \hat{\boldsymbol{p}} \right], \tag{6.50}$$

where $\boldsymbol{e}^{(1)} = (\boldsymbol{\nabla}_{\boldsymbol{x}} \boldsymbol{u}^{(1)} + \boldsymbol{\nabla}_{\boldsymbol{x}} \boldsymbol{u}^{(1)T})/2$ is the rate-of-strain tensor and $\boldsymbol{\omega}^{(1)} = (\boldsymbol{\nabla}_{\boldsymbol{x}} \boldsymbol{u}^{(1)} - \boldsymbol{\nabla}_{\boldsymbol{x}} \boldsymbol{u}^{(1)T})/2$ is the vorticity tensor, at order ε. The translational velocity of the particle may be simplified by evaluating $\langle \hat{\boldsymbol{p}} \rangle^{(0)}$, $\langle \hat{\boldsymbol{p}}\,\hat{\boldsymbol{p}} \rangle^{(0)}$ and $c^{(0)}$. The first moment of $\hat{\boldsymbol{p}}$ is given by

$$\langle \hat{\boldsymbol{p}} \rangle^{(0)} = \frac{1}{4\pi} \int_S \hat{\boldsymbol{p}}\, \mathrm{d}\hat{\boldsymbol{p}}. \tag{6.51}$$

Writing the particle director in spherical coordinates, $\hat{\boldsymbol{p}} = (\sin\theta\cos\chi, \sin\theta\sin\chi, \cos\theta)$, $\chi \in [0, 2\pi)$ and $\theta \in [0, \pi]$,

$$\begin{aligned} \frac{1}{4\pi} \int_S \hat{\boldsymbol{p}}\, \mathrm{d}\hat{\boldsymbol{p}} =& \frac{1}{4\pi} \int_{\chi=0}^{\pi} \int_{\theta=0}^{2\pi} (\sin\theta\cos\chi, \sin\theta\sin\chi, \cos\theta)\, \mathrm{d}\theta\, \mathrm{d}\chi, \\ &= \frac{1}{4\pi} \int_{\chi=0}^{\pi} \left(\left[-\cos\theta\cos\chi \right]_{\theta=0}^{2\pi}, \left[-\cos\theta\cos\chi \right]_{\theta=0}^{2\pi}, \left[\sin\theta \right]_{\theta=0}^{2\pi} \right) \mathrm{d}\chi, \\ &= \boldsymbol{0}. \end{aligned} \tag{6.52}$$

To calculate the second moment of $\hat{\boldsymbol{p}}$ notice the integral is isotropic, *i.e.* there are no special directions involved either in the domain of integration or in the integrand [79], to give

$$\langle \hat{\boldsymbol{p}}\,\hat{\boldsymbol{p}} \rangle^{(0)} = \frac{1}{4\pi} \int_S \hat{\boldsymbol{p}}\,\hat{\boldsymbol{p}}\, \mathrm{d}\hat{\boldsymbol{p}} = \lambda \boldsymbol{I}, \tag{6.53}$$

where λ is a constant that must be found. Writing equation (6.53) in index notation

$$\frac{1}{4\pi}\int_S \hat{p}_i\hat{p}_j \,\mathrm{d}\hat{\boldsymbol{p}} = \lambda\delta_{ij}. \tag{6.54}$$

Using the summation convention $\hat{p}_i\hat{p}_i = 1$ (since $\hat{\boldsymbol{p}}$ is a unit vector) and $\delta_{ii} = 3$ (as we are working in Cartesian space with three dimensions),

$$\lambda = \frac{1}{12\pi}\int_S \mathrm{d}\hat{\boldsymbol{p}} = \frac{1}{3}. \tag{6.55}$$

The second moment of $\hat{\boldsymbol{p}}$, to leading order, is therefore

$$\langle \hat{\boldsymbol{p}}\,\hat{\boldsymbol{p}}\rangle^{(0)} = \frac{\boldsymbol{I}}{3}. \tag{6.56}$$

Substituting the flux velocities (6.49) and (6.50) into the Fokker-Planck equation (6.6) gives

$$\begin{aligned}\frac{1}{4\pi}\frac{\partial}{\partial t}\left(1+\varepsilon N^{(1)}\right) = &-\frac{1}{4\pi}\boldsymbol{\nabla}_{\boldsymbol{x}}\cdot\left[\left(\hat{\boldsymbol{p}}+\varepsilon\boldsymbol{u}^{(1)}\right)\left(1+\varepsilon N^{(1)}\right)\right]\\ &-\frac{1}{4\pi}\boldsymbol{\nabla}_{\boldsymbol{p}}\cdot\left[(\boldsymbol{I}-\hat{\boldsymbol{p}}\,\hat{\boldsymbol{p}})\cdot\left(\alpha_0\boldsymbol{e}^{(1)}+\boldsymbol{\omega}^{(1)}\right)\cdot\hat{\boldsymbol{p}}\left(1+\varepsilon N^{(1)}\right)\right].\end{aligned} \tag{6.57}$$

Equation (6.57) may be simplified by noting the rate-of-strain and vorticity tensors are zero at leading order and the fluid is incompressible,

$$\frac{\partial N^{(1)}}{\partial t} = -\boldsymbol{\nabla}_{\boldsymbol{x}}\cdot\left(\hat{\boldsymbol{p}}N^{(1)}\right) - \boldsymbol{\nabla}_{\boldsymbol{p}}\cdot\left[(\boldsymbol{I}-\hat{\boldsymbol{p}}\,\hat{\boldsymbol{p}})\cdot\left(\alpha_0\boldsymbol{e}^{(1)}+\boldsymbol{\omega}^{(1)}\right)\cdot\hat{\boldsymbol{p}}\right]. \tag{6.58}$$

The final term of equation (6.58) may be simplified further, to see this we use index notation

$$\boldsymbol{\nabla}_{\boldsymbol{p}} \cdot \left[(\boldsymbol{I} - \hat{\boldsymbol{p}}\,\hat{\boldsymbol{p}}) \cdot \left(\alpha_0 \boldsymbol{e}^{(1)} + \boldsymbol{\omega}^{(1)} \right) \cdot \hat{\boldsymbol{p}} \right] = \frac{\partial}{\partial \hat{p}_i} \left[\left(\delta_{ij} - \hat{p}_i\,\hat{p}_j \right) \left(\alpha_0 e^{(1)}_{jk} + \omega^{(1)}_{jk} \right) p_k \right],$$
$$= - \left(\alpha_0 e^{(1)}_{ik} + \omega^{(1)}_{ik} \right) \frac{\partial \hat{p}_k}{\partial \hat{p}_i} + \alpha_0 e^{(1)}_{jk} \frac{\partial}{\partial \hat{p}_i} \left(\hat{p}_i \hat{p}_j \hat{p}_k \right) + \frac{\partial}{\partial p_i} \left(\hat{p}_i \left[\hat{p}_j \hat{p}_k \omega^{(1)}_{jk} \right] \right). \tag{6.59}$$

The first term in equation (6.59) is zero due to the incompressibility condition (6.12) and also that the vorticity tensor is traceless, *i.e.*

$$\left(\alpha_0 e^{(1)}_{ik} + \omega^{(1)}_{ik} \right) \frac{\partial \hat{p}_k}{\partial \hat{p}_i} = \left(\alpha_0 e^{(1)}_{ik} + \omega^{(1)}_{ik} \right) \delta_{ki}, \tag{6.60}$$
$$= \alpha_0 e^{(1)}_{ii} + \omega^{(1)}_{ii}, \tag{6.61}$$
$$= \alpha_0 \frac{\partial u^{(1)}_i}{\partial x_i} + \frac{1}{2} \left(\frac{\partial u^{(1)}_i}{\partial x_i} - \frac{\partial u^{(1)}_i}{\partial x_i} \right), \tag{6.62}$$
$$= 0. \tag{6.63}$$

The final term is also zero, to see this we write the vorticity tensor in terms of velocity gradients and simplify:

$$2 \hat{p}_j \hat{p}_k \omega_{jk} = \frac{\partial u^{(1)}_j}{\partial x_k} \hat{p}_j \hat{p}_k - \frac{\partial u^{(1)}_k}{\partial x_j} \hat{p}_j \hat{p}_k, \tag{6.64}$$
$$= \frac{\partial u^{(1)}_j}{\partial x_k} \hat{p}_j \hat{p}_k - \frac{\partial u^{(1)}_j}{\partial x_k} \hat{p}_k \hat{p}_j, \tag{6.65}$$
$$= 0. \tag{6.66}$$

Therefore equation (6.59) is given by

$$\boldsymbol{\nabla}_{\boldsymbol{p}} \cdot \left[(\boldsymbol{I} - \hat{\boldsymbol{p}}\,\hat{\boldsymbol{p}}) \cdot \left(\alpha_0 \boldsymbol{e}^{(1)} + \boldsymbol{\omega}^{(1)} \right) \cdot \hat{\boldsymbol{p}} \right] = \alpha_0 e^{(1)}_{jk} \frac{\partial}{\partial \hat{p}_i} \left(\hat{p}_i \hat{p}_j \hat{p}_k \right),$$

$$= \alpha_0 e^{(1)}_{jk} \left[\hat{p}_i \hat{p}_j \delta_{ki} + \hat{p}_i \hat{p}_k \delta_{ji} + \hat{p}_j \hat{p}_k \delta_{ii} \right], \tag{6.67}$$

$$= \alpha_0 e^{(1)}_{jk} \left[\hat{p}_j \hat{p}_k + \hat{p}_j \hat{p}_k + 3 \hat{p}_j \hat{p}_k \right]$$

$$= 5\alpha_0 \boldsymbol{e}^{(1)} : \hat{\boldsymbol{p}}\,\hat{\boldsymbol{p}}. \tag{6.68}$$

Substituting equation (6.68) into equation (6.59) gives the first order Fokker-Planck equation

$$\frac{\partial N^{(1)}}{\partial t} = -\hat{\boldsymbol{p}} \cdot \boldsymbol{\nabla}_{\boldsymbol{x}} N^{(1)} + \underbrace{5\alpha_0 \hat{\boldsymbol{p}}\,\hat{\boldsymbol{p}} : \boldsymbol{e}^{(1)}}_{(*)}. \tag{6.69}$$

We note the final term $(*)$ differs from Saintillan & Shelley [73], due to an error made when calculating δ_{ii} in equation (6.67). We find $\delta_{ii} = 3$ not 1, as we sum over all indices in Cartesian space.

To calculate the constitutive equation for stress we must evaluate the fourth-order moment of $\hat{\boldsymbol{p}}$ at leading order; to do this we note the integral is isotropic and so must have the following form [23, 79]

$$P_{ijkl} = \langle \hat{p}_i \hat{p}_j \hat{p}_k \hat{p}_l \rangle^{(0)} = \lambda_1 \delta_{ij} \delta_{kl} + \lambda_2 \delta_{ik} \delta_{jl} + \lambda_3 \delta_{il} \delta_{jk}, \tag{6.70}$$

Furthermore, since $P_{ijkl} = P_{ikjl} = P_{iljk}$, we deduce that

$$\lambda_1 = \lambda_2 = \lambda_3 = \lambda^*. \tag{6.71}$$

Equation (6.70) is therefore given by

$$\langle \hat{p}_i \hat{p}_j \hat{p}_k \hat{p}_l \rangle^{(0)} = \lambda^* \left(\delta_{ij} \delta_{kl} + \delta_{ik} \delta_{jl} + \delta_{il} \delta_{jk} \right). \tag{6.72}$$

To evaluate this integral we utilise that $\hat{\boldsymbol{p}}$ is a unit vector and evaluate P_{iikl} to find λ^*

$$\langle \hat{p}_k \hat{p}_l \rangle^{(0)} = \lambda^* \left(\delta_{ii}\delta_{kl} + \delta_{ik}\delta_{il} + \delta_{il}\delta_{ik} \right). \tag{6.73}$$

Substituting for the known value for the second moment of $\hat{\boldsymbol{p}}$ (given in equation (6.56))

$$\lambda^* = \frac{1}{15}. \tag{6.74}$$

Using this value for λ^* we may evaluate

$$\boldsymbol{e}^{(1)} : \int_S \hat{\boldsymbol{p}}\,\hat{\boldsymbol{p}}\,\hat{\boldsymbol{p}}\,\hat{\boldsymbol{p}}\,\mathrm{d}\hat{\boldsymbol{p}} = \frac{e_{kl}}{15}\left(\delta_{ij}\delta_{kl} + \delta_{ik}\delta_{jl} + \delta_{il}\delta_{jk} \right), \tag{6.75}$$

which upon applying the incompressibility condition (6.12) gives

$$\boldsymbol{e}^{(1)} : \int_S \hat{\boldsymbol{p}}\,\hat{\boldsymbol{p}}\,\hat{\boldsymbol{p}}\,\hat{\boldsymbol{p}}\,\mathrm{d}\hat{\boldsymbol{p}} = \frac{2}{15}\boldsymbol{e}^{(1)}. \tag{6.76}$$

The flow velocity (6.12) becomes

$$\boldsymbol{\nabla}_{\boldsymbol{x}} \cdot \boldsymbol{u} = 0, \qquad -\tilde{\mu}\nabla^2_{\boldsymbol{x}}\boldsymbol{u}^{(1)} + \boldsymbol{\nabla}_{\boldsymbol{x}} p^{(1)} = \frac{\alpha_1}{4\pi}\int_S \left(\hat{\boldsymbol{p}}\,\hat{\boldsymbol{p}} - \frac{\boldsymbol{I}}{3} \right) N^{(1)}\,\mathrm{d}\hat{\boldsymbol{p}}, \tag{6.77}$$

where $\tilde{\mu} = 1 + 4\phi(2\alpha_2/15 + 2\alpha_3/3 + \alpha_4)$. We note equation (6.77) is identical to that presented by Saintillan & Shelley [72, 73] by setting $\phi = 0$ and $\delta_{ii} = 3$ not 1. An equation for pressure, which is independent of velocity, may be found by taking the divergence of equation (6.77)

$$-\tilde{\mu}\nabla^2_{\boldsymbol{x}}\left(\boldsymbol{\nabla}_{\boldsymbol{x}} \cdot \boldsymbol{u}^{(1)} \right) + \nabla^2_{\boldsymbol{x}} p^{(1)} = \boldsymbol{\nabla}_{\boldsymbol{x}} \cdot \boldsymbol{\sigma}^S, \tag{6.78}$$

where

$$\boldsymbol{\sigma}^S = \frac{\alpha_1}{4\pi}\int_S \left(\hat{\boldsymbol{p}}\,\hat{\boldsymbol{p}} - \frac{\boldsymbol{I}}{3} \right) N^{(1)}\,\mathrm{d}\hat{\boldsymbol{p}}. \tag{6.79}$$

Applying the incompressibility condition (6.12) yields

$$\nabla_{\boldsymbol{x}}^2 p^{(1)} = \boldsymbol{\nabla}_{\boldsymbol{x}} \cdot \boldsymbol{\sigma}^S. \tag{6.80}$$

6.4.2 Plane wave perturbations

Consider plane wave perturbations

$$N^{(1)} = \tilde{N}(\boldsymbol{k}, \hat{\boldsymbol{p}}) e^{i\boldsymbol{k}\cdot\boldsymbol{x}+st}, \qquad \boldsymbol{u}^{(1)} = \tilde{\boldsymbol{u}}(\boldsymbol{k}) e^{i\boldsymbol{k}\cdot\boldsymbol{x}+st}, \qquad p^{(1)} = \tilde{p}(\boldsymbol{k}) e^{i\boldsymbol{k}\cdot\boldsymbol{x}+st}, \tag{6.81}$$

where $\boldsymbol{k}$ is the wave vector and s is the growth rate.

A dispersion relation for the growth parameter s is derived by substituting the ansatz (6.81) into equations (6.77) and (6.80), eliminating the pressure $\tilde{p}$ and obtaining an eigenvalue relation. By noting this eigenvalue relation is invariant under rotation we choose $\hat{\boldsymbol{k}} = \hat{\boldsymbol{z}}$ without loss of generality, after evaluating the arising surface integrals we have [73]

$$\frac{5i\alpha_0\alpha_1}{4k\tilde{\mu}} \left[2\tilde{\lambda}^3 - \frac{4}{3}\tilde{\lambda} + \left(\tilde{\lambda}^4 - \tilde{\lambda}^2\right) \log\left(\frac{\tilde{\lambda}-1}{\tilde{\lambda}+1}\right) \right] = 1, \tag{6.82}$$

where $\tilde{\lambda} = -i\,s$ and $k = |k|$. A detailed derivation is shown in appendix E. Equation (6.82) is a dispersion relation for the growth rate s (via $\tilde{\lambda}$) and may be solved numerically using Newton's method.

6.4.3 Numerical method

We use Newton's method to solve for $\tilde{\lambda}$, and hence the growth parameter s, in equation (6.82). Convergence of this method is not guaranteed and is dependent on the initial guess, as shown in Figure 6.7; here each colour represents the root an initial guess will converge to, whilst the intensity of the colour describes how quickly the method converges to the root. To calculate the dispersion curves in Figures 6.8 and 6.9 we use a line of

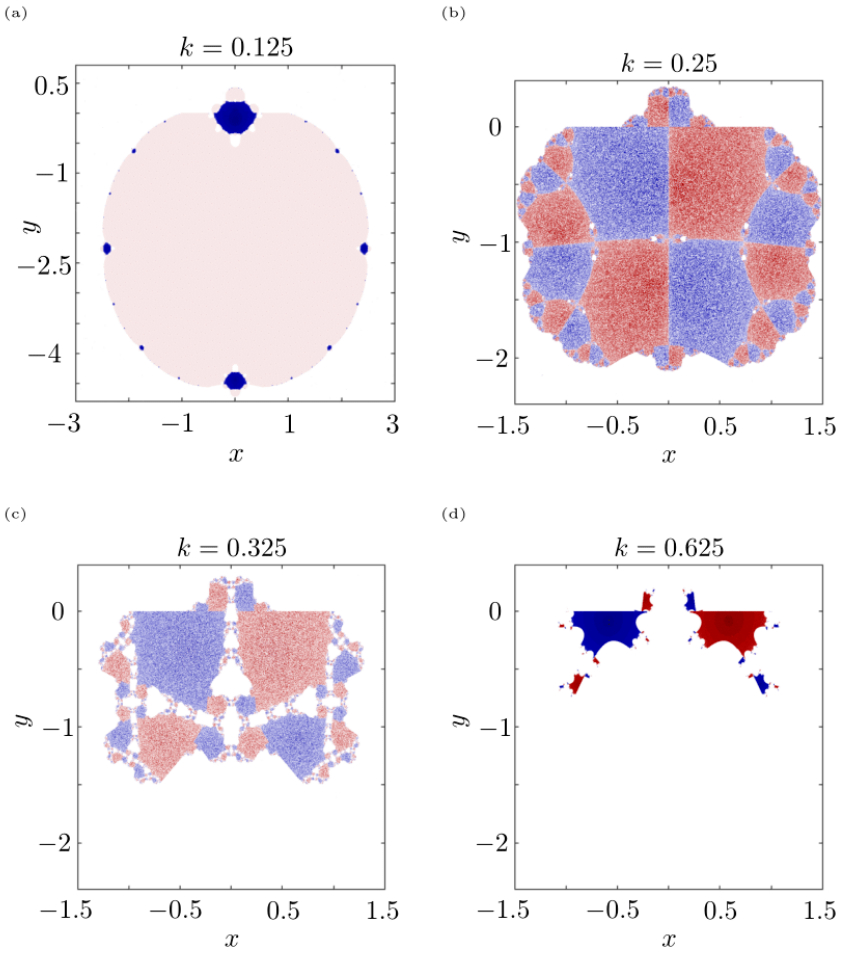

Figure 6.7: A visualisation of the convergence of Newton's method to find the roots of the nonlinear dispersion relation, where $\tilde{\lambda} = x + iy$. The darker the colour the faster the convergence, whilst each colour is a different root. Convergence for (a) $k = 1/8$, (b) $k = 1/4$, (c) $k = 3/8$ and (d) $k = 5/8$.

initial points such that $\mathbb{R}(\tilde{\lambda}) \in [-3, 3]$ and $\mathbb{I}(\tilde{\lambda}) = -0.25$.

6.4.4 Results

The long-wave behaviour of the dispersion relation may be found by expanding equation (6.82) for $|k| \ll 1$,

$$s^3 + \frac{\alpha_0 \alpha_1}{3\tilde{\mu}} s^2 - \frac{\alpha_0 \alpha_1 k^2}{7\tilde{\mu}} + \mathcal{O}\left(k^3\right) = 0. \tag{6.83}$$

Assuming the solution takes the form $s = s_0 + s_2 k^2 + \mathcal{O}(k^3)$ the long-wave solution of equation (6.82) is

$$s = -\frac{\alpha_0 \alpha_1}{3\tilde{\mu}} + \frac{9\tilde{\mu}}{7\alpha_0 \alpha_1} k^2 + \mathcal{O}\left(k^3\right), \tag{6.84}$$

along with the trivial solution $s = 0$; this agrees with the numerical results

Figure 6.8 and 6.9 show the real and imaginary parts of the growth parameter s, respectively, as a function of wave-number k for selected values of the shape parameter α_0 and volume fraction ϕ. We observe for small wave numbers the growth rate is real and positive when $\alpha_1 < 0$, therefore small wave-number disturbances will grow exponentially in suspensions of pushers. For higher wave-numbers the two branches of the growth parameter become a complex conjugate pair with $\mathbb{R}(s) > 0$ for $\alpha_1 < 0$, this implies that any disturbances will grow and also oscillate, when the particles in suspension are pushers. Pushers are cells which are pushed from behind and include most flagellated bacteria, e.g. *Escherichia coli* and *Bacillus subtilis* [50]. Once the real part of the growth parameter becomes zero, the dynamics are no longer described by an eigenfunction, and any disturbances become dampened for wave-numbers larger than this [73]. This is the behaviour observed by Saintillan & Shelley [72, 73]

As the volume fraction is increased the growth rate decreases for corresponding wave-numbers, but will oscillate more as the imaginary part of s increases. We observe that the plot of the dispersion relation takes the same form, becoming dampened as ϕ increases. This means a smaller range of wave-numbers will become unstable for each particle size.

6.5 Summary

In this chapter we have extended the work of Saintillan & Shelley [72, 73] to study how the inclusion of the stress between elongated particles and the solvent fluid affects the linear stability of aligned and isotropic suspensions of elongated particles. Similarly to

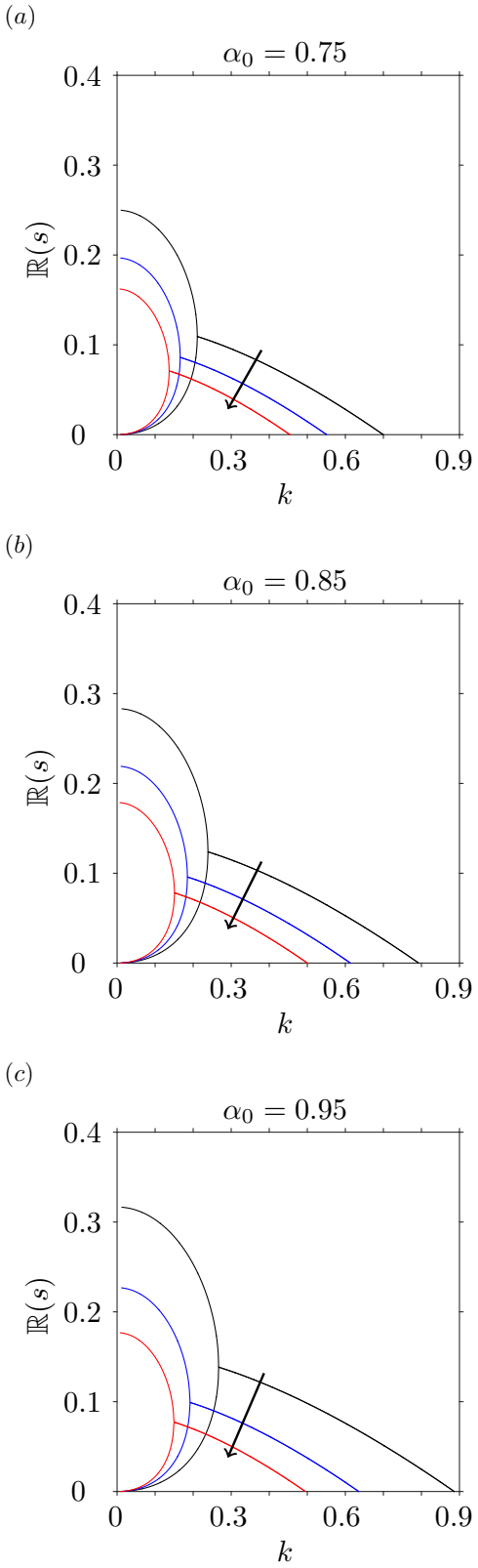

Figure 6.8: The real part of the dispersion relation for changing volume fraction $\phi = 0, 0.05, 0.1$, where the arrow shows the direction of increase, for fixed shape parameters (a) $\alpha_0 = 0.75$, (b) $\alpha_0 = 0.85$, (c) $\alpha_0 = 0.95$.

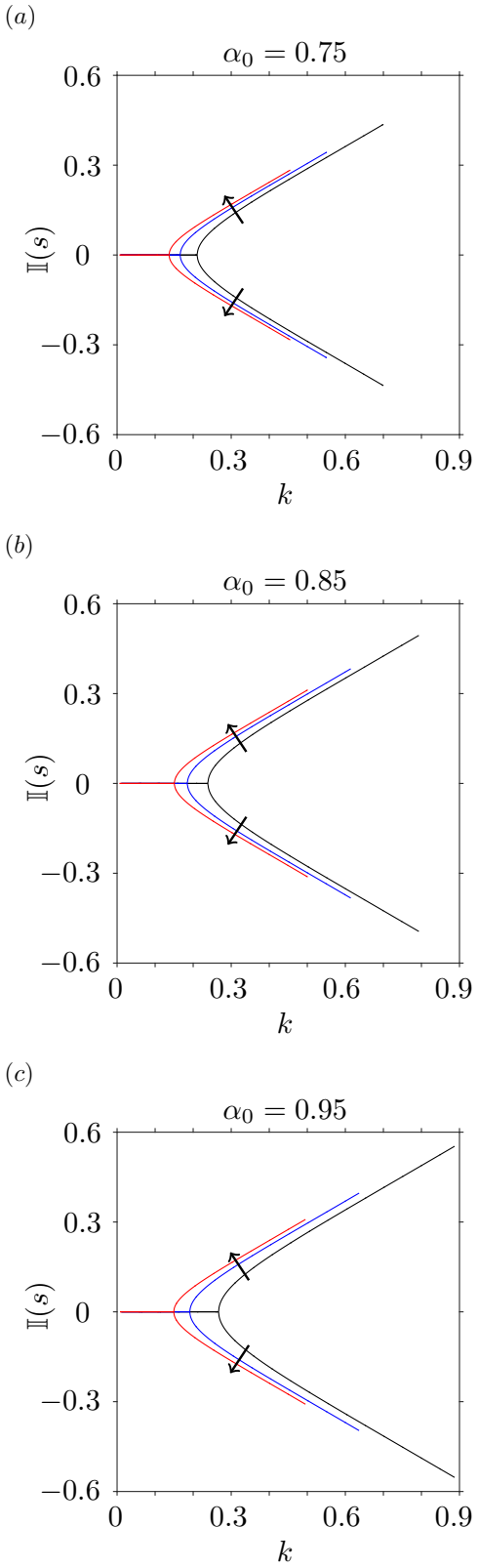

Figure 6.9: The imaginary part of the dispersion relation for changing volume fraction $\phi = 0, 0.05, 0.1$, where the arrow shows the direction of increase, for fixed shape parameters (a) $\alpha_0 = 0.75$, (b) $\alpha_0 = 0.85$, (c) $\alpha_0 = 0.95$.

Saintillan & Shelley [72, 73] we adopt the Fokker-Planck equation to model the particle distribution function, which describes the probability a particle at point $\boldsymbol{x}$ is directed in direction $\hat{\boldsymbol{p}}$, using phenomenological arguments for the translational and rotational flux velocities. We couple this equation to a pair of modified Stokes equations, where we utilise the constitutive relation for stress proposed by Pedley & Kessler [65]. This relation for stress consists of three components, the isotropic and active components were included in the model adopted by Saintillan & Shelley, however they neglect the anisotropic stress generated due to the interactions between elongated particles and the surrounding fluid. The active component arises by considering the addition to the bulk stress caused by force-free Stokesian swimmers. This gives rise to the active stresslet strength, α_1, which is positive when the swimmer is a *'puller'* (cells which are pulled forward, e.g. the biflagellated algae *Chlamydomonas* [50]) and negative when it is a *'pusher'* such as the bacteria *Escherichia coli* or *Bacillus subtilis* [50].

We examined the linear stability of the active suspension in two special cases; the first when the particles are uniformly distributed and perfectly aligned, and the second when the particles are completely randomly orientated (an isotropic suspension). We find, in both cases, the results of Saintillan & Shelley [72, 73] are a limit of the model we use, corresponding to zero volume fraction in our model (subject to an error in their calculation).

To investigate the linear stability of an aligned suspension we first found a base state when the particle distribution function is a delta function and the surrounding fluid is stationary. We showed in chapter 5 this corresponds to Ericksen's model for a transversely isotropic fluid. We then assume the perturbation to the base state is of the form of a plane wave, and note the first order velocity is only non-zero when the wave-vector lies in the $(\hat{\boldsymbol{z}}, \boldsymbol{a}')$-plane. Here $\hat{\boldsymbol{z}}$ is the direction of the base state alignment whilst $\boldsymbol{a}'$ is the alignment of the first order perturbation. This allows us to find the dispersion relation in terms of the wave-angle θ and wave-number k, where the wave-vector is given by $\boldsymbol{k} = k(\cos\theta\hat{\boldsymbol{z}} + \sin\theta\boldsymbol{a}'/a')$. Using the dispersion relation we identify perturbations are

unstable for suspensions of both pusher and puller particles. Similarly to Saintillan & Shelley [72, 73] we predict an increase in growth rate with wave-number, so the most unstable wave-number is the largest. However, it should be expected diffusion would dampen these high wave-number fluctuations if it was included. When the extra stress between elongated particles and the fluid is included, we find the condition upon when instability occurs remains unchanged, however we do predict smaller growth rates for corresponding wave-number as the volume fraction of particles is increased.

When the suspension is initially randomly orientated, termed isotropic, the base state corresponds to a constant particle distribution function and zero fluid velocity. This leads to isotropic integrals for the first, second and fourth moments of the distribution function, which may be evaluated analytically. Hence, by following a similar method to Saintillan & Shelley [72, 73] we ascertain a dispersion relation for the growth rate. We find, for a suspension of pushers, low wave number perturbations ($k \in [0, 0.15]$) grow exponentially with no oscillations, whilst medium wave-number ($k \in [0.15, 0.6]$) perturbations oscillate and grow more slowly. Once the wave-number is large enough perturbations are dampened. The inclusion of the extra stress due to interactions between elongated particles and the surrounding fluid simply decreases the growth rate for corresponding wave-numbers as the volume fraction of particles is increased. This leads to a smaller range of wave-numbers when the perturbation is unstable.

In this chapter we adopt the governing equations of Simha and Ramaswamy [76], where we include the transversely-isotropic effects identified by Batchelor [6]. We follow the analysis of Saintillan and Shelley [73] to determine the linear stability of both nearly aligned and isotropic suspensions of particles. The linear stability analysis we carry out has not been completed before, and therefore the understanding of the effect of the anisotropic parameters μ_2 and μ_3 on the stability characteristics of the fluid is novel. However, we note in the case of the isotropic suspension the anisotropic viscosities may be combined with the isotropic component of viscosity μ, and therefore the subsequent linear stability analysis does not differ from that performed by Saintillan and Shelley [73].

In future work we will consider the numerical solution to the full nonlinear model. This will allow the extra nonlinear terms in the stress tensor to be expressed as well as allowing us to introduce a more realistic confined geometry. The model we adopt is also only valid when direct interactions between the particles are negligible, and occur through the fluid velocity only. We would like to incorporate direct interactions between the particles that allow us to study a more concentrated suspension.

CHAPTER 7

CONCLUSIONS

In this thesis we have discussed both transversely isotropic passive and active fluids, with a particular focus on suspensions of elongated particles. In this chapter we summarise our results, discuss the impact our work has on current research and real-world applications, concluding with some further work which could be carried out.

In chapters 2 and 5 we present models for transversely isotropic and active fluids respectively, identifying the fundamental connection between these two models in chapter 5. Throughout we have applied our findings to suspensions of elongated particles/fibres, such as solutions of DNA and sperm, highlighting the importance of understanding the behaviour of the models we have adopted. In chapters 3 and 4 we examined the linear stability of the Taylor-Couette and Rayleigh-Bénard flow of a transversely isotropic fluid respectively; here we interpreted our results in the framework of passive suspensions of fibres such as DNA and other large biomolecules in suspension. In chapter 6 we investigated the linear stability of aligned and isotropic suspensions of active elongated particles; this has applications to self-propelling bacteria, and other micro-organisms, which are are known to exhibit collective behaviour.

7.1 Summary of findings

In chapter 2 we introduce Ericksen's model for a transversely isotropic fluid, this is the simplest model of a transversely isotropic fluid where the constitutive relation for stress is linear in strain rate and has all the required invariances. This model allows us to treat suspensions of elongated particles/fibres as a continuum with an evolving preferred direction ($\boldsymbol{a}$), through a modified stress tensor incorporating four viscosity-like parameters. We show the parameters may be interpreted physically as the isotropic component of viscosity modified by the volume fraction of fibres (μ^*), an active component (μ_1^*) and also anisotropic extensional (μ_2^*) and shear (μ_3^*) viscosities. Due to uncertainty in the parameter values we have examined a large range of parameters when presenting our results in chapters 3 and 4.

In chapter 3 we investigated the linear Taylor-Couette stability of a transversely isotropic fluid. This was motivated by applications to flow linear dichroism, an experimental technique used to determine the structure of biological molecules, particularly useful for molecules which have a high aspect ratio.

We adopted the model proposed in chapter 2 and closed it with appropriate boundary conditions; these conditions were the inner cylinder rotates whilst the outer remains fixed. Non-dimensionalising the model led to the introduction of five non-dimensional parameter groups, these were the gap ratio of the inner to outer cylinder radii η; a non-dimensional rotational velocity of the inner cylinder Ω, equivalent to a Reynolds number; a ratio of the tension in the fibres to the transverse shear viscosity μ_1; and the ratios of the extensional and shear viscosities in the fibre direction to the transverse shear viscosity, μ_2 and μ_3 respectively.

After non-dimensionalising the model, we found a steady state where the velocity profile differs from the Newtonian case only by a constant factor, due to the presence of fibres in the solution, and the fibres are aligned in the azimuthal direction. Determining the stability of this regime is important to flow linear dichroism as a trade-off exists; as the flow velocity is increased, the fibres become more aligned due to shear and hence

flow linear dichroism signal will increase, however if the velocity becomes too high then instability will occur, and all signal will be destroyed.

Drawing parallels with existing research in to the linear Taylor-Couette stability of fluids [18, 19, 68, 85], we assumed the first instability to occur would be axisymmetric. This corresponds to the appearance of '*fluid doughnuts*' or '*fluid-rolls*'. Assuming this form for the perturbation, we found the first-order stability equations and assumed the solution could be expressed as normal modes; here a growth parameter (s) and wave-number (k) were introduced. The growth parameter indicates whether a perturbation will grow or decay exponentially in time, whilst the wave-number is related to the size of the fluid doughnuts that appear. After substituting the normal mode solutions into the first order equations it was clear the fibre direction was unperturbed, and the tension in the fibres μ_1 played no role in determining the stability of the perturbation (at this order). It is also interesting to note the enhancement to the extensional viscosity versus that perpendicular to the fibres ($\mu_2 + 4\mu_3$) appears in the governing equation for the radial velocity, while the shear viscosity of the fluid in the fibre direction appears in the governing equation for the azimuthal velocity.

Solving the resulting eigenvalue problem numerically, we determined the critical wave and Taylor numbers for a wide range of η, μ_2 and μ_3. The Taylor number relates the importance of inertial to viscous effects, and is proportional to angular velocity [46]. Through comparison of the critical values for different combinations of parameters η, μ_2 and μ_3, we identify some key results. The parameter μ_3, which describes the ratio of the shear viscosity in the fibre direction to the transverse shear viscosity, is much more important in determining the stability of the flow than μ_2, which describes the ratio of the extensional viscosity to the transverse shear viscosity. While our results agree with those of Wan and Lin [88] in the effect of μ_2, we find that μ_3 has a more significant effect and therefore must be included.

For values of the gap ratio less than 0.8, *i.e.* for a large gap width (relative to the outer cylinder's radius) between the cylinders, the critical angular velocity of the inner

cylinder is a decreasing function of the gap ratio. However for larger values of the gap ratio, *i.e.* a narrow gap width, the critical angular velocity increases as viscous effects dominate over the inertial effects giving rise to instability; more energy is then needed for the perturbation to become unstable.

These results have a direct impact on flow linear dichroism spectroscopy, in a Couette device. By considering the rheological changes induced by the presence of fibres, we showed that the critical angular velocity of the inner cylinder at the onset of instability is much higher than previously thought. Hence the maximum shear rate is also increased. Exploiting this understanding may enable stronger signals to be recovered from the use of flow linear dichroism Couette devices across a range of fibre types. Relating our results on the critical angular velocity to the strength of shear-induced alignment allows us to propose the dimensions of an optimal device design, related to the mechanical properties of the fibres. An optimal device design exists due to the trade-off between higher shear-induced alignment of fibres in a narrow gap, and higher amount of sample to interact with incident light in a wide gap.

In chapter 4 we investigate the linear Rayleigh-Bénard stability of a transversely isotropic fluid. This is a canonical example in traditional fluid mechanics for the stability analysis of viscous flows, investigation into this topic was motivated by the appearance of convection currents in fibrous materials, as well as temperature variations in Couette devices.

We first extended the equations proposed in chapter 2 to include variable density and temperature. To do this we made use of the Boussinesq approximation, where the variable density is modelled as a linear function of temperature. The model is closed with appropriate boundary conditions for velocity and temperature, consisting of two possible types of boundary: rigid and free.

By non-dimensionalising the model we formed five non-dimensional parameter groups. These are the Prandtl ($\mathcal{P}$) and Rayleigh numbers ($\mathcal{R}$), as well as the three viscosity-like parameters μ_1, μ_2 and μ_3 identified in the Taylor-Couette analysis. The Prandtl number

relates the kinematic viscosity of the fluid to its thermal conductivity, while the Rayleigh number relates the stabilising effects of the molecular diffusion of momentum to the destabilising effects of buoyancy.

We found a steady state exists when the fluid is stationary, the preferred direction of the fluid is constant and both density and temperature vary linearly with height z. Perturbing this state, and assuming the solution of the resulting first order equations may be represented by normal modes, the kinematic equation decouples from the governing equations for velocity and temperature, and so may be solved for separately, although it does not affect the stability problem.

The resulting system is solved for different combinations of the steady state preferred direction ($\theta^{(0)}$), μ_2 and μ_3. The parameter μ_3 is again more important in determining the stability of the flow than μ_2. The impact changes in $\theta^{(0)}$ have on the stability of the steady state velocity are dependent on both the boundary type and the anisotropic viscosities. For values of $\mu_3 \gtrsim 100$ the Rayleigh number's dependence on the steady state preferred direction is approximately $\cos 4\theta^{(0)}$. The amplitude of these fluctuations increases with μ_2, and while the dependence of the Rayleigh number on $\theta^{(0)}$ occurs for all combinations of boundaries, oscillations are greatest when both boundaries are free. Increasing the anisotropic shear viscosity does not have a large effect on the dependence of the Rayleigh number on the $\cos 4\theta^{(0)}$ mode, but does dampen higher modes that exist for small values of μ_3.

From our analysis we are also able to predict how the size of the convection cells changes with the non-dimensional parameters, this relates to changes in the dimensionless wave-number k. Fluctuations to the wave-number with $\theta^{(0)}$ only occur when $\mu_2 \neq 0$, with the dependence on $\theta^{(0)}$ being approximately $\cos 4\theta^{(0)}$. The amplitude of these fluctuations increases with μ_2, but is dampened much more quickly by increases in μ_3. For large values of μ_3 the wave-number is approximately the same as the Newtonian value, with little to no dependence on $\theta^{(0)}$.

We are therefore able to conclude the inclusion of fibrous material in a solvent fluid

changes the stability characteristics of the Rayleigh-Bénard problem significantly. The introduction of a preferred direction in the fluid changes both the onset of stability and the size of convection cells which occur, therefore the rheological effects induced by the presence of fibres must be taken into account.

In chapter 5 we introduce a model for active particle suspensions, originally proposed by Pedley & Kessler [65]. These suspensions may represent suspensions of self-propelling bacteria or other micro-organisms which exhibit phenomena such as collective behaviour and superfluidity. There are also technological applications of this type of suspension, such as collections of artificial swimmers.

Pedley & Kessler's [65] original application of their model was to near-spherical algae, in this case it is reasonable to assume the stress generated due to interactions between the fluid and particles will be small, justifying it's neglect [65]. However, this near-spherical limit of the model has also been used to give insight into the dynamics of elongated rod-like bacterial suspensions [72, 73, 82]. The stress due to interactions between elongated particles and fluid has been shown to have a significant effect on the system's emergent properties and flow stability within the transversely isotropic fluid research literature, as highlighted in chapters 2-4 and references [22, 23, 29]; these terms therefore seem likely to have implication for earlier analysis of the critical concentration threshold and wavelengths of emergent patterns in active suspensions [71, 73, 82, 83].

When the suspension is of spatially-uniform volume fraction and has perfect but perhaps spatially varying alignment, the active suspension model is equivalent to Ericksen's model of a transversely isotropic fluid. This highlights the important of the stress due to interactions between the fluid and elongated particles, commonly neglected in the current literature.

The transversely isotropic fluid of Ericksen may be used to model actively motile 'fibres' by a simple modification to the fibre evolution equation. Linking these two frameworks provides a basis to extend Ericksen's model to include effects such as dispersion about the preferred direction. Our modification to Ericksen's model can be considered

as the simplest describing an orientated active suspension and including transversely isotropic effects; more refined approaches take into account fibre-dispersion formulated via the Q-tensor which is defined as the nematic moment $\langle \hat{\boldsymbol{p}}\hat{\boldsymbol{p}} - \boldsymbol{I}/3 \rangle$ [12, 90].

In chapter 6 we adopt the governing equations proposed in chapter 5, for an active fluid, to examine the linear stability of isotropic and nearly-aligned suspensions of elongated particles. Studying these special cases provides preliminary information on the behaviour of full nonlinear simulations, and hence the underlying biological application.

To consider the linear stability of an aligned suspension we split the Fokker-Planck equation, governing the particle distribution, into two equations for the concentration and director fields of the particles. The governing equations, for an aligned suspension of active particles, therefore consisted of modified Navier-Stokes equations for the fluid velocity, where the constitutive relation for stress includes the isotropic, active, and fluid-particle interaction terms; coupled with equations for the concentration and director fields. The base state of these equations is given when the particles are perfectly aligned in the $\hat{\boldsymbol{z}}$ direction, the fluid is motionless, pressure is constant, and the dimensionless concentration $c = 1$. The stability of this steady state is examined by considering a perturbation to each of the independent variables.

Assuming the solution of the first order equations takes the form of plane waves, and identifying that the velocity is only non-zero if the wave-vector lies in the $(\boldsymbol{a}, \hat{\boldsymbol{z}})$-plane, we derive a dispersion relation for the growth rate s. This dispersion relation is identical to that of Saintillan & Shelley [73] when the parameter representing volume fraction of particles is set to zero in our model; this is equivalent to setting the extra particle stress to zero. The dispersion relation implies the suspension is unstable for both pusher and puller particles, this agrees with the findings of Saintillan & Shelley [73]. However, the extra stress does lead to smaller growth rates for corresponding wave-numbers as the volume fraction is increased, although the condition upon when instability occurs remains unchanged.

Next we considered the linear stability of a randomly-orientated (isotropic) suspension

of particles. The governing equations consisted of the full Fokker-Planck equation, coupled to the Cauchy momentum equations. A base state of these equations exists when the fluid is motionless and the non-dimensional particle distribution function is given by $N = 1/4\pi$. Perturbing the base state and assuming the solution may be expressed in terms of plane waves, we were able to derive a dispersion relation, which we solved using Newton's method.

We found for a suspension of pushers, low wave number perturbations grow exponentially with no oscillations, whilst medium wave-number perturbation oscillate and grow more slowly. Once the wave-number is large enough perturbations are dampened. The inclusion of the extra stress due to interactions between elongated particles and the surrounding fluid decreases the growth rate for corresponding wave-numbers as the volume fraction of particles is increased. This also leads to a smaller range of wave-numbers for which a perturbation is unstable.

For both aligned and isotropic suspensions, we have only considered when the suspension is dilute, as the parameter values are known in this case. It is likely that as the concentration of particles is increased the inclusion of the extra stress term will become more important.

7.2 Future work

To extend our analysis of the linear Taylor-Couette stability of a transversely isotropic fluid, we will consider the instability of a non-symmetric perturbation to the steady state, in addition to incorporating the dispersion of fibres about the average direction. We also aim to include the effect of entanglement between individual fibres and establish how this may change the stability of the flow. Studying the entanglement between fibres has applications to pathogen detection in flow linear dichroism, where proteins which bind to pathogens in a sample are attached to fibres, changing the degree of alignment of the fibres. The stability analysis undertaken to examine the linear Rayleigh-Bénard stability

of a transversely isotropic fluid may be extended similarly, as well as considering the full three-dimensional problem in a closed box. Incorporating active behaviour is also of interest.

We will examine how the inclusion of the anisotropic viscosities affects the solution of the full nonlinear model for an active suspensions of elongated particles. This will allow the extra nonlinear terms in the stress tensor to be expressed as well as allowing us to investigate different flow-regimes and introduce a more realistic confined geometry. In formulating the model for an active suspension, we have neglected interesting effects such as gravitational fields and temperature variations, which we aim to include in future. The model we adopt is also only valid when direct interactions between the particles are negligible, and interactions occur through the fluid velocity only. We would like to incorporate these direct interactions between the particles to allow us to study a more concentrated suspension. One of the key improvements we aim to make to both the transversely isotropic and active models is the identification of parameter values in a semi-dilute regime, this will allow more physically realistic results to be calculated using the continuum model we have described.

Transversely isotropic fluids and active suspensions are both ubiquitous within industrial and biological contexts, it is therefore important to gain a better understanding of the underlying mechanics of these fascinating states of matter. We hope the research carried out in this thesis provides new insight into this interesting and captivating area of research.

Appendices

APPENDIX A

BOUSSINESQ APPROXIMATION

This appendix follows Spiegel & Veronis [81] to determine the conditions under which a compressible fluid may be represented using the Boussinesq approximation.

A.1 Equations

The equations governing the thermal convection of a compressible Newtonian fluid are given by conservation of mass, momentum and energy statements:

$$\frac{\partial \rho^*}{\partial t^*} + (\boldsymbol{u}^* \cdot \boldsymbol{\nabla}_{\boldsymbol{x}}^*)\, \rho^* + \rho^* \left(\boldsymbol{\nabla}_{\boldsymbol{x}}^* \cdot \boldsymbol{u}^*\right) = 0, \tag{A.1}$$

$$\frac{\partial \boldsymbol{u}^*}{\partial t^*} + (\boldsymbol{u}^* \cdot \boldsymbol{\nabla}_{\boldsymbol{x}}^*)\, \boldsymbol{u}^* = -\frac{1}{\rho^*}\boldsymbol{\nabla}_{\boldsymbol{x}}^* p^* - g^* \hat{\boldsymbol{z}} + \frac{\bar{\mu}^*}{\rho^*}\nabla_x^{*2}\boldsymbol{u}^* + \frac{\bar{\mu}^*}{3\,\rho^*}\boldsymbol{\nabla}_{\boldsymbol{x}}^* \left(\boldsymbol{\nabla}_{\boldsymbol{x}}^* \cdot \boldsymbol{u}^*\right), \tag{A.2}$$

$$C_V^* \left[\frac{\partial T^*}{\partial t^*} + (\boldsymbol{u}^* \cdot \boldsymbol{\nabla}_{\boldsymbol{x}}^*)\, T^*\right] + \frac{p^*}{\rho^*}\left(\boldsymbol{\nabla}_{\boldsymbol{x}}^* \cdot \boldsymbol{u}^*\right) = \frac{\kappa_C^*}{\rho^*}\nabla_x^{*2} T^* + \frac{\bar{\mu}^*}{\rho^*}\boldsymbol{\nabla}_{\boldsymbol{x}}^* \cdot \left((\boldsymbol{u}^* \cdot \boldsymbol{\nabla}_{\boldsymbol{x}}^*)\, \boldsymbol{u}^*\right) - \frac{2\bar{\mu}^*}{3\rho^*}\left(\boldsymbol{\nabla}_{\boldsymbol{x}}^* \cdot \boldsymbol{u}^*\right)^2. \tag{A.3}$$

Here ρ^* is the variable density, t^* time, $\boldsymbol{u}^*$ velocity, $\boldsymbol{\nabla}_{\boldsymbol{x}}^*$ is the gradient operator in $\boldsymbol{x}^*$, p^* pressure, g^* acceleration due to gravity, $\hat{\boldsymbol{z}}$ the unit vector in the z-direction, $\bar{\mu}^*$ dynamic shear viscosity (assumed constant), C_V^* the specific heat capacity at constant volume, T^* temperature, κ_C^* the (constant) thermal conductivity and we neglect the radiation source

and viscous dissipation.

The equation of state for a homogeneous system is of the form

$$\rho^* = \rho^*(p^*, T^*), \tag{A.4}$$

i.e. the variable density relies on the pressure and temperature of the fluid only.

Let f^* represent any one of the state variables: density (ρ^*), temperature (T^*), or pressure (p^*). These may be expressed in terms of the constant space average f_0^* of f^*, the variation in the absence of motion $\bar{f}^*$, and the fluctuation resulting from motion $\tilde{f}^*$, *i.e.*

$$f(x^*, y^*, z^*, t^*)^* = f_0^* + \bar{f}^*(z^*) + \tilde{f}^*(x^*, y^*, z^*, t^*). \tag{A.5}$$

We assume f_0^* and $\bar{f}^*$ to be independent of t^* as the boundary conditions do not depend on time. We may also introduce the scale heights,

$$\bar{H}_f^* = \left| \frac{1}{f_0^*} \frac{\mathrm{d}\bar{f}^*}{\mathrm{d}z^*} \right|^{-1}. \tag{A.6}$$

We apply the basic approximation that the fluid is confined to a layer whose thickness, h^*, which is much less than the smallest scale height, $\bar{H}_f^*$. Therefore, throughout the fluid we have

$$h^* \ll \bar{H}^*. \tag{A.7}$$

where $\bar{H}^* = (\bar{H}_f^*)_{min}$. In particular this condition implies

$$\frac{h^*}{\bar{H}_\rho^*} \ll 1. \tag{A.8}$$

Integrating equation (A.8) across the level of minimum to the level of maximum density

within the layer gives

$$\frac{\Delta\rho_0^*}{\rho_0^*} \equiv \bar{\varepsilon} \ll 1, \tag{A.9}$$

where $\Delta\rho_0^*$ is the maximum variation of ρ_0^* accross the layer.

We Taylor expand equation (A.4) for ρ^* about $p^* = p_0^*$ and $T^* = T_0^*$ to give

$$\begin{aligned}\rho^* =& \rho^*\left(\rho_0^*, T_0^*\right) + \left[p^* - p_0^*\right]\frac{\partial\rho^*}{\partial p^*}\left(\rho_0^*, T_0^*\right) + \left[T^* - T_0^*\right]\frac{\partial\rho^*}{\partial T^*}\left(\rho_0^*, T_0^*\right) \\ &+ \frac{1}{2}\Bigg\{\left[p^* - p_0^*\right]^2\frac{\partial^2\rho^*}{\partial p^{*2}}\left(\rho_0^*, T_0^*\right) + 2\left[p^* - p_0^*\right]\left[T^* - T_0^*\right]\frac{\partial^2\rho^*}{\partial p^*\partial T^*}\left(\rho_0^*, T_0^*\right) \\ &+ \left[T^* - T_0^*\right]\frac{\partial^2\rho^*}{\partial T^{*2}}\left(\rho_0^*, T_0^*\right) + \cdots\Bigg\}\end{aligned} \tag{A.10}$$

Now denoting

$$\rho_0^* = \rho^*\left(\rho_0^*, T_0^*\right), \qquad K_0^* = \frac{1}{\rho_0^*}\frac{\partial\rho^*}{\partial p^*}\left(\rho_0^*, T_0^*\right), \qquad a_0^* = -\frac{1}{\rho_0^*}\frac{\partial\rho^*}{\partial T^*}\left(\rho_0^*, T_0^*\right), \tag{A.11}$$

and

$$\left(\frac{1}{\rho^*}\frac{\partial^2\rho^*}{\partial p^{*2}}\right)_0 = \frac{1}{\rho_0^*}\frac{\partial^2\rho^*}{\partial p^{*2}}\left(\rho_0^*, T_0^*\right) \qquad \text{etc.}, \tag{A.12}$$

equation (A.10) becomes

$$\begin{aligned}\rho^* =& \rho_0^*\Bigg\{1 + K_0^*\left(p^* - p_0^*\right) - a_0^*\left(T^* - T_0^*\right) + \frac{1}{2}\left(\frac{1}{\rho^*}\frac{\partial^2\rho^*}{\partial p^{*2}}\right)_0\left(p^* - p_0^*\right)^2 \\ &+ \left(\frac{1}{\rho^*}\frac{\partial^2\rho^*}{\partial p^*\partial T^*}\right)_0\left(p^* - p_0^*\right)\left(T^* - T_0^*\right) + \frac{1}{2}\left(\frac{1}{\rho^*}\frac{\partial^2\rho^*}{\partial T^{*2}}\right)_0\left(T^* - T_0^*\right)^2 + \cdots\Bigg\}.\end{aligned} \tag{A.13}$$

If the fluid is an ideal gas, *i.e.* we neglect the (usually) small corrections required by

variation in mean molecular weight and by the effect of the radiation pressure, then

$$\rho^* = \frac{p^*}{R^*\, T^*}, \tag{A.14}$$

where R^* is the ideal gas constant. Under this assumption, we have

$$\left(\frac{1}{\rho^*}\frac{\partial \rho^*}{\partial p^*}\right)_0 = \left(\frac{R^* T_0^*}{p_0^*}\right)\left(\frac{1}{R^* T_0^*}\right) = \frac{1}{p_0^*}, \tag{A.15}$$

$$-\left(\frac{1}{\rho^*}\frac{\partial \rho^*}{\partial T^*}\right)_0 = \left(\frac{R^* T_0^*}{p_0^*}\right)\left(\frac{p^*}{R^* T_0^{*2}}\right) = \frac{1}{T_0^*}, \tag{A.16}$$

$$\left(\frac{1}{\rho^*}\frac{\partial^2 \rho^*}{\partial p^{*2}}\right)_0 = 0, \tag{A.17}$$

$$\left(\frac{1}{\rho^*}\frac{\partial^2 \rho^*}{\partial T^{*2}}\right)_0 = \left(\frac{R^* T_0^*}{p_0^*}\right)\left(\frac{p_0^*}{R^* T_0^{*3}}\right) = \frac{1}{T_0^{*2}}, \tag{A.18}$$

$$\left(\frac{1}{\rho^*}\frac{\partial^2 \rho^*}{\partial p^* \partial T^*}\right)_0 = \left(\frac{R^* T_0^*}{p_0^*}\right)\left(-\frac{1}{R^* T_0^{*2}}\right) = -\frac{1}{p_0^* T_0^*}. \tag{A.19}$$

Substituting these expressions in to equation (A.13) gives

$$\rho^* = \rho_0^*\left[1 - \frac{T^* - T_0^*}{T_0^*} + \frac{p^* - p_0^*}{p_0^*} + \left(\frac{T^* - T_0^*}{T_0^*}\right)^2 + \left(\frac{p^* - p_0^*}{p_0^*}\right)\left(\frac{T^* - T_0^*}{T_0^*}\right) + \cdots\right]. \tag{A.20}$$

From equation (A.7) we identify

$$\left(\frac{T^* - T_0^*}{T_0^*}\right)^2 = \mathcal{O}\left(\bar{\varepsilon}^2\right), \qquad \left(\frac{p^* - p_0^*}{p_0^*}\right)\left(\frac{T^* - T_0^*}{T_0^*}\right) = \mathcal{O}\left(\bar{\varepsilon}^2\right). \tag{A.21}$$

Hence,

$$\frac{\rho^* - \rho_0^*}{\rho_0^*} = -\frac{T^* - T_0^*}{T_0^*} + \frac{p^* - p_0^*}{p_0^*}, \tag{A.22}$$

to $\mathcal{O}(\bar{\varepsilon})$. We may therefore write

$$\bar{\rho}^* = \rho_0^* \left(K_0^* \bar{p}^* - \alpha^* \bar{T}^* \right), \tag{A.23}$$

$$\tilde{\rho}^* = \rho_0^* \left(K_0^* \tilde{p}^* - \alpha^* \tilde{T}^* \right), \tag{A.24}$$

where K_0^* and α^* are the adverse pressure and temperature gradients respectively.

A.2 Equations of motion

In the absence of motion equation (A.2) becomes

$$\frac{\mathrm{d}\bar{p}^*}{\mathrm{d}z^*} = -g\rho_0^* - g\bar{\rho}^*, \tag{A.25}$$

where we have the relation (A.5). Now accounting for an infinitesimal velocity (at most $\mathcal{O}(\bar{\varepsilon})$) and using equation (A.25)

$$\begin{aligned}(\rho_0^* + \bar{\rho}^* + \tilde{\rho}^*) \left(\frac{\partial \boldsymbol{u}^*}{\partial t^*} + (\boldsymbol{u}^* \cdot \boldsymbol{\nabla}_{\boldsymbol{x}}^*) \boldsymbol{u}^* \right) = -\boldsymbol{\nabla}_{\boldsymbol{x}}^* \tilde{p}^* - g^* \tilde{\rho}^* \hat{\boldsymbol{z}} + \frac{\mu^*}{\rho_0^*} (\rho_0^* + \bar{\rho}^* + \tilde{\rho}^*) \nabla_x^{*2} \boldsymbol{u} \\ + \frac{\mu^*}{3\rho_0^*} (\rho_0^* + \bar{\rho}^* + \tilde{\rho}^*) \boldsymbol{\nabla}_{\boldsymbol{x}}^* (\boldsymbol{\nabla}_{\boldsymbol{x}}^* \cdot \boldsymbol{u}^*).\end{aligned} \tag{A.26}$$

This may be rewritten using the assumption (A.9),

$$\begin{aligned}\rho_0^* \left(1 + \frac{\bar{\varepsilon}\bar{\rho}^*}{\Delta\bar{\rho}^*} + \frac{\bar{\varepsilon}\tilde{\rho}^*}{\Delta\bar{\rho}^*} \right) \left(\frac{\partial \boldsymbol{u}^*}{\partial t} + (\boldsymbol{u}^* \cdot \boldsymbol{\nabla}_{\boldsymbol{x}}^*) \boldsymbol{u}^* \right) = -\boldsymbol{\nabla}_{\boldsymbol{x}}^* \tilde{p}^* - g^* \tilde{\rho}^* \hat{\boldsymbol{z}} \\ + \frac{\mu^*}{\rho_0^*} \left(1 + \frac{\bar{\varepsilon}\bar{\rho}^*}{\Delta\bar{\rho}^*} + \frac{\bar{\varepsilon}\tilde{\rho}^*}{\Delta\bar{\rho}^*} \right) \nabla_x^{*2} \boldsymbol{u}^* + \frac{\mu^*}{3\rho_0^*} \left(1 + \frac{\bar{\varepsilon}\bar{\rho}^*}{\Delta\bar{\rho}^*} + \frac{\bar{\varepsilon}\tilde{\rho}^*}{\Delta\bar{\rho}^*} \right) \boldsymbol{\nabla}_{\boldsymbol{x}}^* (\boldsymbol{\nabla}_{\boldsymbol{x}}^* \cdot \boldsymbol{u}^*)\end{aligned} \tag{A.27}$$

Using equation (A.5) we may rewrite the conservation of mass equation as

$$\left(1+\frac{\bar{\rho}^*}{\rho_0^*}+\frac{\tilde{\rho}^*}{\rho_0^*}\right)\left(\boldsymbol{\nabla}_{\boldsymbol{x}}^*\cdot\boldsymbol{u}^*\right)=-\left[\frac{\partial\tilde{\rho}^*}{\partial t^*}+\left(\boldsymbol{u}^*\cdot\boldsymbol{\nabla}_{\boldsymbol{x}}^*\right)\left(\frac{\bar{\rho}^*}{\rho_0^*}+\frac{\tilde{\rho}^*}{\rho_0^*}\right)\right]. \tag{A.28}$$

The assumption (A.9) gives

$$\boldsymbol{\nabla}_{\boldsymbol{x}}^*\cdot\boldsymbol{u}^*+\left(\bar{\varepsilon}\frac{\bar{\rho}^*}{\Delta\bar{\rho}^*}+\bar{\varepsilon}\frac{\tilde{\rho}^*}{\rho_0^*}\right)\left(\boldsymbol{\nabla}_{\boldsymbol{x}}^*\cdot\boldsymbol{u}^*\right)=-\left(\frac{\partial}{\partial t^*}+\boldsymbol{u}^*\cdot\boldsymbol{\nabla}_{\boldsymbol{x}}^*\right)\left(\bar{\varepsilon}\frac{\bar{\rho}^*}{\Delta\bar{\rho}^*}+\bar{\varepsilon}\frac{\tilde{\rho}^*}{\rho_0^*}\right), \tag{A.29}$$

which upon assuming the velocity perturbations occur at most $\mathcal{O}(\bar{\varepsilon})$ gives

$$\boldsymbol{\nabla}_{\boldsymbol{x}}^*\cdot\boldsymbol{u}^*=-\left(\frac{\partial}{\partial t^*}+\boldsymbol{u}^*\cdot\boldsymbol{\nabla}_{\boldsymbol{x}}^*\right)\left(\bar{\varepsilon}\frac{\bar{\rho}^*}{\Delta\bar{\rho}^*}+\bar{\varepsilon}\frac{\tilde{\rho}^*}{\rho_0^*}\right)+\mathcal{O}\left(\bar{\varepsilon}^2\right). \tag{A.30}$$

Hence, the conservation of mass and momentum equations (A.30) and (A.27) may be rewritten (upto $\mathcal{O}(\bar{\varepsilon})$) as

$$\boldsymbol{\nabla}_{\boldsymbol{x}}^*\cdot\boldsymbol{u}^*=0, \tag{A.31}$$

$$\frac{\partial\boldsymbol{u}^*}{\partial t^*}+\left(\boldsymbol{u}^*\cdot\boldsymbol{\nabla}_{\boldsymbol{x}}^*\right)\boldsymbol{u}^*=-\frac{1}{\rho_0^*}\boldsymbol{\nabla}_{\boldsymbol{x}}^*\tilde{p}^*-\bar{\varepsilon}\frac{g^*\tilde{\rho}^*}{\Delta\bar{\rho}^*}\hat{\boldsymbol{z}}+\frac{\mu^*}{\rho_0^*}\nabla_x^{*2}\boldsymbol{u}^*. \tag{A.32}$$

In equation (A.32) we have retained the $\bar{\varepsilon}g^*\tilde{\rho}^*/\Delta\bar{\rho}^*\hat{\boldsymbol{z}}$ term, as for convection problems we must assume the acceleration due to gravity is much larger than the characteristic acceleration; therefore this term may not be small, even though it is multiplied by $\bar{\varepsilon}$. The z^*-component of equation (A.32) is given by

$$\frac{\partial w^*}{\partial t^*}+\left(\boldsymbol{u}^*\cdot\boldsymbol{\nabla}_{\boldsymbol{x}}^*\right)w=-\frac{1}{\rho_0^*}\frac{\partial\tilde{p}^*}{\partial z}-\bar{\varepsilon}\frac{g^*\tilde{\rho}^*}{\Delta\bar{\rho}^*}+\frac{\mu^*}{\rho_0^*}\nabla_x^{*2}w^*, \tag{A.33}$$

where w^* is the z^*-component of velocity. Using the relation for the fluctuation in density (A.24) gives

$$\frac{\partial w^*}{\partial t^*}+\left(\boldsymbol{u}^*\cdot\boldsymbol{\nabla}_{\boldsymbol{x}}^*\right)w^*=-\frac{1}{\rho_0^*}\left(\frac{\partial\tilde{p}^*}{\partial z^*}+\frac{1}{H^*}\tilde{p}^*\right)+\frac{g^*\tilde{T}^*}{T_0^*}+\frac{\mu^*}{\rho_0^*}\nabla_x^{*2}w^*, \tag{A.34}$$

where

$$H^* = \frac{p_0^*}{g\rho_0^*}. \tag{A.35}$$

The quantity H^* is the thickness of a layer with uniform density and pressure varying from p_0^* at the bottom to zero at the top. Using the conservation of momentum equation (A.25) for a motionless fluid

$$H^* \left(\frac{\mathrm{d}\bar{p}^*}{\mathrm{d}z^*} + g^* \bar{\rho}^* \right) = -p_0^*, \tag{A.36}$$

$$H^* + \frac{\bar{\rho}^* p_0^*}{\rho_0^* \dfrac{\mathrm{d}\bar{p}^*}{\mathrm{d}z}} = -H_p^*, \tag{A.37}$$

$$\Rightarrow H^* = -H_p^* + \mathcal{O}(\varepsilon). \tag{A.38}$$

Now, since

$$\frac{\partial \tilde{p}^*}{\partial z^*} \geq \frac{\tilde{p}^*}{h^*}, \tag{A.39}$$

this implies $\tilde{p}^*/H^*$ is negligible compared to $\dfrac{\partial \tilde{p}^*}{\partial z^*}$ as $h^* \ll H^*$. Therefore equation (A.32) becomes

$$\frac{\partial \boldsymbol{u}^*}{\partial t^*} + (\boldsymbol{u}^* \cdot \boldsymbol{\nabla}_{\boldsymbol{x}}^*)\, \boldsymbol{u}^* = -\frac{1}{\rho_0^*} \boldsymbol{\nabla}_{\boldsymbol{x}}^* \tilde{p}^* + g^* \alpha^* \tilde{T}^* \hat{\boldsymbol{z}} + \frac{\mu^*}{\rho_0^*} \nabla_x^{*2} \boldsymbol{u}^*. \tag{A.40}$$

A direct consequence of the contribution of $\tilde{p}^*$ being small compared to that of the temperature fluctuation $\tilde{T}^*$ is that we can rewrite equation (A.24) as

$$\frac{\tilde{\rho}^*}{\rho_0^*} = -\frac{\tilde{T}^*}{T_0^*} = -\alpha^* \tilde{T}^*. \tag{A.41}$$

A.3 Heat equation

In the absence of motion, the heat equation (A.3) becomes

$$k_C \nabla_x^{*2} \bar{T}^* = 0. \tag{A.42}$$

The equation for the temperature fluctuation is therefore given by

$$\rho_0^* C_V^* \left(\frac{\partial \tilde{T}^*}{\partial t} + (\boldsymbol{u}^* \cdot \boldsymbol{\nabla}_{\boldsymbol{x}}^*) T \right) + p^* \left(\boldsymbol{\nabla}_{\boldsymbol{x}}^* \cdot \boldsymbol{u}^* \right) = k_C \nabla_x^{*2} \tilde{T}^*. \tag{A.43}$$

The term $p^*(\boldsymbol{\nabla}_{\boldsymbol{x}}^* \cdot \boldsymbol{u}^*)$ is retained here as it is of the same order as the other terms in the equation. This may be observed by noting $\bar{p}^*/p_0^* = \mathcal{O}(h/H)$ and $\left|\tilde{p}^*/p_0^*\right| = \mathcal{O}(\Delta\bar{p}^*/p_0^*)$. Hence $p = p_0^* + \mathcal{O}(h/H)$.

It is possible to simplify equation (A.43) by making the following steps. Multiply equation (A.30) by p^* and noting $\delta\bar{\rho}^* = \varepsilon\rho_0^*$, to give

$$p^* \boldsymbol{\nabla}_{\boldsymbol{x}}^* \cdot \boldsymbol{u}^* = -p_0^* \left(\frac{\partial}{\partial t} + \boldsymbol{u}^* \cdot \boldsymbol{\nabla}_{\boldsymbol{x}}^* \right) \left(\frac{\rho^*}{\rho_0^*} + \frac{\tilde{\rho}^*}{\rho_0^*} \right) + \mathcal{O}\left(\frac{h^*}{H^*} \right), \tag{A.44}$$

where we have used $p^* = p_0^* + \mathcal{O}(h^*/H^*)$. Substituting for $\bar{\rho}^*$ from equation (A.23) and $\tilde{\rho}^*$ from equation (A.41) allows us to rewrite equation as

$$p^* \boldsymbol{\nabla}_{\boldsymbol{x}}^* \cdot \boldsymbol{u}^* = p_0^* \left(\frac{\partial}{\partial t} + \boldsymbol{u}^* \cdot \boldsymbol{\nabla}_{\boldsymbol{x}}^* \right) \left(\frac{\bar{T}^* + \tilde{T}^*}{T_0^*} - \frac{\bar{p}^*}{p_0^*} \right) + \mathcal{O}\left(\frac{h^*}{H^*} \right). \tag{A.45}$$

Now using equation (A.25)

$$\left(\frac{\partial}{\partial t} + \boldsymbol{u}^* \cdot \boldsymbol{\nabla}_{\boldsymbol{x}}^* \right) \frac{\bar{p}^*}{p_0^*} = \frac{w^*}{p_0^*} \frac{\mathrm{d}\bar{p}^*}{\mathrm{d}z} = -\frac{w^* g^* \rho_0^*}{p_0^*} + \mathcal{O}(h^*/H^*), \tag{A.46}$$

where we have used $w^* g^* \bar{\rho}^*/p_0^* = \mathcal{O}(h^*/H^*)$. Therefore equation (A.44) becomes

$$p^* \boldsymbol{\nabla}_{\boldsymbol{x}}^* \cdot \boldsymbol{u}^* = p_0^* \left(\frac{\partial}{\partial t^*} + \boldsymbol{u}^* \cdot \boldsymbol{\nabla}_{\boldsymbol{x}}^* \right) \left(\frac{\bar{T}^* + \tilde{T}^*}{T_0^*} \right) + w^* g^* \rho_0^* + \mathcal{O}\left(\frac{h^*}{H^*} \right). \tag{A.47}$$

Equation (A.43) may therefore be rewritten as

$$\rho_0^* C_p^* \left(\frac{\partial \tilde{T}^*}{\partial t^*} + \boldsymbol{u}^* \cdot \boldsymbol{\nabla}_{\boldsymbol{x}}^* T^* \right) + w^* g^* \rho_0^* = k^* \nabla_x^{*2} \tilde{T}^*, \tag{A.48}$$

where $C_p^* = C_V^* + p_0^*/(\rho_0^* T_0^*)$ is the specific heat capacity at constant pressure. This equation may be simplified by neglecting the nonlinear terms to give

$$\left(\frac{\partial}{\partial t^*} + \boldsymbol{u}^* \cdot \boldsymbol{\nabla}_{\boldsymbol{x}}^* \right) \tilde{T}^* + w^* \left(\frac{\mathrm{d}\bar{T}^*}{\mathrm{d}z^*} + \frac{g^*}{C_p^*} \right) = K^* \nabla_x^{*2} \tilde{T}^*, \tag{A.49}$$

where $-g^*/C_p^*$ is the adiabatic gradient and

$$K^* = \frac{k_C^*}{\rho_0^* C_p^*}, \tag{A.50}$$

is the thermal diffusivity.

A.4 Condensed form

The conservation of mass equation is already in the simplest form, *i.e.*

$$\boldsymbol{\nabla}_{\boldsymbol{x}}^* \cdot \boldsymbol{u}^* = 0. \tag{A.51}$$

However we aim to write more condensed forms of the conservation of momentum and conservation of energy equations. We may write an equation for the density as

$$\rho^* = \rho_0^* \left(1 - \alpha^* \left(T^* - T_0^* \right) \right), \tag{A.52}$$

where we have combined together equations (A.23) and (A.41) and neglected terms of $\mathcal{O}(h^*/H^*)$ (*i.e.* $K_0^* \bar{p}^*$ and $K_0^* \tilde{p}^*$). This allows us to write the conservation of momentum

equation as

$$\frac{\partial \boldsymbol{u}^*}{\partial t^*} + (\boldsymbol{u}^* \cdot \boldsymbol{\nabla}_{\boldsymbol{x}}^*)\, \boldsymbol{u}^* = -\frac{1}{\rho_0^*} \boldsymbol{\nabla}_{\boldsymbol{x}}^* p^* + \frac{\mu^*}{\rho_0^*} \nabla_x^{*2} \boldsymbol{u}^* - \frac{\rho^*}{\rho_0^*} g^* \hat{\boldsymbol{z}}, \tag{A.53}$$

where ρ^* is defined in equation (A.52). Now (assuming the adiabatic gradient is small) the conservation of energy equation is given by

$$\frac{\partial T^*}{\partial t^*} + (\boldsymbol{u}^* \cdot \boldsymbol{\nabla}_{\boldsymbol{x}}^*)\, T^* = K^* \nabla_x^{*2} T^*. \tag{A.54}$$

APPENDIX B

ELIMINATING PRESSURE FROM THE CONSERVATION OF MOMENTUM EQUATION FOR THE TRANSVERSELY ISOTROPIC RAYLEIGH-BÉNARD PROBLEM

To eliminate pressure from the momentum equation (4.44), we apply the following steps (in three-dimensions). Apply the operator

$$\epsilon_{ijk}\frac{\partial}{\partial x_j} \tag{B.1}$$

to the k-th component of equation (4.44), where ϵ_{ijk} is the Levi-Civita symbol or alternating tensor, to give

$$\frac{\partial}{\partial t}\left(\epsilon_{ijk}\frac{\partial u_k^{(1)}}{\partial x_j}\right) = \frac{\partial}{\partial x_a}\left(\epsilon_{ijk}\frac{\partial \sigma_{ka}^{(1)}}{\partial x_j}\right) - \frac{gd^3}{\kappa^2}\epsilon_{ijk}\frac{\partial \rho^{(1)}}{\partial x_j}\hat{z}_k. \tag{B.2}$$

Applying the curl operator again gives

$$\frac{\partial}{\partial t}\left(\epsilon_{ijk}\epsilon_{klm}\frac{\partial^2 u_m^{(1)}}{\partial x_j \partial x_l}\right) = \frac{\partial}{\partial x_a}\left(\epsilon_{ijk}\epsilon_{klm}\frac{\partial^2 \sigma_{ma}^{(1)}}{\partial x_j \partial x_l}\right) - \frac{gd^3}{\kappa^2}\epsilon_{ijk}\epsilon_{klm}\frac{\partial^2 \rho^{(1)}}{\partial x_j \partial x_l}\hat{z}_m. \tag{B.3}$$

Making use of the identity

$$\epsilon_{ijk}\epsilon_{klm} = \delta_{il}\delta_{jm} - \delta_{im}\delta_{jl}, \tag{B.4}$$

equation (B.3) may be rewritten

$$\frac{\partial}{\partial t}\left(\frac{\partial^2 u_j^{(1)}}{\partial x_j \partial x_i} - \frac{\partial^2 u_i^{(1)}}{\partial x_j \partial x_j}\right) = \frac{\partial}{\partial x_a}\left(\frac{\partial^2 \sigma_{ja}}{\partial x_i \partial x_j} - \frac{\partial^2 \sigma_{ia}}{\partial x_j \partial x_j}\right) - \frac{g d^3}{\kappa^2}\left(\frac{\partial^2 \rho}{\partial x_j \partial x_i}\,\hat{z}_j - \frac{\partial^2 \rho}{\partial x_j \partial x_j}\,\hat{z}_i\right), \tag{B.5}$$

which upon applying the incompressibility condition (4.12) becomes

$$\frac{\partial}{\partial t}\left(\frac{\partial^2 u_i}{\partial x_j \partial x_j}\right) = \frac{\partial}{\partial x_a}\left(\frac{\partial^2 \sigma_{ia}^{(1)}}{\partial x_j \partial x_j} - \frac{\partial^2 \sigma_{ja}^{(1)}}{\partial x_i \partial x_j}\right) + \frac{g d^3}{\kappa^2}\left(\frac{\partial^2 \rho^{(1)}}{\partial x_j \partial x_i}\,\hat{z}_j - \frac{\partial^2 \rho^{(1)}}{\partial x_j \partial x_j}\,\hat{z}_i\right), \tag{B.6}$$

Taking the dot product of equation (B.6) with $\hat{x}_i$, $\hat{y}_i$ and $\hat{z}_i$ in turn gives the x, y and z components of equation (B.6) respectively:

$$\frac{\partial}{\partial t}\left(\frac{\partial^2 u^{(1)}}{\partial x_j \partial x_j}\right) = \frac{\partial}{\partial x_a}\left(\frac{\partial^2 \sigma_{xa}^{(1)}}{\partial x_j \partial x_j} - \frac{\partial^2 \sigma_{ja}^{(1)}}{\partial x \partial x_j}\right), \tag{B.7}$$

$$\frac{\partial}{\partial t}\left(\frac{\partial^2 v^{(1)}}{\partial x_j \partial x_j}\right) = \frac{\partial}{\partial x_a}\left(\frac{\partial^2 \sigma_{ya}^{(1)}}{\partial x_j \partial x_j} - \frac{\partial^2 \sigma_{ja}^{(1)}}{\partial y \partial x_j}\right), \tag{B.8}$$

$$\frac{\partial}{\partial t}\left(\frac{\partial^2 w^{(1)}}{\partial x_j \partial x_j}\right) = \frac{\partial}{\partial x_a}\left(\frac{\partial^2 \sigma_{za}^{(1)}}{\partial x_j \partial x_j} - \frac{\partial^2 \sigma_{ja}^{(1)}}{\partial z \partial x_j}\right) + \frac{g d^3}{\kappa^2}\left(\frac{\partial^2 \rho^{(1)}}{\partial z^2} - \frac{\partial^2 \rho^{(1)}}{\partial x_j \partial x_j}\right). \tag{B.9}$$

Equations (B.7)-(B.9) can be expanded to give

$$\frac{\partial}{\partial t}\nabla_{\boldsymbol{x}}^2 u^{(1)} = \nabla_{\boldsymbol{x}}^2\left(\frac{\partial \sigma_{xx}^{(1)}}{\partial x}+\frac{\partial \sigma_{xy}^{(1)}}{\partial y}+\frac{\partial \sigma_{xz}^{(1)}}{\partial z}\right) \tag{B.10}$$
$$-\frac{\partial}{\partial x}\left(\frac{\partial^2 \sigma_{xx}^{(1)}}{\partial x^2}+\frac{\partial^2 \sigma_{yy}^{(1)}}{\partial y^2}+\frac{\partial^2 \sigma_{zz}^{(1)}}{\partial z^2}+2\left(\frac{\partial^2 \sigma_{xz}^{(1)}}{\partial x\partial z}+\frac{\partial^2 \sigma_{xy}^{(1)}}{\partial x\partial y}+\frac{\partial^2 \sigma_{yz}^{(1)}}{\partial y\partial z}\right)\right)$$

$$\frac{\partial}{\partial t}\nabla_{\boldsymbol{x}}^2 v^{(1)} = \nabla_{\boldsymbol{x}}^2\left(\frac{\partial \sigma_{yx}^{(1)}}{\partial x}+\frac{\partial \sigma_{yy}^{(1)}}{\partial y}+\frac{\partial \sigma_{yz}^{(1)}}{\partial z}\right) \tag{B.11}$$
$$-\frac{\partial}{\partial y}\left(\frac{\partial^2 \sigma_{xx}^{(1)}}{\partial x^2}+\frac{\partial^2 \sigma_{yy}^{(1)}}{\partial y^2}+\frac{\partial^2 \sigma_{zz}^{(1)}}{\partial z^2}+2\left(\frac{\partial^2 \sigma_{xz}^{(1)}}{\partial x\partial z}+\frac{\partial^2 \sigma_{xy}^{(1)}}{\partial x\partial y}+\frac{\partial^2 \sigma_{yz}^{(1)}}{\partial y\partial z}\right)\right)$$

$$\frac{\partial}{\partial t}\nabla_{\boldsymbol{x}}^2 w^{(1)} = \nabla_{\boldsymbol{x}}^2\left(\frac{\partial \sigma_{zx}^{(1)}}{\partial x}+\frac{\partial \sigma_{zy}^{(1)}}{\partial y}+\frac{\partial \sigma_{zz}^{(1)}}{\partial z}\right) \tag{B.12}$$
$$-\frac{\partial}{\partial z}\left(\frac{\partial^2 \sigma_{xx}^{(1)}}{\partial x^2}+\frac{\partial^2 \sigma_{yy}^{(1)}}{\partial y^2}+\frac{\partial^2 \sigma_{zz}^{(1)}}{\partial z^2}+2\left(\frac{\partial^2 \sigma_{xz}^{(1)}}{\partial x\partial z}+\frac{\partial^2 \sigma_{xy}^{(1)}}{\partial x\partial y}+\frac{\partial^2 \sigma_{yz}^{(1)}}{\partial y\partial z}\right)\right)$$
$$+\frac{gd^3}{\kappa^2}\left(\frac{\partial^2 \rho^{(1)}}{\partial z^2}-\frac{\partial^2 \rho^{(1)}}{\partial x_j \partial x_j}\right),$$

where $v^{(1)}$ is the y-component of velocity. Setting $v^{(1)}=0$ and assuming all y-derivatives are zero, we recover the two-dimensional equations

$$\frac{\partial}{\partial t}\nabla_{\boldsymbol{x}}^2 u = \nabla_{\boldsymbol{x}}^2\left(\frac{\partial \sigma_{xx}}{\partial x}+\frac{\partial \sigma_{xz}}{\partial z}\right)-\frac{\partial \gamma}{\partial x}, \tag{B.13}$$

$$\frac{\partial}{\partial t}\nabla_{\boldsymbol{x}}^2 w = \nabla_{\boldsymbol{x}}^2\left(\frac{\partial \sigma_{xz}}{\partial x}+\frac{\partial \sigma_{zz}}{\partial z}\right)-\frac{\partial \gamma}{\partial z}+\frac{gd^3}{\kappa^2}\left(\frac{\partial^2 \rho}{\partial z^2}-\frac{\partial^2 \rho}{\partial x_j \partial x_j}\right), \tag{B.14}$$

$$\text{where } \gamma = \frac{\partial^2 \sigma_{xx}}{\partial x^2}+2\frac{\partial^2 \sigma_{xz}}{\partial x\partial z}+\frac{\partial^2 \sigma_{zz}}{\partial z^2}. \tag{B.15}$$

APPENDIX C

DERIVING AN EQUATION FOR CONCENTRATION OF A SELF-MOTILE SUSPENSION WITH TRANSLATIONAL BROWNIAN MOTION

To derive a governing equation for the concentration field $c^*(\boldsymbol{x}^*, t^*)$ integrate equation (5.4) over $\hat{\boldsymbol{p}}$ and substitute for the translational flux velocity $\boldsymbol{U}$ (equation (5.5)) to give [73]

$$\begin{aligned}\frac{\partial}{\partial t}\int_S N\,\mathrm{d}\hat{\boldsymbol{p}} &= -\boldsymbol{\nabla}_{\boldsymbol{x}}\cdot\left(\int_S U_s\hat{\boldsymbol{p}}N\,\mathrm{d}\hat{\boldsymbol{p}}+\int_S \boldsymbol{u}N\,\mathrm{d}\hat{\boldsymbol{p}}\right)-\int_S \boldsymbol{\nabla}_{\boldsymbol{p}}\cdot(\boldsymbol{\Omega}N)\,\mathrm{d}\hat{\boldsymbol{p}},\\ &= -U_s\boldsymbol{\nabla}_{\boldsymbol{x}}\cdot\int_S N\,\mathrm{d}\hat{\boldsymbol{p}}\left(\frac{1}{\int_S N\,\mathrm{d}\hat{\boldsymbol{p}}}\int_S \hat{\boldsymbol{p}}N\,\mathrm{d}\hat{\boldsymbol{p}}\right)-\boldsymbol{\nabla}_{\boldsymbol{x}}\cdot\left(\boldsymbol{u}\int_S N\,\mathrm{d}\hat{\boldsymbol{p}}\right)\\ &\quad -\int_S \boldsymbol{\nabla}_{\boldsymbol{p}}\cdot(\boldsymbol{\Omega}N)\,\mathrm{d}\hat{\boldsymbol{p}}. \qquad \text{(C.1)}\end{aligned}$$

Here, we have rearranged the equation so that spatial derivatives are performed outside the surface integrals. We observe the final term in equation (C.1) is zero by setting $\boldsymbol{F}(\boldsymbol{x},\theta,\chi)=\boldsymbol{\Omega}N$, where θ and χ are the azimuthal and axial components of the spherical coordinate system which describes the orientation of the particles, and noting

$$\int_S \boldsymbol{\nabla}_{\boldsymbol{p}}\cdot\boldsymbol{F}\sin\theta\,\mathrm{d}\theta\,\mathrm{d}\chi = 3\int_{V_S}\boldsymbol{\nabla}_{\boldsymbol{p}}\cdot\boldsymbol{F}r^2\sin\theta\,\mathrm{d}r\,\mathrm{d}\theta\,\mathrm{d}\chi. \qquad \text{(C.2)}$$

Here S is the surface and V_S the volume of a unit sphere, we may apply Green's theorem to equation (C.2) to give

$$\int_{V_S} \boldsymbol{\nabla_p} \cdot \boldsymbol{F} r^2 \sin\theta \, \mathrm{d}r \, \mathrm{d}\theta \, \mathrm{d}\chi = \int_S \boldsymbol{F} \cdot \hat{\boldsymbol{r}} \, \mathrm{d}\theta \, \mathrm{d}\chi. \tag{C.3}$$

Since $\boldsymbol{F} \in span\{\hat{\boldsymbol{x}}, \hat{\boldsymbol{\theta}}, \hat{\boldsymbol{\chi}}\}$, where $\hat{\boldsymbol{\theta}}$ and $\hat{\boldsymbol{\chi}}$ are the unit vectors for θ and χ respectively,

$$\int_S \boldsymbol{F} \cdot \hat{\boldsymbol{r}} \, \mathrm{d}\theta \, \mathrm{d}\chi = 0. \tag{C.4}$$

Combining equations (6.1), (6.2) and (C.1) the governing equation for the concentration field is [73]:

$$\frac{\partial c^*}{\partial t^*} + \boldsymbol{u}^* \cdot \boldsymbol{\nabla}^*_{\boldsymbol{x}} c^* = -U^*_s \boldsymbol{\nabla}^*_{\boldsymbol{x}} \cdot (c^* \boldsymbol{a}), \tag{C.5}$$

where we have made use of the incompressibility condition (5.7). Equation (6.3) is an advection-diffusion equation for the local concentration field c^*, with a source term $-U^*_s \boldsymbol{\nabla}^*_{\boldsymbol{x}} \cdot (c^* \boldsymbol{a})$.

APPENDIX D

DERIVING AN EQUATION FOR THE DIRECTOR FIELD OF A SELF-MOTILE SUSPENSION WITH TRANSLATIONAL BROWNIAN MOTION

To derive the evolution equation for the director field $\boldsymbol{a}$, multiply equation (6.6) by $\hat{\boldsymbol{p}}$ and integrate over $\hat{\boldsymbol{p}}$ to give [73]

$$\int_S \hat{\boldsymbol{p}} \frac{\partial N}{\partial t} \, \mathrm{d}\hat{\boldsymbol{p}} = \int_S -\hat{\boldsymbol{p}} \boldsymbol{\nabla}_{\boldsymbol{x}} \cdot (\boldsymbol{U} N) - \hat{\boldsymbol{p}} \boldsymbol{\nabla}_{\boldsymbol{p}} \cdot (\boldsymbol{\Omega} N) \, \mathrm{d}\hat{\boldsymbol{p}}. \tag{D.1}$$

Substituting for the translation flux velocity $\boldsymbol{U}$ from equation (6.7) and making use of the integration by parts formula

$$\int_S \hat{\boldsymbol{p}} \boldsymbol{\nabla}_{\boldsymbol{p}} \cdot (\boldsymbol{\Omega} N) \, \mathrm{d}\hat{\boldsymbol{p}} = - \int_S \boldsymbol{\Omega} N \, \mathrm{d}\hat{\boldsymbol{p}}, \tag{D.2}$$

equation (D.1) becomes

$$\begin{aligned} \int_S \hat{\boldsymbol{p}} \frac{\partial N}{\partial t} \, \mathrm{d}\hat{\boldsymbol{p}} = & - \boldsymbol{\nabla}_{\boldsymbol{x}} \cdot \int_S \hat{\boldsymbol{p}} \, \hat{\boldsymbol{p}} N + \hat{\boldsymbol{p}} \boldsymbol{u} N \hat{\boldsymbol{p}} \\ & + \int_S (\boldsymbol{I} - \hat{\boldsymbol{p}} \, \hat{\boldsymbol{p}}) \cdot \left[(\alpha_0 \boldsymbol{e} + \boldsymbol{\omega}) \cdot \hat{\boldsymbol{p}} \right] N \, \mathrm{d}\hat{\boldsymbol{p}}. \end{aligned} \tag{D.3}$$

The integrals in equation (D.3) may be evaluated using the assumed form of the distribution function in equation (6.14),

$$c\,\frac{\partial \boldsymbol{a}}{\partial t} + \boldsymbol{a}\,\frac{\partial c}{\partial t} = -\,\boldsymbol{a}\boldsymbol{\nabla}_{\boldsymbol{x}} \cdot \big(c\boldsymbol{a}\,(\boldsymbol{a}+\boldsymbol{u})\big) - c\,(\boldsymbol{a}+\boldsymbol{u}) \cdot \boldsymbol{\nabla}_{\boldsymbol{x}}\boldsymbol{a} + c\,(\boldsymbol{I}-\boldsymbol{a}\,\boldsymbol{a}) \cdot \big[(\alpha_0 \boldsymbol{e}+\boldsymbol{\omega}) \cdot \boldsymbol{a}\big]\,. \tag{D.4}$$

Finally, the evolution equation for $\boldsymbol{a}$ is found by eliminating c using equation (6.15) and assuming the concentration is non-zero everywhere

$$\frac{\partial \boldsymbol{a}}{\partial t} = -\,(\boldsymbol{a}+\boldsymbol{u}) \cdot \boldsymbol{\nabla}_{\boldsymbol{x}}\boldsymbol{a} + (\boldsymbol{I}-\boldsymbol{a}\,\boldsymbol{a}) \cdot \big[(\alpha_0 \boldsymbol{e}+\boldsymbol{\omega}) \cdot \boldsymbol{a}\big]\,. \tag{D.5}$$

APPENDIX E

DERIVING A DISPERSION RELATION FOR A SUSPENSION OF SELF-MOTILE NEARLY-ALIGNED PARTICLES

In this section we follow Saintillan & Shelley [72, 73] to derive a dispersion relation for s. Substituting the ansatz (6.81) into equations (6.77) and (6.80) gives

$$i\boldsymbol{k}\cdot\boldsymbol{u}=0, \tag{E.1}$$

$$\tilde{\mu}k^2\tilde{\boldsymbol{u}}+i\boldsymbol{k}\tilde{p}=i\boldsymbol{k}\cdot\tilde{\boldsymbol{\sigma}}^S, \tag{E.2}$$

$$\tilde{p}=\hat{\boldsymbol{k}}\cdot\tilde{\boldsymbol{\sigma}}^S\cdot\hat{\boldsymbol{k}}, \tag{E.3}$$

where $\hat{\boldsymbol{k}}=\boldsymbol{k}/|\boldsymbol{k}|$ and

$$\tilde{\boldsymbol{\sigma}}^S=\frac{\alpha_1}{4\pi}\int_S\left(\hat{\boldsymbol{p}}\,\hat{\boldsymbol{p}}-\frac{\boldsymbol{I}}{3}\right)\tilde{N}\,\mathrm{d}\hat{\boldsymbol{p}}. \tag{E.4}$$

Substituting equation (E.3) into equation (E.2) allows us to eliminate pressure

$$\tilde{\mu}k^2\tilde{\boldsymbol{u}}+i\boldsymbol{k}\left(\hat{\boldsymbol{k}}\cdot\tilde{\boldsymbol{\sigma}}^S\cdot\hat{\boldsymbol{k}}\right)=i\boldsymbol{I}\cdot\tilde{\boldsymbol{\sigma}}^S\cdot\boldsymbol{k}, \tag{E.5}$$

$$\Rightarrow\tilde{\boldsymbol{u}}=\frac{i}{k\tilde{\mu}}\left(\boldsymbol{I}-\hat{\boldsymbol{k}}\,\hat{\boldsymbol{k}}\right)\cdot\tilde{\boldsymbol{\sigma}}^S\cdot\hat{\boldsymbol{k}}. \tag{E.6}$$

Using equation (E.6) the rate-of-strain tensor is

$$\tilde{\boldsymbol{e}} = \frac{i}{2}\left(\boldsymbol{k}\,\boldsymbol{u} + \boldsymbol{u}\,\boldsymbol{k}\right), \tag{E.7}$$

$$= \frac{-1}{\tilde{\mu}}\left(\hat{\boldsymbol{k}}\left(\boldsymbol{I} - \hat{\boldsymbol{k}}\,\hat{\boldsymbol{k}}\right)\cdot\boldsymbol{\sigma}^S\cdot\hat{\boldsymbol{k}}\right). \tag{E.8}$$

Substituting for the active stress $\boldsymbol{\sigma}^S$ from equation (E.4) gives

$$\tilde{\boldsymbol{e}} = \frac{-\alpha_1}{4\pi\tilde{\mu}}\left(\hat{\boldsymbol{k}}\left(\boldsymbol{I} - \hat{\boldsymbol{k}}\,\hat{\boldsymbol{k}}\right)\cdot\int_S \hat{\boldsymbol{p}}'\,\hat{\boldsymbol{p}}' - \frac{\boldsymbol{I}}{3}\tilde{N}\,\mathrm{d}\hat{\boldsymbol{p}}'\cdot\hat{\boldsymbol{k}}\right), \tag{E.9}$$

using that $\hat{\boldsymbol{k}}$ is a unit vector gives

$$\tilde{\boldsymbol{e}} = \frac{-\alpha_1}{4\pi\tilde{\mu}}\left(\hat{\boldsymbol{k}}\left(\boldsymbol{I} - \hat{\boldsymbol{k}}\,\hat{\boldsymbol{k}}\right)\cdot\int_S \hat{\boldsymbol{p}}'\left(\hat{\boldsymbol{p}}'\cdot\hat{\boldsymbol{k}}\right)\tilde{N}\,\mathrm{d}\hat{\boldsymbol{p}}'\right). \tag{E.10}$$

To write this in a more compact form we introduce the vector

$$\boldsymbol{F}\left(\tilde{N}\right) = \left(\boldsymbol{I} - \hat{\boldsymbol{k}}\,\hat{\boldsymbol{k}}\right)\cdot\int_S \hat{\boldsymbol{p}}'\left(\hat{\boldsymbol{p}}'\cdot\hat{\boldsymbol{k}}\right)\tilde{N}\,\mathrm{d}\hat{\boldsymbol{p}}', \tag{E.11}$$

such that

$$\tilde{\boldsymbol{e}} = \frac{-\alpha_1}{4\pi\tilde{\mu}}\hat{\boldsymbol{k}}\,\boldsymbol{F}\left(\tilde{N}\right). \tag{E.12}$$

Substituting the ansatz (equation (6.81)) and the rate of strain tensor (equation (E.12)) into the Fokker-Planck equation (6.69) gives

$$\tilde{N} = \frac{-5\alpha_0\alpha_1\left(\hat{\boldsymbol{k}}\cdot\hat{\boldsymbol{p}}\right)}{4\pi\tilde{\mu}\left(s + i(\boldsymbol{k}\cdot\hat{\boldsymbol{p}})\right)}\hat{\boldsymbol{p}}\cdot\boldsymbol{F}(\tilde{N}). \tag{E.13}$$

To obtain an eigenvalue relation, apply $\boldsymbol{F}$ to both sides of equation (E.13)

$$\boldsymbol{F}(\tilde{N}) = \frac{-5\alpha_0\alpha_1}{4\pi\tilde{\mu}}\int_S \frac{(\hat{\boldsymbol{k}}\cdot\hat{\boldsymbol{p}})^2(\boldsymbol{I} - \hat{\boldsymbol{k}}\,\hat{\boldsymbol{k}})\cdot\hat{\boldsymbol{p}}\,\hat{\boldsymbol{p}}\cdot\boldsymbol{F}(\tilde{N})}{s + i(\boldsymbol{k}\cdot\hat{\boldsymbol{p}})}\,\mathrm{d}\hat{\boldsymbol{p}}. \tag{E.14}$$

Observing that equation (E.14) is invariant under rotation (in Cartesian space) we may choose $\hat{\boldsymbol{k}} = \hat{\boldsymbol{z}}$ without loss of generality. Substituting this condition into equation (E.11)

$$\boldsymbol{F}(\tilde{N}) = (\hat{\boldsymbol{x}}\,\hat{\boldsymbol{x}} + \hat{\boldsymbol{y}}\,\hat{\boldsymbol{y}}) \cdot \int_S \hat{\boldsymbol{p}}' \left(\hat{\boldsymbol{p}}' \cdot \hat{\boldsymbol{z}}\right) \tilde{N}\, \mathrm{d}\hat{\boldsymbol{p}}', \tag{E.15}$$

we observe $\boldsymbol{F}$ must lie in the $\boldsymbol{x}$-$\boldsymbol{y}$ plane. Using this we may rewrite equation (E.15) as

$$\boldsymbol{F}(\tilde{N}) = \frac{-5\alpha_0\alpha_1}{4\pi\tilde{\mu}} \int_S \frac{(\hat{\boldsymbol{z}} \cdot \hat{\boldsymbol{p}}')\,(\hat{\boldsymbol{x}}\,\hat{\boldsymbol{x}} + \hat{\boldsymbol{y}}\,\hat{\boldsymbol{y}}) \cdot \hat{\boldsymbol{p}}'\,\hat{\boldsymbol{p}}' \cdot \left(F_x\hat{x} + F_y\hat{y}\right)}{s + ik\,(\hat{\boldsymbol{z}} \cdot \hat{\boldsymbol{p}}')}\, \mathrm{d}\hat{\boldsymbol{p}}', \tag{E.16}$$

where F_x and F_y are the x and y components of $\boldsymbol{F}$ respectively. To evaluate equation (E.14) write the director field in spherical coordinates ($\hat{\boldsymbol{p}} = (\sin\theta\cos\chi, \sin\theta\sin\chi, \cos\theta)$, $\chi \in [0, 2\pi)$ and $\theta \in [0, \pi]$)

$$\begin{aligned}
\boldsymbol{F}(\tilde{N}) =& \frac{-5\alpha_0\alpha_1}{4\pi\tilde{\mu}} \int_{\theta=0}^{\pi} \int_{\chi=0}^{2\pi} \frac{\cos^2\theta\,(\sin\theta\cos\chi\hat{\boldsymbol{x}} + \sin\theta\sin\chi\hat{\boldsymbol{y}})}{s + ik\cos\theta} \\
&\times \left(\sin\theta\cos\chi F_x + \sin\theta\sin\chi F_y\right) \sin\theta\,\mathrm{d}\chi\,\mathrm{d}\theta, \qquad \text{(E.17)} \\
=& \frac{-5\alpha_0\alpha_1}{4\pi\tilde{\mu}} \int_{\theta=0}^{\pi} \frac{\cos^2\theta\sin^3\theta}{s + ik\cos\theta} \\
&\times \left(\int_{\chi=0}^{2\pi} \left(\cos^2\chi F_x + \frac{1}{2}\sin 2\chi F_y\right)\hat{\boldsymbol{x}} + \left(\frac{1}{2}\sin 2\chi F_x + \sin^2\chi F_y\right)\hat{\boldsymbol{y}}\,\mathrm{d}\chi \right) \mathrm{d}\theta. \qquad \text{(E.18)}
\end{aligned}$$

Evaluating the inner integral with respect to χ, noting $\boldsymbol{F}$ is independent of χ and θ (equation (E.15)), yields

$$\boldsymbol{F}(\tilde{N}) = \frac{-5\alpha_0\alpha_1\boldsymbol{F}(\tilde{N})}{4\tilde{\mu}} \int_{\theta=0}^{\pi} \frac{\cos^2\theta\sin^3\theta}{s + ik\cos\theta}\, \mathrm{d}\theta. \tag{E.19}$$

This integral may be solved using the substitution

$$\tan\frac{\theta}{2} = t, \tag{E.20}$$

where we state explicitly

$$\sin\theta = \frac{2t}{t^2+1}, \qquad \cos\theta = \frac{1-t^2}{1+t^2}, \qquad \frac{\partial\theta}{\partial t} = \frac{2}{t^2+1}. \tag{E.21}$$

Using equation (E.20), the eigenvalue relation (E.19) becomes

$$\boldsymbol{F}(\tilde{N}) = \frac{-20\,\alpha_0\,\alpha_1 \boldsymbol{F}(\tilde{N})}{\tilde{\mu}} \int_0^\infty \frac{t^3}{(1-t^2)^3(\tilde{\lambda}(1+t^2)-(1-t^2))}\,\mathrm{d}t, \tag{E.22}$$

where $\tilde{\lambda} = -i(s + D_T k^2)$. Evaluating the integral gives

$$\boldsymbol{F}(\tilde{N}) = \frac{5i\alpha_0\alpha_1 \boldsymbol{F}(\tilde{N})}{4k\tilde{\mu}} \left[2\tilde{\lambda}^3 - \frac{4}{3}\tilde{\lambda} + \left(\tilde{\lambda}^4 - \tilde{\lambda}^2\right) \log\left(\frac{\tilde{\lambda}-1}{\tilde{\lambda}+1}\right) \right]. \tag{E.23}$$

Now, either $\boldsymbol{F}(\tilde{N}) = \mathbf{0}$, or

$$\frac{5i\alpha_0\alpha_1}{4k\tilde{\mu}} \left[2\tilde{\lambda}^3 - \frac{4}{3}\tilde{\lambda} + \left(\tilde{\lambda}^4 - \tilde{\lambda}^2\right) \log\left(\frac{\tilde{\lambda}-1}{\tilde{\lambda}+1}\right) \right] = 1. \tag{E.24}$$

LIST OF REFERENCES

[1] D J Acheson. *Elementary fluid dynamics*. Oxford University Press, 1990.

[2] M Achilli and D Mantovani. Tailoring mechanical properties of collagen-based scaffolds for vascular tissue engineering: the effects of pH, temperature and ionic strength on gelation. *Polymers*, 2(4):664–680, 2010.

[3] G Ahlers, S Grossmann, and D Lohse. Heat transfer and large scale dynamics in turbulent Rayleigh-Bénard convection. *Rev. Mod. Phys.*, 81(2):503, 2009.

[4] H A Barnes, J F Hutton, and K Walters. *An introduction to rheology*. Elsevier, 1989.

[5] G K Batchelor. Slender-body theory for particles of arbitrary cross-section in Stokes flow. *J. Fluid Mech.*, 44(03):419–440, 1970.

[6] G K Batchelor. The stress system in a suspension of force-free particles. *J. Fluid Mech.*, 41(03):545–570, 1970.

[7] G K Batchelor. The stress generated in a non-dilute suspension of elongated particles by pure straining motion. *J. Fluid Mech.*, 46(04):813–829, 1971.

[8] H Bénard. Les tourbillons cellulaires dans une nappe liquide.-méthodes optiques d'observation et d'enregistrement. *J. Phys.–Paris*, 10(1):254–266, 1901.

[9] J R Blake. A spherical envelope approach to ciliary propulsion. *J. Fluid Mech.*, 46 (01):199–208, 1971.

[10] H Brenner and M H Weissman. Rheology of a dilute suspension of dipolar spherical particles in an external field. II. effects of rotary Brownian motion. *J. Colloid Interface Sci.*, 41(3):499–531, 1972.

[11] A D Brent, V R Voller, and K J Reid. Enthalpy-porosity technique for modeling convection-diffusion phase change: Application to the melting of a pure metal. *Numer. Heat Transfer, Part A*, 13(3):297–318, 1988.

[12] T Brotto, J B Caussin, E Lauga, and D Bartolo. Hydrodynamics of confined active fluids. *Phys. Rev. Lett.*, 110(3):038101, 2013.

[13] S Chandrasekhar. *Hydrodynamic and Hydromagnetic Stability*. Courier Dover Publications, 2013.

[14] M Couette. Études sur le frottement des liquides. *Ann. Chim. Phys.*, 6(21):433–510, 1890.

[15] T R Dafforn and A Rodger. Linear dichroism of biomolecules: Which way is up? *Curr. Opin. Struct. Biol.*, 14(5):541–546, 2004.

[16] T R Dafforn, J Rajendra, D J Halsall, L C Serpell, and A Rodger. Protein fiber linear dichroism for structure determination and kinetics in a low-volume, low-wavelength Couette flow cell. *Biophys. J.*, 86(1):404–410, 2004.

[17] M Doi and S F Edwards. *The theory of polymer dynamics*, volume 73. Oxford University Press, 1988.

[18] M A Dominguez-Lerma, G Ahlers, and D S Cannell. Marginal stability curve and linear growth rate for rotating Couette–Taylor flow and Rayleigh–Bénard convection. *Phys. Fluids*, 27(4):856–860, 1984.

[19] R J Donnelly and K W Schwarz. Experiments on the stability of viscous flow between rotating cylinders. VI. finite-amplitude experiments. *Proc. R. Soc. London, Ser. A*, 283(1395):531–556, 1965.

[20] P G Drazin. *Introduction to hydrodynamic stability.* Cambridge University Press, 2002.

[21] R Dreyfus, J Baudry, M L Roper, M Fermigier, H A Stone, and J Bibette. Microscopic artificial swimmers. *Nature*, 437(7060):862–865, 2005.

[22] R J Dyson and O E Jensen. A fibre-reinforced fluid model of anisotropic plant cell growth. *J. Fluid Mech.*, 655:472–503, 2010.

[23] R J Dyson, J E F Green, J P Whiteley, and H M Byrne. An investigation of the influence of extracellular matrix anisotropy and cell–matrix interactions on tissue architecture. *J. Math. Biol.*, 72:1775–1809, 2015.

[24] J L Ericksen. Transversely isotropic fluids. *Colloid. Polym. Sci.*, 173(2):117–122, 1960.

[25] G Garab and H van Amerongen. Linear dichroism and circular dichroism in photosynthesis research. *Photosynth. Res.*, 101(2-3):135–146, 2009.

[26] H Giesekus. Elasto-viskose flüssigkeiten, für die in stationären schichtströmungen sämtliche normalspannungskomponenten verschieden gross sind. *Rheol. Acta*, 2(1): 50–62, 1962.

[27] R J Goldstein and D J Graham. Stability of a horizontal fluid layer with zero shear boundaries. *Phys. Fluids (1958-1988)*, 12(6):1133–1137, 1969.

[28] R Golestanian, T B Liverpool, and A Ajdari. Propulsion of a molecular machine by asymmetric distribution of reaction products. *Phys. Rev. Lett.*, 94(22):220801, 2005.

[29] J E F Green and A Friedman. The extensional flow of a thin sheet of incompressible, transversely isotropic fluid. *Eur. J. Appl. Math.*, 19(3):225–258, 2008.

[30] B M Haines, I S Aranson, L Berlyand, and D A Karpeev. Effective viscosity of dilute bacterial suspensions: A two-dimensional model. *Phys. Bio.*, 5(4):046003, 2008.

[31] B M Haines, A Sokolov, I S Aranson, L Berlyand, and D A Karpeev. Three-dimensional model for the effective viscosity of bacterial suspensions. *Phys. Rev. E*, 80(4):041922, 2009.

[32] D L Hartmann, L A Moy, and Q Fu. Tropical convection and the energy balance at the top of the atmosphere. *J. Clim.*, 14(24):4495–4511, 2001.

[33] J P Hernandez-Ortiz, C G Stoltz, and M D Graham. Transport and collective dynamics in suspensions of confined swimming particles. *Phys. Rev. Lett.*, 95(20):204501, 2005.

[34] M R Hicks, A Rodger, C M Thomas, S M Batt, and T R Dafforn. Restriction enzyme kinetics monitored by UV linear dichroism. *Biochemistry*, 45(29):8912–8917, 2006.

[35] N A Hill and T J Pedley. Bioconvection. *Fluid Dyn. Res.*, 37(1):1–20, 2005.

[36] E J Hinch and L G Leal. The effect of brownian motion on the rheological properties of a suspension of non-spherical particles. *J. Fluid Mech.*, 52(04):683–712, 1972.

[37] J Hoepffner. Implementation of boundary conditions. `http://www.fukagata.mech.keio.ac.jp/~jerome/web/boundarycondition.pdf`, 2007. [Online; accessed 07-Nov-2015].

[38] C R Holloway, R J Dyson, and D J Smith. Linear Taylor–Couette stability of a transversely isotropic fluid. *Proc. R. Soc. Lond. A*, 471(2178):20150141, 2015. ISSN 1364-5021.

[39] J R Howse, R A L Jones, A J Ryan, T Gough, R Vafabakhsh, and R Golestanian. Self-motile colloidal particles: From directed propulsion to random walk. *Phys. Rev. Lett.*, 99(4):048102, 2007.

[40] B D Hull, T G Rogers, and A J M Spencer. A linear stability analysis of flows of transversely isotropic non-Newtonian fluids. *J. Non-Newt. Fluid Mech.*, 43(2): 325–349, 1992.

[41] G R Hunt and P P Linden. The fluid mechanics of natural ventilation displacement ventilation by buoyancy-driven flows assisted by wind. *Build. Sci.*, 34(6):707–720, 1999.

[42] Y Hwang and T J Pedley. Bioconvection under uniform shear: Linear stability analysis. *J. Fluid Mech.*, 738:522–562, 2014.

[43] G B Jeffery. The motion of ellipsoidal particles immersed in a viscous fluid. *Proc. R. Soc. Lond. A*, 102(715):161–179, 1922.

[44] S Kim and S J Karrila. *Microhydrodynamics: Principles and selected applications*. Butterworth-Heinemann, 1991.

[45] D L Koch and G Subramanian. Collective hydrodynamics of swimming microorganisms: Living fluids. *Annu. Rev. Fluid Mech.*, 43:637–659, 2011.

[46] E L Koschmieder. *Bénard cells and Taylor vortices*. Cambridge University Press, 1993.

[47] K Kruse, J F Joanny, F Jülicher, J Prost, and K Sekimoto. Generic theory of active polar gels: A paradigm for cytoskeletal dynamics. *Euro. Phys. J. E*, 16(1):5–16, 2005.

[48] J C Lagarias, J A Reeds, M H Wright, and P E Wright. Convergence properties of the nelder–mead simplex method in low dimensions. *SIAM J. Control*, 9(1):112–147, 1998.

[49] E Lauga and T R Powers. The hydrodynamics of swimming microorganisms. *Rep. Prog. Phys.*, 72(9):096601, 2009.

[50] Eric Lauga and Sébastien Michelin. Stresslets induced by active swimmers. *Phys. Rev. Lett.*, 117(14):148001, 2016.

[51] L G Leal and E J Hinch. The effect of weak brownian rotations on particles in shear flow. *J. Fluid Mech.*, 46(04):685–703, 1971.

[52] M E M Lee and H Ockendon. A continuum model for entangled fibres. *Eur. J. Appl. Math.*, 16(2):145–160, 2005.

[53] F M Leslie. The stability of Couette flow of certain anisotropic fluids. *Proc. Camb. Phil. Soc*, 60:949–955, 1964.

[54] G G Lipscomb, M M Denn, DU Hur, and DV Boger. The flow of fiber suspensions in complex geometries. *J. Non-Newton. Fluid.*, 26(3):297–325, 1988.

[55] H M López, J Gachelin, C Douarche, H Auradou, and E Clément. Turning bacteria suspensions into superfluids. *Phys. Rev. Lett.*, 115:028301, 2015.

[56] R Marrington, E Small, A Rodger, T R Dafforn, and S G Addinall. FtsZ fiber bundling is triggered by a conformational change in bound GTP. *J. Biol. Chem.*, 279(47):48821–48829, 2004.

[57] R Marrington, T R Dafforn, D J Halsall, J I MacDonald, M Hicks, and A Rodger. Validation of new microvolume Couette flow linear dichroism cells. *Analyst*, 130(12): 1608–1616, 2005.

[58] J Marshall and F Schott. Open-ocean convection: Observations, theory, and models. *Rev. Geophys.*, 37(1):1–64, 1999.

[59] J R A McLachlan, D J Smith, N P Chmel, and A Rodger. Calculations of flow-induced orientation distributions for analysis of linear dichroism spectroscopy. *Soft Matt.*, 9(20):4977–4984, 2013.

[60] R Meyer-Spasche. *Pattern Formation in Viscous Flows: The Taylor-Couette Problem and the Rayleigh-Bénard Convention*. Springer, 1999.

[61] C B Moler and G W Stewart. An algorithm for generalized matrix eigenvalue problems. *SIAM J. Numer. Anal.*, 10(2):241–256, 1973. doi: 10.1137/0710024.

[62] H Ockendon and J R Ockendon. *Viscous flow*, volume 13. Cambridge University Press, 1995.

[63] R Pacheco-Gómez, J Kraemer, S Stokoe, HJ England, CW Penn, E Stanley, A Rodger, J Ward, MR Hicks, and TR Dafforn. Detection of pathogenic bacteria using a homogeneous immunoassay based on shear alignment of virus particles and linear dichroism. *Anal. Chem.*, 84(1):91–97, 2011.

[64] A E Patteson, A Gopinath, and P E Arratia. Active colloids in complex fluids. *Curr. Opin. Colloid Interface Sci.*, 21:86–96, 2016.

[65] T J Pedley and J O Kessler. A new continuum model for suspensions of gyrotactic micro-organisms. *J. Fluid Mech.*, 212:155–182, 1990.

[66] T J Pedley and J O Kessler. Hydrodynamic phenomena in suspensions of swimming microorganisms. *Annu. Rev. Fluid Mech.*, 24(1):313–358, 1992.

[67] Lord Rayleigh. On convection currents in a horizontal layer of fluid, when the higher temperature is on the under side. *Philos. Mag. (1798-1977)*, 32(192):529–546, 1916.

[68] A Recktenwald, M Lücke, and HW Müller. Taylor vortex formation in axial throughflow: Linear and weakly nonlinear analysis. *Phys. Rev. E*, 48(6):4444–4454, 1993.

[69] A Rodger, R Marrington, MA Geeves, M Hicks, L de Alwis, DJ Halsall, and TR Dafforn. Looking at long molecules in solution: What happens when they are subjected to Couette flow? *Phys. Chem.*, 8(27):3161–3171, 2006.

[70] T G Rogers. Squeezing flow of fibre-reinforced viscous fluids. *J. Eng. Math.*, 23(1): 81–89, 1989.

[71] D Saintillan. The dilute rheology of swimming suspensions: A simple kinetic model. *Exp. Mech.*, 50(9):1275–1281, 2010.

[72] D Saintillan and M J Shelley. Orientational order and instabilities in suspensions of self-locomoting rods. *Phys. Rev. Lett.*, 99(5):058102, 2007.

[73] D Saintillan and M J Shelley. Instabilities, pattern formation, and mixing in active suspensions. *Phys. Fluids*, 20(12):123304, 2008.

[74] D Saintillan and M J Shelley. Active suspensions and their nonlinear models. *C. R. Phys.*, 14(6):497–517, 2013.

[75] Eric SG Shaqfeh and Glenn H Fredrickson. The hydrodynamic stress in a suspension of rods. *Phys. Fluids*, 2(1):7–24, 1990.

[76] R A Simha and S Ramaswamy. Hydrodynamic fluctuations and instabilities in ordered suspensions of self-propelled particles. *Phys. Rev. Lett.*, 89(5):058101, 2002.

[77] E Small, R Marrington, A Rodger, DJ Scott, K Sloan, D Roper, TR Dafforn, and SG Addinall. FtsZ polymer-bundling by the Escherichia coli ZapA orthologue, YgfE, involves a conformational change in bound GTP. *J. Mol. Biol.*, 369(1):210–221, 2007.

[78] A Sokolov, I S Aranson, J O Kessler, and R E Goldstein. Concentration dependence of the collective dynamics of swimming bacteria. *Phys. Rev. Lett.*, 98(15):158102, 2007.

[79] B Spain. *Tensor calculus*. University mathematical texts. Oliver and Boyd, 1953.

[80] A J M Spencer. Fibre-streamline flows of fibre-reinforced viscous fluids. *Eur. J. Appl. Math.*, 8(02):209–215, 1997.

[81] E A Spiegel and G Veronis. On the Boussinesq approximation for a compressible fluid. *ApJ*, 131:442, 1960.

[82] G Subramanian and D L Koch. Critical bacterial concentration for the onset of collective swimming. *J. Fluid Mech.*, 632:359–400, 2009.

[83] G Subramanian, D L Koch, and S R Fitzgibbon. The stability of a homogeneous suspension of chemotactic bacteria. *Phys. Fluids*, 23(4):041901, 2011.

[84] O G Sutton. On the stability of a fluid heated from below. *Proc. R. Soc. London, Ser. A*, 204(1078):297–309, 1950.

[85] G I Taylor. Stability of a viscous liquid contained between two rotating cylinders. *Proc. R. Soc. London, Ser. A*, 102(718):541–542, 1923.

[86] L N Trefethen. *Spectral methods in MATLAB*, volume 10. Siam, 2000.

[87] J Wagner. Taylor-wirbel zwischen zwei zylinderwnden, sichtbar gemacht mit einer farb-partikel-mischung in wasser, 1992. URL `https://commons.wikimedia.org/wiki/File:Taylor_Wirbel_02.jpg`.

[88] Z H Wan and J Z Lin. Hydrodynamic instability of semi-concentration fiber suspensions between two rotating coaxial cylinders. *Int. J. Nonlin. Sci. Num.*, 5(3): 211–216, 2004.

[89] Wikimedia-Commons. Gold paint dissolved in acetone, 2005. URL `https://commons.wikimedia.org/wiki/File:Bnard_cells_convection.ogv`.

[90] F G Woodhouse and R E Goldstein. Spontaneous circulation of confined active suspensions. *Phys. Rev. Lett.*, 109(16):168105, 2012.

[91] T S Yu, E Lauga, and A E Hosoi. Experimental investigations of elastic tail propulsion at low reynolds number. *Phys. Fluids*, 18(9):091701, 2006.